



MONASH University

Towards multi-SAR-mission retrieval of soil moisture

LiuJun Zhu

MSc in Geographical Information Science

BSc in Geographical Science

A thesis submitted for the degree of Doctor of Philosophy at
Monash University in 2019
Department of Civil Engineering
Faculty of Engineering

Copyright Notice

© Liujun Zhu (2019).

Under the Copyright Act 1968, this thesis must be used only under the normal conditions of scholarly fair dealing. In particular no results or conclusions should be extracted from it, nor should it be copied or closely paraphrased in whole or in part without the written consent of the author. Proper written acknowledgement should be made for any assistance obtained from this thesis.

I, Liujun Zhu, certify that I have made all reasonable efforts to secure copyright permissions for third-party content included in this thesis and have not knowingly added copyright content to my work without the owner's permission.

Abstract

Remote sensing of near surface soil moisture is of tremendous scientific interest and practical value due to its importance for various applications. Over the past four decades, a large number of remote sensing approaches have been developed and tested to measure soil moisture. Products at low resolution (tens km) are provided routinely by several passive microwave missions, while regular soil moisture monitoring at high spatial resolution (0.1 – 1 km) is still unresolved. Spaceborne Synthetic Aperture Radars (SARs) provide a promising alternative for high spatial resolution soil moisture mapping, with operational use now possible due to the number of existing and planned SAR missions in the next decade. However, these multiple SAR missions need to be combined to reach the science requirements for sampling a variable like soil moisture that is characterized by a high temporal variability (2 – 3 days), with the way to combine the multiple SAR missions still unresolved.

Therefore, this research has focused on developing a methodology that can combine data from a multi-SAR-mission approach to derive reliable soil moisture (better than $0.06 \text{ m}^3/\text{m}^3$) with high spatial (tens m) and temporal (2 – 3 days) resolution. The method follows the assumption of time-invariant roughness and vegetation for the retrieval period, with the first step ensuring the assumption, the second and third steps retrieving soil moisture from time series multi-angular and multi-frequency data, respectively. This research is mostly based on field data collected from two Soil Moisture Active Passive Experiments (SMAPEX-4 and -5) as part of this PhD.

First, the airborne L-band radar system was calibrated to provide a unique dense L-band data set for development of the proposed multi-SAR-mission retrieval. The calibration based on SMAPEX-4 and -5 showed a radiometric root mean square error (RMSE) of better than 0.65 dB, an average channel imbalance of 0.17 dB in amplitude and 3.87° in phase. Cross-validation with PALSAR-2 confirmed the calibration accuracy of the PLIS data over various land cover types and the potential for SAR system cross-calibration.

The state-of-the-art numerical and physical scattering models were combined to build a series of look up tables (LUTs), covering typical remote sensing radar configurations and landcover types. An unsupervised change detection method was subsequently proposed to ensure the time-invariant roughness and vegetation changes for the period of interest, being a pre-processing procedure of the subsequent soil moisture retrieval. Results showed an accurate identification of changed paddocks ($> 90\%$) while presenting a low false-alarm rate ($< 10\%$).

After the detection of changed paddocks, SAR time series observations were separated into multiple sub-series for those with roughness and/or VWC changes. To retrieve soil moisture from a single SAR mission operating with time-varying imaging modes, orbits and radar beams, a time series multi-angular retrieval method was proposed, using a genetic algorithm to minimize the difference between LUTs and time series multi-angular radar observations with the constraint of a drying down soil moisture. Evaluation based on the SMAPE_{x-5} dataset showed a retrieval RMSE of $0.07 \text{ m}^3/\text{m}^3$ at the 25-m pixel scale and $0.056 \text{ m}^3/\text{m}^3$ at the paddock scale respectively. The effectiveness of the proposed method for irregularly collected data with different imaging modes was also confirmed.

A multi-frequency framework was finally presented as an extension of the above time series multi-angular method for joint multi-SAR mission soil moisture retrieval. The input multi-frequency data with negligible scattering (low soil contribution) from the soil surface was removed before undertaking soil moisture retrieval. Soil moisture retrieval was carried out independently for each landcover type using an optimization method and forward LUTs. Retrieval from 20 multi-frequency (L-, C- and X-band) images collected in 15 days of a three-week period showed an acceptable overall RMSE of $0.058 \text{ cm}^3/\text{cm}^3$ at the paddock scale ($\sim 0.1 - 0.5 \text{ km}$). The comparison with single and dual frequency retrieval suggests that multi-frequency retrieval does not necessarily lead to the highest accuracy. However, it leads to significantly enhanced temporal resolution with only minimal deterioration in accuracy.

Declaration

This thesis contains no material which has been accepted for the award of any other degree or diploma at any university or equivalent institution and that, to the best of my knowledge and belief, this thesis contains no material previously published or written by another person, except where due reference is made in the text of the thesis.

Signature:

Print Name: LiuJun Zhu

Date: 28/04/2019

Acknowledgements

I would like to appreciate various people sincerely, who have helped in carrying out this thesis.

First of all, I would like to express my very great gratitude to my main supervisor Professor Jeffrey Walker for his patience, generosity, encouragement throughout my study. His systematic guidance has helped improve my scientific thinking competence, linguistic competence and public speaking skills, and his passion for research has strengthened my conviction of being a scientist. I have been greatly benefited from his serious attitude towards almost everything in work and life. I am particularly grateful to my co-supervisor Dr. Christoph Rüdiger for his constructive suggestions, insightful comments and useful critiques regarding this thesis.

Special thanks should be given to Professor Leung Tsang of the University of Michigan-Ann Arbor. With his expert guidance, I solved some key problems and made a significant progress on my study during the half a year of visiting. Warm hospitality provided by Dr. Huanting Huang and the accompany of Dr. Surun Tan, Dr. Tai Qiao, Jiyue Zhu, Yanlei Du and Weihui Gu in the USA made my visiting an unforgettable experience.

I want to thank all participants in two Soil Moisture Active and Passive campaigns (SMAPEX-4 and -5) for their help on collecting the in-situ and airborne data and making the campaigns enjoyable.

I would also like to extend my thanks to my colleagues Dr. Nan Ye, Dr. Xiaoling Wu, and Dr. Ying Gao, who are like my families, supporting me selflessly in both academic field and daily life, especially Nan who set up the “base of U2 2027 Dandenong Road”, making research and life much more convenient. Thank my colleague Xiaoji Shen for cooking every day, without whom I should be 10 kg less. More importantly, they together with all the other members in the group have made this journey more colorful.

At the end, my thanks would go to my beloved family for their loving considerations and great confidence in me through all these years. I would finally like to express my

gratitude to my wife Hui Gao, who has always been encouraging me, bothering me and supporting me without a word of complaint. Thank you for always being “around”.

Table of Contents

Copyright Notice	i
Abstract	ii
Declaration.....	iv
Acknowledgements.....	vi
Table of Contents.....	viii
List of Symbols.....	xii
List of Abbreviations.....	xiv
List of Figures	xviii
List of Tables	xxiv
1 Introduction	1-1
1.1 Background.....	1-1
1.2 Problem and Objective.....	1-2
1.3 Outline of Approach.....	1-3
1.4 Thesis organization.....	1-4
2 Literature Review.....	2-1
2.1 Importance of Soil Moisture.....	2-1
2.2 Techniques for Soil Moisture Estimation	2-5
2.2.1 <i>In-situ</i> soil moisture measurement.....	2-5
2.2.2 Remote sensing techniques.....	2-6
2.2.3 Present and projected SAR satellite missions.....	2-12
2.3 Scattering from the Earth’s Surface	2-15
2.3.1 Characterization of soil parameters	2-16
2.3.2 Scattering models for bare soil.....	2-18
2.3.3 Scattering models for vegetated surfaces.....	2-21
2.4 Soil Moisture Retrieval from SAR Data.....	2-24
2.4.1 Multi-configuration methods.....	2-24
2.4.2 Multi-temporal methods.....	2-27
2.5 Knowledge Gap and Proposed Approach.....	2-29
2.6 Chapter Summary.....	2-31

3	Data Sets	3-1
3.1	The SMAPEX Campaign Data	3-1
3.1.1	Airborne radar observations.....	3-3
3.1.2	Ground observations.....	3-7
3.2	Satellite Data	3-10
3.3	Chapter Summary.....	3-13
4	Calibration and Validation of PLIS	4-1
4.1	Background	4-1
4.2	Calibration Site and data	4-4
4.2.1	Experiments and the Calibration Site	4-4
4.2.2	Data.....	4-6
4.3	Method.....	4-8
4.3.1	Calibration method.....	4-8
4.3.2	Evaluation and cross-validation method.....	4-9
4.4	Results.....	4-11
4.4.1	Calibration accuracy over point targets	4-11
4.4.2	Comparison of PLIS and PALSAR-2.....	4-17
4.5	Chapter Summary.....	4-20
5	Forward Scattering Models	5-1
5.1	Forward models used in this thesis	5-1
5.1.1	NMM3D based LUTs.....	5-2
5.1.2	Oh model	5-3
5.1.3	Distorted Born approximation	5-3
5.2	Data sets	5-6
5.2.1	Ground measurements.....	5-6
5.2.2	Radar data	5-9
5.3	Development of the look up tables	5-9
5.3.1	LUTs for bare soil.....	5-10
5.3.2	LUTs for vegetated area	5-12
5.4	Forward model evaluation	5-14
5.4.1	Evaluation of L-band LUTs.....	5-14
5.4.2	Evaluation of C- and X-band LUTs	5-16

5.5	Chapter Summary.....	5-18
6	Surface Anomaly Change Detection.....	6-1
6.1	Background.....	6-1
6.2	SMAPEx-5 Data Set.....	6-4
6.2.1	Ground measurements	6-4
6.2.2	Radar data.....	6-5
6.3	Synthetic Data Set.....	6-9
6.3.1	Synthetic surface parameters	6-9
6.3.2	Construction of synthetic radar data	6-10
6.3.3	Validation metrics.....	6-11
6.4	Method	6-14
6.4.1	Feature selection and extraction at the paddock scale.....	6-15
6.4.2	Determination of the change maps	6-17
6.5	Results	6-20
6.5.1	Optimal feature space.....	6-21
6.5.2	Evaluation using synthetic data sets	6-23
6.5.3	Evaluation using real observational data set.....	6-27
6.6	Chapter Summary.....	6-29
7	Time Series Multi-Angular Retrieval.....	7-1
7.1	Background.....	7-1
7.2	Data set	7-2
7.3	Method	7-3
7.4	Results	7-6
7.4.1	Retrieval results.....	7-6
7.4.2	The effect of time interval and polarization combination.....	7-12
7.5	Chapter Summary.....	7-14
8	Time series multi-frequency retrieval.....	8-1
8.1	Background.....	8-1
8.2	Data set	8-2
8.3	Method	8-3
8.3.1	Overview of the framework.....	8-3
8.3.2	Determination of effective radar configuration.....	8-5

8.3.3	Multi-frequency retrieval method.....	8-7
8.4	Results.....	8-8
8.4.1	Effective radar configuration	8-8
8.4.2	Multi-frequency retrieval.....	8-10
8.4.3	The effect of abrupt cultivation activities.....	8-16
8.5	Chapter Summary.....	8-17
9	Conclusions and Future Work.....	9-1
9.1	Conclusions.....	9-1
9.1.1	Calibration and validation of PLIS.....	9-1
9.1.2	Forward scattering models	9-2
9.1.3	Surface anomaly change detection	9-3
9.1.4	Time series multi-angular retrieval	9-4
9.1.5	Time series multi-frequency retrieval.....	9-5
9.2	Future Work.....	9-5
	References.....	1

List of Symbols

Symbols	Units	Definitions
a	[°]	Azimuth angle of vegetation scatters
β	[°]	Elevation angle of vegetation scatters
ρ	-	Fresnel reflection coefficient
ε_s	-	Relative permittivity of soil
ε_s'	-	Real part of soil relative permittivity
ε_s''	-	Imaginary part of soil relative permittivity
ε_v	-	Relative permittivity of vegetation material
μ	-	Average feature vector
θ	[°]	Incidence angle
mv	[m ³ /m ³]	Soil moisture
λ	[m]	Wavelength
τ	-	Optical depth
σ	[dBsm]	Radar cross section
σ^o	[dB]	Backscattering coefficient
σ_s^o	[dB]	Backscattering coefficient for bare soil
σ_{pq}^o	[dB]	Backscattering coefficient at polarization pq
$\sigma_{pq, sr}^o$	-	Double bounce scattering (Scattered-Reflected)
$\sigma_{pq, rs}^o$	-	Double bounce scattering (Reflected-Scattered)
$\sigma_{pq, v}^o$	-	Volume scattering from vegetation layer
C_s	-	Relative contribution related to soil surface

CF_a	[dB]	The absolute calibration factor
CF_{tri}	[dB]	The absolute calibration factor from a trihedral
C^*	-	Covariance matrix
d	[m]	The depth of the vegetation layer
E_{cal}	[dB]	Calibration accuracy
f_{pq}	-	Scattering amplitude at polarization pq
H	-	Horizon
H_R	[cm]	Surface root mean square
K	-	Effective propagation constants
k	[1/m]	Wave number
k_0	[1/m]	Wave number in free space
l	[m]	Length of a vegetation scatter (cylinder)
L_C	[cm]	Correlation length
l_{tri}	[m]	Length of the trihedral leg
M_{veg}	m^3/m^3	Volumetric vegetation water content
N_s	-	Number of the selected feature
N_a	-	Number of available features
n	[1/m ³]	Number density of vegetation scatters (cylinder) in a vegetation layer
p, q	-	Polarization, either horizontal (H) or vertical (V)
r	[cm]	Radius of a cylinder
R	-	Correlation coefficient
R_p	-	Coherent reflectivity at polarization p

List of Abbreviations

ACF	Autocorrelation function
ALOS	Advanced Land Observing Satellite
AIRSAR	AIRborne Synthetic Aperture Radar
AR	Accuracy rate
COSMO-SkyMed	Constellation of Small Satellites for Mediterranean basin Observation
DBA	Distorted Born approximation
DBSAR	Digital Beamforming Synthetic Aperture Radar
DBSCAN	Density-Based Spatial Clustering of Applications with Noise
DLR	Deutsches Zentrum für Luft- und Raumfahrt
DTM	Digital Terrain Model
ESA	European Space Agency
ESCAT	European C-band scatterometer
FAR	False alarm rate
GPS	Global Position System
GIS	Geographic Information System
ICA	Infinite Cylinder Approximation
IEM	Integral Equation Model
InSAR	Interferometric synthetic aperture radar
IRF	Impulse Response Function
ISLR	Integrated Side Lobe Ratio
JAXA	Japan Aerospace Exploration Agency

LULC	Land Use Land Cover
LUT	Look Up Table
MIMICS	Michigan Microwave Canopy Scattering Model
NASA	National Aeronautics and Space Administration
NDVI	Normalized Difference Vegetation Index
NDWI	Normalized Water Index
NISAR	NASA–Indian Space Research Organization Synthetic Aperture Radar
NMM3D	Numerical solutions of Maxwell’s question in three demission
OLI	Operational Land Imager
PALSAR	Phased Array type L-band Synthetic Aperture Radar
PARC	Polarimetric Active Radar Calibrator
PRC	Passive Radar Calibrator
Pi-SAR-L2	Polarimetric and Interferometric Airborne Synthetic Aperture Radar L2
PSLR	Peak-to-Side Lobe Ratio
RCS	Radar Cross Section
RMSD	Root Mean Squared Difference
RMSE	Root Mean Squared Error
RT	Radiative Transfer
RVI	Radar Vegetation Index
SAR	Synthetic Aperture Radar
SLC	Single Look Complex
SMAP	Soil Moisture Active Passive
SMAPE_x	Soil Moisture Active Passive Experiment

SMOS	Soil Moisture and Ocean Salinity
TopSAR	Terrain Observation with Progressive Scan SAR
WCM	Water Cloud Model
WI	Wetness Index
WMO	World Meteorological Organization

List of Figures

Figure 2-1: The capability of techniques for soil moisture measurements, together with the spatial and temporal requirements of various applications.....2-4

Figure 2-2: Conceptual figure of the synthesized expanding beamwidth, adapted from Ulaby et al. (2014).....2-10

Figure 2-3: Imaging modes of SAR.....2-15

Figure 2-4: Conceptual scattering of an incident radar signal by a vegetated surface; modified from Ulaby et al. (2014).....2-22

Figure 2-5: Conceptual relationship among the multi-configuration methods, multi-temporal methods, and the proposed method for multi-SAR mission retrieval.....2-30

Figure 3-1: Layout of the SMAPEX study area showing the location of six focus areas and the landcover during SMAPEX-5.....3-2

Figure 3-2: Time series of the top 5 cm soil moisture and rainfall measurements from all OzNet sites over the Yanco area 2015; the solid black line and dashed black lines show the mean and 25th/75th percentiles of soil moisture respectively.....3-2

Figure 3-3: Schematic of PLIS mapping geometry at a flight height of 3000 m.....3-6

Figure 3-4: An example of ground soil moisture sampling on Sep. 9th, 2015 for the focus area YA4, with the background being the Landsat-8 near-infrared/red/green composition. Three point-based soil moisture measurements were made within a 1 m radius at each location for small scale variability.....3-7

Figure 3-5: Main steps for soil roughness calculation: roughness photo (top), extracted pin profile (middle) and digital profile (bottom).....3-10

Figure 3-6: Examples of radar data (HH polarization), covering the YA4, YA7 and YE areas, with the PLIS, PALSAR-2, RADARSAT-2 and COSMO SkyMed data collected on Sep. 11, 24, 11, and 10, 2015 respectively.....3-12

Figure 4-1: Calibration sites and flights used in the calibration and validation, as well as the PLIS and PALSAR2 coverage during the SMAPE-4 and -5. The top left shows the location of the Yanco agricultural area and the spatial coverage of PLIS and PALSAR-2 data. The middle left is the land

cover map of SMAPEx-5 with the main calibration sites delineated in black rectangles. Areas A and B show the deployment of PARCs and trihedrals for the corresponding calibration flights (the yellow lines in the bottom panel) respectively. Area C includes the forest areas used in the polarimetric calibration. The middle right is an example of PLIS HH data acquired on September 17, 2015.....	4-5
Figure 4-2: RCS patterns of the trihedral (a) and PARC (b) for L-band.....	4-6
Figure 4-3: Definition of point target area and background area for extracting the response of a point target. The range and azimuth spacing are 3.75 m and 2 m respectively.....	4-9
Figure 4-4: Schematic of PLIS and PALSAR-2 comparison. The grid cell size in azimuth and look direction is the same, but the real ground size ranges from 500 – 750m for different PLIS strips because of the variation of ground range spacing.....	4-11
Figure 4-5 Response of trihedral PRCs after calibration. (a) and (b) are the RCSs and co-polarized phase differences of all trihedrals during SMAPEx-4 and 5, respectively. (c) and (d) are the time series average RCS of trihedrals and the averaged crosstalk estimated from trihedrals and forest respectively.....	4-14
Figure 4-6: Amplitude (a) and phase (b) differences of the polarimetrically calibrated PLIS data from PARCs.....	4-15
Figure 4-7: RGB image of the Freeman-Durden decomposition powers in dB where red, green and blue are dihedral, volume and surface component respectively. (a) and (b) are results over an urban and forest area respectively. (c) - (f) are results of May 3rd, September 24th and 27th of an agricultural area where the irrigated fields were delineated with white boundaries.....	4-16
Figure 4-8: Comparison of PLIS and PALSAR-2 backscattering coefficient in dB. (a) and (b) are HH and HV for SMAPEx-5 (PLIS and PALSAR-2 Stripmap) respectively while (c) and (d) are HH and HV for SMAPEx-4 (PLIS and PALSAR-2 ScanSAR).....	4-18
Figure 4-9: The relationship between the correlation coefficient and spatial heterogeneity.....	4-20
Figure 5-1: Schematic of vegetation layer and soil surface as well as the scattering mechanisms in distorted Born approximation (DBA), adapted from Huang et al. (2017a). The subscripts v , sr , rs , and s are the volume, scattered-reflected, reflected-scattered and surface scattering, respectively.	

q and p are either horizontal (H) or vertical (V) polarization of the incident and scattered fields; a , β , r and l are the azimuth angle, elevation angle, radius, and length of a cylinder, respectively.	5-4
Figure 5-2: Landcover and paddocks in the three SMAPEx-5 focus farms used in the development and evaluation of the forward models. The focus farms include YA4 (left), YA7 (middle) and YE (right). The paddocks with ID are those with ground roughness and/or vegetation measurements as given in Table 5-2.	5-6
Figure 5-3: Fitted relationship between vegetation water content and vegetation height	5-8
Figure 5-4: The effect of L_C/H_R on L-band forward accuracy over bare soil at a spatial resolution of 25 m.	5-11
Figure 5-5: Comparison of forward NMM3D-DBA σ^0 and PLIS multi-angular observations at the paddock scale ($\sim 0.1 - 0.5$ km). The dash lines denote the ± 1 dB offset. R refers to Pearson correlation coefficient.	5-14
Figure 5-6: The difference of measured and predicted σ^0 at HH polarization versus incidence angle. The circled points belong to paddock #80 that was ploughed nearly perpendicular to the radar look directions.	5-15
Figure 5-7: Comparison of forward and observed σ^0 at the paddock scale ($\sim 0.1 - 0.5$ km) for available C- and X-band data. The dash lines denote the ± 1 dB offset. R refers to Pearson correlation coefficient.	5-17
Figure 5-8: Conceptual figure showing the two potential reasons for the overestimated attenuation in DBA. (a) shows the attenuation overestimation caused by the overestimation of incident field in a single cylinder. (b) shows the effect of a 20 % gap between vegetations on attenuation estimation.	5-18
Figure 6-1: Flowchart showing the factors affecting backscatter changes from multi-temporal SAR images. The solid rectangles at the bottom level show the sources that should be considered before applying soil moisture retrieval from multi-temporal SAR images with short time interval.	6-2
Figure 6-2: Focus area selected for algorithm evaluation using ground measurements. The right panel shows two examples where roughness changed during the period of SMAPEx-5.	6-4
Figure 6-3: Anomaly surface changes at L-band (PLIS) multi-temporal SAR images. (a) shows the changed paddocks observed between DOY 267 and 270, 2015 on a false color composite Landsat 8 OLI image (RGB: near-	

infrared/red/green); (b), (c), (d) are the backscatter difference maps in HH, HV and VV polarizations between images acquired on DOY 267 and 270 with the changed paddocks delineated as well, respectively; (e), (f) and (g) are respectively the time series HH, HV and VV of several examples, which also include the average backscattering coefficient of the whole area labeled as “All”. 6-8

Figure 6-4: Flowchart of synthetic radar data construction (a) and the validation process over the synthetic radar data using the Wanger’s method (b). The s and VWC are roughness RMS height and vegetation water content with the superscript 1 and 2 being the initial and changed states. $m_{1,q}$ denote time series soil moisture from the first to q^{th} dates. 6-13

Figure 6-5: Flowchart of the proposed change detection method. 6-14

Figure 6-6: An example showing the process of generating the change map for the period of t and $t-1$ using an L-band series. White paddocks are those identified as changed. The label C refer to over-detected maps with the subscripts denoting the periods. Three over-detected maps for the periods of t and $t-1$ were generated first and then merged to remove the false alarms. 6-19

Figure 6-7: Performance of the proposed method on single-look synthetic data sets. (a) - (d) are the AR , FAR , F and RMSE of wetness index at L-, C- and X-bands with various incidence angles, respectively. The error bars denote the standard deviation of metrics. 6-24

Figure 6-8: Impact of noise on performance at L-band synthetic data. (a) shows the average AR , FAR , and F versus the number of looks; (b) shows the RMSE of wetness index versus the number of looks. The error bars denote the standard deviation of metrics..... 6-26

Figure 6-9: Impact of roughness and VWC change amplitude on performance at L-band synthetic data. (a) shows the average AR , FAR , and F versus change amplitude; (b) shows the RMSE of wetness index versus change amplitude. The error bars denote the standard deviation of metrics. 6-27

Figure 6-10: Change detection results versus ground truth at real SAR data collected during SMAPEX-5 study period. The dashed lines show the start and end time of the period of interest for each change map..... 6-28

Figure 7-1: Observation geometry of airborne PLIS for each flight in SMAPEX-5. 7-3

Figure 7-2: Flowchart of the soil moisture retrieval method..... 7-6

Figure 7-3: In-situ versus retrieved soil moisture at the 25m pixel scale. The dash lines denote the target accuracy of $\pm 0.06 \text{ m}^3/\text{m}^3$	7-7
Figure 7-4: Time series soil moisture maps of focus farms YA4 (a), YA7 (b) and YE (c) during the eight observation dates of the SMAPEX-5 period.....	7-8
Figure 7-5: Comparison of retrieved and in situ soil moisture values for multiple algorithms at the paddock scale; (a) snapshot retrieval, (b) multi-temporal retrieval and (c) multi-temporal retrieval with the dry down constraint. The dash lines denote the target accuracy of $\pm 0.06 \text{ m}^3/\text{m}^3$	7-10
Figure 7-6: Comparison of in-situ and retrieved (a) soil surface root mean square height and (b) VWC. The cycled points belong to the paddocks ploughed nearly perpendicular to the radar look directions with their paddock ID as labeled. A, B and C denote results of snapshot retrieval, multi-temporal retrieval and multi-temporal retrieval with the dry down constraint.	7-11
Figure 7-7: Effect of polarization combinations on soil moisture retrieval using eight multi-angular images at the paddock scale. a-f denote HH+HV+VV, HH+VV, HH+HV, VH+VV, HH, VV, and HV respectively. ubRMSE denotes the unbiased RMSE.	7-12
Figure 7-8: Effect of time interval on soil moisture retrieval using two multi-angular images at the paddock scale. A-G denote two images with a time interval of 17, 15, 12, 9, 7, 4 and 2 days with the corresponding average soil moisture difference being 0.218, 0.181, 0.136, 0.094, 0.052, 0.015 and $0.007 \text{ m}^3/\text{m}^3$ respectively.	7-14
Figure 8-1: Summary of SAR data used in this chapter, showing acquisition date (day of year), frequency, polarization and orbit.	8-3
Figure 8-2: Conceptual framework of the proposed time series multi-frequency retrieval method. The inputs include time series L-, C- and X-band data acquired from both ascending and descending orbits; the landcover map, and the forward data cubes (multi-dimensional look up tables).....	8-4
Figure 8-3: Relative contributions related to the soil surface (C_s) for wheat at C-band VV polarization with incidence angles from left to right being 20° , 30° and 40°	8-6
Figure 8-4: Simulated relative contribution of the soil surface from under a wheat canopy. The m_v and H_R were $0.15 \text{ m}^3/\text{m}^3$ and 2 cm.....	8-9
Figure 8-5: Retrieved soil moisture maps in YA7 with the day of year listed in top left. The paddocks in black circles are these with soil ploughing, while the red circles are those with irrigation.....	8-11

Figure 8-6: In situ versus retrieved soil moisture at the 25-m pixel (a) and paddock scale (b) using time series L-, C- and X-band data. The dash lines denote the $\pm 0.06 \text{ cm}^3/\text{cm}^3$ 8-12

Figure 8-7: Retrieved H_R and VWC values for wheat paddocks with a periodical soil surface. The red and black lines are paddocks with a row direction perpendicular and parallel to the radar look direction, respectively. 8-15

Figure 8-8: Time series average soil moisture of paddocks with/without integrating change detection results. The error bar denotes the standard deviation. 8-17

List of Tables

Table 2-1: Characteristics of soil moisture needs for science and application2-3

Table 2-2: Present and planed spaceborne SAR missions.....2-13

Table 3-1: Characteristics of the six focus areas, adapted from Gao (2016).....3-3

Table 3-2: PLIS system specification.....3-4

Table 3-3: A summary of ground sampling schedule, adapted from(Ye et al., In Review)3-8

Table 3-4: A summary of data used in each chapter.3-13

Table 4-1: PLIS and PALSAR-2 images used in the cross-validation4-7

Table 4-2: PLIS calibration accuracy and its comparison with another two L-band airborne SAR system. PSLR and ISLR are peak-to-side-lobe-ratio and integrated-side-lobe-ratio. $A \pm B$ represents an average of A and a standard deviation of B. * denotes the design requirement4-12

Table 4-3: The comparison of PLIS and PALSAR2 over different landcover types and look directions. Values in bold indicate the lowest RMSD among different landcover types. A(B) represents a root mean square difference of A and a correlation coefficient of B. Only the grids whose fractions of dominant landcover type were $> 80\%$ were included.....4-19

Table 5-1: A summary of scattering models used. Wheat and grass were simplified as a random layer of cylinders, with the required parameters being that of cylinders.....5-2

Table 5-2: Available roughness and vegetation measurements of the paddocks in three SMAPEX-5 focus farms used in this chapter.....5-8

Table 5-3: Specification of SAR data in a format of incidence angle/orbit/polarization, where A and D are ascending and descending pass, respectively.....5-9

Table 5-4: Parameters used in building lookup tables, $U(a, b)$ denotes a uniform distribution ranging from a to b ; and $N(a, b)$ is a normal distribution with a mean of a and a standard deviation of b5-13

Table 6-1: Available roughness and vegetation measurements of the paddocks with cultivation activities6-6

Table 6-2: The input for generating time series maps of surface parameters. U (A , B) denotes a uniform distribution ranging from A to B..... 6-11

Table 6-3: Candidature feature index for SAR data acquired at phase t and $t-1$ 6-16

Table 6-4: Synthetic data sets used in this study. DS denotes dataset 6-20

Table 6-5: Selected optimal feature space and the corresponding J-M distance for different radar configurations based on synthetic SAR data sets with various surface changes, where the grey grids denote the unavailable features. Q and D denote Quad and Dual (HV+VV) polarization, respectively. 6-22

Table 8-1: Accuracy of soil moisture retrieval at the paddock scale. The bold styles denote the best case for each land cover. 8-13

Table 8-2: Accuracy of rms height and VWC retrieval at the paddock scale. The bold styles denote the best case in RMSE. ubRMSE refers to unbiased RMSE..... 8-14

1 Introduction

This thesis presents a multi-SAR retrieval framework towards reliable soil moisture mapping with high spatial (tens m) and temporal (2 – 3 days) resolution. The principle of the proposed method is to enhance the revisit and retrieval stability through the combination of multiple SAR missions, with the main novelty being a proper way to combine time-varying multi-configured radar data in soil moisture retrieval. Data used for framework development and evaluation were primarily collected from two Soil Moisture Active Passive Experiment (SMAPEX) field campaigns in Australia. Whilst the work in this research focused on a single site using radar data collected from three platforms, the methodology is developed with a global application in mind, utilizing the radar data from in-orbit and forthcoming spaceborne radar satellites.

1.1 Background

Near-surface soil moisture (top 5 cm) information is important for its partitioning of rainfall into runoff through regulation of the infiltration capacity of the soil ([Demargne et al., 2014](#)), impact on contaminant retention within the catchment, including erosion and sedimentation processes, and on dust storm generation through the moisture control on soil cohesion ([Kurosaki et al., 2011](#)). Additionally, economic, social and environmental planning for a water-limited future requires a capacity to monitor soil moisture content at a level of spatial and temporal detail that does not currently exist. The challenge is to economically monitor this critical environmental variable across vast landscapes at an appropriate spatial and temporal resolution; the only way to provide such information is from remote sensing. Currently, soil moisture products are only routinely available at low resolution (tens km); missions providing these products include the European Space Agency's (ESA) Soil Moisture and Ocean Salinity (SMOS, [Kerr et al., 2001](#)) and National Aeronautics and Space Administration (NASA) Soil Moisture Active Passive (SMAP, [Entekhabi et al., 2010](#)). Consequently, routine soil moisture monitoring at high spatial resolution (0.1 – 1 km) is still unresolved.

The Synthetic Aperture Radar (SAR) approach provides a promising alternative for global soil moisture mapping at high spatial resolutions (< 1 km), with currently more than ten spaceborne SAR missions launched or proposed for launch, most of which can collect data at multi-polarization. Moreover, several of these missions are/will provide free global coverage routinely (e.g., the ESA Sentinel-1 constellation). This situation provides an ideal opportunity to explore the application of radar remote sensing to routine high-resolution soil moisture retrieval.

1.2 Problem and Objective

Despite the increased availability of SAR data and its more frequent revisit, including through satellite constellations, e.g. Sentinel-1 and SAOCOM, the revisit of each individual mission (6 – 12 days) is still unable to meet the 2 – 3 day requirement for soil moisture mapping ([Walker and Houser, 2004](#)). In addition, soil moisture retrieval from SAR observations is commonly an ill-posed problem, because of the great number of unknowns ([Kornelsen and Coulibaly, 2013](#)) e.g., surface roughness and vegetation structure. The use of data from multiple SAR missions will enable a denser time series of observations, providing a great opportunity to solve the temporal repeat problem. However, this also means that SAR data with various observation configurations (wavelength, incidence angle, spatial resolution, polarization combinations etc.) need combining in an appropriate way. Enhancing the revisit by combining multi-SAR-missions can thus also benefit the conversion of an ill-posed soil moisture retrieval to a well-posed problem if the multi-polarization, multi-frequency and varying incidence angle observations from these missions can be combined appropriately. However, the way to combine multiple SAR missions with time-varying radar configurations in soil moisture retrieval is still unresolved ([Kornelsen and Coulibaly, 2013](#)). Therefore, this thesis is focused on developing a methodology that can combine data from multi-SAR-mission to derive reliable soil moisture (better than $0.06 \text{ m}^3/\text{m}^3$) with high spatial (tens m) and temporal (2 – 3 days) resolution.

1.3 Outline of Approach

The proposed multi-SAR-mission soil moisture retrieval framework was designed for SAR missions operating at the commonly used remote sensing frequency bands of L-, C- and X-band. The assumption of time-invariant (over short time periods) roughness and vegetation is used for soil moisture retrieval from the combined multi-SAR-mission time series data, thus removing the major unknowns in soil moisture inversion. The approach of this thesis includes four main parts:

Prior to soil moisture retrieval, airborne L-band data collected from the two Soil Moisture Active and Passive Experiments (SMAPEX-4 and -5) were calibrated and cross-validated with the Phased Array type L-band Synthetic Aperture Radar 2 (PALSAR-2). Moreover, state-of-the-art numerical and physical scattering models were combined to build a series of Look Up Tables (LUTs), covering typical remote sensing radar configurations and landcover types.

An unsupervised change detection method was subsequently proposed to ensure the time-invariant roughness and vegetation changes for the period of interest, being a pre-processing procedure of the subsequent soil moisture retrieval. The roughness and vegetation changes in L-band data were first investigated to guide the design of the method. The optimal feature space was then selected using a feature selection algorithm and an LUT-based intensive synthetic data set. The changed paddocks were determined in the selected feature space using an unsupervised density-based algorithm.

Time series SAR observations were then separated into multiple sub-series according to the presence of roughness and VWC changes provided in the previous step. To retrieve soil moisture from a single SAR mission operating with time-varying imaging modes, orbits, and radar beams, a time series multi-angular retrieval method was proposed. In the method, a genetic algorithm was used to minimize the difference between LUTs and time series multi-angular radar observations with a constraint of dry down soil moisture.

A multi-frequency framework was finally proposed as an extension of the above time series multi-angular method for joint multi-SAR mission soil moisture retrieval. The input multi-frequency backscattering coefficient (σ^0) with negligible scattering (low soil relative contribution) from soil surface was removed before soil moisture retrieval. Soil moisture retrieval was carried out independently for each landcover type using an optimization method and forward LUTs.

1.4 Thesis organization

This thesis consists of 9 chapters. Chapter 2 is an extensive review of the literature pertaining to the different aspects of the proposed multi-sensor methodology for soil moisture retrieval. Chapter 3 is a description of the key data sets used in this study, with a particular focus on the radar data and ground sampling collected during SMAPEX-5. Aspects of this chapter are included in the following co-authored paper. My main role was in soil moisture and roughness samplings during the SMAPEX-5 field campaign, calibration of the radar observations, classification of landcover maps and preprocessing of the roughness measurement.

- Ye, N., WALKER, J. P., X. WU, JEU, R. D., GAO, Y., JACKSON, T. J., JONARD, F., KIM, E., MERLIN, O., PAUWELS, V., RENZULLO, L. J., RÜDIGER, C., SABAGHY, S., C., HEBEL, V., YUEH, S. H. & **ZHU, L.** The Soil Moisture Active Passive Experiments: Towards calibration and validation of the SMAP mission. *Remote Sensing of Environment*. In Review.

Chapter 4 presents the calibration methodology and results for the airborne L-band data in the two SMAPEX campaigns, demonstrating the potential of cross-validation/calibration among SAR systems. The work presented in this chapter has been published in the following paper:

- **ZHU, L.**, WALKER, J. P., YE, N., RÜDIGER, C., HACKER, J., PANCIERA, R., TANASE, M. A., WU, X., GRAY, D., STACY, N., GOH, A., YARDLEY, H. & MEAD, J. 2018. The Polarimetric L-band Imaging

Synthetic aperture radar (PLIS): description, calibration and cross-validation. *IEEE Journal of Selected Topics in Applied Earth Observations and Remote Sensing*, 11, 4513 – 4525.

Chapter 5 is focused on the development and evaluation of forward LUTs built by a combination of current numerical, physical and empirical scattering models. Together with the data from Chapter 3 as calibrated in Chapter 4, these LUTs are used in Chapters 6-8 for soil moisture retrieval. An investigation of using effective soil roughness value in forward modeling has been published in the following paper:

- **ZHU, L.**, WALKER, J. P., YE, N. & RUDIGER, C. The effect of radar configuration on effective correlation length. 2016 International Conference on Electromagnetics in Advanced Applications (ICEAA), 820-823.

Chapter 6 proposes an unsupervised change detection algorithm to ensure the assumption of time-invariant roughness and vegetation. This work has been published in the following paper:

- **ZHU, L.**, WALKER, J. P., YE, N. & RÜDIGER, C. 2019. Roughness and vegetation change detection: a pre-processing for soil moisture retrieval from multi-temporal SAR imagery. *Remote Sensing of Environment*, 225, 93-106

Chapter 7 proposes a time series multi-angular retrieval method, which was extended to be compatible with time series multi-frequency data in Chapter 8. The work in these chapters is in the process of being published as follows:

- **ZHU, L.**, WALKER, J. P., TSANG, L., HUANG, H., YE, N. & RÜDIGER, C. 2019. Soil moisture retrieval from time series multi-angular radar data using a dry down constraint. *Remote Sensing of Environment*. 231, 111237.
- **ZHU, L.**, WALKER, J. P., TSANG, L., HUANG, H., YE, N. & RÜDIGER, C. 2019. A multi-frequency framework for soil moisture retrieval from time series radar data. *Remote Sensing of Environment*. In Review.

- **ZHU, L.**, WALKER, J. P., TSANG, L., HUANG, H., YE, N. & RÜDIGER, C. 2018. Soil moisture retrieval over agricultural fields from time series multi-angular L-band radar data. In, *2018 IEEE International Geoscience and Remote Sensing Symposium*, 6139 – 6142.

Finally, Chapter 9 presents the conclusions and outlooks based on the work carried out.

2 Literature Review

This chapter presents the importance of soil moisture measurement and the requirements of spatial and temporal resolutions in different fields, followed by a review of soil moisture measurement techniques, with a focus on the capability to measure soil moisture reliably at an appropriate spatial and temporal resolution. Subsequently, radar surface scattering models for soil moisture retrieval are discussed, including a review of the models for bare soil and vegetated surfaces. Moreover, the range of radar-based soil moisture retrieval methods are discussed, with a focus on the multi-temporal and multi-configuration techniques. The knowledge gap in existing soil moisture retrieval algorithms identified from this review, and to be addressed by this thesis, is then presented together with the proposed approach.

2.1 Importance of Soil Moisture

The most common understanding of the term soil moisture is the total amount of water between the soil surface and the water table ([Seneviratne et al., 2010](#)), also known as the unsaturated zone. It can be further separated into surface and root zone soil moisture for practical application; the former commonly refers to the water in the top approximately 5 cm layer of soil while the latter can extend from depths of around 30 cm to over two meters. Most modelling studies focus on a shallow zone of less than 100 cm (e.g., [Baldwin et al., 2017](#), [Albergel et al., 2008](#), [Walker et al., 2001](#)). Soil moisture is usually defined as the ratio of water to the total soil media in terms of mass units (kg/m^3), volumetric units (m^3/m^3), or relative saturation, depending on the way it is measured. Sometimes it is expressed as a function of the wilting point and the field capacity, both of which are soil and vegetation dependent ([Kerr, 2007](#)).

Despite the small volume of water compared to other components of the hydrologic cycle, soil moisture plays a significant role in land-atmosphere interactions ([Entekhabi et al., 1996](#), [Seneviratne et al., 2010](#)). It controls the partitioning of precipitation into

infiltration and runoff; influences the evaporation and evapotranspiration through the availability of water and thus the latent and sensible heat flux ([Seneviratne et al., 2010](#)); and impacts soil micro-organism activities. Therefore, availability of such information is critical to achieve state-of-the-art advancements in early warning systems (e.g. flood and fire forecasting), weather and climate prediction, climate-sensitive socioeconomic activities (e.g. agriculture and water management) and policy planning (e.g. drought relief and carbon accounting).

More specifically, soil moisture can aid in the parameterization and calibration of hydrological models, improving the run off simulations, particularly in small watersheds (<1000 km²) with highly variable flow ([Pauwels et al., 2001](#), [Brocca et al., 2010](#), [Brocca et al., 2012](#), [Alvarez-Garreton et al., 2014](#), [Chiffard et al., 2018](#)). Multiple studies have shown that the determination of soil moisture through remote sensing, together with the knowledge of precipitation, land cover, land surface temperature can improve the prediction accuracy of flood events ([Nied et al., 2013](#), [Massari et al., 2014a](#), [Massari et al., 2014b](#), [Wanders et al., 2014](#), [Parinussa et al., 2016](#), [Chiffard et al., 2018](#)). Similarly, soil moisture can also benefit early drought prediction through better prediction of plant stress, and objective drought monitoring over time and spatial scales ([Cáceres et al., 2015](#), [Vijaya Kumar et al., 2005](#)).

The initial soil moisture condition is also a vital input for most weather forecasting systems ([Seneviratne et al., 2010](#), [Engman, 1992](#), [Koster et al., 2004](#), [Scipal et al., 2008](#), [Gutman and Ignatov, 1998](#), [Hunt and Turner, 2017](#)). Numerical studies have shown that accurate soil moisture is as important as wind, air temperature and water vapor to weather prediction skills ([Seneviratne et al., 2010](#)). Changes to soil moisture patterns are also expected to be an important indicator of climate change ([Seneviratne et al., 2010](#)). For example, the change of soil moisture spatial pattern in the European continent shows a trend of decreasing mean precipitation in mid-latitude and sub-arid regions (especially in the Mediterranean region), and an increase in mean precipitation in the high latitudes ([Seneviratne et al., 2006](#), [Hirschi et al., 2011](#)).

Soil moisture stress also has a great impact on the length of the growing season and on the seed development and growth phases, thus controlling agricultural productivity ([Waite et al., 1984](#), [Kramer, 2017](#), [Krishnan et al., 2006](#)). The use of accurate soil moisture information in agricultural applications can therefore lead to more accurate productivity forecasting ([Ines et al., 2013](#), [Cleverly et al., 2016](#)), water conservation benefits ([Bayer et al., 2013](#), [Volo et al., 2014](#)) and better management of agricultural practices such as trafficability in the fields ([Stevens et al., 2016](#), [Schulte et al., 2012](#)).

Despite the great benefit that can be derived from the knowledge of soil moisture, providing soil moisture information that meets the requirements of most applications, remains many challenging ([Engman, 1991](#), [Entin et al., 2000](#)). This is largely due to the high variability of soil moisture across temporal and spatial scales and the limitation of

Table 2-1: Characteristics of soil moisture needs for science and application

Reference	Application	Spatial resolution (km)	Revisit (days)	Accuracy m ³ /m ³
Engman (1992)	Climate studies	10 – 100	1 – 10	-
	Weather Forecasting	1	1	-
	Hydrology	0.01 – 1	2 – 3	-
	Agriculture	0.1 – 1	3 – 5	-
Waite et al. (1984)	Precision crop management	0.1 – 1	1 – 2	-
Jackson et al. (1999)	Various applications	10	2 – 3	0.04
Hoeben and Troch (2000) ; Calvet and Noilhan (2000)	Soil moisture profile estimation	-	< 3	-
Walker and Houser (2004)	Data assimilation	Less than land surface model resolution	1 – 5	0.05
WMO basic requirements (http://www.wmo-sat.info/oscar/requirements)	Agricultural meteorology	1	7	0.05
	Hydrology	250	3	0.05
	Global numerical weather prediction	100	5	0.08

measurements with respect to the high cost of in situ measurement, and the typically low spatial or temporal resolution of available remote sensing approaches. A summary of soil moisture requirements in various fields is provided in Table 2-1.

In hydrological and meteorological applications, [Hoeben and Troch \(2000\)](#) suggested a daily observation, while [Calvet and Noilhan \(2000\)](#) recommended a 3 day repeat for retrieving accurate soil moisture profile. [Walker and Houser \(2004\)](#) found that daily near-surface soil moisture observations with a spatial resolution finer than the land surface model (e.g., 30 arc-min) achieved the best results in soil moisture and evapotranspiration forecasts when used for data assimilation purposes. Moreover, [Pan and Wood \(2010\)](#) found that the assimilation performance was most sensitive to the spatial resolution of the soil moisture observations, followed by the revisit time and retrieval accuracy. [Jackson et al. \(1999\)](#) suggested an accuracy of $0.04 \text{ m}^3/\text{m}^3$ with a 10

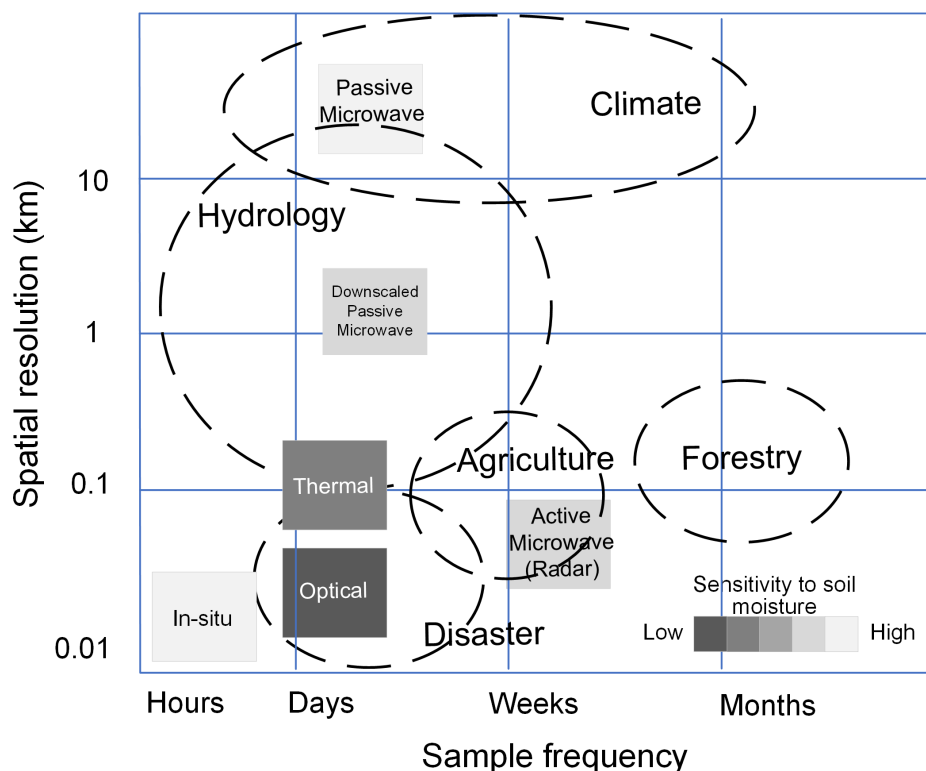


Figure 2-1: The capability of techniques for soil moisture measurements, together with the spatial and temporal requirements of various applications.

km spatial resolution and 2 – 3 sample frequency, which is also the objective of the NASA SMAP mission. Agricultural applications require a similar repeat frequency of 1 – 3 days, but requiring finer spatial resolutions of 0.1 – 1 km ([Waite et al., 1984](#)). The more recent studies complement the “best guess” estimates of [Engman \(1992\)](#) for a range of applications, some of which require a spatial resolution of 10 m. In summary, soil moisture with a tens-of-meters spatial resolution and 2 – 3 days repeat is required to meet most the needs of most applications.

2.2 Techniques for Soil Moisture Estimation

Over the past four decades, researchers have made significant advances in developing the algorithms and techniques for monitoring soil moisture, including point-based techniques and the remote sensing techniques. A summary of the capabilities of these in terms of sensitivity to soil moisture, spatial resolution and temporal repeat is presented in Figure 2-1. In the following sections, these techniques are reviewed with a focus on the active microwave techniques, current and forthcoming SAR missions, and their capability in soil moisture mapping.

2.2.1 *In-situ* soil moisture measurement

The traditional techniques have measured soil moisture *in-situ* either directly or indirectly. The most straightforward method is the thermo-gravimetric measurement, with soil moisture being determined from the weight difference of a soil sample before and after the oven drying at 105 °C ([Robinson, 2009](#)). It is also the standard venue to calibrate other indirect approaches. Limited by its destructive nature, repetitive observation at the same location is impossible, with other disadvantages including the difficulty to remove the effect of organic matter, and the complex and time-consuming laboratory processing.

Rather than directly measuring the amount of water, many commercial sensors have been developed to measure other physical variables that depend on the amount of soil water, and then relate these variables to the soil moisture either physically or

empirically. The most commonly used are dielectric sensors, mainly including the capacitance probes ([Nadler and Lapid, 1996](#)), time-domain reflectometry probes ([Davis and Chudobiak, 1975](#)), and frequency domain reflectometry probes ([Campbell and Anderson, 1998](#)). They exploit the changes in soil relative permittivity (also known as dielectric constant) as a function of soil moisture. The large difference between the relative permittivity of soil particles and that of water allows a reliable and sensitive approach for soil moisture measurements. While these approaches directly respond to the soil dielectric properties, which are closely related to soil moisture, other techniques have also been developed ([Schmugge et al., 1980](#)), such as tensiometric methods, neutron methods, acoustic wave methods and gravity measurements. All these techniques can be applied to a permanent station for continuous observations at various depths, with a minimum destruction to the soil at the time of insertion.

Despite the recently developed Cosmic-ray neutron probes with a 150-250 m radius footprint ([Montzka et al., 2017](#)), the major disadvantage of *in-situ* measurements is the relatively small zone of influence of these sensors, generally limited to a small adjacent area. Hence, a dense network of sensors is required for the spatial distribution of soil moisture, which makes it expensive and impractical to deploy and maintain for large areas. Moreover, soil type-specific calibration is required to ensure that the volumetric water contents at different field sites are accurately interpreted and represented ([Kizito et al., 2008](#), [Rüdiger et al., 2010](#)), especially for heavy clay soils ([Schmugge et al., 1980](#)).

2.2.2 Remote sensing techniques

An economical alternative for soil moisture monitoring is remote sensing techniques. In principle, sensors are installed on a remote sensing platform (e.g., aircraft, satellite or balloon etc.) to measure the emitted, reflected and/or scattered electromagnetic signal of the soil surface. The measured electromagnetic signals affected by the amount of soil water are then related to the soil moisture content through either physical or empirical models. Compared with the *in-situ* approaches, remote sensing techniques have the desired capability of providing spatially explicit maps of near-surface soil moisture, with up to global coverage. Extensive research has been conducted over the

past four decades toward soil moisture retrieval from remote sensing techniques ([Petropoulos et al., 2015](#)), with the main difference in techniques being the measured frequency within the electromagnetic spectrum and the source of the radiation.

- Optical, near- and thermal-infrared

Optical methods exploit the relationship between soil moisture and spectral reflectance in the visible/near-infrared bands to empirically determine the soil moisture in the top millimeters or so of the soil surface. In general, the absorption of visible bands increases as soil moisture is increased, resulting in a decrease of reflectance at these bands ([Weidong et al., 2002](#), [Gao et al., 2013](#)). However, this tenuous relationship and the optimal spectrum bands vary significantly from site to site ([Huan-Jun et al., 2009](#)), because of the additional dependence of reflectance on organic matter content, roughness, texture and observation geometry ([Petropoulos et al., 2015](#)). Moreover, the optical signal has limited capability to penetrate cloud and vegetation, requiring careful correction to eliminate the effect of the atmosphere ([Zhao and Li, 2013](#)). These are the main reasons for the limited use of visible/near-infrared bands in soil moisture retrieval, despite the multitude of optical sensors currently in orbit ([Petropoulos et al., 2015](#)).

Apart from the visible/near-infrared bands, thermal infrared sensors can also measure soil moisture with an enhanced but still insufficient sensitivity to soil moisture. The common scheme starts from the estimation of thermal inertia, being a measure of the surface resistance to temperature change caused by the ambient temperature ([Pratt and Ellyett, 1979](#)). The thermal inertia is then related to the soil moisture through the thermal conductivity and/or the heat capacity ([Petropoulos et al., 2015](#)). The use of thermal infrared in soil moisture retrieval has shown promising results over bare soil ([Leng et al., 2016](#), [Matsushima et al., 2018](#), [Minacapilli et al., 2009](#)) and for sparse vegetation areas with the knowledge of ground flux ([Maltese et al., 2013a](#), [Maltese et al., 2013b](#)), however is still questionable for dense vegetated areas ([Petropoulos et al., 2015](#)). Similar to the visible/near-infrared bands, application of thermal data over large areas is still challenging, limited by the short wavelength used. Many studies have also

applied a combination of the normalized difference vegetation index (NDVI) from optical data and the surface temperature T_s in soil moisture mapping ([Patel et al., 2009](#), [Rahimzadeh-Bajgiran et al., 2012](#), [Schirmbeck et al., 2017](#)), known as temperature/vegetation condition index (TVDI) methods. Recently, optical and thermal sensors on unmanned aerial vehicle platforms are being developed for field scale irrigation management ([Hassan-Esfahani et al., 2014](#), [Nieto et al., 2018](#)).

Despite the limitation of optical and thermal data, it is of great value as a supplement to microwave remote sensing techniques in soil moisture retrieval (e.g. the downscaling of passive microwave), because of its high spatial resolution (better than 1 km) and the capability to describe the vegetation in detail.

- Passive microwave

In contrast, microwave (0.3 to 300 GHz) observations are widely acknowledged as the most promising portion of the spectrum ([Petropoulos et al., 2015](#), [Karthikeyan et al., 2017b](#)), with advantages including 1) the high sensitivity to water content in the soil media; 2) the negligible influence of the atmosphere; and 3) the independence of weather and daylight conditions. The microwave remote sensing can be divided into two categories: passive and active methods. Passive sensors (known as radiometers) measure the naturally emitted emission from the earth's surface, expressed as brightness temperature. The emissivity of soil generally varies from ~ 0.6 to ~ 0.95 for a soil moisture value ranging from 0.05 to 0.4 m^3/m^3 , depending on electromagnetic wavelength, incidence angle, surface roughness and soil properties ([Jackson and Le Vine, 1996](#)). Given a surface temperature of 300K, such a variation can introduce a variation of 100 K in brightness temperature, which is much larger than the sensitivity of typical microwave radiometers (~ 1 K).

Most spaceborne radiometers operate at low frequencies (0.4 – 35 GHz), where the effect of the atmosphere and vegetation is much lower than that at visible, near-infrared and thermal bands. However, the field of view is inversely proportional to wavelength and antenna size, leads to a much lower spatial resolution constrained by

the limited antenna size on a spaceborne platform. Currently, two L-band (~ 1.41 GHz) passive microwave missions are operationally providing global soil moisture products at low resolutions (10 – 40 km). These include of the NASA SMAP and ESA SMOS missions. There are also soil moisture records derived from the C-band Advanced Microwave Scanning Radiometer for EOS (6.925 GHz) and WindSat (6.8 GHz) but also suffer from the coarse resolution. Consequently, a number of downscaling approaches have been developed for enhancing the spatial resolution, see [Sabaghy et al. \(2018\)](#) for a review. However, passive microwave based approaches are not yet able to provide spatial soil moisture detail at less than 1 km resolution with an appropriate level of accuracy. Notably, the spatial resolution was shown to be more critical than the temporal repeat and retrieval accuracy for assimilation into land surface models ([Pan and Wood, 2010](#)).

- Active microwave

For a higher spatial resolution, extensive research has been conducted using active (radar) microwave data. Radar is the acronym for RAdio Detection And Ranging, which was first used to detect ships and aircraft during the Word War II. The main components of a radar system include a transmitter, and an antenna which transmits a microwave signal towards the target and receives the backscattered part of the signal. While the strength of the backscattered signal is measured to discriminate between different targets, the time delay between the transmitted and reflected signals can also be used to determine the distance to the target ([Ulaby et al., 1982b](#)). There are several classifications of radar systems, with some commonly used being: 1) the imaging and non-imaging radar, 2) the real and synthetic aperture radar (SAR), 3) the airborne and spaceborne radar, and 4) monostatic and bistatic radar. Two kinds of active sensors, i.e. scatterometer and SAR, are commonly used for soil moisture retrieval.

A scatterometer is a sensor used to make precise quantitative measurements of the amount of energy backscattered from targets ([Ulaby et al., 2014](#)). In general, scatterometers are non-imaging sensors which take measurements in one linear dimension along the move direction of remote sensing platform. Limited by the beam

width on the earth surface, the spatial resolution of a spaceborne scatterometer is fairly low (tens km). Spaceborne scatterometers have a long history in global soil moisture mapping at a relatively low spatial resolution (50 km), starting from the launch of the first European C-band scatterometer on the ERS-1/2 in the 1990s. Its successive instruments on MetOp-A/B/C (2006; 2012 and 2018) enables a long-term soil moisture record despite a short gap between 2003 and 2006 ([Wagner et al., 2015](#)). Importantly, the measurements from ground based scatterometers (tower or truck) have enabled the initial investigations of various applications in earth observation ([Ulaby et al., 1982b](#)).

A SAR is a coherent mostly side-looking radar system which utilizes signal processing and the movement of the platform to simulate an extremely large antenna or aperture, resulting in a high resolution in azimuth (up to half of the real aperture length). SAR can be examined from several different points of views ([Ulaby et al., 2014](#)), including synthesized antenna aperture; doppler beam sharpening and optical-focusing equivalent. Please refer to [Cumming and Wong \(2005\)](#) for more details about the formation of SAR images. In view of synthesized antenna aperture (Figure 2-2), the

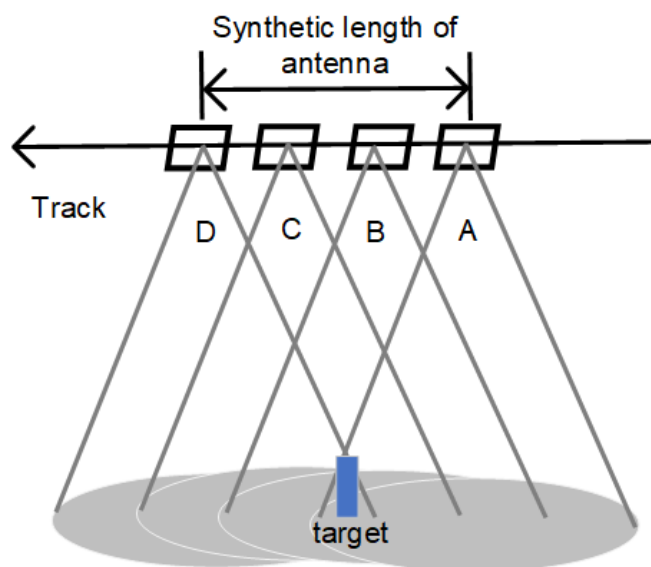


Figure 2-2: Conceptual figure of the synthesized expanding beamwidth, adapted from [Ulaby et al. \(2014\)](#)

SAR stores all the radar returned signals (amplitudes and phases) from position A to D, with all echoes of the same target being reconstructed as if they were simultaneously collected by a huge array antenna ([Ulaby et al., 2014](#)). Accordingly, SARs are mostly installed on a moving platform (airborne or spaceborne).

Airborne SAR systems are commonly used as a testing platform for the development, implementation, and verification of potential spaceborne SAR applications. Currently there are several airborne SAR systems that have been developed by different organizations throughout the world ([Ouchi, 2013](#)). Some of the most commonly used include the AIRborne Synthetic Aperture Radar (AIRSAR), Uninhabited Aerial Vehicle SAR (UAVSAR; [Rosen et al., 2006](#)) and the Digital Beamforming Synthetic Aperture Radar (DBSAR; [Rincon et al., 2011](#)) of the NASA; E-SAR and F-SAR of the German Aerospace Center; and the Polarimetric and Interferometric Airborne Synthetic Aperture Radar L2 (Pi-SAR-L2) of the JAXA ([Shimada et al., 2013a](#)). Most of these airborne SAR systems can operate in quad-polarization and interferometric modes. The significant flexibility of the airborne platforms enables extremely dense observations and variable acquisition geometries, e.g. incidence and azimuth angles. These characteristics allow for a better understanding of the surface scattering as well as the temporal behavior, which are essential for the successful development of applications.

The first civilian spaceborne SAR was on the Oceanographic satellite Seasat, operating from June to September 1978. Several shuttle SAR missions were flown before 2000, including the L-band SIRA-A/SIR-B, the multi-frequency SIR-C/X-SAR and the interferometry Shuttle Radar Topography Mission. In addition, a number of SARs have been flown and retired, such as the ERS-1/2, RADARSAT-1, and ENVISAT/ASAR, providing valuable data for historical analysis.

Whilst spaceborne SAR has shown positive results for soil moisture retrieval at high spatial resolution (0.1 – 1 km), the revisit of each satellite (> 1 week) is insufficient to reach the requirements for soil moisture monitoring, which is characterized by a high temporal variability (2 – 3 days). Fortunately, the increasing availability of radar data

from new missions enables the possibility for combining the data across these missions for an enhanced temporal resolution. In the following sub-section, the current and proposed spaceborne SARs are reviewed for the potential soil moisture mapping.

2.2.3 Present and projected SAR satellite missions

Currently, more than ten spaceborne SAR missions are in operation, some of which are constellations containing 2 – 4 satellites to provide an improved revisit. At least six more missions have been scheduled for launch in the next 5 years. An overview of these missions is presented in Table 2-2. All these missions operate at the low edge of microwave (0.3 – 10 GHz) frequencies, being mostly in the L-, C- and X-bands. The validity of this spectrum for soil moisture retrieval has been confirmed in numerous studies ([Kornelsen and Coulibaly, 2013](#), [Karthikeyan et al., 2017a](#)), although the lower frequency / longer wavelength is most desirable for a larger penetration into the soil and vegetation layers.

The nominal revisit of these missions can reach up to several hours if tasked to point at a focus area, e.g., two hours for the COSMO-SkyMed constellation ([Covello et al., 2010](#)), providing valuable data for monitoring urgent events. However, routine global observation commonly occurs on a much longer period. Currently, only the Sentinel-1 ([Torres et al., 2012](#)), SAOCOM, PALSAR-2 ([Kankaku et al., 2014](#)), Biomass mission ([Le Toan et al., 2011](#)) and NIRSAR ([Rosen et al., 2017](#)) can/plan to provide regular global observations, with repeats ranging from every 6 – 60 days. It is therefore important that a way be found to combine these missions to reach the revisit requirement of 2 – 3 days.

The spatial resolution of most SAR missions ranges from 1 – 100 m depending on the imaging mode. Four imaging modes are used in these missions (Figure 2-3).

- StripMap: A continuous imaging mode with a fixed pointing direction of the radar antenna relative to the flight direction. A strip map is an image formed in

Table 2-2: Present and planed spaceborne SAR missions.

Instrument/Platform	Launch or planed date	band	Spatial resolution(m)	Revisit (days)
COSMO-SkyMed 1– 4	2007 – 2011	X	1 – 100	1
TerraSAR-X	2007	X	1 – 16	1 – 11
RADARSAT-2	2007	C	3 – 100	9 – 30
PALSAR-2/ALOS	2014	L	~1 – 100	14 – 46
Sentinel-1A/B	2014 and 2016	C	5 – 100	6 – 12
GaoFen-3	2016	C	~1 – 500	
NovaSAR 1 – 4	2018	S	6 – 30	< 4
PAZ	2018	X	1 – 15	
ICEYE-X (18 satellites)	2018-2020	X	< 10	<1
SAOCOM-1A/B	2018 – 2019	L	7 – 100	8 – 16
RADARSAT Constellation 1, 2, 3	2019	C	~3 – 10	1
RISAT-1A/B	2019 – 2021	C	< 50	
COSMO-SkyMed (2ndGen)	2020	X	~1 – 60	<1
NISAR	2021	L, S	100 – 50,000	12 – 60
Biomass P-SAR	2022	P	100 – 200	25 – 45
Tandem-L	2023	L	3 – 20	8

width, according to the swath of the SAR, following the motion of the platform. StripMap is a standard mode of all airborne and spaceborne systems.

- Spotlight: A mode for obtaining high spatial resolution by steering the radar beam to remain over the target of interest as the platform passes by, to achieve a longer illumination period ([Jakowatz et al., 2012](#)). This greatly improves the resolution in azimuth at the expense of coverage (mostly less than 20 km swath width). Spotlight is commonly used over focus areas and is a favorite mode for military reconnaissance.

- ScanSAR: A special type of StripMap with the antenna beam periodically scanning several sub-swaths to achieve a much wider imaged swath. It also leads to a shorter revisit and thus is the optimal mode for global observation.
- Terrain Observation with Progressive Scan (TopSAR): An improved ScanSAR mode used in the Sentinel-1 ([Torres et al., 2012](#), [De Zan and Guarnieri, 2006](#)), with the main improvement being the capability to collect data with an azimuth-stationary Impulse Response Function (IRF). In TopSAR, additional rotating of the antenna beams in azimuth was applied to achieve the same resolution, ambiguity and noise equivalent σ^0 along the flight direction ([De Zan and Guarnieri, 2006](#)), at the expense of more complex signal processing.

Despite the spatial resolution, imaging modes also tightly relate to the polarization of the data collected. In general, ScanSAR collects data with Dual (HH+HV or VH+VV) or single polarization because of the limited data downlink, while StripMap and Spotlight may record the full scattering matrix.

In practice, SAR missions have more complex imaging modes with different polarizations and spatial resolutions. For example, PALSAR-2 has three different StripMap modes, namely, Fine Beam Single, Fine Beam Dual and Polarimetric ([Rosenqvist et al., 2014](#)). Sentinel-1 has two ScanSAR modes with one used for interferometry ([Torres et al., 2012](#)). The imaging modes are switched on a scheduled basis with special programming for abrupt events, e.g., natural disasters. The transition of imaging modes also results into the change of local incidence angle at the same location. Moreover, SAR missions collect data in both ascending and descending orbits, and even from both sides of the flight direction, introducing changes in local incidence angle, azimuth and spatial resolution.

Consequently, the available data from a single SAR mission or constellation is a time series data set with time-varying incidence angle, azimuth, polarization combination and spatial resolution. Combining data from multiple SAR missions introduces an additional challenge including changes in frequency over time. Soil moisture retrieval

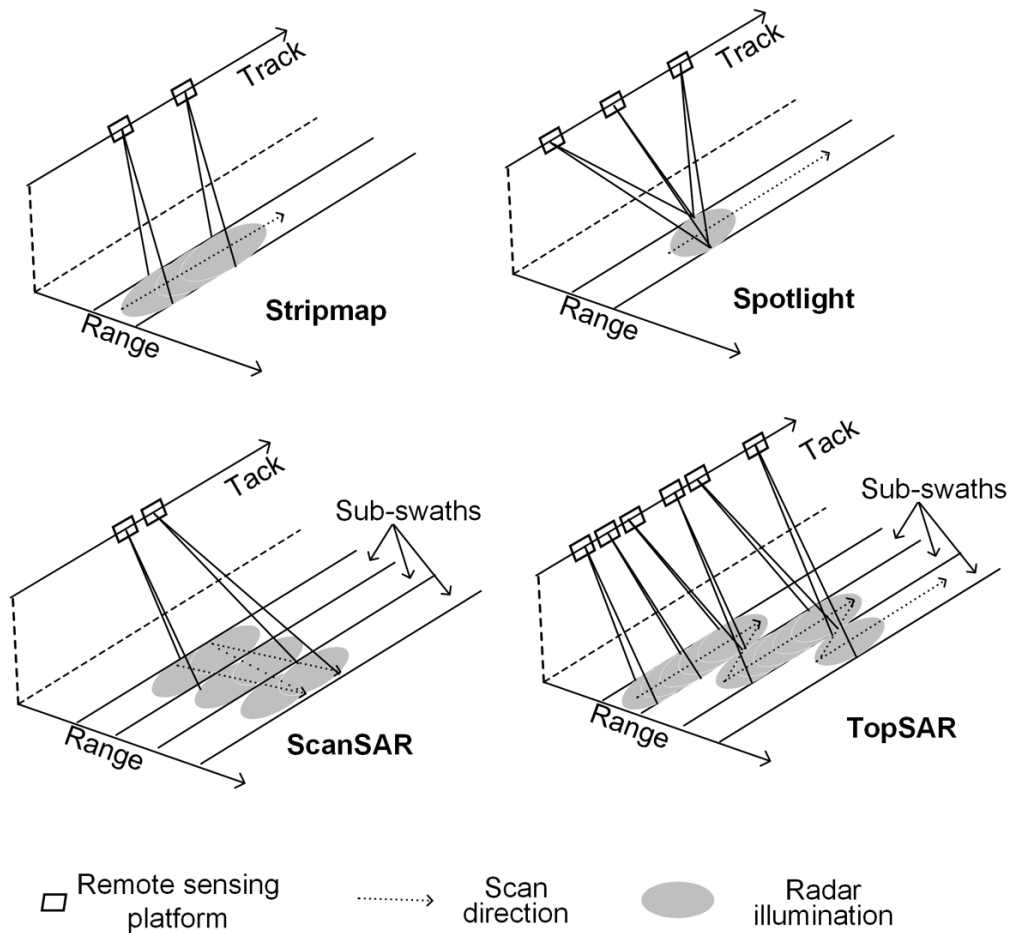


Figure 2-3: Imaging modes of SAR.

from such data is therefore more complex than the retrieval from data with a fixed radar configuration, because the retrieval method and forward model should be compatible with the range of potential radar configurations. In the following sections, scattering models that describe the scattering behavior of a surface at different configurations are reviewed, followed by the inversion methods used for soil moisture retrieval.

2.3 Scattering from the Earth's Surface

Soil moisture retrieval commonly starts from the development of scattering models that can accurately describe the relationships between surface parameters and radar observations. In principle, the backscattering coefficient σ^0 is a function of incidence

angle θ , frequency f and polarization pq as well as surface roughness (commonly described by the root mean square height H_R and surface correlation length L_C) and soil relative permittivity ϵ_s , with additional dependence on the vegetation relative permittivity ϵ_v and structure for a vegetated area ([Ulaby et al., 2014](#)). Despite the complex relationship, the ϵ_s can be decoupled and thus the soil moisture content can be determined with proper treatment ([Ulaby et al., 2014](#)). The characterization of surface parameters and scattering models are reviewed below.

2.3.1 Characterization of soil parameters

The theoretical basis of soil moisture retrieval from SAR is the large contrast between the relative permittivity of liquid water (~ 80) and dry soil ($2 - 3$). For the common microwave bands used in remote sensing, i.e. L-, C- and X-band the real part of the soil-water mixture's ϵ_s can increase to a value of 20 or greater as the soil moisture increases from 0 to $0.4 \text{ m}^3/\text{m}^3$ ([Ulaby et al., 1986](#)). The dielectric properties of a soil are also influenced by the distribution of soil grain size, temperature and bulk density. Several empirical models have been proposed to show the relationships among soil moisture, soil properties and relative permittivity at various frequencies ([Dobson et al., 1985b](#), [Hallikainen et al., 1985](#), [Peplinski et al., 1995](#), [Mironov et al., 2009](#)).

Apart from soil properties, the collected radar signal is heavily dependent on surface roughness. When a wave impinges on a smooth soil surface, some of the energy is scattered in non-specular directions, with a small amount returning to the radar as backscatter. As surface roughness increases, the amount of reflection in the specular direction decreases and consequently the surface scattering increases ([Ulaby et al., 1982b](#)). In some cases, e.g., high incidence angles and a relatively smooth surface, the σ^0 is more sensitive to roughness than soil moisture ([Bourgeau-Chavez et al., 2007](#), [Fung and Chen, 1992](#)). As a result, accurate characterization of surface roughness is the key to successful soil moisture retrieval ([Verhoest et al., 2008](#)). However, capturing the exact nature of soil surface is almost impossible because of its multi-scale nature and great spatial and temporal variations ([Ulaby et al., 2014](#)). Rather than physically describing the soil surface, two widely used semi-empirical surface scattering models

([Oh, 2004](#), [Dubois et al., 1995](#)) use a single one-scale parameter of root mean square height (H_R) for describing the surface roughness. This simplification was however thought to introduce considerable uncertainty ([Zribi and Dechambre, 2003](#)). In contrast, the Integral Equation Model (IEM) and its further modifications use the H_R and additionally the correlation length L_C and an autocorrelation function ([Chen et al., 2003](#), [Fung et al., 1992](#), [Wu et al., 2001](#), [Chen et al., 2000](#)). Roughness parameterization has been widely claimed as the main source of inconsistency between the modelled and observed σ^0 ([Álvarez-Mozos et al., 2006](#), [Panciera et al., 2014a](#), [Baghdadi et al., 2002b](#), [Joseph et al., 2010](#), [Lievens et al., 2011a](#), [Choker et al., 2017](#)).

The uncertainty of surface roughness characterization partly comes from the difficult to measure the inherent heterogeneity at the field scale. The ground measured roughness may not properly represent the soil surface viewed by the radar. Large variation and uncertainty has been found in estimating the roughness parameters for the same site, especially in calculating the L_C ([Lievens et al., 2011a](#), [Davidson et al., 2003](#), [Mattia et al., 2003](#), [Zribi et al., 1997](#)). An increase in H_R and L_C was found to occur as the length of the measured profile was increased, with the optimal length still unsolved ([Baghdadi et al., 2000](#), [Callens et al., 2006](#)). Another uncertainty source is the description of soil surface as a one-scale stationary random process. For agricultural areas, the soil surface is often anisotropic due to ploughed periodical row features ([Ulaby et al., 2014](#), [Davidson et al., 2000](#)). Whilst multi-scale scattering models have shown some positive results over such soil surfaces ([Mattia and Le Toan, 1999](#), [Fung, 1994](#), [Ulaby et al., 1982a](#)), isolating ε_s for soil moisture retrieval becomes more difficult because of the additional multi-scale roughness parameters.

To solve these problems, some other roughness parameterizations have been proposed. For example, [Zribi and Dechambre \(2003\)](#) introduced a roughness parameter $Z_S = H_R^2/L_C$, showing a high correlation coefficient of 0.995 with the σ^0 difference of two acquisitions acquired from different incidence angles. This was successfully applied in soil moisture retrieval using empirical relationships ([Rahman et al., 2007](#), [Rahman et al., 2008](#), [Zribi and Dechambre, 2003](#)). The Z_S was further

improved by [Zribi et al. \(2014\)](#) through considering the autocorrelation function (ACF) shape. In addition, effective roughness parameters of the IEM have been proposed to replace the physical parameters, which were widely confirmed to have a better fit between the observed and simulated σ^0 ([Baghdadi et al., 2002c](#), [Baghdadi et al., 2004](#), [Baghdadi et al., 2011](#), [Su et al., 1997](#), [Baghdadi et al., 2006b](#), [Panciera et al., 2014a](#)). Effective roughness parameters have also been used for surfaces with periodic row structure ([Champion and Faivre, 1996](#), [Joseph et al., 2010](#)), providing a simple alternative for soil moisture retrieval. However, the effective roughness parameters depend on radar configuration, with larger effective L_C and effective H_R observed at lower incidence angles over the same location ([Lievens et al., 2011a](#)). Moreover, L-band tends to have larger L_C values than at C- and X-band, whereas the C- and X-bands values are typically similar ([Zhu et al., 2016](#)). Accordingly, the use of those parameters in forward prediction requires radar-configuration-specific calibration. Similarly, effective roughness values directly retrieved from radar data using theoretical forward models ([Bai et al., 2016](#)), also depend on the input radar measurements and thus cannot be used for soil moisture retrieval from other radar data.

2.3.2 Scattering models for bare soil

The most simple and straightforward model is the linear relationship between the backscatter coefficient in dB and soil moisture content in the top few centimeters ([Dobson and Ulaby, 1986](#)), with the general formulation being:

$$\sigma_{\text{dB}}^0 = A \cdot mv + B, \quad \text{Eq. 2-1}$$

where A and B are empirical parameters representing the sensitivity to soil moisture and the effect of vegetation and soil roughness respectively. Many studies have successfully applied this relationship or its variant in soil moisture retrieval ([Zribi and Dechambre, 2003](#), [Zribi et al., 2005b](#), [Quesney et al., 2000](#), [Zribi et al., 2011](#), [Zhang et al., 2017](#), [Baghdadi et al., 2007](#)), with different fitted A and B . Despite the simplicity and satisfactory results, the parameters need to be calibrated for each site and radar configuration (e.g., [Baghdadi et al., 2008](#), [Baghdadi et al., 2007](#)) or be estimated by

using long time series SAR observations (e.g., [Hégarat-Masclé et al., 2002](#), [Moran et al., 2000](#)).

For more general application, several semi-empirical models based on multiple ground scatterometer experiments have been developed. Among these, the most commonly used are those derived by [Oh et al. \(1992\)](#) and [Dubois et al. \(1995\)](#). The Oh model was developed based on a comprehensive investigation of the observed σ^0 under different configurations. The co- ($\sigma_{HH}^0/\sigma_{VV}^0$) and cross-polarized ($\sigma_{HV}^0/\sigma_{VH}^0$) ratios are found to follow a function of kH_R , whose slope increases steep at first and then forms an asymptote. The model was improved by considering the surface autocorrelation ([Oh et al., 1994](#)) and incidence angle ([Oh et al., 1994](#), [Oh et al., 2002](#)), and was further modified by removing L_C ([Oh, 2004](#)). The Oh model has been applied to various soil conditions with typical radar configurations. [Fung and Chen \(2004\)](#) reported that the Oh model accurately estimated σ^0 for larger incidence angles ($\theta > 30^\circ$). It was also found to fit observations well at various θ ([Baghdadi and Zribi, 2006](#), [Choker et al., 2017](#)). While underestimation in σ^0 was reported in several studies ([Baghdadi and Zribi, 2006](#), [Merzouki et al., 2010](#), [Panciera et al., 2014a](#), [Boisvert et al., 1997](#)), some studies found a systematical overestimation using various data ([Merzouki et al., 2011](#), [Gherboudj et al., 2011](#), [Sahebi and Angles, 2010](#)). Consequently, a correction factor was suggested in the Oh model for achieving accurate soil moisture retrieval ([Merzouki et al., 2011](#), [Baghdadi and Zribi, 2006](#)).

The Dubois model differs from the Oh model in that it directly relates the co-polarized σ^0 (HH and VV) to the ε_s , θ and f ([Dubois et al., 1995](#)). The validity range of this model is $kH_R < 2.5$ and $\theta > 30^\circ$. For the vegetated area, a further constraint of Normalized Difference Vegetation Index (NDVI) less than 0.4 is required ([Dubois et al., 1995](#)). The Dubois model was found to overestimate σ^0 by as much as 4 – 6 dB in [Merzouki et al. \(2011\)](#), 1.7 dB in HH polarization in [Baghdadi and Zribi \(2006\)](#) and 1.8 dB in co-polarization in [Panciera et al. \(2014a\)](#). In contrast, [Álvarez-Mozos et al. \(2007\)](#) found that the model tended to underestimate σ^0 at moist conditions.

A number of physically-based models have been proposed to describe the behavior of σ^0 over bare soil ([Elfouhaily and Guérin, 2004](#)). Some representative ones are the small perturbation model, the geometric optics model, the small slope approximation model and the IEM ([Ulaby et al., 1982b](#)). Among these, the IEM ([Fung and Chen, 1992](#)) and its variants ([Hsieh et al., 1997](#), [Wu et al., 2001](#), [Chen et al., 2003](#), [Fung and Chen, 2004](#)) have been the most popular ones in soil moisture retrieval because of their wide validity range ($kH_R < 3$). Given a ε_s , the radar configuration and the three roughness parameters (H_R , L_C and ACF), both the co- and cross-polarized σ^0 can be simulated by the IEM.

Laboratory experiments have confirmed the effectiveness of the IEM ([Hsieh et al., 1997](#), [Mancini et al., 1999](#), [Macelloni et al., 2000](#)). However, σ^0 estimated by IEM can have a large bias with that observed from a natural surface ([Álvarez-Mozos et al., 2006](#), [Panciera et al., 2014a](#), [Baghdadi et al., 2002b](#), [Joseph et al., 2010](#), [Lievens et al., 2011a](#), [Choker et al., 2017](#)). As mentioned above, this bias is often suggested to be the result of a failure in the roughness parameterization ([Baghdadi et al., 2004](#), [Baghdadi et al., 2011](#), [Baghdadi et al., 2006b](#), [Lievens et al., 2011b](#)). Effective roughness parameters or correction factors have therefore been suggested in order to achieve better fitting results. Moreover, the IEM has been modified to include a revised Green's function, multiple scattering, and a transition function for the Fresnel coefficients ([Hsieh et al., 1997](#), [Wu et al., 2001](#), [Chen et al., 2003](#), [Fung and Chen, 2004](#)).

The other category of physically-based models is the numerical backscattering model, which directly solves the Maxwell's equations on a conducting surface. The method of moments is the most commonly used numerical method for σ^0 simulation over a bare soil. It was initially limited in the evaluation of other simplified physical models because of the large computation cost and the fact that it can only be used to model a small surface of 8 – 10 times of the wavelength ([Huang et al., 2010](#), [Ulaby et al., 1986](#), [Liao et al., 2016a](#)). Recently, the numerical solutions of Maxwell's question in three demission (NMM3D; [Huang et al., 2010](#), [Huang and Tsang, 2012](#)) was used to build look up tables (LUTs) for operational soil moisture retrieval using the SMAP radar

([Kim et al., 2012a](#), [Huang et al., 2010](#)). Despite the great potential of numerical methods, faster algorithms, more powerful computer systems or new conceptions of computation (e.g., cloud computing) are required for their routine applications in soil moisture retrieval.

2.3.3 Scattering models for vegetated surfaces

For a vegetated surface, the scattering and absorption of vegetation layers should be included in the above scattering models. Since the vegetation materials are commonly less than 1% of the vegetation layer in volume, the relative permittivity of the vegetation layer (ϵ_v) is slightly larger than air, meaning that the surface scattering at the top boundary of the vegetation layer can be ignored ([Ulaby et al., 2014](#)). Moreover, the first-order scattering contributions are significantly larger than those of higher-order ones for natural vegetation ([Ulaby et al., 2014](#)). Figure 2-4 shows the conceptual first-order scattering mechanisms over a vegetated surface, including the volume scattering, the attenuated soil scattering and the double bounce scattering between the soil surface and vegetation layers. The optical depth τ , a measure of the vegetation penetration, mainly depends on the radar frequency and ϵ_v . The other two scattering components are functions of vegetation structure, geometry, ϵ_v and radar configuration ([Wigneron et al., 2004](#)).

In the early growth stages, the biomass of crops is very low with an undetectable effect on radar signal, especially for long wavelengths. Accordingly, the effect of vegetation was not considered for areas with low biomass ([Dubois et al., 1995](#), [Moran et al., 2000](#), [McNairn and Brisco, 2004](#)). As the crop grows, the radar signal becomes increasingly sensitive to the canopy. The volume scattering increases in a linear fashion in relation to the vegetation water content (VWC) or plant density until a saturation point ([Ulaby et al., 1986](#)), which varies for different radar configurations. [Imhoff \(1995\)](#) reported that the saturation points for C-, L- and P- band are about 2 kg/m², 4 kg/m² and 10 kg/m² respectively. Moreover, it has been found that the VV polarization tends to saturate at a lower level than HV and HH polarization, because of the dominant vertical structure of most vegetation types ([Bindlish and Barros, 2001](#)).

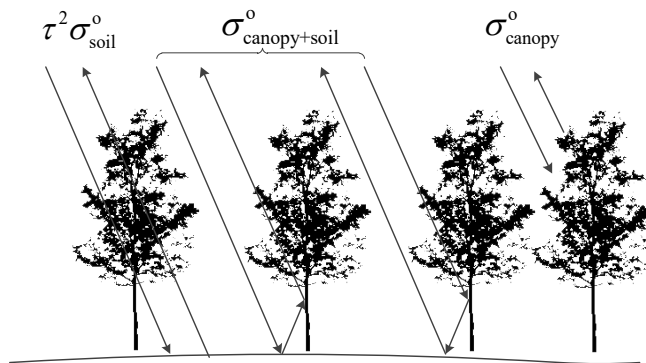


Figure 2-4: Conceptual scattering of an incident radar signal by a vegetated surface; modified from [Ulaby et al. \(2014\)](#).

Many scattering models have been developed to account for the effect of vegetation and thereby to assist soil moisture retrieval from SAR data ([Kornelsen and Coulibaly, 2013](#)). These models are either based on the radiative transfer theory ([Ulaby et al., 1990](#), [Bracaglia et al., 1995](#), [Stiles and Sarabandi, 2000](#), [Karam et al., 1992](#)) or the distorted Born approximation (DBA; [Lang and Sighu, 1983](#), [Saatchi and McDonald, 1997](#), [Sarabandi and Lin, 2000](#), [Burgin et al., 2011](#)). Both models fall into the general category of wave theory and energy transport approach, with the main difference being inclusion of the coherent effect in the DBA ([Saatchi and McDonald, 1997](#)). All these models treat the vegetation layer as a discrete random medium consisting of single microwave scatterers that represent vegetation components (e.g., trunks, branches, and foliage). Among these, the Michigan Microwave Canopy Scattering Model (MIMICS; [Ulaby et al., 1990](#)) is the most popular first-order solution of the radiative transfer equations, and is widely used in soil moisture retrieval ([Balenzano et al., 2011](#), [De Roo et al., 2001](#), [Dobson et al., 1992](#), [Lin et al., 2009](#), [Song et al., 2014](#)). The DBA has also achieved promising results in soil moisture mapping ([O'Neill et al., 1996](#), [Chauhan, 2002](#), [Kurum et al., 2009](#), [Huang et al., 2017a](#)). However, the use of those physical models in operational soil moisture retrieval still suffers from the great number of vegetation parameters required, including the dielectric properties, geometry, and density distribution of scatterers. Recently, the DBA was used to build a series of look up tables (LUTs) for global soil moisture mapping from the SMAP radar ([Kim et al.,](#)

[2014a](#)), where the required vegetation parameters were determined by the VWC and allometric relationships.

The water cloud model (WCM) ([Attema and Ulaby, 1978](#)) is a less complicated alternative that is widely used in soil moisture retrieval ([Prakash et al., 2012](#), [Gherboudj et al., 2011](#), [El Hajj et al., 2016](#), [Askne et al., 2017](#), [Li and Wang, 2018](#)). The principles behind the WCM include that: 1) the vegetation is described as a homogeneous cloud of identical water spheres, uniformly distributed between the ground and the vegetation height; 2) neglecting multiple scattering between the ground and vegetation constituents $\sigma_{\text{canopy+soil}}^0$; and 3) the crop height and cloud density are the only parameters required. In this context, the total backscatter is represented by:

$$\sigma^0 = \tau^2 \sigma_{\text{soil}}^0 + \sigma_{\text{canopy}}^0, \quad \text{Eq. 2-2}$$

with

$$\tau = \exp(-BV_2 \sec \theta), \quad \text{Eq. 2-3}$$

and

$$\sigma_{\text{canopy}}^0 = AV_1 \cos \theta (1 - \tau^2), \quad \text{Eq. 2-4}$$

where A and B are fitted parameters dependent on the vegetation type and radar configuration, and V_1 and V_2 are bulk vegetation parameters, being various biophysical properties of the canopy ([Graham and Harris, 2003](#)). Some commonly used parameters include VWC, leaf area index, leaf water area index and NDVI ([Joseph et al., 2010](#)). [Lievens and Verhoest \(2011\)](#) compared the performance of the WCM using different bulk vegetation parameters and found the leaf area index to be the optimal choice, while NDVI was suggested by [Wang et al. \(2019\)](#). The main limitation of the WCM is the single scattering assumption, hampering its application in areas with significant multiple scattering (e.g., dense vegetated areas). Moreover, since the parameters A and B are dependent on the canopy type and radar

configuration, generalization of the model and integration of the WCM in a multi-configuration inversion scheme is still challenging.

2.4 Soil Moisture Retrieval from SAR Data

The scattering models introduced above suggest that soil moisture retrieval is a process of separating the contribution of soil moisture from a few other surface parameters. From the view of finding a solution, this process is commonly ill-posed as the number of observations is usually less than that of the unknowns, especially in vegetated areas. It is widely acknowledged that a single configuration was insufficient to retrieve soil moisture accurately ([Altese et al., 1996](#)), with most methods using multi-configured and/or multi-temporal data. Accordingly, multi-configuration methods are reviewed first, followed by multi-temporal methods where the major unknowns representing the roughness and vegetation can be assumed time-invariant.

2.4.1 Multi-configuration methods

Multi-polarization radar has been successfully applied for soil moisture retrieval from SAR observation alone. The availability of multi-polarized data has allowed the application of both the Dubois model ([Dubois et al., 1995](#)) and Oh model ([Oh, 2004](#)). The former needs HH and VV polarization, while the latter requires both the cross- and co-polarization ratios. Multi-polarized data also benefit the soil moisture retrieval using IEM like models and various inversion methods, such as the LUT ([Van Oevelen and Hoekman, 1999](#), [Bryant et al., 2007](#), [Baghdadi et al., 2002a](#), [Bai et al., 2016](#)), neural networks ([Baghdadi et al., 2002a](#), [Notarnicola et al., 2008](#)) and Bayesian methods ([Notarnicola et al., 2008](#), [Paloscia et al., 2008](#)). Multi polarized data in these inversion methods help turn the ill-posed retrieval problem into a well-posed one.

For a vegetated area, the advantage of multi-polarization may be the availability of cross- (HV/VV) and co-polarization (HH/VV) ratios, which closely relate to vegetation parameters ([Kornelsen and Coulibaly, 2013](#)). Simple empirical models based on these ratios can be built to remove the influence of vegetation ([Gherboudj](#)

[et al., 2011](#)). Moreover, polarimetric decomposition methods that were initially used in landcover classification ([Freeman and Durden, 1998a](#), [Yamaguchi et al., 2005](#)) were introduced in soil moisture retrieval, to better utilize the information contained in multi-polarized data. Individual contributions of the three components depicted in Figure 2-4 can be separated by proper decomposition models, with soil moisture then being retrieved from the soil surface contribution ([Hajnsek et al., 2009](#), [Jagdhuber et al., 2013](#), [Jagdhuber et al., 2015](#), [He et al., 2016](#), [Wang et al., 2017](#)). Despite some positive results, polarimetric decomposition models need further development for the purpose of soil moisture retrieval. For example, [Baghdadi et al. \(2013\)](#) found that the polarimetric parameters calculated from multi-frequency data were not very relevant to soil moisture over bare agricultural soils. Moreover, these methods need well calibrated data in terms of both amplitude and phase, with the influence of calibration uncertainty being unclear.

The σ^0 collected from multiple incidence angles shows great promise for soil moisture retrieval. The difference of σ^0 collected from two incidence angles was found to be relatively insensitive to soil moisture but very sensitive to soil roughness ([Boisvert et al., 1997](#), [Zribi and Dechambre, 2003](#)), and thus being an effective indicator of roughness for improving the empirical soil moisture retrieval models ([Srivastava et al., 2003, 2009](#)). Alternatively, roughness can be estimated from the σ^0 difference of two incidence angles, thereby simplifying the soil moisture retrieval. [Zribi and Dechambre \(2003\)](#) proposed an empirical model that relates roughness parameter Z_s with the σ^0 difference of HH polarization from 23° and 39°. [Rahman et al. \(2008\)](#) then extended this method for soil moisture and roughness retrieval based on an extra observation of dry season. [Wang et al. \(2011\)](#) further developed this method by integrating the empirical relationship between σ^0 and the effective L_C developed by [Baghdadi et al. \(2006a\)](#). Studies have also directly used multi-angular data (commonly multi-polarized) in inverse scattering models ([Sahebi and Angles, 2010](#), [Bryant et al., 2007](#), [Merzouki and McNairn, 2015](#), [Baghdadi et al., 2006b](#)).

Of greater promise in soil moisture retrieval is the use of satellites to obtain multi-frequency data. A two-frequency polarimetric radar (such as a C- and L-band system) is expected to derive more accurate soil moisture over bare soil than a single frequency radar, as the different roughness scales respond differently to the different frequencies ([Ulaby et al., 2014](#)). Despite the great potential, only limited studies so far have applied multi-frequency data in soil moisture retrieval ([Bindlish and Barros, 2000](#), [Bindlish and Barros, 2001](#), [Pierdicca et al., 2008](#), [Zhang et al., 2016](#), [Zhang et al., 2018](#)). The main challenging has to do with the dependency of oversimplified scattering models (e.g., the IEM, Oh, and WCM) on frequency. For a bare soil surface, the single scale roughness parameters (H_R , L_C and isotropic ACF) are insufficient to represent the real roughness viewed by radar with different frequencies. As a result, effective roughness parameters of one frequency are not optimal for another frequency, requiring frequency-specific calibration. For vegetated surfaces, the fitted parameters of simplified radiative transfer models such as the WCM are also dependent on the radar configuration ([Bindlish and Barros, 2001](#), [Zribi et al., 2005a](#), [Joseph et al., 2010](#), [Hosseini and McNairn, 2017](#)). Consequently, successful soil moisture retrieval from multi-frequency data either requires more complex model calibrations or includes more unknown parameters (e.g., multi-scale roughness) to represent the real roughness viewed by a multi-frequency radar. More frequencies also mean more unknowns to be determined in soil moisture retrieval.

Moreover, current and the forthcoming satellites (Table 2-1) cannot simultaneously image surfaces with multi-frequency. Therefore, collecting multi-frequency data at the same location is only possible by combining multi-SAR missions. However different SAR missions often do not pass by the same location on the same date, resulting in a delay between images with different frequencies. A potential solution is to use the different temporal behaviors of surface parameters. For instance, for short periods roughness and vegetation can be assumed as time-invariant with the soil moisture being the only parameter varying over time. This is the main principle of the multi-temporal methods introduced below.

2.4.2 Multi-temporal methods

The temporal behavior of soil moisture is usually characterized by a relatively fast dry down process following an abrupt increase from precipitation, compared to the changes in soil roughness and vegetation which undergo relatively smooth transition in time, except for deliberate cultivation practices. Accordingly, roughness and vegetation parameters may be considered constant for acquisitions over sufficiently short time intervals. This assumption allows for a simple empirical relationship between soil moisture change and the σ^0 difference of two images. This method is called the change detection or image difference technique accordingly.

A general formulation is given as follows:

$$\sigma^0 - \sigma_{\text{benchmark}}^0 = A(mv - mv_{\text{benchmark}}), \quad \text{Eq. 2-5}$$

where mv and $mv_{\text{benchmark}}$ are the soil moisture of the target image and the benchmark image (e.g., the σ^0 of a dry season). The right hand side can also be written as a wetness index by dividing the left hand side by the σ^0 difference of extreme wet and dry conditions ([Sano et al., 1998](#), [Wagner et al., 1999a, 1999b](#)). Some studies have directly applied such methods with satisfactory results ([Moran et al., 2000](#), [Thoma et al., 2006](#), [Hornáček et al., 2012](#), [Hoshino et al., 2012](#), [Wagner et al., 2015](#)). Other researchers have improved this method by removing the area with a low sensitivity of σ^0 to soil moisture. For example, [Quesney et al. \(2000\)](#) used an unsupervised classification to first mask the insensitive dense wheat fields, and then applied the change detection to the remaining area. Likewise, [Hégarat-Mascle et al. \(2002\)](#) classified the landcover using multi-temporal SAR images and proposed a set of rules to determine the insensitive targets based on different landcover types and different vegetation growing stages. Similarly, [Zribi et al. \(2007\)](#) used NDVI, Normalized Difference Water Index (NDWI) and Digital Terrain Model (DTM) to mask the insensitive areas. Moreover, some studies have combined other source data with SAR observations in the change detection method, such as radiometer data ([Kim and Van Zyl, 2009](#), [Piles et al., 2009](#)) and optical data ([Kurucu et al., 2009](#)).

There are several other soil moisture retrieval methods using multi-temporal data. [Joseph et al. \(2008\)](#) first estimated the roughness using ground measured soil moisture and the IEM, with time series soil moisture retrieved from images over the whole crop growing season. Similarly, [Rahman et al. \(2008\)](#) estimated the roughness parameter Z_s ([Zribi and Dechambre, 2003](#)) using two images of dry condition first, and then applied the retrieved roughness in the following moisture retrieval. [Mattia et al. \(2006b\)](#) took a previously retrieved soil moisture map as the prior information and updated the soil moisture using subsequent images. This method was then extended to estimate time-series soil moisture, and one H_R and L_C , through numerical inversion of the IEM from time-series measurements of HH backscatter ([Mattia et al., 2009](#)). [Pierdicca et al. \(2010\)](#) proposed a two-step multi-temporal soil moisture retrieval method, with the first step being vegetation correction of time-series SAR observations taking the image achieved before the vegetation growing season as the benchmark. These corrected images are then integrated into an inversion scheme based on Bayesian theory. [Balenzano et al. \(2011\)](#) related the multi-temporal alpha approximation for the HH polarization to the soil moisture, which was further extended for multi-polarization data ([Ouellette et al., 2017](#)). Taking another approach, [Kim et al. \(2012a\), \(2014a\)](#) implemented a LUT times-series method to estimate time-series soil moisture by minimizing a cost function of the LUT calculated by NMM3D ([Huang et al., 2010](#)) using time series HH and VV observations. In another approach again, [Kweon and Oh \(2014\)](#) developed an approximation method called “juxtaposition/possibility” to derive time-series soil moisture and one invariant H_R from time-series single polarization data; this was found to perform as well as the Oh model using quad polarizations.

Currently, there are two main limiting factors of the multi-temporal methods. The first has to do with the assumption of invariant roughness. Although many studies have confirmed the time-stationarity of roughness in grasslands and agricultural fields after seeding ([Callens et al., 2006](#), [Jackson et al., 1997](#), [Moeremans and Dautrebande, 2000](#)), care is still needed to identify when surface cultivation practices have been executed between acquisitions. To this end, [Notarnicola \(2014\)](#) proposed a Bayesian change detection approach in which the possible roughness change is accounted for. [Gorab](#)

[et al. \(2015\)](#) applied roughness correction in multi-temporal retrieval, resulting in improved retrieval accuracy. The other limitation is that current multi-temporal methods have focused on soil moisture retrieval from data with the same configuration. As mentioned in 2.2.3, there is usually a long time-lag between images with the same configuration. Despite these limitations, integrating multi-temporal data in soil moisture retrieval is becoming increasingly popular for large scale applications, because of its operational simplicity and the increased revisit of satellites ([Pierdicca et al., 2014](#), [Fascetti et al., 2015](#), [Tomer et al., 2015](#), [Wagner et al., 2015](#), [Naeimi et al., 2009](#), [Mattia et al., 2017](#)).

2.5 Knowledge Gap and Proposed Approach

Joint use of multi-SAR missions is a promising way to meet the spatial (tens m) and temporal (2 – 3 days) requirements of soil moisture measurement. The abundant information contained in multi-SAR-mission data is also promising to derive more reliable soil moisture retrieval in view of solving an ill-posed inversion problem. However, there is no sophisticated approach to derive time series soil moisture from multi-SAR-mission data. The multi-angular, multi-frequency and multi-temporal methods are being developed. But current multi-angular and multi-frequency methods can only work for multi-configuration data acquired simultaneously. Otherwise, soil moisture should be time-invariant during the acquisitions of multi-configuration data and thus can only derive the average soil moisture. Current multi-temporal approaches are only suitable for time series data with the same incidence angle, polarization and frequency. Figure 2-5 shows the conceptual relationship among multi-configuration methods, multi-temporal methods and the proposed method for multi-SAR mission retrieval.

Inheriting from multi-temporal methods, the main principle behind the proposed multi-SAR-mission method is the assumption of time-invariant surface roughness and vegetation parameters. This is valid for time series data acquired over a short time interval. However, unexpected surface preparation and animal activities may change the surface drastically and there is no sophisticated method to eliminate the influence of such changes. Therefore, a roughness change detection algorithm is required to identify the roughness variations before combining multi-SAR-mission in soil moisture retrieval.

Some studies have retrieved time series soil moisture from time series multi-angular data in view of extending the multi-temporal methods ([Naeimi et al., 2009](#), [Zribi et al., 2007](#)). An incidence angle normalization procedure is required before soil moisture retrieval in these studies. Although incidence angle normalization methods are well developed ([Karvonen et al., 2002](#), [Ye et al., 2015](#), [Zribi et al., 2005a](#), [Ulaby et al., 1986](#)), this procedure not only introduces additional uncertainties but also removes the abundant information contained in the multi-angular data. [Balenzano et al. \(2011\)](#) proposed a multi-temporal method and claimed the temporal backscatter changes is relatively insensitive to changes in the incidence angle between subsequent L-band acquisitions. This is, however, not confirmed by its further applications ([Balenzano et al., 2012](#), [Balenzano et al., 2013](#), [Mattia et al., 2014](#)). A novelty method without

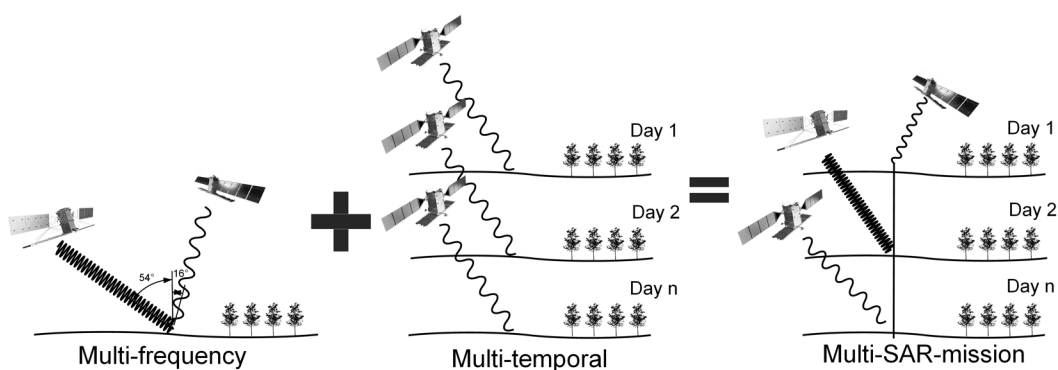


Figure 2-5: Conceptual relationship among the multi-configuration methods, multi-temporal methods, and the proposed method for multi-SAR mission retrieval.

incidence angle normalization is needed in view of extending multi-angular methods. For a further extension to cover multi-frequency data, a combination of current scattering models covering all potential radar configurations are required. The effectiveness of high frequency bands (e.g., the X-band) over vegetated area still need to be addressed although some successful cases were reported recently ([Aubert et al., 2011](#), [El Hajj et al., 2016](#), [Bai et al., 2015](#)). More importantly, the dilemma that more frequencies equal to more unknowns should be carefully considered.

In summary, there is no sophisticated method to collectively retrieve soil moisture from radar data with time-varying incidence angle and frequency. A multi-SAR mission retrieval framework was designed to be compatible with SAR missions operating at the commonly used remote sensing frequency bands, i.e., L-, C- and X-band. Similar to the multi-temporal methods above, the assumption of time-invariant roughness and vegetation is used to remove the major unknowns in soil moisture inversion. The main steps include: 1) development of LUTs covering potential radar configurations; 2) a change detection algorithm to ensure the basic assumption; 3) a time series multi-angular retrieval method and 4) a further extension for multi-frequency data.

2.6 Chapter Summary

This chapter has provided an overview of the importance of soil moisture measurement and techniques for soil moisture measurements. In particular, the potential of using current and forthcoming SAR missions for a reliable soil moisture mapping with high spatial and temporal resolution is discussed; the scattering models relating soil moisture to radar observations and the retrieval methods are presented. Among those retrieval methods, multi-temporal and multi-configuration methods have been widely accepted as promising approaches for the ill-posed soil moisture estimation. The application of those methods, however, are limited in specific radar configuration or data source. Therefore, a framework that can collectively retrieve soil moisture from multi-SAR missions was proposed.

3 Data Sets

This chapter presents an overview of the data sets used in this study, including the field data from the fourth and fifth Soil Moisture Active Passive Experiment (SMAPEX-4 and -5) and associated satellite data. The SMAPEX data sets include airborne SAR data and ground sampling of soil moisture, vegetation and soil surface roughness. The satellite data used include radar data from the L-band PALSAR-2, C-band RADARSAT-2 and X-band COSMO SkyMed, and optical data from the Landsat-8 Operational Land Imager (OLI). These data were used to validate the airborne SAR system in Chapter 4, develop and evaluate the forward scattering models in Chapter 5, identify abrupt surface roughness and vegetation changes in Chapter 6, and demonstrate the multi-angular and multi-frequency soil moisture retrieval algorithms in Chapter 7 and Chapter 8, respectively.

3.1 The SMAPEX Campaign Data

The SMAPEX-4 and -5 were conducted at the beginning of the SMAP operational phase for the purpose of in-orbit calibration/validation of the NASA's SMAP conception ([Ye et al., In Review](#)). These experiments were made in the austral autumn from April 30th to May 23rd, and austral spring from September 6th to 28th 2015, covering various stages of the crop growing season and across a wide range of soil moisture conditions ([Ye et al., In Review](#)). The time series soil moisture and rainfall measurements during this period is presented in Figure 3-2. The SMAPEX study site is a semi-arid cropping and grazing area near the Yanco agricultural institute, located in the center of the Murrumbidgee River catchment, Australia (Figure 3-1). The airborne mapping area is a 71 km × 89 km rectangle with a mostly flat topography. Soil types are predominantly clays, red brown earths, sands over clay and deep sands ([Panciera et al., 2014b](#)). The main landcover types during SMAPEX-4 were bare soil, grass, open wood land and early-stage wheat, with two additional crops (canola and lupine) being observed during SMAPEX-5. A total of six 3 km × 3 km focus areas,

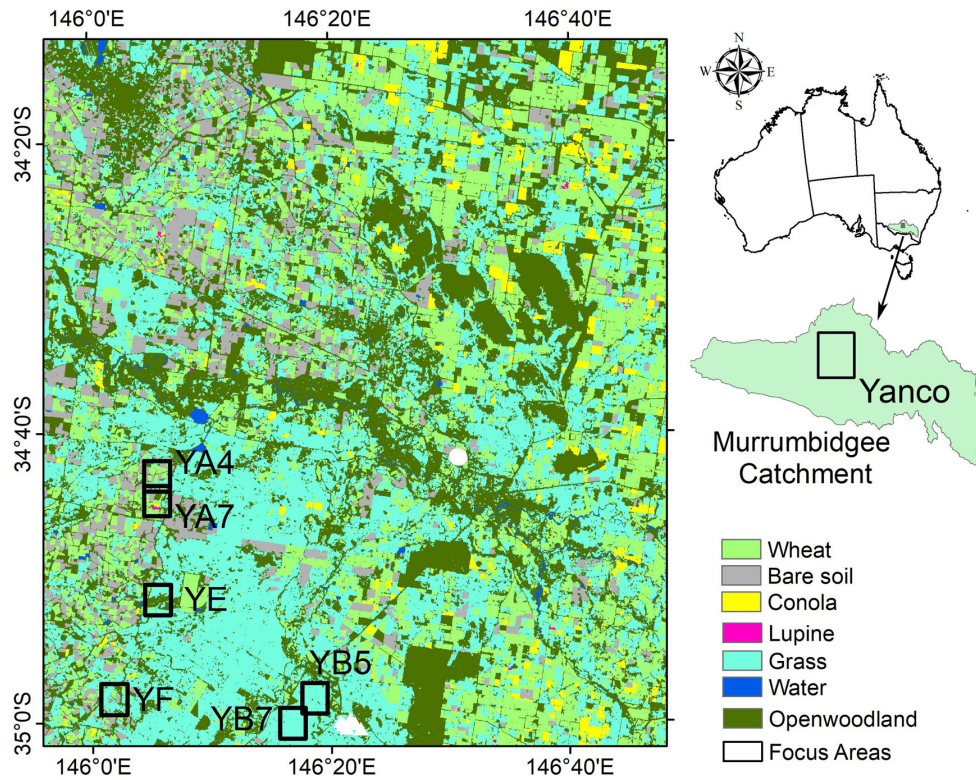


Figure 3-1: Layout of the SMAPEX study area showing the location of six focus areas and the landcover during SMAPEX-5.

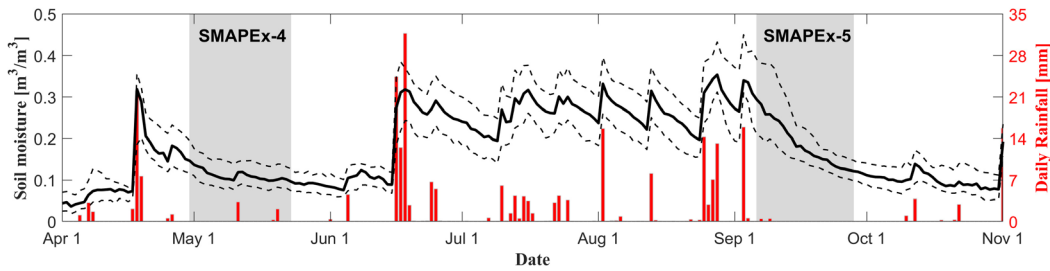


Figure 3-2: Time series of the top 5 cm soil moisture and rainfall measurements from all OzNet sites over the Yanco area 2015; the solid black line and dashed black lines show the mean and 25th/75th percentiles of soil moisture respectively.

YA4, YA7, YB5, YB7, YE and YF, were selected for intensive ground sampling. These areas were selected to cover the land cover conditions represented within the airborne mapping area. Table 3-1 lists the characteristics of the six focus areas.

Table 3-1: Characteristics of the six focus areas, adapted from [Gao \(2016\)](#).

Area ID	Land Use	Landcover Types	Soil Texture (%C/%Si/%S)
YA4	Irrigated cropping (90%); Grazing (10%)	Wheat, bare, grass, open wood land	Clay loam (31/48/20)
YA7	Irrigated cropping (90%); Grazing (10%)	Wheat, bare, naturalised grass, canola, lupine, open wood land	Clay loam (31/48/20)
YE	Grazing (100%)	Grass, open wood land	Silty clay loam (39/43/17)
YF	Irrigated cropping (85%); Grazing (15%)	Bare, wheat, rice, grass	Loam (23/47/29)
YB5	Grazing (100%)	Grass	Loam (24/44/25)
YB7	Grazing (100%)	Grass	Loams (24/44/25)

While the SMAPEX campaigns were a major initiative involving many people, I made extensive contributions to the SMAPEX-5 campaign, including key responsibilities for the soil surface roughness and soil moisture sampling. I performed all processing of the surface roughness sampling data of SMAPEX-5 as well as calibration and processing of all the airborne radar data.

3.1.1 Airborne radar observations

The Polarimetric L-band Imaging Synthetic aperture radar (PLIS) was used to collect L-band (1.26 GHz) radar data during the SMAPEX-4 and 5. PLIS was developed in 2010 by ProSensing Inc. to provide high spatial resolution L-band radar observations using a small low-cost aircraft. The weight of the system is about 38 kg, including i) a radio frequency unit, ii) main and auxiliary dual polarized antenna pairs which can be used separately, iii) a radar data system and iv) external support components including cables, heaters and power supply. A detailed description of the PLIS system is provided below (see also Table 3-2 for a summary):

Signal Generation and Radio Frequency Circuits. A direct digital synthesizer generates either an unmodulated or linear frequency modulated waveform which is then single stage up-converted to radio frequency by mixing with the output from a 1170 MHz phase locked oscillator. For unmodulated waveforms, the pulse width can be varied from

Table 3-2: PLIS system specification

System Parameter	Value
Frequency	L-Band, 1.26 GHz
Peak transmit power	30 W
Pulse repetition frequency	Up to 20 kHz
Transmitter duty cycle	< 4%
Pulse width	0.1- 20 μ s
Maximum bandwidth	30 MHz
Polarization	HH, VV, HV, VH
Beamwidth (H- and E-plane)	$\sim 51^\circ$
Antenna gain	9 dBi
System noise figure	~ 5.2 dB
Antenna cross polarization	< - 30 dB
Flight height / swath width	Typically 3 km / 2.2 km ($15 - 45^\circ$)
Measured noise equivalent normalized	< -47 dB m^2/m^2 (10 m range resolution)
Typical range spacing	3.75 m
Typical azimuth spacing	2 m

100 ns to 10 μ s resulting in a maximum slant range resolution of 15 meters. For linear frequency modulated waveforms the maximum bandwidth that can be chosen is 30 MHz giving a slant range resolution of 5 meters. More commonly a bandwidth of 20 MHz is used giving a slant range resolution of 7.5 m. Subject to the constraint that the duty cycle not exceed 4%, the pulse repetition frequency can be varied to 20 KHz allowing unambiguous Doppler measurements up to 10 KHz. When using a 20 KHz pulse repetition frequency the unambiguous range is 7.5 km. To minimize transmitted power leaking into the nearby GPS band a 25 MHz cavity filter has been placed prior to a 30W peak solid-state amplifier. PLIS also employs an internal calibration loop where the transmit signal can be fed via an attenuator directly to the down-converters prior to the digital receiver.

Antennas. The main antennas are usually installed beneath the aircraft and consists of a right and left pointing antennas mounted at 30 degrees off nadir. A programmable switching network enables transmission through the right and left pointing antennas to be interleaved. Each antenna is a 2 \times 2 patch array with an ~ 20 cm aperture, giving

a measured one-way beamwidth of $\sim 51^\circ$ and theoretical gain of approximately 7 dBi. A similar auxiliary antenna pair can be mounted with an offset enabling interferometric processing to be undertaken. To avoid detuning, the working temperature of each antenna is maintained at a constant 20°C using temperature-controlled heater strips.

Polarimetry. Prior to each antenna there is a two-port network that allows switching the antenna from H to V polarization, thus enabling the full polarization scattering matrix to be estimated on both sides of the aircraft; when the switching is enabled there is a resultant reduction in effective pulse repetition frequency. The cross-polarization isolation has been measured at less than 30 dB.

Radar Data System. The radar data system consists of a standard server mainboard, a two-channel digital receiver and GPS receiver/timestamp card. The two-channel digital receiver samples the data using two 16-bit digitizers at a sampling rate of 120 M samples/s, with an on-board field-programmable gate array employed to implement I/Q demodulation and decimation filtering. The GPS receiver/timestamp card together with the radar control board is employed to determine the absolute time of acquisition.

External support components. An inertial measurement unit aboard the aircraft platform provides navigation and flight attitude data with a sample rate of 10 Hz. This ensures precise flight track control and are used in the motion compensation during the off-line pre-processing stage. In addition, a graphical user interface provides a friendly environment to configure PLIS, and real-time monitoring including raw I/Q voltages, the corresponding power, the filtered pulse power, and the phase after application of the optimal pulse compression filter.

During SMAPEX-4 and -5, the PLIS was flown at an altitude of 10,000ft with a speed of 75 m/s. The main antennas were installed beneath the aircraft with their broadside direction at 30° to nadir to collect full polarimetric data with incidence angles ranging from approximately 15° to 45° , across an ~ 2 km swath. Data was collected on both sides of the flight track with a 2 km gap in the middle, resulting a nominal swath of 6

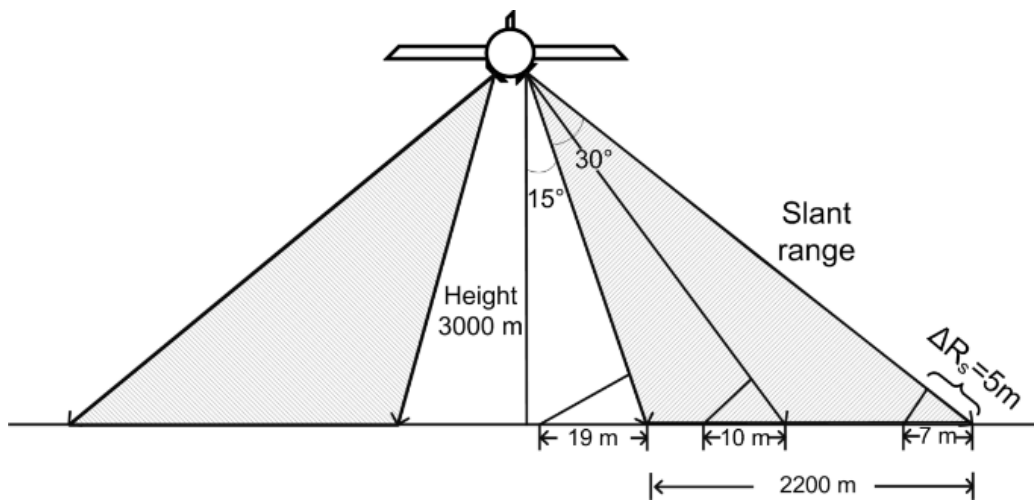


Figure 3-3: Schematic of PLIS mapping geometry at a flight height of 3000 m.

km (Figure 3-3). The collected single look complex (SLC) data had a spacing of 2 m in azimuth and 3.75 m in slant range. Flight lines were designed in a north-south direction with spacing of 5 km, such that the far bins of each swath were overlapped between adjacent flight lines, ensuring full coverage of PLIS over all six focus areas (Ye et al., In Review). An extended swath up to 2.8 km was available for each side with incidence angles being up to 53° , resulting into two radar observations at most parts of the focus areas in each flight date.

A total of 16 out of the 17 scheduled flights were conducted, with the 5th flight in SMAPEX-4 being cancelled due to a rainfall event. Each flight was made over an approximately 6 hour time window from 3 am to 9 am (local time), in order to minimize temporal deviation from the SMAP nominal overpass time of 6 am (Ye et al., In Review). PLIS calibration was conducted using a modified version of the distributed target method (Ainsworth et al., 2006) and six trihedral passive radar calibrators (PRCs). Three Polarimetric Active Radar Calibrators (PARCs) were used for independent evaluation. A comprehensive description of the PLIS calibration and cross-validation with PALSAR-2 are provided in Chapter 4.

3.1.2 Ground observations

Ground observations during the SMAPEX campaigns included intensive soil moisture sampling, vegetation sampling and roughness sampling over the six focus areas. A summary of ground sampling schedule during SMPAEx-4 and -5 is presented in Table 3-3. Ground soil moisture of top 5 cm was sampled concurrently with PLIS observations using the Hydraprobe Data Acquisition System (HDAS, [Merlin et al., 2007](#)). The HDAS consists of a Hydraprobe soil moisture sensor and a micro-computer integrated with a Geographic Information System (GIS) and Global Position System (GPS). During each flight, three of the six focus areas were sampled in rotation with at least one being characterized by cropping and one being grazing land use. Measurements were made on a north-south oriented regular grid, with a spacing of 250 m (Figure 3-4). At each sampling location, three point-based soil moisture measurements were made within a 1 m radius for capturing small scale soil moisture variability. At the end of each intensive sampling day, three gravimetric soil

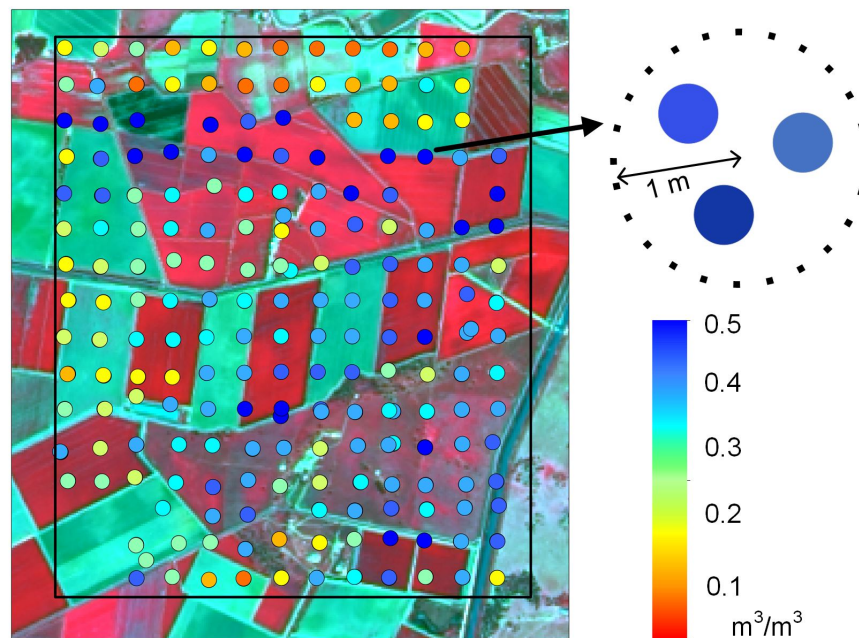


Figure 3-4: An example of ground soil moisture sampling on Sep. 9th, 2015 for the focus area YA4, with the background being the Landsat-8 near-infrared/red/green composition. Three point-based soil moisture measurements were made within a 1 m radius at each location for small scale variability.

Table 3-3: A summary of ground sampling schedule, adapted from (Ye et al., In Review) .

UTC Date	Ground sampling of focus area		
	Soil moisture	Vegetation	Roughness
May 02	YA4, YB5, YF		
May 03	YA7, YB7, YE		
May 04	Regional	YA4, YA7	YA4
May 05	YA4, YB5, YF		
May 06	Regional	YA4, YA7	YA7
May 07	Regional	YE, YF, YB	YB/YE/YF
May 10	YA7, YB7, YE		
May 11	YA4, YB5, YF		
May 12	Regional	YA4, YA7	YA4
May 13	YA7, YB7, YE		
May 14	Regional	YA4, YA7	YA7
May 15	Regional	YE, YF, YB	YB/YE/YF
May 18	YA4, YB5, YF		
May 19	YA7, YB7, YE		
May 20	Regional	YA4, YA7	YA
May 21	YA4, YB5, YF		
Sep 08	YA4, YB5, YE		
Sep 09	Regional	YA4, YA7	YA4
Sep 10	YA7, YB7, YF		
Sep 11	Regional	YE, YF, YB	YA7
Sep 13	YA4, YB5, YE		
Sep 14	Regional	YA4, YA7	YB/YE/YF
Sep 15	Regional	YE, YF, YB	YA4
Sep 16	YA7, YB7, YF		
Sep 17	Regional	YA4, YA7	YB/YE/YF
Sep 18	YA4, YB5, YE		
Sep 21	YA7, YB7, YF		
Sep 22	Regional	YA4, YA7	YA4
Sep 23	YA4, YB5, YE		
Sep 24	Regional	YE, YF, YB	YB/YE/YF
Sep 25	Regional	YA4, YA7	YA4
Sep 26	YA7, YB7, YF		

samples representing low, medium, and high soil moisture within each sampled 3-km focus area were collected for the calibration of HDAS. The comparison between

HDAS and gravimetric soil samples showed a root mean square difference (RMSD) of better than $0.04 \text{ m}^3/\text{m}^3$.

Vegetation samples for the six focus areas were collected between the airborne sampling days, including spectral and intensive vegetation sampling. Spectral observations of the major vegetation types within the focus areas were collected for VWC extrapolation, also being basis of landcover mapping from optical data. Intensive vegetation sampling focused on detailed plant biophysical parameters of cropping and grazing areas ([Ye et al., In Review](#)). The plant density and height, leaves and stalks geometry and orientation were sampled over dominant vegetation types within the 3-km focus areas. A minimum of 3 samples were made within homogenous vegetation paddocks for each major vegetation types or growth stages of the same vegetation type, with the measured values presented in following chapters. Additional information on row spacing, plant spacing, and row direction were recorded for crop paddocks ([Ye et al., In Review](#)).

Surface roughness was characterized at 2 – 3 locations within each dominant land cover type in the six focus farms. Roughness Measurements were made along a 3 m segment using a pin profiler with pins at 0.5 cm spacing in two orthogonal directions (along and across rows or north-south and east-west in the case of no row structure). A digital camera was fixed in front of the profiler to capture the images of soil surface profiles. A software package based on Matlab was developed to automatically process these photos (see Figure 3-5 for an example), with the main outputs being the digital profiles and roughness statistics (H_R and L_C). Measurements for paddocks were then averaged for these with an isotropic surface or averaged along and across rows respectively in presence of periodical row features. Note that the roughness was expected to be fairly constant over the 3-week period of each SMAPEX campaign, so resampling was only made in paddocks with soil cultivation activities. It was however resampled in several selected paddocks to show the natural evolution. The roughness measurements used in this study is provided in Chapter 5.

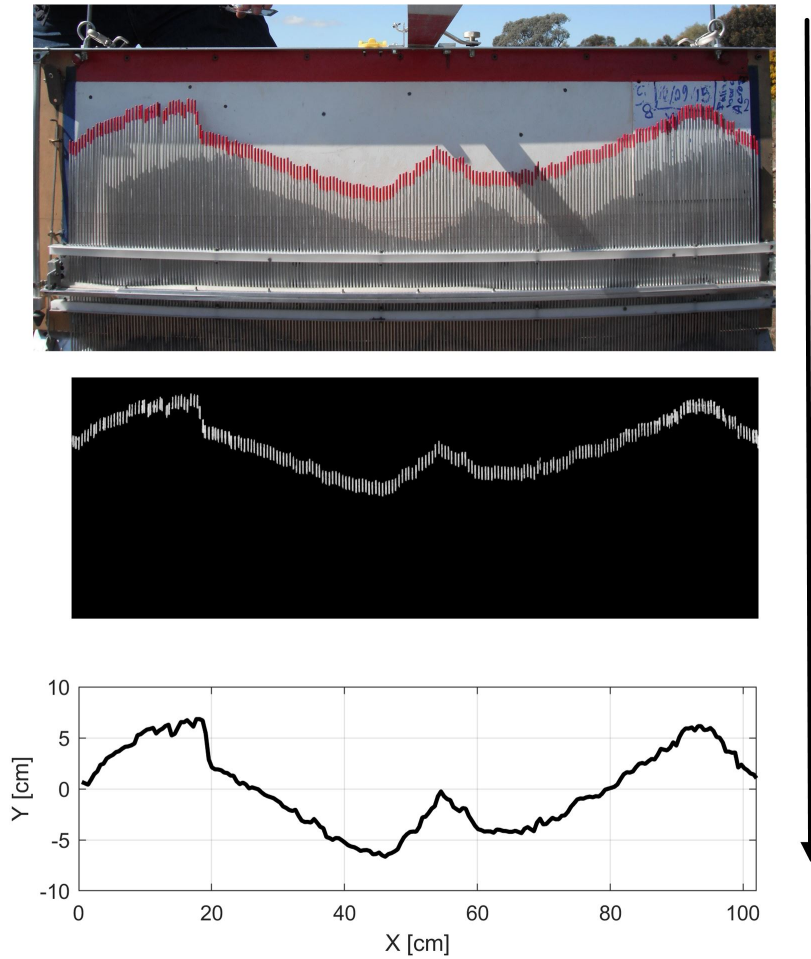


Figure 3-5: Main steps for soil roughness calculation: roughness photo (top), extracted pin profile (middle) and digital profile (bottom).

Cultivation activities within the focus areas, including tillage and irrigation, occurred during the SMAPEX-5. The dates of these activities were also recorded and summarized in Chapter 6. These details were used as ground truth for evaluating the proposed change detection algorithm (Chapter 6) and exploring the effect of abrupt roughness and vegetation changes on multi-temporal retrieval approaches (Chapter 8).

3.2 Satellite Data

The spaceborne radar data from four platforms was used in this study; PALSAR-2, RADARSAT-2 and COSMO-SkyMed. The PALSAR-2 data were used in cross-validation of the PLIS data. The data from RADARSAT-2 and COSMO-SkyMed,

together with the PLIS data were used in the development and evaluation of the proposed multi-SAR retrieval framework. An example of radar data collected from all platforms is presented in Figure 3-6.

The PALSAR-2 is an L-band (1.26 GHz) SAR aboard the JAXA's Advanced Land Observing Satellite 2 (ALOS-2). It was launched in 2014, as an enhanced successor of the PALSAR-1 that retired in 2011. PALSAR-2 has 7 SAR observation modes for various applications, with different polarization, swath, incidence angle and bandwidth ([Rosenqvist et al., 2014](#)). Although the nominal revisit is 14 days, global coverage requires a much longer period dependent on the observation mode ranging from 42 days to 5 years ([Rosenqvist et al., 2014](#)). One Fine Beam Stripmap image and one ScanSAR image are available from during the SMAPEX-4 & 5 respectively and were used in the cross-validation with the PLIS data.

The RADARSAT-2 is a C-band (5.4 GHz) SAR of the Canadian Space Agency that was launched in 2007, as a follow-on to the RADARSAT-1 which terminated in 2013. RADARSAT-2 can collect data from both left and right sides with more than 10 observation modes. The details of the mission can be found in [Morena et al. \(2004\)](#). The available C-band data was all collected during the SMAPEX-5, including three wide-swath standard quad-polarization SLC products and four standard dual polarization SLC products. The slant range spacing is either 8 or 11.8 m with a consistent azimuth spacing of 5.1 m. The incidence angle of these images varied between 22° – 40° .

The COSMO-SkyMed (Constellation of Small Satellites for Mediterranean basin Observation) is a 4-satellite constellation developed by the Italian Space Agency. Each of the satellites is equipped with an X-band SAR operating at 9.3 GHz collecting single or dual polarized data. The nominal incidence angle varies from 25° to 50° and can be extended to between 20° and 59° . The main purposes of this constellation are environmental risk management for both civilian institutional and defense needs, and commercial services ([Covello et al., 2010](#)). Consequently, data is only collected based on scheduled orders without routine global coverage, despite the extremely high revisit

of up to 2 hours (Covello et al., 2010). The available data was all collected during SMAPEX-5 consisting of two interferometric subsets of STRIPMAP HIMAGE. One was acquired from ascending and the other was from descending orbits.

Apart from radar data, two Landsat-8 Operational Land Imager (OLI) image were acquired, one on June 10 and the other on September 30, 2015. These were used for: 1) landcover mapping of the airborne area; 2) geo-registration of multi-temporal SAR data; and 3) extraction of paddock boundaries. The Landsat-8 was launched in 2013, successfully extending the 40 + year Landsat record. The OLI on board Landsat-8 is a multi-spectral sensor operating in 11 spectral bands ranging from 0.43 to 12.51 um

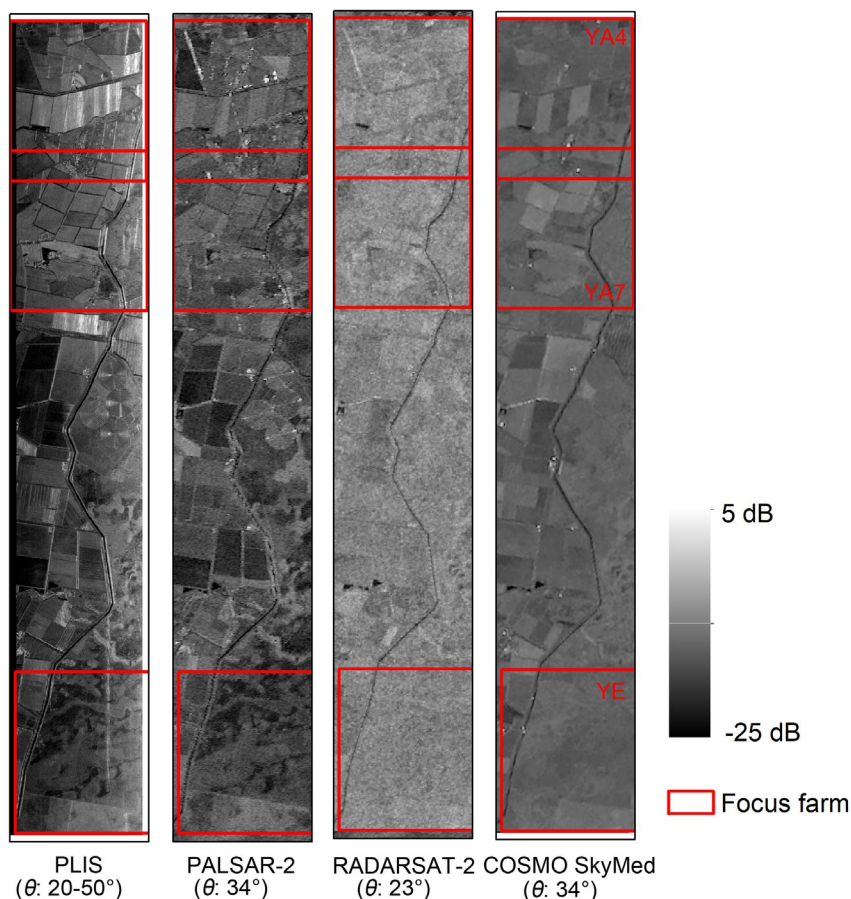


Figure 3-6: Examples of radar data (HH polarization), covering the YA4, YA7 and YE areas, with the PLIS, PALSAR-2, RADARSAT-2 and COSMO SkyMed data collected on Sep. 11, 24, 11, and 10, 2015 respectively..

Table 3-4: A summary of data used in each chapter.

Chapter	Focus area	Campaign	Data
4	The whole SMAPE _x area (Figure 3-1)	SMAPE _x -4 & 5	PLIS and PALSAR-2 data; landcover maps
5	YA4, YA7, YE	SMAPE _x -5	PLIS, RADARSAT-2, COSMO SkyMed data; ground measured <i>m</i> , roughness, all vegetation parameters
6	YA4, YA7, YE	SMAPE _x -5	PLIS, RADARSAT-2, COSMO SkyMed data; records of vegetation and roughness changes
7	YA4, YA7, YE	SMAPE _x -5	PLIS data; ground measured <i>m</i> , roughness, VWC; landcover
8	YA4, YA7, YE	SMAPE _x -5	PLIS, RADARSAT-2, COSMO SkyMed data; ground measured <i>m</i> , roughness, VWC; landcover

([Roy et al., 2014](#)). The spatial resolution is 30 m for visible to shortwave infrared, 15 m for panchromatic and 100 m for two thermal infrared bands.

Two landcover maps were generated using the 7 visible to shortwave infrared bands of OLI for SMAPE_x-4 and -5 respectively, with the map for SAMPE_x-5 shown in Figure 3-1. Briefly, the boundaries of paddocks were generated using the multiresolution segmentation algorithm ([Baatz, 2000](#)) embedded in the commercial software eCognition Developer 8. Paddock based features, including the spectral and texture parameters, were then calculated as input of classification. A Support Vector Machine was trained using half of the ground observations of land cover types. The evaluation based on the other half of ground truth showed an overall accuracy and kappa coefficient of 91.02% and 0.877, respectively.

3.3 Chapter Summary

This chapter has presented an overview of the data sets used in this research, including the existing satellite data and field data from the two SMAPE_x campaigns. The SMAPE_x data sets, comprising airborne active observations from PLIS, ground sampling of soil moisture, vegetation and roughness data, together with their sampling strategy were described in detail. While the chapter is only a brief overview of the data

used in this thesis with a focus on how those data were collected, the details of specific data sets used in each of the research steps are described more fully in the “Date Sets” section of the respective chapters. A summary of specific data used in the following chapters is presented in Table 3-4. Please also refers to the workplans of the two SMAPEX campaigns for more details (available at: <http://www.smapex.monash.edu.au/>).

4 Calibration and Validation of PLIS

The airborne PLIS system introduced in Chapter 3 provided a unique and dense L-band data set for development of the proposed multi-SAR-mission approach. However, accurate polarimetric and radiometric calibration is critical for validation of the proposed soil moisture mapping concept, and this task had not been completed for the SMAPEX-4 and 5 data sets. Therefore, the calibration of the PLIS data is presented in this chapter. Moreover, the potential for cross-validation/calibration among SAR systems is demonstrated through a comparison between PLIS and ALOS-2/PALSAR-2 data. The work in this chapter has been published in [Zhu et al. \(2018\)](#).

4.1 Background

Despite the increased availability of spaceborne SAR data (Table 2-1), airborne SAR systems still play a vital role in the development, implementation, testing and verification of potential spaceborne SAR applications. Several popular airborne SAR systems have already been mentioned in Chapter 2. Most of these airborne SAR systems can operate in quad-polarization and interferometric modes. The significant flexibility provided by these airborne platforms enables extremely dense observations and variable acquisition geometries, e.g. incidence and azimuth angles. These characteristics allow for a better understanding of the surface scattering and its temporal behavior, which are essential for the successful development of applications.

The PLIS is Australia's first L-band polarimetric airborne interferometric SAR system dedicated to scientific research into civilian applications. The main objective of the PLIS system is to provide hydrologic, ecologic, atmospheric and oceanic researchers with a capability for high temporal and spatial resolution observations over Australia. Compared to other airborne SAR systems ([Ouchi, 2013](#)), the weight of PLIS is significantly lower (~ 38 kg) allowing integration aboard much smaller and lower-cost

aircraft, thus making the SAR capability available to a much wider range of users. Since its first flight in 2010, PLIS has been used for a range of applications.

PLIS together with the Polarimetric L-band Multibeam Radiometer was used as an active-passive microwave simulator ([Wu et al., 2015b](#)) of NASA's Soil Moisture Active Passive (SMAP) mission ([Entekhabi et al., 2010](#)). Three pre-launch experiments (SMAPEx-1, 2 and 3) ([Panciera et al., 2014b](#)) and two post-launch experiments (SAMPEX-4 and 5) ([Ye et al., In Review](#)) were carried out in 2010 - 2011 and 2015 respectively, for the calibration/validation of the SMAP concept. The data acquired by the PLIS system have been extensively used for testing active-passive soil moisture downscaling algorithms for SMAP ([Wu et al., 2014](#), [Wu et al., 2015a](#), [Wu et al., 2016](#)).

By making full use of the flexible acquisition geometries of PLIS, data from the SMAPEx campaigns also allowed the development of novel algorithms for measuring critical environmental variables. Such algorithms include soil moisture retrieval using polarimetric decomposition ([He et al., 2016](#)), evaluation and calibration of surface scattering models ([Zhu et al., 2016](#), [Panciera et al., 2014a](#)), vegetation biomass estimation ([Tanase et al., 2013](#), [Tanase et al., 2014a](#), [Tanase et al., 2014b](#)), estimation of vegetation water content ([Huang et al., 2016](#), [Tanase et al., 2015](#)) and inland water body detection ([Elhassan et al., 2013](#)).

More applications of PLIS are expected in the near future, including the development and evaluation of soil moisture retrieval algorithms for the recently launched L-band SAOCOM constellation ([Giraldez, 2003](#)), monitoring the effect of bushfires and the subsequent recovery of affected areas throughout Australia ([Menges et al., 2004](#)), and high spatial resolution Land Use Land Cover (LULC) mapping. All these applications need an accurate calibration of the PLIS sensor in terms of both polarimetry and radiometry as per the requirements for the various applications provided in ([Freeman, 1992](#)). Briefly, the absolute and relative calibration accuracy is required to be better than ± 1 dB and ± 0.5 dB respectively. For polarimetric data, additional requirements are that the polarimetric channel balance be better than ± 0.4 dB and $\pm 5^\circ$ in phase, with the cross-talk isolation better than 30 dB ([Dubois et al., 1992](#)).

To verify that such criteria have been met, active or passive point targets with large Radar Cross Section (RCS) and known polarimetric characteristics (e.g. trihedrals and transponders) are commonly used. Radiometric calibration factors, polarimetric calibration parameters, and image quality are derived from the impulse response functions (IRFs) of these point targets ([Freeman et al., 1990](#), [Gray et al., 1990](#), [Sarabandi et al., 1995](#), [Christensen et al., 1998](#), [Shimada et al., 2009](#)). The main challenges of using point targets are i) the uncertainty introduced by the interaction with the background; ii) the need to carefully set and maintain their orientation angles; iii) the poor visibility in coarse SAR images (e.g., the 3-km resolution SMAP radar); and iv) their relatively large size compared to the spatial sampling of high resolution SARs. Alternatively, a uniformly distributed scene (clutter), such as homogeneous dense forests, can be used for calibration; the RCS and polarimetric characteristics of which are either measured by ground-based scatterometers ([Sarabandi et al., 1994](#)) or assumed to satisfy some time-invariant prior-knowledge ([Shimada et al., 2009](#), [Shimada, 2011](#), [Ainsworth et al., 2006](#), [Sarabandi et al., 1995](#), [Gupta et al., 2016](#)). The former is commonly unavailable for a large area while the latter may suffer from uncertainty of the prior knowledge.

Cross-calibration among different radar systems is another promising approach where airborne SAR observations can be the intermediate step for the calibration of space-based SARs ([Freeman, 1992](#)). However, very few studies on this topic have been carried out mainly because of the difference in observation time, radar configuration, and look direction (azimuth and elevation angle). In [Sarabandi et al. \(1994\)](#), a ground-based scatterometer was used to calibrate AIRSAR, and different tracks and polarizations of SIR-C/X-SAR were cross-calibrated in [Zink et al. \(1993\)](#). More recently, QuikSCAT and Oceansat-2 were cross-calibrated in [Jaruwatanadilok et al. \(2014\)](#).

4.2 Calibration Site and data

4.2.1 Experiments and the Calibration Site

The PLIS has been used in five SMAPEX campaigns. The detail of SMAPEX-1, 2 and 3 as well as a brief introduction to the corresponding calibration is provided in [Tanase et al. \(2014b\)](#) and [Panciera et al. \(2014b\)](#). Similar to these three campaigns, two types of targets were used for calibration in SMAPEX-4 and 5. One is a large forest area (area C in Figure 4-1) which was used in the polarimetric calibration on a daily basis. The other was artificial reflectors including trihedral Passive Radar Calibrators (PRCs) otherwise known as corner reflectors, and Polarimetric Active Radar Calibrators (PARCs). Specifically, six metallic trihedrals with a leg length (l_{tri}) of 1.665 m were deployed at a single calibration site located in a flat, uniformly grazed area (area B in Figure 4-1). The theoretical radar cross section of these targets is 27.5 dBsm, given by $4\pi l_{tri}^4 / 3\lambda^2$ with λ being the wavelength. Figure 4-2(a) shows the RCS pattern along the azimuth and elevation directions. The trihedrals were uniformly distributed across the PLIS swath, with their symmetric axis parallel to the direction of incident signal. The local incidence angle at the six trihedrals was 15°, 21°, 27°, 33°, 39° and 45° respectively in SMAPEX-4, while the 15° trihedral was moved to a location with an incidence angle of 51° in SMAPEX-5 to represent the far edge beam.

A PARC aligning to receive 45° linear polarization and re-transmit -45° linear polarization was also deployed within the Narrandera airport grounds (the area A in Figure 4-1) for calibration during the SMAPEX-4 and -5 campaigns. The theoretical polarimetric response of this PARC is:

$$S = \begin{bmatrix} -1 & -1 \\ 1 & 1 \end{bmatrix}, \quad \text{Eq. 4-1}$$

depicted in Figure 4-2(b). The temperature of the PARC antennas was recorded to determine the real-time RCS, using a carefully measured temperature-RCS look up table. The response of this PARC is expected to independently provide polarimetric

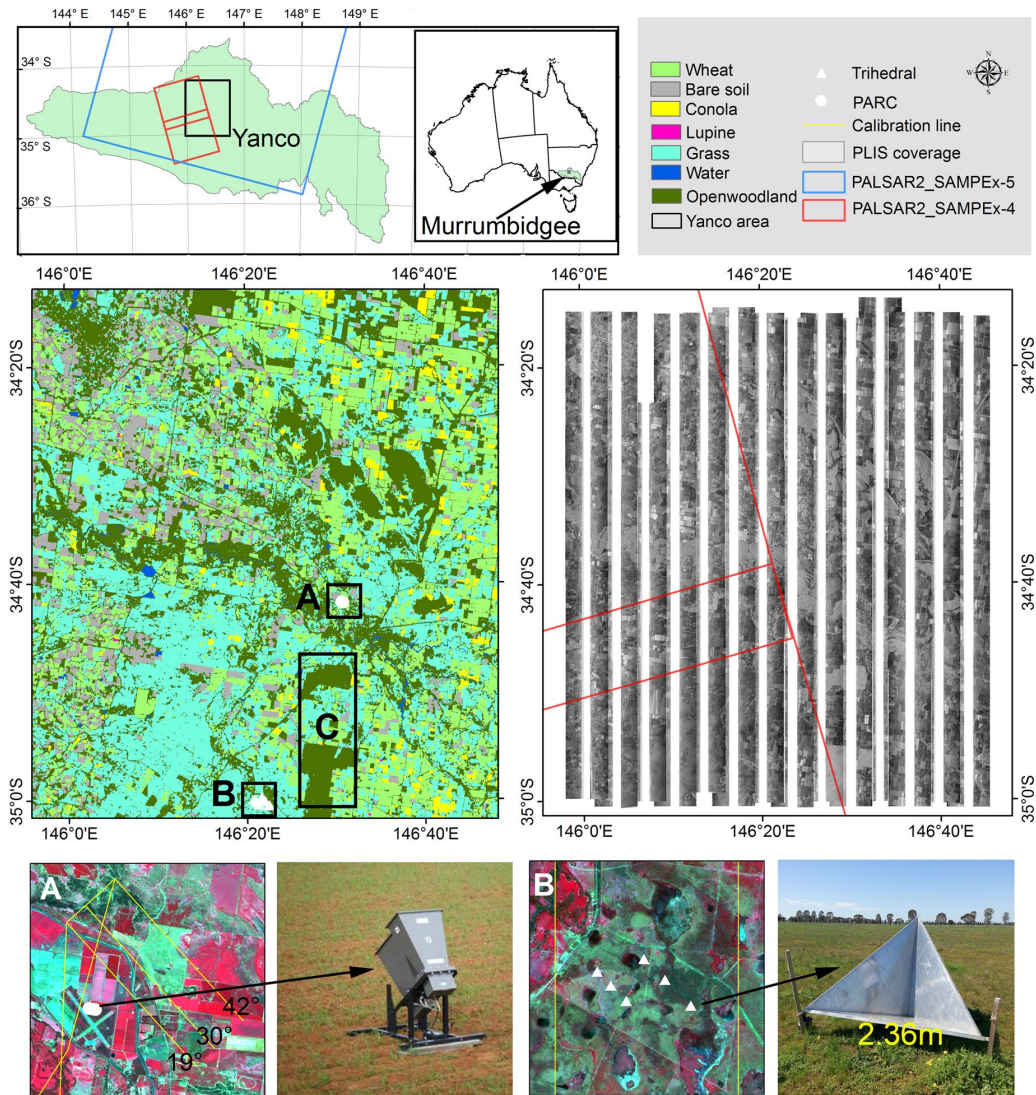


Figure 4-1: Calibration sites and flights used in the calibration and validation, as well as the PLIS and PALSAR2 coverage during the SMAPE-4 and -5. The top left shows the location of the Yanco agricultural area and the spatial coverage of PLIS and PALSAR-2 data. The middle left is the land cover map of SMAPEx-5 with the main calibration sites delineated in black rectangles. Areas A and B show the deployment of PARCs and trihedrals for the corresponding calibration flights (the yellow lines in the bottom panel) respectively. Area C includes the forest areas used in the polarimetric calibration. The middle right is an example of PLIS HH data acquired on September 17, 2015.

accuracy estimates of the calibrated data (Freeman et al., 1990). Calibration flights with the PARC falling towards the far edge of run 1 (42° incidence angle), in the center (30° incidence angle) of run 2, and towards the near edge of run 3 (19° incidence angle)

respectively. The calibration circuits were undertaken only at the start and end of the airborne campaigns.

4.2.2 Data

Two PALSAR-2 images acquired during the SMAPEX-4 (May 1st to May 22nd, 2015) and -5 (September 7th to September 27th) experiments were available for cross-

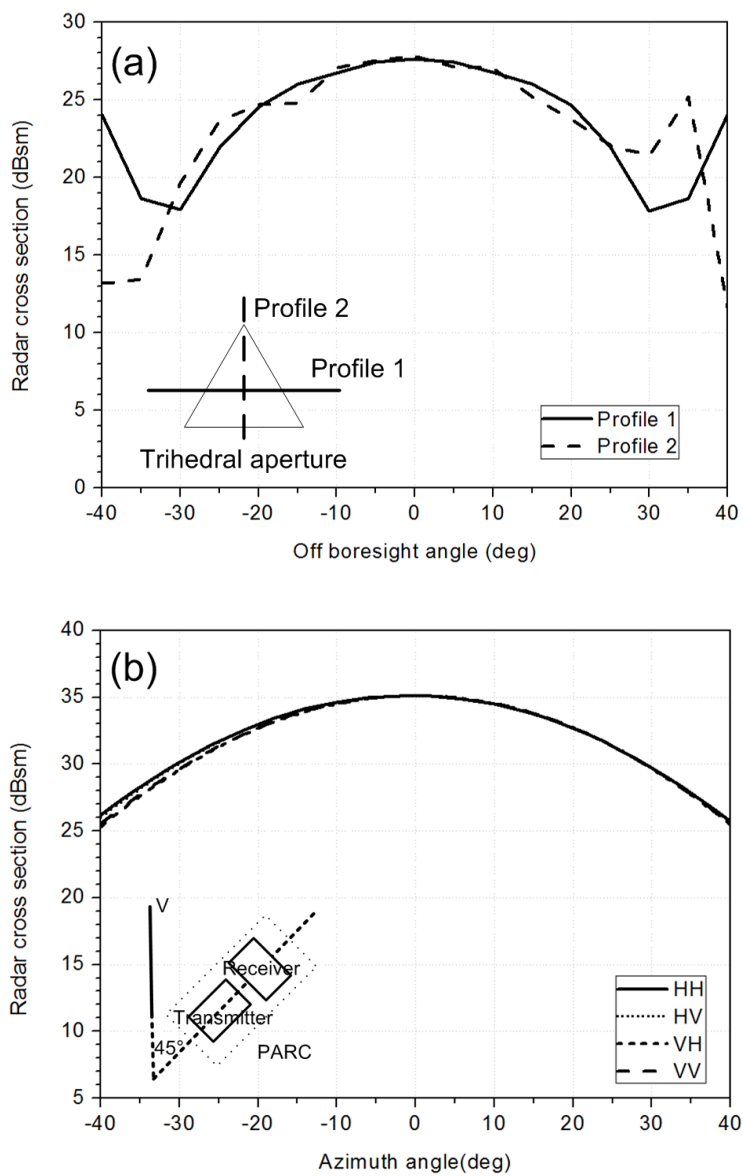


Figure 4-2: RCS patterns of the trihedral (a) and PARC (b) for L-band

validation. The PLIS data with a minimum time offset (32 and 19 hours respectively) with respect to the PALSAR-2 data were selected. Notably, the PLIS data used in cross-validation was the calibrated and multi-looked products with a pixel size of 10 m. The details of the data used in comparison are summarized in Table 4-1 with their spatial coverage shown in Figure 4-1. Geo-registration of both the PALSAR-2 and PLIS images was carried out taking the Landsat-8 OLI image acquired on 30th September 2015 as reference. The spatial miss-registration error was less than 1 pixel (10 m) for PLIS and PALSAR-2 Stripmap images. PALSAR-2 ScanSAR image showed a larger spatial uncertainty (70 m) because of the difficulty in identifying point targets during geo-registration.

Table 4-1: PLIS and PALSAR-2 images used in the cross-validation

	SMAPEX-4 scenario		SMAPEX-5 scenario	
	PLIS	PALSAR-2	PLIS	PALSAR-2
Imaging mode	Stripmap	ScanSAR	Stripmap	Stripmap
Day of year (UTC)	130	132	266	267
Overpass time offset	~ 32 hours		~ 19 hours	
Incidence angle	15° - 50°	36.5° - 43.5°	15° - 50°	31.5° - 34.5°
Polarization	HH+VV+HV+VH	HH+HV	HH+VV+HV+VH	HH+HV
Orbit/direction	North-South, South-North	Descending	North-South, South-North	Ascending
Spatial resolution	10 m	100 m	10 m	10 m
Soil moisture* (m ³ /m ³)	0.172	0.143	0.107	0.105

*: Average soil moisture is estimated from OzNet and ground sampling.

4.3 Method

4.3.1 Calibration method

The calibration of PLIS data included two steps, taking the pre-processed 16-bit slant-range SLC as the input:

1) Polarimetric calibration. The a posteriori method based on a distributed target ([Ainsworth et al., 2006](#)) was used to estimate cross-talk parameters (u, v, w, z) and one of the channel imbalance parameters a . The distortion model relating the actual ($[s_{bb}, s_{bw}, s_{vb}, s_{vw}]^T$) and observed ($[O_{bb}, O_{bw}, O_{vb}, O_{vw}]^T$) scattering matrixes, and derivation of the corresponding calibration matrix can be found in [Ainsworth et al. \(2006\)](#). Briefly, this algorithm iteratively updates u, v, w, z and a , with an initial guess of zero cross-talk using data over a distributed area, e.g. dense forest. The trihedrals were then used to estimate the other imbalance parameter k' denoting the reception imbalance between HH and VV. Finally, the estimated cross-talk and imbalance parameters were employed to correct the observed SLC data:

$$\begin{bmatrix} s_{bb} \\ s_{bw} \\ s_{vb} \\ s_{vw} \end{bmatrix} = \begin{bmatrix} k' \alpha & u \alpha^{-1} & w \alpha & v w k'^{-1} \alpha^{-1} \\ z k' \alpha & \alpha^{-1} & w z \alpha & w k'^{-1} \alpha^{-1} \\ u k' \alpha & w \alpha^{-1} & \alpha & v k'^{-1} \alpha^{-1} \\ u z k' \alpha & u \alpha^{-1} & z \alpha & k'^{-1} \alpha^{-1} \end{bmatrix} \begin{bmatrix} O_{bb} \\ O_{bw} \\ O_{vb} \\ O_{vw} \end{bmatrix}, \quad \text{Eq. 4-2}$$

2) Absolute radiometric calibration. The well-known integral method based on trihedrals ([Gray et al., 1990](#)) was used to estimate the absolute calibration coefficient. Figure 4-3 illustrates the definition of point target area A_{pnu} and background area A_{nu} for the purpose of extracting the point energy in this study. The energy of the trihedrals was estimated as:

$$E_p = \left(\sum_{A_{pnu}} I_{ij} - \frac{A_{pnu}}{A_{nu}} \sum_{A_{nu}} I_{ij} \right) \cdot \delta_a \cdot \delta_r / \sin \theta, \quad \text{Eq. 4-3}$$

where I_{ij} is the intensity of the pixel ij and θ is the incidence angle. δ_a and δ_r are the azimuth and range spacing respectively. The absolute calibration factor from a trihedral (CF_{tri}) can thus be estimated using $CF_{tri} = \sigma / E_p$ where σ is the theoretical RCS of the

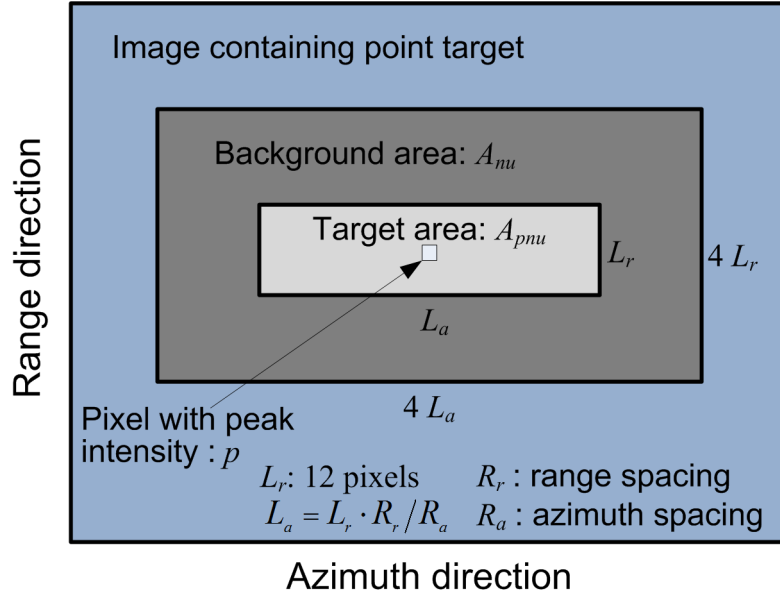


Figure 4-3: Definition of point target area and background area for extracting the response of a point target. The range and azimuth spacing are 3.75 m and 2 m respectively.

trihedral. Six trihedrals were deployed for different range bins and accordingly CF_{tri} could be calculated for different range bins for each calibration flight. The average (CF_a) of all calibration coefficients of a campaign were used to provide a single set of calibration parameters for all observations throughout the campaign. The absolute calibrated σ^0 (dB) for each pixel was then calculated:

$$\sigma^0 = 10 \log_{10}(s \cdot s^*) - CF_a, \quad \text{Eq. 4-4}$$

where s^* is the complex conjugate of the polarimetric calibrated SLC s . The CF_a of SMAPEX-4 were -37.74 dB (left) and -37.69 dB (right) respectively, while they were -37.59 dB (left) and -37.79 dB (right) for SMAPEX-5. The stability of CF_{tri} in the range direction and time for each campaign is provided below in terms of the residual RCS ($CF_a - CF_{tri}$) after calibration.

4.3.2 Evaluation and cross-validation method

The PLIS 3-dB resolution, the Peak-to-Side Lobe Ratio (PSLR), and the Integrated Side Lobe Ratio (ISLR) were estimated using the IRFs of the PARCs. Specifically, the target area in Figure 4-3 was interpreted into 1024×1024 pixels using the fast Fourier

Transform. Two 1-D profiles (azimuth and range) through the peak pixel were then used to estimate these quantities. In addition, the polarimetric matrix of the PARC was used to provide independent evaluation of the calibrated data. The integration method was also used to estimate the amplitudes of the PARC by simply replacing the intensity with amplitude in Eq. 4-3, while the phase of the peak pixel was treated as that of the PARC. The residual radiometric and polarimetric error over trihedrals after calibration was estimated to show the quality of the calibrated data in terms of accuracy and stability in time and space, though they had been used in the estimation of k' and C_a .

Since PLIS and PALSAR-2 have different incidence angles and spatial resolutions, they were resampled onto a coarser grid for cross-validation (Figure 4-4). Specifically, the average incidence angle (θ_{pal}) of PALSAR-2 within the PLIS coverage was calculated, with grids generated to include the PLIS pixels whose incidence angles fall within $\theta_{pal} \pm 3^\circ$. These grid cells have the same size in the azimuth and range directions. It's worth noting that the ground resolution in the range direction is different, resulting in different sizes of the grid cells (500 - 750 m) at different incidence angles. The ensemble mean of PLIS and PALSAR-2 for each grid was calculated for further comparison. Four metrics, i.e., correlation coefficient (R), Bias, Root-Mean-Squared Difference (RMSD) and unbiased RMSD (ubRMSD) were used to represent the agreement between PLIS and PALSAR-2. The ubRMSD is defined as:

$$\text{ubRMSD} = \sqrt{\sum_i^N (x_i - y_i - (\mu_x - \mu_y))^2 / N}, \quad \text{Eq. 4-5}$$

where x_i and y_i are the i th grid of PLIS and PALSAR-2, N is the number of grid cells in comparison. μ_x and μ_y are the mean of x and y respectively. In addition, land cover maps of SMAPE_{x-4} and -5 derived from Landsat-8 OLI images were used to analyze the effect of LULC on cross-validation/calibration.

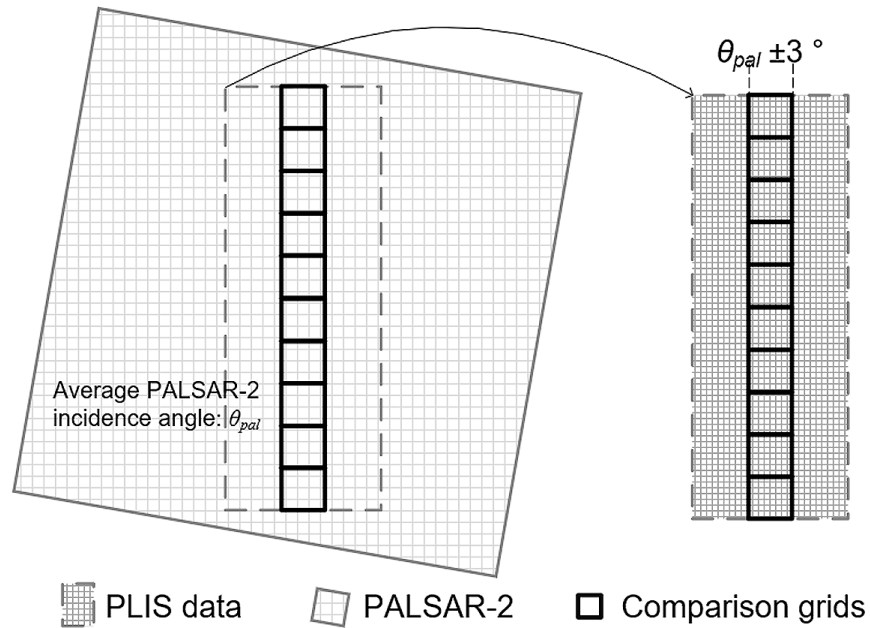


Figure 4-4: Schematic of PLIS and PALSAR-2 comparison. The grid cell size in azimuth and look direction is the same, but the real ground size ranges from 500 – 750m for different PLIS strips because of the variation of ground range spacing.

4.4 Results

4.4.1 Calibration accuracy over point targets

A summary of PLIS image quality parameters is provided in Table 4-2. The estimated azimuth and range 3-dB resolutions were 2.07 m and 5.97 m respectively. The average PSNR were -16.13 dB in azimuth and -16.07 dB in range, the latter of which can be further improved using data specific least mean square filter coefficients in the range compression, but at the cost of broadening point target responses.

Figure 4-5(a) shows the difference between observed and theoretical RCS (residual error) over all trihedrals of SMAPEX-4. In general, this difference was less than 0.5 dBsm for most of the trihedrals which satisfies the absolute calibration accuracy requirement ([Freeman, 1992](#)). A satisfactory balance between HH and VV phase was also observed with an RMSD of 0.17 dBsm. In addition, no clear pattern of residual RCS could be found with respect to the incidence angle, although trihedrals with incidence angles of 23° and 27° had negative residuals while positive residuals were

Table 4-2: PLIS calibration accuracy and its comparison with another two L-band airborne SAR system. PSLR and ISLR are peak-to-side-lobe-ratio and integrated-side-lobe-ratio. $A \pm B$ represents an average of A and a standard deviation of B. * denotes the design

Items	PLIS	Pi-SAR-L2 (Shimada et al., 2013a)	UAVSAR (Fore et al., 2015 , Chamberlain et al., 2006)	Requirement (Dubois et al., 1992 , Freeman, 1992)
3dB resolution				
Azimuth (m)	2.07 ± 0.12	1.01 ± 0.25	0.94	
Range (m)	5.97 ± 0.28	1.8 ± 0.06	2.53	
Side lobe				
PSLR in azimuth (dB)	-16.13 ± 3.19	-9.05 ± 3.42	Azimuth Tx: -11*	
ISLR in range (dB)	-12.12 ± 2.51	-9.05 ± 3.42	Azimuth Ty: -20*	
PSLR in range (dB)	-16.07 ± 2.90	-7.04 ± 1.26	Range: -30*	
ISLR in azimuth (dB)	-11.04 ± 2.65			
Polarimetric calibration				
Amplitude imbalance (dB)	0.17 ± 0.15 ; 0.22 (RMS)	0.09 ± 0.10	0.17 (RMS)	0.4
Phase imbalance (°)	3.87 ± 2.86 ; 4.81 (RMS)	1.368 ± 2.142	5.3 (RMS)	5
Crosstalk (PRC) (dB)	-27.58 ± 1.02	<-32	-30	-30
Crosstalk (nature target) (dB)	-30.55 ± 1.01	-38.62		
Radiometric calibration (dB)				
Radiometric calibration (dB)	0.58 (RMS) 0.82 (1 sigma)	1.16 (1 sigma)	0.7 (RMS)	
Comparison with PALSAR-2				
RMSD with ScanSAR (dB)	2.47 (HH); 1.92 (HV)			
RMSD with Stripmap (dB)	1.29 (HH); 1.01 (HV)			

observed over others. This can be partly explained by the limitation of the trihedral approach and the integral method used to extract its RCS. The interaction between trihedral and background is well known to introduce uncertainty in the estimation of the RCS, which cannot be removed by the integral method ([Ulaby et al., 2014](#), [Sarabandi et al., 1994](#)). This uncertainty can vary from trihedral to trihedral because of the variation of the background over the time and space domain. The variation in time series can in turn partly explain the variation of RCS of trihedrals at the same incidence angle. The instability of the small aircraft platform from day to day (e.g., slight changes of flight track and observation geometry) is another explanation for these phenomena. Figure 4-5 also includes the co-polarized phase difference (HH/VV) of all trihedrals, which should be close to zero. The co-polarized phase difference of less than 5° achieved in almost all cases satisfies the accuracy requirement in phase. It's worth noting that as all trihedrals were involved in the polarimetric calibration (estimation of the imbalance of HH and VV), the near zero phase difference was expected with further validation using the PARC required, as presented below.

Figure 4-5 (b) depicts the results of SMAPEx-5, which are similar to those observed for SMAPEx-4. The residual RMSE of HH and VV were 0.62 dBsm and 0.68 dBsm respectively. The RMSD between HH and VV was 0.21 dBsm. Notably, the trihedral deployed at the outer edge of the PLIS swath during SMAPEx-5 did not have much variation from the remaining ones, suggesting that the PLIS data from far range bins was also of high quality. The negative difference between the observed and theoretical RCS of the 23° trihedral in SMAPEx-4 was not found in SAMPEx-5, refuting any suggestion of angular instability of PLIS.

The small difference (< 0.2 dB) between the SMAPEx-4 and -5 absolute calibration coefficient CF_a confirmed the sensor stability of sensor between campaigns. The short-term relative calibration accuracy of PLIS data is reflected in Figure 4-5 (c). The largest day to day difference with respect to the theoretical cross-section were 0.56 dBsm observed between DOY 126 and 134, and 0.58 dBsm observed between DOY

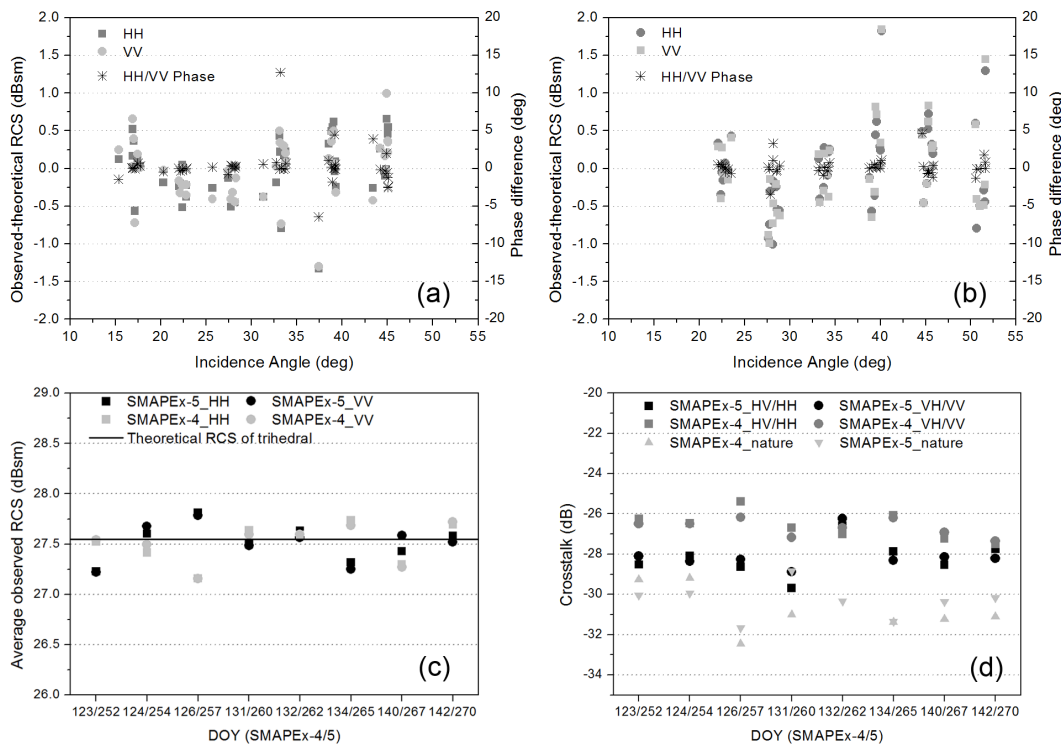


Figure 4-5 Response of trihedral PRCs after calibration. (a) and (b) are the RCSs and co-polarized phase differences of all trihedrals during SMAPEX-4 and 5, respectively. (c) and (d) are the time series average RCS of trihedrals and the averaged crosstalk estimated from trihedrals and forest respectively.

252 and 257, for SAMPEX-4 and 5 respectively, which slightly exceed the target calibration requirements of < 0.5 dB (Freeman, 1992). The instability of trihedral orientation and aircraft platform mapping geometry may be the main reason for this larger short-term variation. Figure 4-5 (d) depicts the corresponding averaged crosstalk estimated from trihedrals, which were 2 - 4 dB greater than the calibration requirements of -30 dB. This was mainly caused by the stronger multiple scattering between the trihedrals and ground surface compared to those directly from ground. The difference in ground response under the trihedrals between two field campaigns may be the main reason for the higher crosstalk in SMAPEX-4. The crosstalk (the correlation of HV and HH) estimated from a distributed area (i.e., the forest area C in Figure 4-1), was on the order of -30 dB, which is similar to the calibrated UAVSAR data (Fore et al., 2015) using the same polarimetric calibration method (Ainsworth et al., 2006).

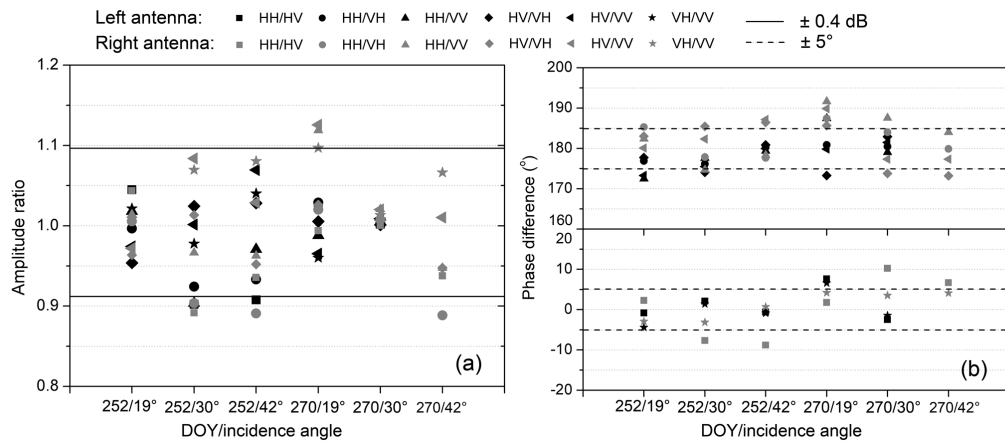


Figure 4-6: Amplitude (a) and phase (b) differences of the polarimetrically calibrated PLIS data from PARCs.

Figure 4-6 shows the channel imbalance of PARCs after calibrating the SMAPE_x-5 data. The PARC with local incidence angle of 42° could not be identified in the image of 27 September 2015 (DOY 270) and thus was not included. In general, the calibrated PLIS data achieved satisfactory accuracy in both amplitude and phase. The amplitude imbalance of most channels at the three different incidence angles was less than ± 0.4 dB. The observed phase differences among different polarizations are very close to the theoretical ones (i.e. 0° for HH/HV and VH/VV, and 180° for the rest). The average phase imbalance was 3.87°. No clear angular pattern was observed despite the large variation of amplitude ratio and phase difference among the different incidence angles.

To demonstrate the quality of the calibrated PLIS data, examples of Freeman-Durden polarimetric decomposition ([Freeman and Durden, 1998b](#)) are analyzed in Figure 4-7 where the dihedral, volume, and surface power in dB are set to red, green, and blue respectively. Figure 4-7 (a) and (b) show results of an urban area and dense forest area. Significant difference was observed between the forest and urban area with the dominant components being the volume and dihedral scattering respectively. Strong volume scattering was also observed in some parts of the urban area (yellow patches). This was mainly caused by dense trees near buildings. The field within the black boundary (Figure 4-7 b) was bare soil with a significant row structure perpendicular to the radar look direction, and thus dihedral scattering was the dominant component.

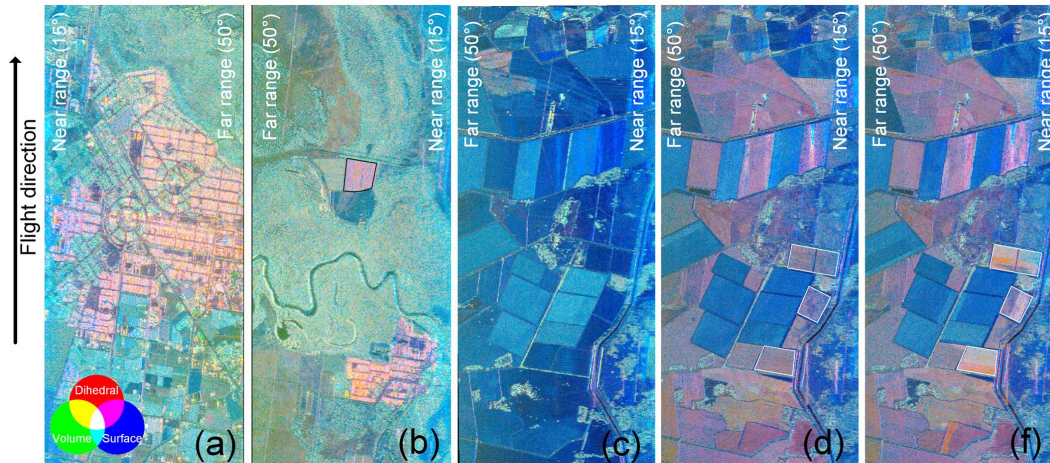


Figure 4-7: RGB image of the Freeman-Durden decomposition powers in dB where red, green and blue are dihedral, volume and surface component respectively. (a) and (b) are results over an urban and forest area respectively. (c) - (f) are results of May 3rd, September 24th and 27th of an agricultural area where the irrigated fields were delineated with white boundaries.

Figure 4-7 (c)-(e) show the decomposition results over agricultural areas at three different times, the beginning (May 3rd, 2015) and end (September 24th and 27th, 2015 irrigated and non-irrigated) of the winter wheat growing cycle. In May, almost all fields were bare and thus the surface component (blue shades) was predominant. In September, some fields were covered with fully developed dry wheat characterized by increased dihedral and volume scattering contributions. Irrigation was carried out in the fields with white boundary between September 24th and 27th, resulting in an abrupt increase in all three mechanisms because of the sudden supplement of water in both soil surface and vegetation.

It's worth noting that the actual incident radar signal is not strictly perpendicular to the aperture of the PARCs and trihedrals. The angle offsets, which were less than 3° as shown in Figure 4-6 (a) and (b), can introduce uncertainty in estimating the scattering characteristics of these targets. Fortunately, both the trihedrals and PARCs have a very wide beamwidth (Figure 4-2), meaning that the effect of the observed offsets on the RCS of the trihedral and PARC were less than 0.1 dB with negligible channel imbalances. However, the angle offsets can also introduce a small co-polarized phase difference ($< 3^\circ$) for the trihedral at L-band ([Kahny and van Zyl, 1990](#), [Craeye et al.,](#)

1997). With respect to the PARC, the phase of all polarizations was retained and thus the phase differences are independent on the angle offsets. Nonetheless, the interaction between calibration targets and background can be different for different incidence angle, introducing unclear uncertainty.

4.4.2 Comparison of PLIS and PALSAR-2

The PLIS data shows a high agreement with the PALSAR-2 Stripmap image, with R better than 0.87 and RMSD better than 1.25 dB for both channels (Figure 4-8). The HV polarization showed the highest agreement with an ubRMSD of 0.94 dB. The biases between PLIS and PALSAR-2 Stripmap for HH and HV were 0.32 dB and 0.25 dB respectively. This difference may be related to uncertainties in the calibration of both sensors, or a small drift between the PLIS and PALSAR-2 Stripmap, as soil moisture was nearly constant between the two acquisitions (Table 4-1).

The agreement between PLIS and PALSAR-2 ScanSAR is not as good (Figure 4-8). The RMSD for HH and HV were 2.47 and 1.92 dB, nearly double compared to those observed between PLIS and PALSAR-2 Stripmap. The average HH and HV measured by PLIS were respectively 1.45 dB and 0.73 dB larger than those of PALSAR-2 ScanSAR image. Such large positive biases can be partly explained by the change of soil moisture between the two acquisitions, which decreased from 0.17 to 0.14 m³/m³ during the overpass of PLIS and PALSAR-2. This difference in soil moisture is predicted to result in a decrease in backscattering coefficient of 0.5 dB and 0.6 dB for HH and HV respectively; simulated using the IEM given a H_R of 1 cm and L_c of 10 cm. In addition, the relatively large geometric uncertainty of the PALSAR-2 ScanSAR (Shimada et al., 2009) can also introduce large uncertainties, especially for areas with high spatial heterogeneity. Figure 4-9 shows the relationship between R of PLIS and PALSAR-2 and spatial homogeneity, where homogeneity is described as the fraction of the dominant land cover. The R of PLIS and PALSAR-2 ScanSAR gradually increased as the spatial heterogeneity decreased, while no clear tendency was observed for the comparison of PLIS and PALSAR-2 Stripmap. This is reasonable because the spatial heterogeneity itself does not introduce uncertainty into the comparison of two

well spatially located images. In other words, the effect of spatial registration error on the comparison is more significant over a heterogeneous area.

The impact of land cover type and azimuth difference between the two sensors is further illustrated in Table 4-3. Only grid cells with a high spatial homogeneity (where the fraction of dominant land cover type was $> 80\%$) were used to eliminate the potential influence of geo-registration error. Since the PALSAR-2 Stripmap only covered the south-west part of the SMAPEX-5 area (Figure 4-1), less than 10

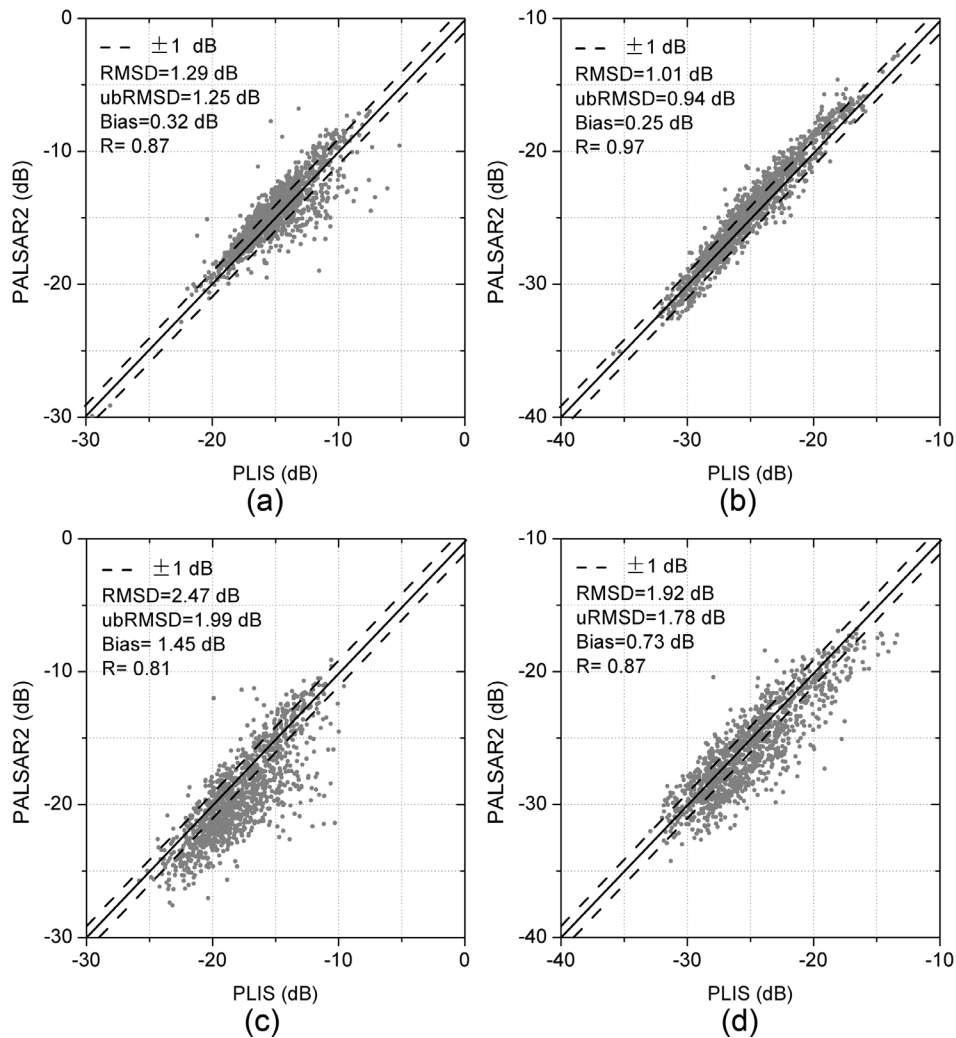


Figure 4-8: Comparison of PLIS and PALSAR-2 backscattering coefficient in dB. (a) and (b) are HH and HV for SMAPEX-5 (PLIS and PALSAR-2 Stripmap) respectively while (c) and (d) are HH and HV for SMAPEX-4 (PLIS and PALSAR-2 ScanSAR).

homogeneous forest grid cells were achieved and thus comparison over forest was not included in Table 4-3. In addition, a large bare soil area in SMAPEx-4 was covered by milk-stage wheat in SMAPEx-5, and thus the comparison over wheat was included in the SMAPEx-5 scenario.

In the SMAPEx-4 scenario, PLIS and PALSAR-2 ScanSAR had much higher RMSD over bare soil than over grass, forest and open woodland. The highest agreement was observed over forest with RMSD of 1.17 dB for HH and 1.02 dB for HV. The smallest RMSD were all achieved when the PLIS observed from west to east. Note that the look direction of PALSAR-2 is also nearly west to east (the inclination of satellite platform is $\sim 97.9^\circ$), indicating that azimuth direction had an impact on the backscatter observations. The impact of look direction for PLIS also varied for different landcover types, resulting in the largest RMSD over bare soil followed by open woodland, grass

Table 4-3: The comparison of PLIS and PALSAR2 over different landcover types and look directions. Values in bold indicate the lowest RMSD among different landcover types. A(B) represents a root mean square difference of A and a correlation coefficient of B. Only the grids whose fractions of dominant landcover type were $> 80\%$ were included.

Look direction	HH		HV	
	East-West	West-East	East-West	West-East
SMAPEx-4 scenario				
Bare soil	2.71(0.53)	2.53(0.63)	2.77(0.42)	2.05(0.60)
Wheat	-	-	-	-
Grass	1.42 (0.82)	1.54(0.80)	1.53(0.78)	1.38(0.81)
Forest	1.34 (0.96)	1.17(0.95)	1.22(0.95)	1.02(0.95)
Open woodland	1.37 (0.89)	1.47 (0.92)	1.48(0.76)	1.02(0.97)
SMAPEx-5 scenario				
Bare soil	2.23 (0.59)	1.33(0.83)	1.27(0.82)	0.76(0.95)
Wheat	0.91 (0.88)	1.05 (0.91)	0.74(0.98)	0.58(0.99)
Grass	0.74 (0.91)	0.63 (0.91)	0.79(0.95)	0.70(0.98)
Forest	-	-	-	-
Open woodland	1.63 (0.71)	1.40 (0.51)	1.09(0.94)	0.93(0.94)

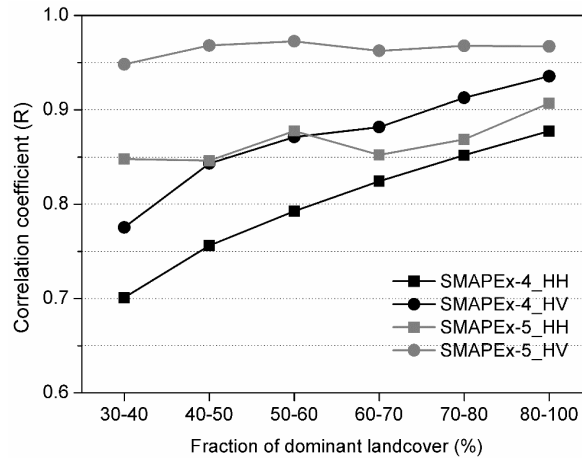


Figure 4-9: The relationship between the correlation coefficient and spatial heterogeneity.

and forest. This is consistent with the fact that uniform grass and forest is nearly azimuth symmetric to radar remote sensing, while bare soil, especially with row structures, commonly has different backscattering behavior for different azimuth angles. Similar results were observed in the SMAPEx-5 scenario. The highest agreement was achieved over grass for HH and over wheat for HV, with RMSD less than 0.65 dB and R larger than 0.9. The largest RMSD and lowest R were observed over the bare soil, when PLIS look direction was not aligned to that of PALSAR-2.

4.5 Chapter Summary

The stability, accuracy and image quality of PLIS data was comprehensively evaluated using two airborne campaigns (SMAPEx-4 and 5), with the calibrated data used in the following chapters. The calibration results based on PRC and PARCs were found to be close to those observed for other L-band airborne SAR systems (Table 4-2), i.e. NASA UAVSAR ([Fore et al., 2015](#)) and JAXA Pi-SAR-L2 ([Shimada et al., 2013b](#)), which meet the accuracy requirements for the applications listed in [Freeman \(1992\)](#) and references therein, including age of lava flows classification, ice classification and motion monitoring, vegetation mapping/monitoring, wind speed monitoring over ocean, and soil moisture retrieval. PLIS / PALSAR-2 cross validation confirmed the calibration accuracy of the PLIS data over various land cover types and the potential

for cross-calibration of SAR systems. Homogeneous dense forest and grass land were suggested as optimal cross-calibration targets to reflect the accuracy of high and low backscattering observations respectively. Uncertainties in cross-validation/calibration caused by the difference of incidence angle, azimuth, spatial resolution and spatial miss-registration can be partly removed using a uniform area and large comparison grids.

5 Forward Scattering Models

The proposed multi-SAR-mission retrieval is designed for SAR missions operating at L-, C- and X-bands. The commonly used scattering models have been introduced in Chapter 2. While these models have achieved positive results for forward simulation and soil moisture retrieval, currently a single model is unable to satisfy the validity range requirements for multi-SAR-mission retrieval. Consequently, a combination of scattering models covering the range of radar remote sensing configurations and natural surface conditions expected were selected for developing look up tables (LUTs) in this chapter. LUTs were developed to overcome the intensive computation demands of these models. The SMAPEX-5 data set presented in Chapter 3 was used in the development and evaluation of these LUTs. This work forms the basis of two papers with one published ([Zhu et al., 2019a](#)) and the other in review.

5.1 Forward models used in this thesis

A summary of the scattering models used in this study is presented in Table 5-1. For bare soil surfaces, the NMM3D ([Huang et al., 2017b](#), [Huang et al., 2010](#), [Huang and Tsang, 2012](#)) was used to simulate the L-band (1.26 GHz) backscattering coefficients. Use of the NMM3D was motivated by its successful application in the SMAP baseline algorithm for radar soil moisture products ([Kim et al., 2012a](#), [Kim et al., 2014a](#)) and its satisfactory forward simulation results over a wide range of soil roughness and soil moisture ([Huang et al., 2010](#)). Despite the improved accuracy of the NMM3D compared with other models ([Huang et al., 2010](#)), the H_R of available NMM3D simulations for the SAMP products was limited to 0.168 of the wavelength ([Kim et al., 2012a](#)), being ~ 0.93 and 0.54 cm for C- and X-band respectively. Some simulation cases for larger H_R values are available in [Liao et al. \(2016b\)](#). However, they still do not cover the range of natural soil surface. Moreover, it is challenging for this PhD study to generate extended LUTs covering larger H_R , because of the intensive computation demand. Consequently, the Oh model ([Oh et al., 2002](#)) was used to represent the bare

Table 5-1: A summary of scattering models used. Wheat and grass were simplified as a random layer of cylinders, with the required parameters being that of cylinders.

Model	Frequency (GHz)	Landcover	Required unknown parameters*
NMM3D (Huang et al., 2010)	1.26	Bare soil	root mean square height (H_R), correlation length (L_C) and relative permittivity (ϵ_i)
Oh model (Oh et al., 2002)	5.4, 9.3	Bare soil	H_R , L_C , and soil moisture (m)
DBA (Lang and Sighu, 1983)	1.26, 5.4, 9.3	Wheat, grass	radius (r), length (l), relative permittivity (ϵ_r), azimuth (a), elevation (β) angle, and density in m^3 (n)

soil σ^0 at C- and X-band, because of its large validity range and robustness which have been demonstrated by many studies (e.g., [Baghdadi and Zribi, 2011](#), [Panciera et al., 2014a](#), [Choker et al., 2017](#)).

For vegetated areas, the distort Born approximation (DBA; [Lang and Sighu, 1983](#)) was selected for all radar configurations, with the motivation to avoid the radar-configuration-specific calibration required by semi-empirical models, e.g. parameter tuning of the water cloud model ([Attema and Ulaby, 1978](#)). A brief introduction of the forward models used in this thesis are as follows, with the generation of LUTs using those models described in Section 5.3.

5.1.1 NMM3D based LUTs

In the baseline algorithm of the SMAP radar products ([Kim et al., 2012b](#)), precomputed LUTs were used for operational soil moisture retrieval because of the intensive computational demand of the NMM3D. For building those LUTs, the soil surface was simulated as a random surface parameterized according to root mean square height (H_R), correlation length (L_C) and relative permittivity (ϵ_i) with isotropic exponential correlation functions. Accordingly, the Maxwell equations were directly solved at the boundary of air and simulated soil surfaces based on the methods of moments. Results for infinite surfaces were extracted from simulations of finite rough surfaces with a size of 16×16 wavelength (for L-band). Please refer to [Huang et al. \(2010\)](#) for more details. The LUTs for L-band have been generated for the SMAP

baseline algorithm of the radar product (<https://web.eecs.umich.edu/~leutsang/Computer%20Codes%20and%20Simulations.html>) and were directly used in this study.

5.1.2 Oh model

The Oh model ([Oh et al., 2002](#)) is described as follows:

$$\frac{\sigma_{HH}^0}{\sigma_{VV}^0} = 1 - \left(\frac{\theta}{90^\circ}\right)^{0.35mv^{-0.65}} e^{-0.4(k \cdot H_R)^{1.4}} \quad \text{Eq. 5-1}$$

$$\frac{\sigma_{VH}^0}{\sigma_{VV}^0} = 0.1 \left(\frac{H_R}{L_C} + \sin 1.3\theta\right)^{1.2} (1 - e^{-0.9(k \cdot H_R)^{0.8}}) \quad \text{Eq. 5-2}$$

$$\sigma_{VH}^0 = 0.11\theta^{0.7} \cos^{2.2}\theta (1 - e^{-0.32(k \cdot H_R)^{1.8}}), \quad \text{Eq. 5-3}$$

where θ is the incidence angle, $k=2\pi/\lambda$ is the wave number and λ is the wavelength. The validity range of the Oh model is $0.1 < kH_R < 6.0$, $2.6 < kL_C < 19.7$, $0.09 < mv < 0.31 \text{ m}^3/\text{m}^3$ and $10^\circ < \theta < 70^\circ$. Similar to the assumptions made for the NMM3D simulations at L-band, the soil surface of the training data used for the Oh model also follows a stationary Gaussian random process with directionally isotropic correlation functions ([Oh et al., 1992](#)). The required unknown parameters of the Oh model ([Oh et al., 2002](#)) for forward prediction include the H_R , L_C , and mv .

5.1.3 Distorted Born approximation

The DBA assumes that the wave incident on each vegetation scatterer is the mean field in the vegetation layer, and the mean scattered fields then computed by embedding the scatterers in the equivalent medium ([Lang and Sighu, 1983](#)). The assumption is valid when the scatterers have a small albedo, which holds for frequencies up to 10 GHz for plant canopy ([Moghaddam and Saatchi, 1995](#)).

Only the dominant vegetation types (i.e., wheat and grass) were considered, which were simplified as a layer of random distributed cylinders (Figure 5-1). These cylinders are homogeneous, lossy, uniformly distributed with consistent radius (r), length (l) and relative permittivity (ϵ_r) in each radar illumination grid. It was also assumed that the cylinders are distributed with prescribed orientation statistics which are independent

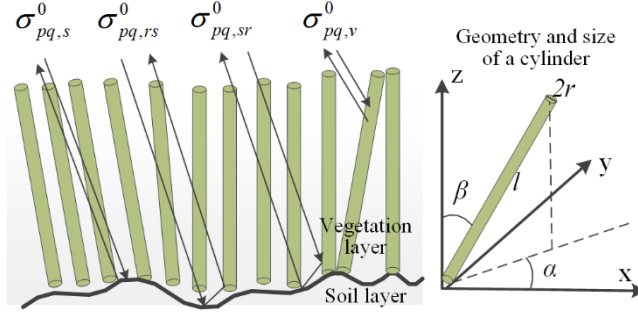


Figure 5-1: Schematic of vegetation layer and soil surface as well as the scattering mechanisms in distorted Born approximation (DBA), adapted from [Huang et al. \(2017a\)](#). The subscripts v , sr , rs , and s are the volume, scattered-reflected, reflected-scattered and surface scattering, respectively. q and p are either horizontal (H) or vertical (V) polarization of the incident and scattered fields; α , β , r and l are the azimuth angle, elevation angle, radius, and length of a cylinder, respectively.

of r , ϵ_v , and l . Figure 5-1 shows the geometry of one particular cylinder in the vegetation layer. The ground underlying the vegetation layer is a rough and lossy soil surface layer.

In the DBA ([Lang and Sighu, 1983](#)), the backscattering coefficients from vegetated area, can be decomposed according to (Figure 5-1):

$$\sigma_{pq}^0 = \sigma_{pq,s}^0 + \sigma_{pq,sr}^0 + \sigma_{pq,rs}^0 + \sigma_{pq,v}^0 \quad \text{Eq. 5-4}$$

where subscripts v , sr , rs and s are the volume, scattered (vegetation)-reflected (soil), reflected-scattered and surface scattering, respectively. subscript q and p refer to either horizontal (H) or vertical (V) polarization, respectively. The commonly used first-order radiative transfer models (e.g., [Ulaby et al., 1990](#)) share a similar form to Eq. 5-4, with the main difference being the enhanced double-bounce scattering in the DBA because of the full simulation in coherent scattering ([Tsang et al., 1985](#)). In principle, the double-bounce scattering ($\sigma_{pq,sr}^0 + \sigma_{pq,rs}^0$) has a significant contribution on the cross-polarization backscatter, while it contributes little to the HH and VV polarization backscatter at L-band, depending on the incidence angle, soil moisture, VWC and roughness. For C- and X-band, the double-bounce is greatly enhanced for co-polarization, with experimental observations available in [Brown et al. \(2003\)](#). The volume scattering is commonly negligible for all polarizations at L-band at an arable area, but it could be dominant at C- and X-band for densely vegetated areas with large

θ . Consequently, an operational method is proposed in Chapter 8 for removing these with negligible soil surface scattering.

The terms in Eq. 5-4 can be expressed as:

$$\sigma_{pq,v}^0 = n\sigma_{pq,v} \frac{1 - \exp(-2 \operatorname{Im}(K_p + K_q)d)}{2 \operatorname{Im}(K_p + K_q)} \quad \text{Eq. 5-5}$$

$$\sigma_{pq,sv}^0 = n\sigma_{pq,sv} \frac{1 - \exp(-2 \operatorname{Im}(K_p - K_q)d)}{2 \operatorname{Im}(K_q - K_p)} |R_p|^2 \exp(-4 \operatorname{Im}(K_p)d) \quad \text{Eq. 5-6}$$

$$\sigma_{pq,rs}^0 = n\sigma_{pq,rs} \frac{1 - \exp(-2 \operatorname{Im}(K_p - K_q)d)}{2 \operatorname{Im}(K_p - K_q)} |R_q|^2 \exp(-4 \operatorname{Im}(K_q)d) \quad \text{Eq. 5-7}$$

$$\sigma_{pq,s}^0 = \sigma_{pq,g}^0 \exp(-2 \operatorname{Im}(K_p + K_q)d), \quad \text{Eq. 5-8}$$

where d and n are the depth (in m) of the vegetation layer and the number density of vegetation scatterers ($1/\text{m}^3$), respectively. K and σ in the above expressions are effective propagation constants in the vegetation layer and the ensemble average of the backscattering cross section of individual cylinders, respectively.

Both K and σ can be calculated using the bistatic scattering amplitude of cylinders f_{pq} . Specifically, σ is given by:

$$\sigma_{pq,\chi} = 4\pi \langle |f_{pq,\chi}|^2 \rangle, \quad \chi \in \{v, sv, rs\}, \quad \text{Eq. 5-9}$$

where $\langle \cdot \rangle$ is the ensemble average over the angular distribution of cylinders, and f_{pq} for cylinders are calculated using the infinite cylinder approximation ([Tsang et al., 1985](#)) with the main difference in Eq. 5-5 – Eq. 5-8 being the directions of the scattered and incident waves. K_p was calculated by Foldy's approximation where scatters were assumed to be embedded in the equivalent (mean) medium ([Lang and Sighu, 1983](#)):

$$K_p = k_0 \cos \theta + \frac{2\pi n \langle f_{pp} \rangle}{k_0 \cos \theta}, \quad \text{Eq. 5-10}$$

where k_0 and θ are the free-space propagation constant and angle of incident wave, respectively. The imaginary part of K_p is the attenuation constant, which is directly related to the optical depth τ_p by $\tau_p = 2\operatorname{Im}(K_p)d$. Accordingly, Eq. 5-8 can be interpreted as two-away attenuated soil surface scattering.

The remaining quantities are: R_p , the coherent reflectivity of ground for polarization p ; and $\sigma_{pq,g}^0$, the backscattering coefficient of ground, both related to the underlying rough surface. In this study, the R_p and $\sigma_{pq,g}^0$ were calculated by NMM3D (Huang and Tsang, 2012) for L-band. The Oh model (Oh et al., 2002) was used to calculate $\sigma_{pq,g}^0$ for C- and X-band, with the R_p being calculated using the Kirchhoff's technique (Ulaby et al., 2014):

$$R_p = |\rho_p|^2 \exp(2k_0 H_R \cos \theta), \quad \text{Eq. 5-11}$$

where ρ_p is the Fresnel reflection coefficient.

5.2 Data sets

5.2.1 Ground measurements

The ground measurements collected in three 3 km × 3 km SMAPEX-5 focus farms (YA4, YA7 and YE) were used for the development and evaluation of forward models, as presented previously in Chapter 3. The main landcover types of these three areas include winter wheat, grass, bare soil and open wood land (Figure 5-2). Since the tree coverage in the open wood land is less than 5% (~2000 – 3000 trees /km²), the open wood land was treated as grass for the purpose of soil moisture retrieval here. The

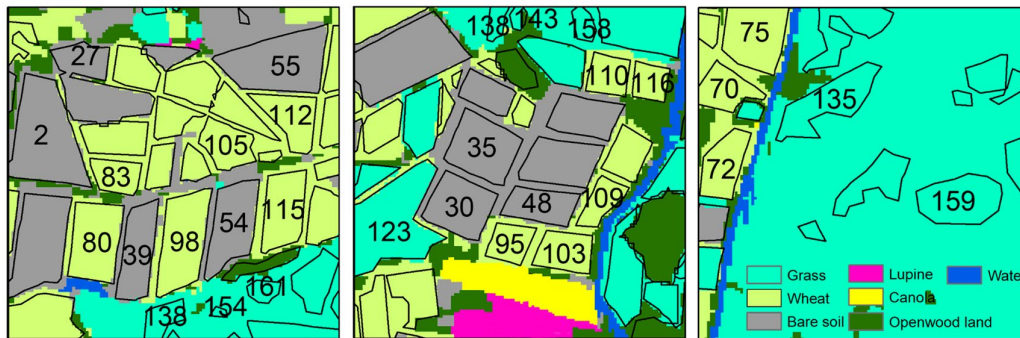


Figure 5-2: Landcover and paddocks in the three SMAPEX-5 focus farms used in the development and evaluation of the forward models. The focus farms include YA4 (left), YA7 (middle) and YE (right). The paddocks with ID are those with ground roughness and/or vegetation measurements as given in Table 5-2.

boundaries of paddocks were delineated using visual-interpretation according to the homogeneity of landcover and the availability of ground measurements. A total of 69 paddocks were extracted, accounting for 48% of the three focus farms. Notably, the boundaries here were only used for analyzing the results at the paddock scale.

Throughout the campaign, intensive soil moisture measurements (m) were made on September 9th, 14th, 19th, and 24th for YA4 and YE, and on September 11th, 17th, 22th, and 27th for YA7 using the HDAS on a regular grid with a spacing of 250 m. A moderate rainfall of ~ 18 mm (measured at the Yanco agricultural institution) occurred prior to the experiment, resulting in m values of larger than $0.3 \text{ m}^3/\text{m}^3$ followed by a three-week dry down period to values around $0.1 \text{ m}^3/\text{m}^3$. As introduced in Chapter 3, soil surface roughness of the paddocks was measured using a pin profiler and parametrized by their H_R and correlation L_C . Paddocks with H_R and L_C measurements in YA4, YA7 and YE are presented in Table 5-2. In general, the wheat and bare soil paddocks had a wide range of roughness, with large values observed on those with furrows due to tillage.

In the selected three focus farms, the wheat had quite varying VWC values ranging from $1.17 - 3.72 \text{ kg}/\text{m}^2$, which is mainly caused by the spatial heterogeneity of plant density ($120 - 370 /\text{m}^2$) and height ($0.35 - 1.0 \text{ m}$). Allometric relationships between VWC and height for grass and wheat were fitted (Figure 5-3), using ground measurements of the whole SMAPEX-5 area. No clear tendency of VWC values was observed but with significant random fluctuations over time for most paddocks during the three-week period (Table 5-2). These fluctuations were mainly caused by the intra-paddock heterogeneity, as it was impossible to resample at exactly the same location using the destructive collection of samples for VWC estimation. Consequently, all vegetation parameters were assumed constant in time and averaged for each paddock with the average values reported in Figure 5-3.

Table 5-2: Available roughness and vegetation measurements of the paddocks in three SMAPEX-5 focus farms used in this chapter

#	LULC	Vegetation parameters					Soil surface parameters			
		VWC (kg/m ²) *			Height (m)	Radius (mm)	Elevation angle (°)	Row direction	H _R ** (cm)	L _C / H _R **
2	Bare	-	-	-	-	-	-	90	1.94(8.66)	6.82(2.44)
27	Bare	-	-	-	-	-	-	-	1.22	14.53
30	Bare	-	-	-	-	-	-	28	2.76(6.33)	5.13(2.95)
35	Bare	-	-	-	-	-	-	28	1.61(5.54)	8.24(3.65)
48	Bare	-	-	-	-	-	-	90	2.12(6.30)	7.76(3.20)
54	Bare	-	-	-	-	-	-	10	-	-
55	Bare	-	-	-	-	-	-	-	1.50	6.98
70	Wheat	-	2.3	1.9	0.46	1.42	25	-	-	-
72	Wheat	2.5	2.6	3.1	0.47	1.49	30	-	1.60	7.44
75	Wheat	3.3	2.6	2.9	0.77	1.50	25	90	1.12(4.05)	6.58(4.99)
80	Wheat	1.9	2.5	2.3	0.62	-	-	10	1.95(3.71)	14.20(5.83)
83	Wheat	3.1	-	-	-	-	-	90	0.87(4.03)	7.19(6.51)
95	Wheat	2.4	2.5	2.5	0.72	-	-	90	1.45(2.58)	5.61(4.59)
98	Wheat	-	-	2.7	0.70	-	-	10	-	-
103	Wheat	2.8	2.8	-	0.74	-	-	90	1.54(2.83)	6.95(5.34)
105	Wheat	1.7	-	-	0.60	1.02	-	-	0.91	20.93
109	Wheat	1.9	2.2	2.9	0.71	-	-	-	-	-
110	Wheat	0.9	1.3	1.3	0.61	-	-	-	-	-
112	Wheat	1.6	1.4	1.9	0.66	1.00	20	90	2.46(3.12)	9.16 (9.91)
115	Wheat	3.5	4	3.6	1.05	1.63	20	10	1.01(2.94)	11.30(6.49)
116	Wheat	2.8	-	-	0.67	1.51	22.5	90	1.06(2.76)	7.24(4.98)
117	Wheat	2.7	3.2	-	0.60	-	-	55	1.18(2.38)	2.94(6.74)
135	Grass	0.6	0.8	0.7	0.32	-	-	-	1.20	17.86
138	Grass	0.7	-	-	0.30	-	-	-	1.21	7.12
143	Grass	1.5	1.7	1.7	0.43	-	-	-	0.71	14.98
154	Grass	1.2	-	-	-	-	-	-	0.71	14.98
158	Grass	0.9	-	-	-	-	-	-	0.71	14.98
159	Grass	-	0.5	-	0.30	-	-	-	0.96	18.21
161	Grass	0.7	1.2	1.0	0.33	-	-	-	1.15	20.34

*: VWC of three weeks during the SMAPEX-5

** : roughness along (perpendicular) to row structure for paddocks with periodic surface

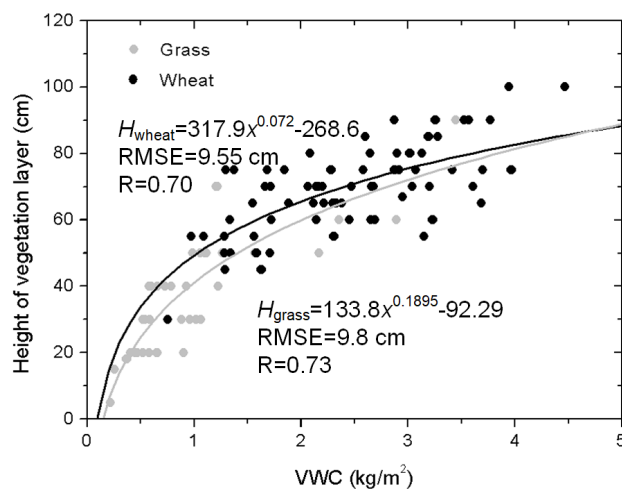


Figure 5-3: Fitted relationship between vegetation water content and vegetation height

5.2.2 Radar data

Radar images for three different microwave bands, i.e., L-band (1.26 GHz), C-band (5.4 GHz) and X-band (9.3 GHz), were used in this chapter. The L-band images were acquired by the Polarimetric L-band Imaging SAR (PLIS) coincident with the eight-ground soil moisture sampling dates mentioned above; details of this data and its calibration were provided in Chapter 4. The C- and X-band images are from satellite data including seven RADARSAT-2 images (C-band) and five COSMOS SkyMed images (X-band). Their details are summarized in Table 5-3.

5.3 Development of the look up tables

Since the NMM3D and DBA are computationally intensive, LUTs were built as representations of forward scattering instead of directly integrating models to an inversion framework. Table 5-1 gives a summary of the inputs of each model, with three and ten parameters required for a bare soil surface and vegetated area, respectively. For soil moisture inversion, these models must be simplified and parameterized in terms of fewer soil and vegetation parameters, considering the limited

Table 5-3: Specification of SAR data in a format of incidence angle/orbit/polarization, where A and D are ascending and descending pass, respectively.

DOY	PLIS (L-band)	RADARSAT -2 (C-band)	COSMO-SkyMed (X-band)
251			33.5°/D/HH
252	20-50°/D/HH, HV, VV	39.5°/D/VV, VH	
253			28.5°/A/HH
254	20-50°/A/HH, HV, VV	22.4°/A/HH, HV, VV	
255		22.7°/D/VV, VH	
257	20-50°/D/HH, HV, VV	39.2°/A/HH, HV, VV	
260	20-50°/A/HH, HV, VV		
261			33.5°/D/HH
262	20-50°/D/HH, HV, VV	28.9°/D/VV, VH	
263			28.5°/A/HH
264		34.1°/A/VV, VH	
265	20-50°/A/HH, HV, VV		
267	20-50°/D/HH, HV, VV		
269		34.5°/D/HH, HV, VV	33.5°/D/HH
270	20-50°/A/HH, HV, VV		

number of independent radar observations and the drastically increased complexity of the inversion problem with more than three geophysical parameters.

5.3.1 LUTs for bare soil

As aforementioned, the rough soil surfaces were assumed to follow a stationary Gaussian random process with an isotropic exponential correlation function in the NMM3D simulation, which have been demonstrated to match well with experimental soil surfaces ([Shi et al., 1997](#), [Oh et al., 1992](#), [Ulaby et al., 2014](#)). However, natural soil surfaces are typically more complex, with rain-eroded and ploughed soil having a shape lying somewhere between an exponential and a Gaussian function ([Zribi et al., 1997](#), [Zribi et al., 2005b](#)). Moreover, directional row or tillage features often exist and were observed over several paddocks (Table 5-2), negating the isotropic assumption. Accordingly, more comprehensive descriptions, e.g., two-dimension roughness ([Blaes and Defourny, 2008](#)) and the Z_g as a function of H_R , L_C and correlation function ([Zribi et al., 2014](#)), are undoubtedly more suitable. But either additional parameters (to represent the two-dimension soil surface) or radar-configuration-specific calibration (for the use of Z_g) are required, leading to an increased complexity, especially when merging multi-SAR missions.

Fortunately, previous studies ([Champion and Faivre, 1996](#), [Joseph et al., 2010](#)) have shown that effective isotropic roughness values can be used to account for the surface scattering of periodic features. Those effective roughness values were either determined via calibration of forward models ([Baghdadi et al., 2002c](#), [Baghdadi et al., 2004](#), [Lievens et al., 2011a](#), [Joseph et al., 2010](#)) or directly retrieved together with soil moisture in an iterative manner ([Bai et al., 2016](#)). Since the effective roughness is dependent on the incidence angle, polarization and frequency ([Joseph et al., 2010](#), [Lievens et al., 2011a](#)), a calibration process is not suitable in this study for combining multiple SAR missions, with the effective roughness being retrieved together with soil moisture. Similarly, the retrieved effective roughness values also depend on the varying configurations of input data, with a detailed discussion provided in Chapter 7 and 8.

In this thesis, H_R was selected as the only independent effective roughness parameter, with the corresponding L_c determined by H_R , considering the poor performance of using the observed L_c values in IEM forward simulations at the same research area (Zhu et al., 2016, Panciera et al., 2014a) and the need to reduce the number of independent soil parameters. Specifically, the available ground measured H_R (Table 5-2) and mv were used to predict the σ^0 at L-band HH and VV polarization, with L_c/H_R ranging from 5 to 15. The simulated σ^0 was then compared with the multi-angular PLIS observations at a resolution of 25 m, with the RMSE and correlation coefficients depicted in Figure 5-4. In general, the RMSE gradually decreased from 3 – 4 dB to 2 dB as the L_c/H_R was increased from 5 to 10, with insignificant difference of both RMSE and R for L_c/H_R ratios larger than 10. This suggests the effectiveness of using a fixed ratio of 10–15 at the pixel/paddock scale in the Yanco area, with the calibrated empirical relationships between L_c and H_R proposed in earlier studies (Baghdadi et al., 2002c, Baghdadi et al., 2004, Lievens et al., 2011a) undoubtedly more reliable. However, re-calibration of those relationships were required in Yanco area as demonstrated in Panciera et al. (2014a), for each polarization, frequency and even incidence angle, leading to an increasingly complex problem. Consequently, a further simplified relationship of $L_c = 10H_R$ was used in this PhD study, as has been used in the SMAP baseline algorithm (Kim et al., 2012a).

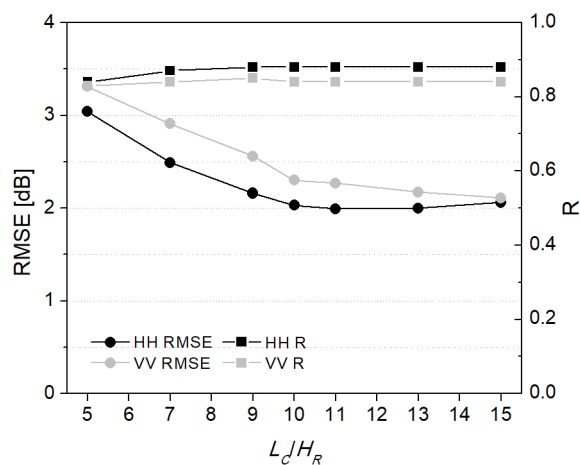


Figure 5-4: The effect of L_c/H_R on L-band forward accuracy over bare soil at a spatial resolution of 25 m.

To further reduce the number of unknowns, only the real part (ϵ_r') of relative permittivity was used, with corresponding imaginary parts being 1 to 4.5 ([Kim et al., 2012a](#)). Accordingly, two unknown parameters (H_R and ϵ_r') need to be determined for a bare soil surface. For the L-band LUTs, ϵ_r' ranged from 3 to 30, covering the very dry ($\sim 0.03 \text{ m}^3/\text{m}^3$) to very wet ($\sim 0.42 \text{ m}^3/\text{m}^3$) soil experienced in the Yanco area ([Dobson et al., 1985b](#)). Different relative permittivity ranges were used for C- and X-band LUTs to have a roughly consistent m^v range ($0.03 - 0.43 \text{ m}^3/\text{m}^3$). The H_R values ranged from 0.5 to 4 cm covering the validity range of all paddocks except the roughness measured across the row structure in several paddocks (#2, #27, #30, #48, #75 and #83) during SMAPE_{x-5} (Table 5-2).

Limited by the NMM3D's computational requirements, only six H_R nodes (0.5, 1, 1.5, 2, 3, and 4 cm) and seven ϵ_r' nodes (2.8, 4, 5.5, 9, 15, 22 and 30) were used for the initial L-band LUTs at an incidence angle (θ) of 20° , 30° , and 50° , while an additional roughness node of 5 cm was included for 40° ([Kim et al., 2012a](#)). These LUTs in dB were then equally interpolated in terms of dB onto a cube with $256 \times 256 \times 31$ nodes using a cubic spline function, with the three axes denoting the H_R , ϵ_r' , and θ respectively. The Oh model was directly used to generate the backscattering coefficient (in dB) for C- and X-band at the same cube. The steps in H_R and ϵ_r' were ~ 0.01 cm and ~ 0.1 , respectively.

5.3.2 LUTs for vegetated area

To calculate the σ^0 from a vegetated surface (Figure 5-1), a total of seven vegetation parameters are required, including the radius (r), length (l) and relative permittivity (ϵ_r) of individual cylinders; the probability density function (pdf) of azimuth (a) and elevation (β) angle; volumetric water content of vegetation materials (M_{veg}) and the number density of cylinder in m^3 (n). The first three parameters are required in the infinite cylinder approximation ([Tsang et al., 1985](#)) for the calculation of bistatic scattering amplitudes, the integration of which with the pdf over a and β is the ensemble average in Eq. 5-9 and Eq. 5-10. Among those parameters, n and l showed large spatial variations as mentioned in section 5.2.1, with other vegetation parameters

being relatively homogenous spatially (Table 5-2). For operational inversion, only the vegetation water content (VWC) was used to represent the effect of vegetation, as in previous studies (e.g., [Kim et al., 2014a](#), [Huang et al., 2017a](#), [Joseph et al., 2010](#)). Specifically, the r , a , β and M_{veg} were set as spatially uniform in the forward simulation and directly determined using the ground measurements summarized (summarized in Table 5-4). The heterogeneous parameters l and n were represented by VWC through the fitted allometric relationships (Figure 5-3) and the equation:

$$n = \frac{\text{VWC}}{\pi r^2 l \rho M_{\text{veg}}} \quad \text{Eq. 5-12}$$

where ρ are water density ($\sim 1000 \text{ kg/m}^3$).

The LUTs built for bare soil were used to account for scattering from the underlying rough surface. The VWC for wheat and grass ranged from $0.5 - 5 \text{ kg/m}^2$ and $0.1 - 3 \text{ kg/m}^2$, respectively. The initial LUTs have a resolution of 0.05 kg/m^2 in VWC, with seven incidence angles ranging from 20° to 50° with an interval of 5° . These LUTs were then equally interpolated to 31 incidence angle specific cubes with the VWC also being interpolated into 256 nodes. A comparison over 1000 random combinations of VWC, ϵ_s' , H_R and θ showed that the maximum difference between LUTs and NMM3D/Oh-DBA was less than 0.2 dB, being equivalent to a soil moisture value of

Table 5-4: Parameters used in building lookup tables, U (a , b) denotes a uniform distribution ranging from a to b ; and N (a , b) is a normal distribution with a mean of a and a standard deviation of b .

Parameter	Wheat	Grass	Bare
a ($^\circ$)	U(0, 360)	U(0, 360)	-
β ($^\circ$)	N(30, 4)	N(60, 15)	-
M_{veg}	0.75	0.65	-
r (mm)	1.4	1.2	-
VWC (kg/m^2)	0.5 – 5	0.1–3	-
ϵ_s'	3 – 30	3 – 30	3 – 30
H_R (cm)	0.5 – 4	0.5 – 4	0.5 – 4
θ ($^\circ$)	20 – 50	20 – 50	20 – 50

$< 0.01 \text{ m}^3/\text{m}^3$ for radar observations. A summary of the parameters used for building these LUTs are listed in Table 5-4.

5.4 Forward model evaluation

5.4.1 Evaluation of L-band LUTs

The LUTs built by NMM3D-DBA were evaluated using the available radar observations (Table 5-3) and ground samples over the paddocks containing roughness and VWC observations (Table 5-2). The model σ^0 were first calculated for each m_v sample and then averaged for each paddock. The roughness values measured along the row structure were used for paddocks #2, 30 and 48, because their average roughness values are out of the range of bare soil LUTs (0.5 – 4 cm). Figure 5-5 shows the predicted σ^0 in dB versus the PLIS observations over bare soil, grass and wheat. The co-polarizations (HH and VV) achieved the best performance over bare soil, followed by the grass and wheat. The root mean square error (RMSE) for all land cover types (1.6 – 3.2 dB) were marginally larger than those reported in other studies using the same models, which are ~ 1.5 dB for bare (Huang et al., 2010), 1.8 dB for grass (Kim et al., 2014a), and 1.1 – 1.7 dB for wheat (Huang et al., 2017a). One reason for the difference is the periodic row structures observed in several paddocks. For example, significantly larger co-polarized σ^0 were observed at paddock #80 (wheat) which was ploughed nearly perpendicular to the radar look directions. After removing these paddocks, the

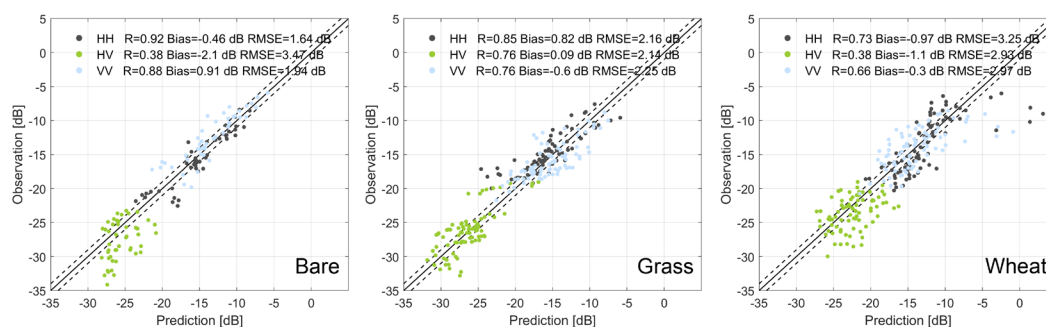


Figure 5-5: Comparison of forward NMM3D-DBA σ^0 and PLIS multi-angular observations at the paddock scale ($\sim 0.1 - 0.5$ km). The dash lines denote the ± 1 dB offset. R refers to Pearson correlation coefficient.

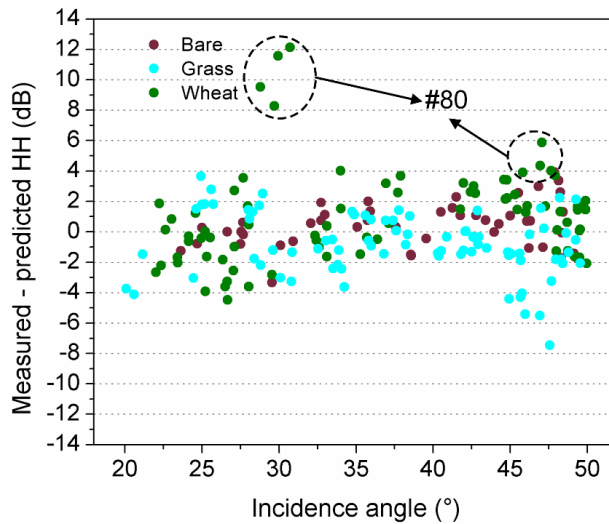


Figure 5-6: The difference of measured and predicted σ^0 at HH polarization versus incidence angle. The circled points belong to paddock #80 that was ploughed nearly perpendicular to the radar look directions.

RMSE for wheat decreased to 2.1 dB (HH), 2.3 dB (VV) and 2.8 dB (HV). The effect of surface row structure on radar observations is well documented ([Ulaby and Bare, 1979](#), [Blanchard and Chang, 1983](#), [Champion and Faivre, 1996](#), [Zribi et al., 2002](#)), with the co-polarized σ^0 observed perpendicular to row structure being up to 10 dB larger than those observed with parallel row direction at L-band ([Ulaby and Bare, 1979](#)). Observations from other azimuth angles also have a relatively larger σ^0 compared to the parallel direction, but with a limited difference when the azimuth angle difference (θ_a) between the incident wave and row direction was less than 60° ([Blanchard and Chang, 1983](#)). This is coincident with the σ^0 observed at other ploughed paddocks in the research area whose θ_a ranged from $0 - 62^\circ$ (e.g., the paddock #2). The predicted σ^0 of these paddocks, based on average or along row direction roughness, matched approximately the observed σ^0 having a difference of less than 4 dB. Notably, this does not mean that the isotropic roughness assumption and the fixed L_w/H_R ratio of 10 accurately describes the periodic soil surface, but rather indicates that the roughness values used in the forward evaluation were close to the perceived effective roughness values for those paddocks.

A further investigation on the angular dependence of forward model performance at HH is depicted in Figure 5-6, with the results for HV and VV being similar. In **general**, no clear angular pattern was observed for all three landcover types, showing the reliability of the angular effect modeling. Different angular behavior was observed for paddock #80, with the PLIS observations being 8-12 dB and 4-6 dB higher than the model predictions at incidence angles of ~ 30 and 48° respectively. Similar results were observed by [Ulaby et al. \(2014\)](#) and [Zribi et al. \(2002\)](#) for 3.25 GHz.

5.4.2 Evaluation of C- and X-band LUTs

The C- and X-band LUTs were evaluated using the RADARSAT-2 and COSMO SkyMed observations and ground samples over the paddocks containing roughness and VWC observations (Figure 5-7). Overestimations of 2 – 4.5 dB for C-band were observed over bare soil using the Oh model, in line with similar results observed in several previous studies ranging from 1 – 5 dB ([Choker et al., 2017](#), [Baghdadi and Zribi, 2006](#), [Merzouki et al., 2010](#)). The Oh model also had a large overestimation of 5.2 dB at X-band HH polarization, being much larger than those (< 1 dB) observed by [Baghdadi and Zribi \(2011\)](#) and [Merzouki et al. \(2010\)](#). The potential reason could be the calibration uncertainty of X-band data, as large offsets have been observed between different beams of the COSMO SkyMed and among different X-band missions ([Pettinato et al., 2013](#)). After removing the biases, an acceptable unbiased RMSE (ubRMSE) of < 2 dB and R of 0.4 – 0.8 were achieved. Therefore, correction factors were used to remove the biases as suggested by [Merzouki et al. \(2010\)](#), with the soil contribution in Eq. 5-8 for vegetated area also being corrected.

Acceptable RMSEs (< 2.2 dB) were observed over grass and wheat paddocks for all available radar configurations except the C-band VV polarization for wheat paddocks. A large underestimation of 12.4 dB was observed for wheat at C-band VV polarization, which could be ascribed as the underestimation of transmission in the DBA ([Huang et al., 2017c](#)). More specifically, the mean field of the vegetation layer is assumed to be the incident wave on each scatterer in DBA and thus is uniform for different parts of

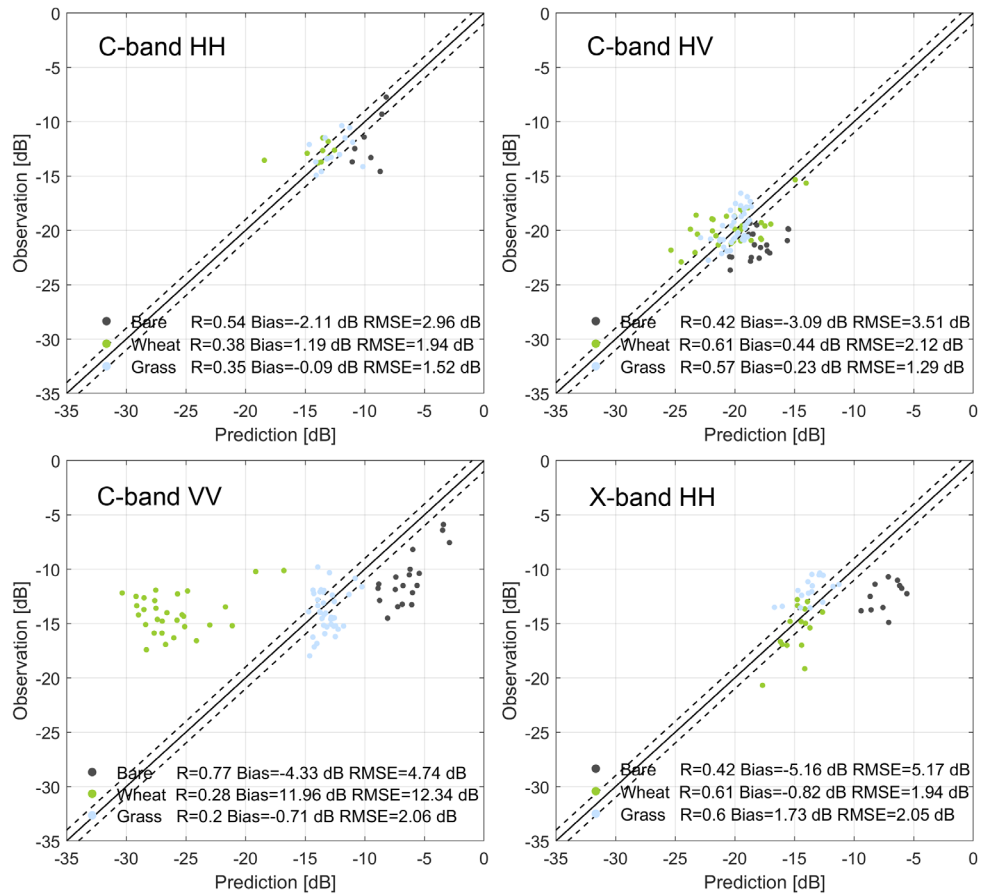


Figure 5-7: Comparison of forward and observed σ^0 at the paddock scale ($\sim 0.1 - 0.5$ km) for available C- and X-band data. The dash lines denote the ± 1 dB offset. R refers to Pearson correlation coefficient.

a single cylinder (Figure 5-8 a). This approximation can greatly overestimate the actual incident wave at low parts of a cylinder (Figure 5-8 a) because of the increasing attenuation caused by the nearby cylinders. Consequently, the scattering field of a single cylinder was overestimated because of the overestimated incident wave, resulting in an overestimated attenuation in Eq. 5-8. Additionally, the assumption of equivalent medium can further underestimate the transmission of areas with a large spatial variation of vegetation density. An example is shown in Figure 5-8 (b) where the vegetation layer has an average τ_p of 4 and a 20% spatial gap without vegetation. The transmission calculated by the DBA is near 0 because of the large average τ_p ; however, this should be near 0.2 because of the 20% spatial gap where the signal can go through without attenuation.

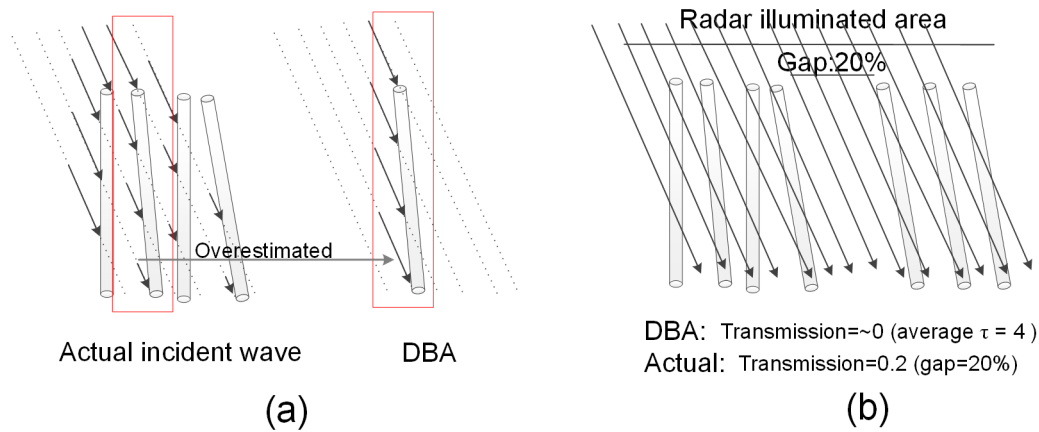


Figure 5-8: Conceptual figure showing the two potential reasons for the overestimated attenuation in DBA. (a) shows the attenuation overestimation caused by the overestimation of incident field in a single cylinder. (b) shows the effect of a 20 % gap between vegetations on attenuation estimation.

The two-potential effects described by Figure 5-8 tend to be more significant at C-band than L-band, with a near-zero bias for L-band at all polarizations (Figure 5-4). This can be explained by the stronger attenuation of nearby cylinders and the relatively larger gaps for a shorter wavelength. In addition, these effects relate to the geometry of the vegetation scatterers and the polarization of incident waves. In this study, wheat was simplified as a layer of near vertical cylinders and thus VV polarization had a more significant underestimation than HH. On the contrary, HH polarization should be more sensitive over grass as it had larger elevation angles. Fortunately, grass commonly has a relatively small VWC value of $<1 \text{ kg/m}^2$, and only slight underestimations of 1 – 2 dB were observed for C- and X-band at HH polarization.

5.5 Chapter Summary

Landcover specific LUTs were built to accurately represent the behavior of surface scattering under various radar configurations using a combination of scattering models (NMM3D-DBA for L-band and Oh-DBA for C- and X-band). The soil surface was assumed to be isotropic, with an assumed effective isotropic roughness value for paddocks with periodic features, as suggested by [Champion and Faivre \(1996\)](#) and [Joseph et al. \(2010\)](#). The performance of these LUTs was evaluated using ground measurements and airborne/spaceborne radar data, showing acceptable representation

of the angular behavior and a forward ubRMSE of 1 – 3.2 dB dependent on the polarization, frequency and land cover type; calibration of the Oh model was undertaken to remove the biases. These LUTs are used to build a synthetic data set in Chapter 6, to retrieval soil moisture from time series multi-angular data in Chapter 7, and multi-frequency data in Chapter 8.

6 Surface Anomaly Change Detection

The different temporal behavior of soil moisture and other earth surface parameters, such as surface roughness and vegetation, are utilized here to remove the major unknowns in the proposed multi-SAR-mission retrieval. The method assumes that only the soil moisture varies in the period of interest, while all other parameters such as vegetation water content and soil surface roughness are sufficiently time invariant. However, this assumption is not always satisfied in agricultural areas, where cultivation practices such as ploughing, irrigation and harvesting are conducted irregularly between radar acquisitions, resulting in abrupt roughness and vegetation changes. Consequently, a roughness and vegetation change detection approach is developed in this chapter as a pre-processing of the soil moisture retrieval presented in Chapters 7 and 8. The work in this chapter has been published in [Zhu et al. \(2019b\)](#).

6.1 Background

The rational and benefit of using time-invariant soil roughness and vegetation in multi-temporal soil moisture retrieval have already been introduced in Chapter 3. However, the assumption that the variation of backscatter in time only relates to a change of soil moisture may not be valid, with a few other factors summarized in Figure 6-1. Specifically, variation of the SAR system can introduce significant changes in SAR observations ([Ulaby et al., 2014](#)), creating a problem in the change detection-type methods ([Wagner et al., 1999a](#)). Relative geometric and calibration errors are tightly related to a specific SAR system, meaning that data acquired from the same observation geometry commonly has great stability, while combining images with different acquisition modes and/or incidence angles may introduce large uncertainties. The third category is the anomaly backscatter changes due to mechanisms that are different from the gradually evolving surface conditions. A heavy rainfall between two observations can cause impulse smoothing of the soil roughness ([Zobeck and Onstad, 1987](#)) and significant change of the vegetation's dielectric constant ([McDonald](#)

[et al., 2002](#)). While identifying extreme rainfall events from light rainfall events using radar-based soil moisture products may be challenging ([Bazzi et al., 2019](#)), the presence/absence of a rainfall event is relatively easy to be determined through either the abrupt increase of average backscatter over time or from rainfall products. The uncertainty caused by the radar system and the input data will be discussed in Chapter 7. This chapter only focuses on the backscatter variations at the paddock scale as a result of cultivation practices, e.g. irrigation, harvest, ploughing and harrowing.

Soil moisture retrieval approaches that consider the paddock scale roughness changes includes the Bayesian change detection method of ([Notarnicola, 2014](#)) and the use of multi-temporal roughness corrections ([Gorrab et al., 2015](#)). A more favorable approach is to include a pre-processing procedure that can determine the changed paddocks, making detection independent of the multi-temporal approach. With knowledge of the changed paddocks, time series SAR data of changed paddocks can then be split into multiple different subseries according to the paddock specific change dates, where multi-temporal retrieval methods can be used safely.

A great number of methods have been proposed for detecting earth surface changes using multi-temporal SAR data, with the main interest focusing on change of landcover types ([Marin et al., 2015](#), [Pantze et al., 2014](#)), flooded area ([Brisco et al., 2013](#)), ship

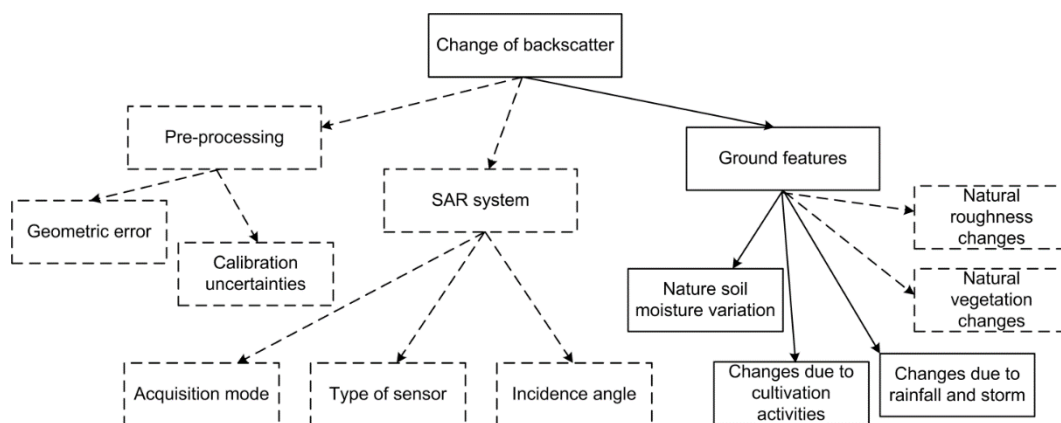


Figure 6-1: Flowchart showing the factors affecting backscatter changes from multi-temporal SAR images. The solid rectangles at the bottom level show the sources that should be considered before applying soil moisture retrieval from multi-temporal SAR images with short time interval.

movements ([Wei et al., 2014](#)) and oil spills ([Konik and Bradtke, 2016](#)). There are two main steps in change detection ([Bruzzone and Prieto, 2002](#)): one is the generation and selection of features (e.g. the difference/ratio maps) at a pixel and/or object basis; the other analyzes the difference between images and identifies the changes. The former is tightly related to specific changes because of their different scattering mechanisms. For the latter, several popular methods include an automatic Bayesian algorithm ([Bruzzone and Prieto, 2002](#)), a Kittler-Illingworth based method ([Satalino et al., 2014](#)), and a method based on enhanced fuzzy clustering ([Gong et al., 2012](#)). Despite the promising performance of these methods in specific applications, two issues need to be further addressed: i) Can slight changes in roughness and vegetation be identified? and ii) What are the optimal polarizations and spatial scale combination in identifying these changes?

In this chapter, an anomaly detection method was developed as a pre-processing step for the safe use of multi-temporal approaches. The spatial/temporal characteristics of roughness and vegetation changes in SAR data were first investigated to guide the development of the method. The proposed method includes two main components: i) extraction of the optimal image ratio/difference for change detection at the paddock scale with the aid of a feature selection algorithm, and ii) a two-step algorithm to identify the changed paddocks with the first step generating multiple over-detection for the same period of interest using different SAR image pairs, which are then combined to remove the false alarms in the second step. The proposed pre-processing method was evaluated using extensive synthetic and real SAR data sets. The multi-temporal soil moisture retrieval method proposed by [Wagner et al. \(1999a\)](#), [\(1999c\)](#) was used to show the initial and residual errors caused by surface changes in multi-temporal soil moisture retrieval before and after application of the pre-processing method.

6.2 SMAPEx-5 Data Set

6.2.1 Ground measurements

A focus area of SMAPEx-5 was selected in this chapter (Figure 6-2) considering the availability of ground truth of cultivation activities. The focus area is a 3 km × 21 km north-south strip covering three SMAPEx-5 focus farms (YE4, YE7 and YE), with the main land cover types being dense winter wheat, grass and bare soil. Some parts of the area undergoing intensive cultivation practices during the later stage of the SMAPEx-5 period. All paddocks with cultivation activities in the focus area were recorded for ground truth, including 8 irrigated wheat paddocks and 13 bare soil or

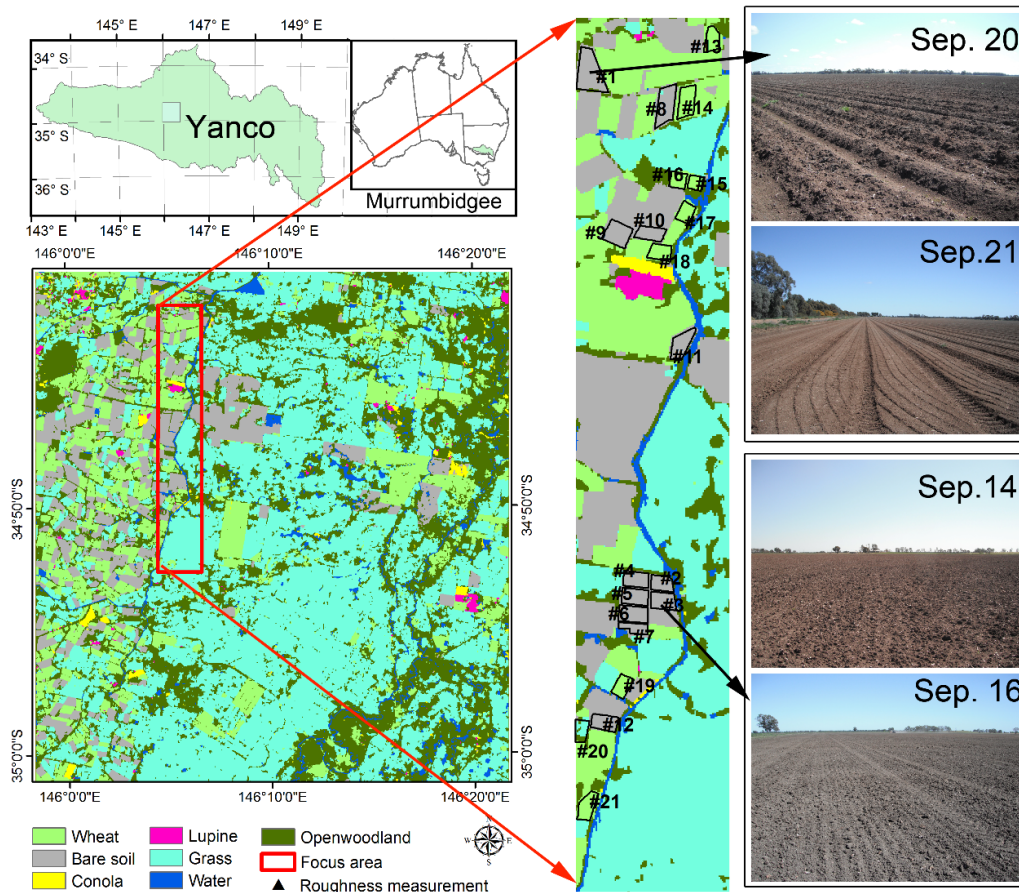


Figure 6-2: Focus area selected for algorithm evaluation using ground measurements. The right panel shows two examples where roughness changed during the period of SMAPEx-5.

grass paddocks. These paddocks account for a small part of the focus area, with their boundary and paddock ID depicted in Figure 6-2.

As introduced in Chapter 3, ground sampling of soil moisture, roughness and vegetation was made in the SAMEPx-5 focus farms. The three-week campaign was a gradual dry-down period because of a moderate rainfall occurred before the experiment. The gradually changing rate can be roughly expressed as $1 - e^{(-I/2)}$, with the I being the order of ground sampling dates from 1 to 8. The available measurements of paddocks with cultivation activities are listed in Table 6-1. H_R and L_C ranged from 0.53 to 3 cm and 5 to 35 cm for isotropic surface, respectively. Large H_R values up to 9 cm were observed across the row in paddocks with row structures. The available measurements for paddocks with cultivation activities during the experiment are listed in Table 6-1. Unfortunately, most of the cultivation events occurred between the last two soil moisture sampling dates (DOY 267 and 269). Only the occurrence of these events was recorded on the last soil moisture sampling date (DOY 269) without any detailed measurements of the roughness and vegetation changes.

6.2.2 Radar data

The radar data from Chapter 5 was used here for the evaluation of the change detection algorithm, including eight acquisitions of L-band PLIS observation, seven C-band RADARSAT-2 images and five X-band COSMO SkyMed acquisitions. An optical image acquired by Landsat 8 Operational Land Imager (OLI) on 30th September 2015 was used as a reference for geo-registration. Images from all three sensors were multi-looked and re-sampled to a grid size of 25 m. The cosine law ([Ulaby et al., 1982b](#)) with a power index of 2 was used to normalize all the backscattering coefficient (dB) data to a reference angle of 30°. This can have a negative effect on change detection. For real applications, the proposed method could be applied to data with similar incidence angle ranges respectively with the presence/absence of roughness and vegetation changes being combined using logical operations. Alternatively, as a pre-processing stage of multi-temporal soil moisture retrieval, the one used in a specific retrieval study/application could also be the optimal choice.

Table 6-1: Available roughness and vegetation measurements of the paddocks with cultivation activities

#	Land cover	VWC (kg/m ²)	Before cultivation		After cultivation		Cultivation DOY
			H_R^* (cm)	L_C / H_R^*	H_R^* (cm)	L_C / H_R^*	
1	Bare	-	1.94(8.66)	6.82(2.44)	0.51(5.47)	5.32(20.7)	264
2 - 3	Bare	-	-	-	-	-	258
4 - 7	Bare	-	-	-	-	-	263
8	Bare	-	-	-	1.16(5.54)	8.24(3.65)	263
9	Bare	-	1.50	14.65	1.90	6.05	268
10	Bare	-	2.12(6.30)	7.76(3.20)	-	-	269
11	Bare	-	-	-	-	-	268
12	Bare	-	-	-	-	-	268
13	Wheat	-	-	-	-	-	269
14	Wheat	3.72	1.01(2.94)	11.30(6.49)	-	-	269
15	Wheat	2.81	1.06(2.76)	7.24(4.98)	-	-	269
16	Wheat	1.17	-	-	-	-	269
17	Wheat	2.32	-	-	-	-	269
18	Wheat	2.82	1.54(2.83)	6.95(5.34)	-	-	269
19, 20	Wheat	-	-	-	-	-	269
21	Wheat	2.78	1.60	7.44	-	-	269

*: roughness along (perpendicular) to row structure for paddocks with periodic surface
 -: not available

The PLIS time series data over the focus area (the red rectangle in Figure 6-3) and the records of cultivation practices between DOY 267 and 270 in 2015 were used to provide an opportunity to investigate the spatial and temporal characteristics of anomaly surface changes. Figure 6-3 shows the difference maps of HH, VH and VV polarized backscatter images acquired on DOY 267 and 270. Ploughing and irrigation practices were observed over five bare soil paddocks and eight winter wheat fields in this period, respectively. Obviously, these cultivation practices were carried out for individual paddocks, resulting in quite different patches in the difference maps and the boundaries of these patches roughly match that of paddocks. Accordingly, it is reasonable to treat all pixels describing a single paddock as an object and applying object-based techniques to detect those that changed. Object-based techniques take the irregular geographical objects in the research area (i.e. the paddocks in this study)

as the analysis unit rather than the uniform pixel/gird, with the first step being the image segmentation to determine the boundaries of geographical objects. For SMAPEX-5 (Yanco area), the area of paddocks ranged from 0.1 km² to 0.5 km², which is also the target scale of this study. However, soil moisture retrieval can still be carried out at a finer or coarse scale simply taking the detection results as a spatial mask. The use of an object-based analysis helps to reduce the effect of geo-referencing and speckle noise ([Hussain et al., 2013](#)), thus reducing the uncertainty caused by data pre-processing.

The time series HH, VH and VV of four bare soil paddocks with soil practices (i.e., #9-12) and four wheat paddocks with irrigation (i.e., #16-19) are also depicted in Figure 6-3. Others were not included in the figure to avoid overlapping data because of similar behavior. In general, the backscattering coefficients for all polarizations gradually decreased over the whole period of DOY 252-270, which is coincident with the decrease of soil moisture over the SMAPEX-5. A significant increase of HH, VH and VV can be observed from DOY 267 to 270 over the winter wheat paddocks due to irrigation. Similar results were found across bare soil paddocks due to soil cultivation activities. However, these changes were generated by different mechanisms. The relationship between irrigation and surface changes is quite complex. Despite a significant increase of soil moisture, irrigation can decrease soil roughness over a short time ([Hunsaker et al., 1999](#)). The sudden increase of soil water can also change the dielectric constant of wheat, with a similar magnitude effect to that of rainfall ([McDonald et al., 2002](#)). With respect to soil cultivation, the soil moisture of the top layer and roughness can be changed simultaneously. As a result, it can be hard to determine the contribution of soil moisture change to the measured backscatter variation. Nevertheless, for detecting these anomalies, it is not critical what causes the backscatter variation. Since the changed paddocks commonly takes only a small part of the whole research area, and the SAR observations of these paddocks deviate a lot in both space and time from that of other paddocks, the changed paddocks may be treated as outliers.

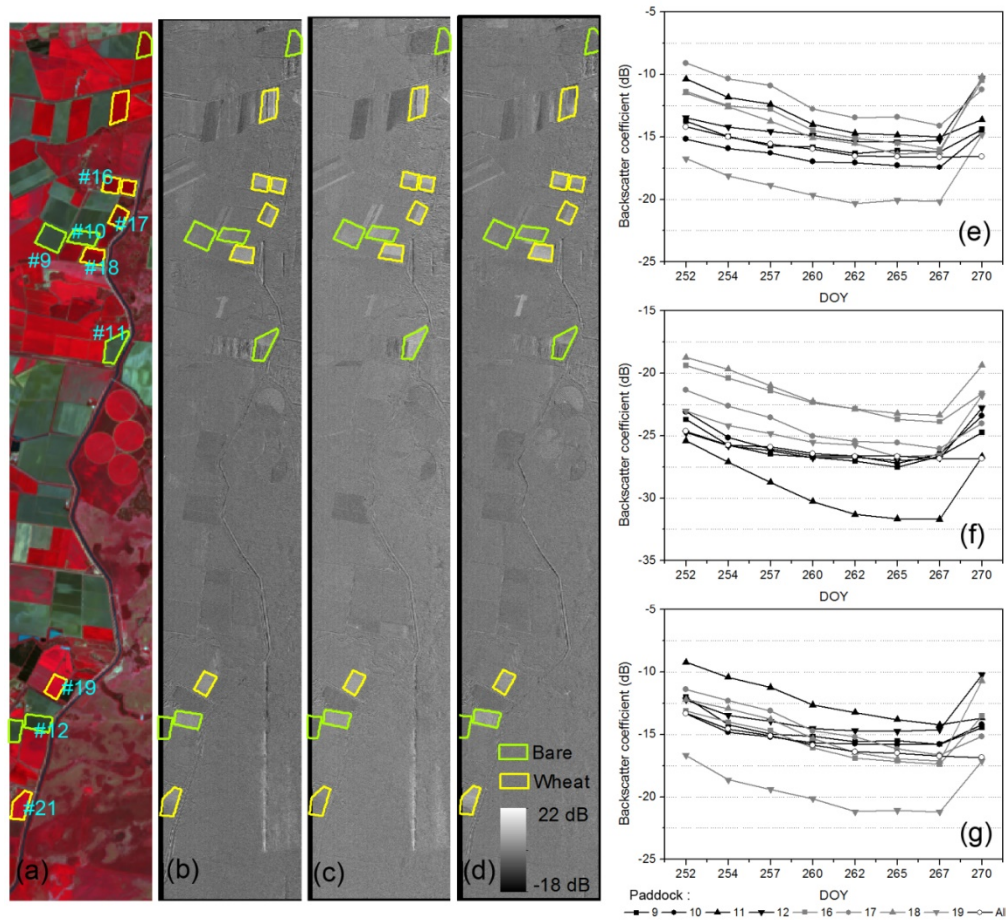


Figure 6-3: Anomaly surface changes at L-band (PLIS) multi-temporal SAR images. (a) shows the changed paddocks observed between DOY 267 and 270, 2015 on a false color composite Landsat 8 OLI image (RGB: near-infrared/red/green); (b), (c), (d) are the backscatter difference maps in HH, HV and VV polarizations between images acquired on DOY 267 and 270 with the changed paddocks delineated as well, respectively; (e), (f) and (g) are respectively the time series HH, HV and VV of several examples, which also include the average backscattering coefficient of the whole area labeled as “All”.

Figure 6-3 also illustrates the sensitivity of different polarizations to these changes. The increase in VH backscatter for all bare soil paddocks was somewhat higher than that in HH and VV from DOY 267 to 270, which can be explained by the different polarization sensitivities to soil roughness. Irrigated paddocks showed significant backscatter increase in all three polarizations. A feature space (e.g. the 2-dimension space spanned by temporal difference of HV and VV) with larger sensitivity is

commonly more powerful in detecting the changed paddocks than one with smaller sensitivity. For multi-temporal polarimetric data, thousands of feature spaces are available and thus a feature selection algorithm is needed to find the optimal feature space.

6.3 Synthetic Data Set

The cultivation practices during the SMAPEX-5 cannot fully represent all possible anomaly changes in real applications. Accordingly, a synthetic SAR data set was generated with various soil moisture, roughness and vegetation changes based on the SMAPEX-5 ground measurements for a comprehensive evaluation. The landcover of the SMAPEX-5 focus area was selected as the based map for the synthetic with a total of 621 paddocks. In this section, the detail of synthetic roughness, vegetation and soil moisture was introduced first, followed by the method to build synthetic radar data and the evaluation process over the generated synthetic data set.

6.3.1 Synthetic surface parameters

Eight soil moisture maps were generated with a time step of 2-3 days according to the eight sampling dates of SMAPEX-5. Specifically, the initial average soil moisture value (m^3/m^3) of each paddock was randomly generated from a uniform distribution of $U(0.25, 0.4)$. From this, the soil moisture of each pixel of a paddock was randomly generated from a normal distribution with a standard deviation of 0.05 (m^3/m^3) to show inner-paddock variability. The dry down process observed during the SMAPEX-5 was used to produce the following seven soil moisture maps.

After soil cultivations, both the H_R and L_C changed (Table 6-1). However, the changes of H_R and L_C can be hardly independent in real applications. Different empirical relationships between s and effective L_C values were observed for various radar configurations in forward prediction, e.g., [Baghdadi et al. \(2002c\)](#), [Baghdadi et al. \(2004\)](#). A fixed L_C/H_R ratio of 10 was suggested by [Kim et al. \(2012a\)](#) for soil moisture mapping at a 3-km grid from L-band data. In addition, more parameters are required

for soil surface with periodical row structures. The effect of row structures and their temporal changes on backscatter is quite complex to model ([Zribi et al., 2002](#), [Blaes and Defourny, 2008](#)). Fortunately, this study only needs to determine the presence/absence of roughness changes, while it is not necessary to know the specific kinds of changes. Different types of roughness changes, including the correlation function shape, row structure, H_R and L_C , can result in similar changes in radar observations. This means effective changes of s can always be found for all potential roughness changes. For instance, effective isotropic roughness described by a single set of H_R and L_C could be used to roughly account for the soil surface with row structures ([Champion and Faivre, 1996](#)).

Accordingly, only H_R was simulated independently with the exponential correlation function and a fixed L_C of $10s$ considering the significantly higher sensitivity of s to the radar observations ([Ulaby et al., 2014](#)). Similar to the generation of soil moisture maps, the initial average H_R value (cm) of each paddock was randomly generated from $U(0.5, 4)$. Then, s values of each paddock were randomly generated from a normal distribution with a standard deviation of 0.3 (cm). A decreasing rate of 0.98 denoting the gradual roughness changes was applied to produce the second to eighth maps.

Random changes were introduced in the H_R and VWC maps with a fixed probability of 10% for two successive roughness and VWC maps in time. Once a paddock was selected with H_R or VWC changes, the average value of the paddock was randomly determined and the value of each pixel in the paddock was re-generated. The input for generating these maps is summarized in Table 6-2. It is worth noting that the VWC of bare soil paddocks was set to 0 without changes in time.

6.3.2 Construction of synthetic radar data

Based on the surface parameter maps, speckle-free backscattering coefficient maps were produced using LUTs built in Chapter 3. Only bare soil was included in X-band data set because it is questionable to use X-band in soil moisture retrieval under vegetation. Speckle noise maps with the same size were produced using the chi-square

Table 6-2: The input for generating time series maps of surface parameters. U (A , B) denotes a uniform distribution ranging from A to B.

Parameter	mv (m ³ /m ³)	H_R (cm)	VWC (kg/m ²)
Distribution for initial mean value	U (0.25, 0.4)	U (0.1, 4)	U (0.2, 4)
Inner-paddock standard deviation	0.5	0.3	0.5
Gradually changing rate	$1 - e^{(-I/2)^*}$	0.98	1.05
Probability of anomaly change	0	10%	10% or 0
Anomaly change amplitude (%)	0	U (10, 70)	U (10, 70)

*: coincident with SMAPEX-5, I is the map time index starting from 1.

distribution with $2N$ degrees of freedom, where N is the number of independent looks ([Bolter et al., 1996](#)). The speckle-free backscattering coefficient maps were then multiplied with their generated speckle noise maps pixel by pixel.

Figure 6-4(a) show the process of generating the time series σ^0 in dB of a given period 1 to q . For one grid with s or VWC changes at a date k , two sub-series σ^0 were simulated with the initial (s^1 and VWC¹) and changed (s^2 and VWC²) surface parameters. The σ^0 of wettest ($mv = 0.43$ m³/m³) and driest ($mv = 0.03$ m³/m³) conditions with the initial s and VWC were also generated, while an additional set of σ^0 representing wettest and driest conditions were calculated for these with s or VWC changes (the part 5 and 6).

6.3.3 Validation metrics

The records of simulated anomalies and cultivation practices observed during SAMPEX-5 (Figure 6-2) were used to produce reference maps for synthetic and real data, respectively. There are four possible outcomes in identifying a paddock as changed or not, when comparing the detection results and the reference maps: true positive (TP), true negative (TN), false positive (FP) and false negative (FN). Based on these, accuracy rate (AR), false alarm rate (FAR), and F score ([Olson and Delen, 2008](#)) were calculated:

$$AR = \frac{TP}{TP + FP}, \quad \text{Eq. 6-1}$$

$$FAR = \frac{FN}{TP + FN}, \quad \text{Eq. 6-2}$$

$$F = \frac{2TP}{2TP + FP + FN}. \quad \text{Eq. 6-3}$$

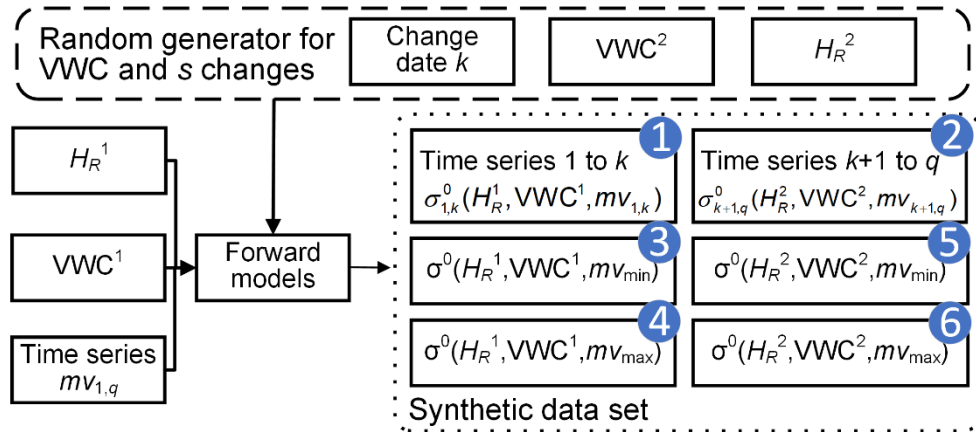
The AR (also known as *precision*) and FAR reflect the missed alarms and the false alarms of change detection results, respectively. F score is a joint measure that penalizes both missed alarms and false alarms. For soil moisture retrieval from multi-temporal SAR data, the missed alarms are the source of error but the FAR is also important because it controls the retrieval rate which is defined as the percentage of areas that can be used in soil moisture retrieval. As an example, with all paddocks identified as changed ($AR=1$; $FAR \sim 1$) no errors will be introduced because the entire image cannot be used in soil moisture retrieval.

In addition, the multi-temporal soil moisture retrieval algorithm proposed by [Wagner et al. \(1999a\)](#) was used to show the effect of s and VWC changes on retrieval before and after the change detection. Specifically, the Wetness Index (WI : 0 to 100%) for a grid is defined as ([Wagner et al., 1999a](#)):

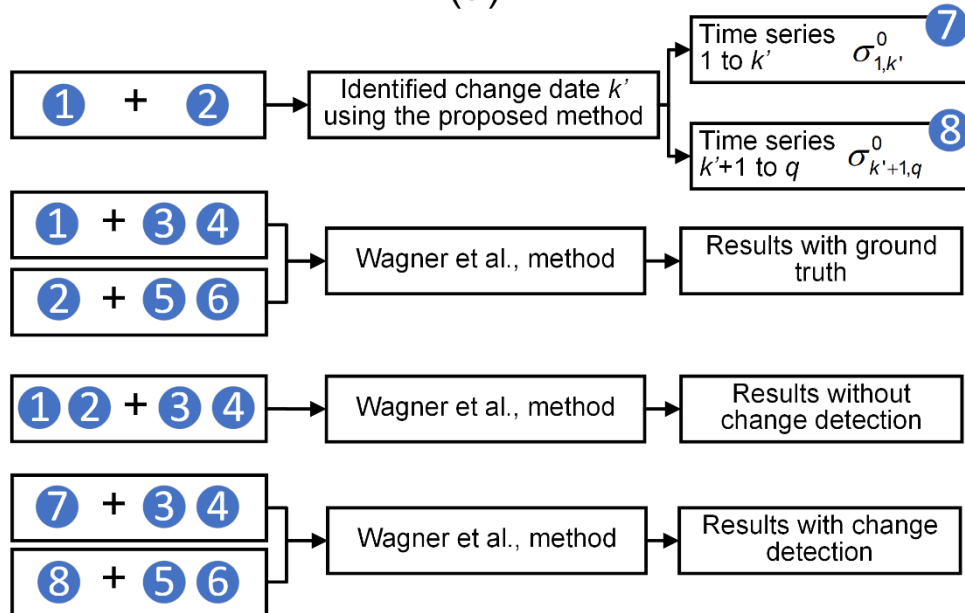
$$WI = \frac{\sigma^0 - \sigma_{dry}^0}{\sigma_{wet}^0 - \sigma_{dry}^0}, \quad \text{Eq. 6-4}$$

where σ^0 , σ_{dry}^0 , and σ_{wet}^0 are the current backscatter values at HH polarization of a pixel and that of the wettest and driest conditions, respectively. Figure 6-4(b) shows the concept of validation process using the WI . The time series σ^0 was first separated into two sub-series at the detected change date k' (The part 7 and 8). Three WIs can

be calculated: i) one without removing the effect of roughness and VWC changes (WI_u);
 ii) one with all changes being removed using the ground truth (WI_{gt}); and iii) one with



(a)



(b)

Figure 6-4: Flowchart of synthetic radar data construction (a) and the validation process over the synthetic radar data using the Wanger's method (b). The s and VWC are roughness RMS height and vegetation water content with the superscript 1 and 2 being the initial and changed states. $mv_{1,q}$ denote time series soil moisture from the first to q^{th} dates.

changes being partly removed by the proposed method (WI_c). The root mean square error (RMSE) of WI_c and WI_u were then calculated taking the WI_{gt} as the truth. Accordingly, the RMSE of WI_c and WI_u can be treat as the error and residual error caused by the roughness and VWC changes before and after change detection, respectively.

6.4 Method

The proposed change detection method consists of two components (Figure 6-5): (i) feature selection and extraction at the paddock scale, and (ii) determination of the change maps. The first component intends to extract the optimal features of paddocks for effectively detecting the anomaly surface changes. The second component is a two-step procedure (ensemble detection) to identify the changed paddocks, where multiple over-detected change maps for the period of interest were first generated using a simple density-based method and then merged using a voting to remove the false changed paddocks.

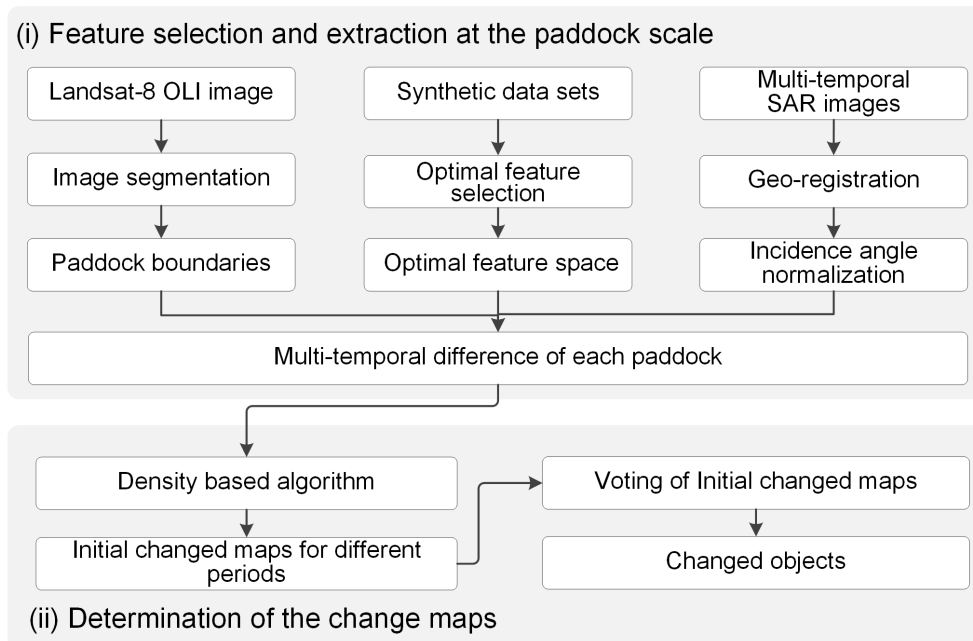


Figure 6-5: Flowchart of the proposed change detection method.

6.4.1 Feature selection and extraction at the paddock scale

As previously addressed, anomaly surface change detection is more suitable to be carried out at the paddock scale within the optimal feature space. Accordingly, a Landsat 8 OLI image was used to provide the paddock boundaries. Several difference/ratio images were then extracted using pixel-wise algebraic operations to be the candidates for an optimal feature space which was further determined using a genetic algorithm (GA)-based feature selection algorithm. Following the extracted boundaries and corresponding difference/ratio values of pixels, the mean vector of each paddock was calculated over the optimal space. These vectors were then normalized between 0-1 along each dimension as the input to the change detection algorithm. The process is detailed as follows:

A. Paddock extraction. The boundaries of paddocks can be conveniently extracted using a range of image segmentation algorithms, some of which were comprehensively evaluated in [Zhang et al. \(2015\)](#). In this study, the multiresolution segmentation algorithm ([Baatz, 2000](#)) embedded in the commercial software eCognition Developer 8 was used, with the scale and shape parameters being 10 and 0.5, respectively, considering the size and shape of paddocks in the study area.

B. Calculation of backscatter difference/ratio images. The candidate difference/ratio images are listed in Table 6-3. The difference and ratio images of two acquisitions t and $t-1$ in dB can be calculated as:

$$f^1(x, y) = f_{pq}^t(x, y) - f_{pq}^{t-1}(x, y) \quad \text{Eq. 6-5}$$

$$f^2(x, y) = f_{pq}^t(x, y) / f_{pq}^{t-1}(x, y) \quad \text{Eq. 6-6}$$

where p and q refer to H and V polarization, and x and y are the row and column of a pixel in the image. The number of features for fully polarized data is 18, resulting in a large number of available feature combinations ($2^{18} = 262,144$) for subsequent refinement using the feature selection algorithm below.

Table 6-3: Candidature feature index for SAR data acquired at phase t and $t-1$.

Family (#)	Candidature features
Difference (6)	$HH_t - HH_{t+1}, HH_t - HV_{t+1}, HH_t - VV_{t+1}, HV_t - HV_{t+1}, HV_t - VV_{t+1}, VV_t - VV_{t+1}$
Ratio (6)	$HH_t / HH_{t+1}, HH_t / HV_{t+1}, HH_t / VV_{t+1}, HV_t / HV_{t+1}, HV_t / VV_{t+1}, VV_t / VV_{t+1}$
Second order features (6)	$HV_t/VV_t - HV_{t+1}/VV_{t+1}, HV_t / HH_t - HV_{t+1}/HH_{t+1}, HH_t/VV_t - HH_{t+1}/VV_{t+1}, (HV_t/VV_t)/(HV_{t+1}/VV_{t+1}), (HV_t/HH_t)/(HV_{t+1}/HH_{t+1}), (HH_t/VV_t)/(HH_{t+1}/VV_{t+1})$

C. Optimal feature space selection. A range of feature selection algorithms are available (see [Guyon and Elisseeff \(2003\)](#) for an introduction and review). Among these, genetic algorithms (GA) are well-known general adaptive optimization methods that can efficiently process large search spaces with a low risk of reaching a local optimum ([Guyon and Elisseeff, 2003](#)). Hence, a GA is employed as the search algorithm in this study to find the optimal feature space.

A GA is a metaheuristic searching algorithm inspired by the process of natural selection. The first step of a GA is chromosome design and population initialization. For fully polarized data, the chromosome is an 18-bit binary value, corresponding to the 18 available features listed in Table 6-3. In the population initialization, 20 chromosomes were randomly generated with several bits of each chromosome being 1, denoting the initial selected features. These chromosomes were then adaptively optimized using three genetic operations, i.e. selection, crossover, and mutation. The selection operation was used to pick good chromosomes from the current population according to the fitness function defined in this study as:

$$fitness = \sqrt{2(1 - e^{-\alpha})} \cdot e^{-Ns/Na} \quad \text{Eq. 6-7}$$

$$\alpha = \frac{1}{8}(\mu_i - \mu_j)^T \left(\frac{C_i^* + C_j^*}{2} \right)^{-1} (\mu_i - \mu_j) + \frac{1}{2} \ln \left(\frac{1}{2} |C_i^* + C_j^*| / \sqrt{|C_i^*| |C_j^*|} \right) \quad \text{Eq. 6-8}$$

where μ_i and μ_j are the mean vector of class i and j (change or unchanged), respectively; C_i^* and C_j^* are the covariance matrix of class i and j , respectively; Ns and Na denote

the number of the selected feature and of all available features, respectively. The first term of the fitness function, i.e. $\sqrt{2(1-e^{-\alpha})}$, is known as the Jeffreys-Matusita (J-M) distance ($0 - \sqrt{2}$) which is a commonly used metric of interclass separability ([Bruzzone et al., 1995](#)). Two classes are partly to fully separable if the J-M distance is larger than 1. The rest of the fitness function is used to limit the number of selected features considering the computational efficiency in the change detection.

The crossover operator refers to the exchange of several bits between two chromosomes, and the mutation operator is used to improve the genetic diversity by randomly modifying some part of a chromosome. Both crossover and exchange can help avoid local optima by exploring new regions of search space. The optimization process is terminated when the number of iterations (also known as generations) reaches a defined value. In this study, the maximum generation, population size, crossover rate, and mutation rate were 100, 20, 0.1, and 0.01 respectively.

6.4.2 Determination of the change maps

After the previous step, each paddock corresponds to a feature vector in the selected optimal feature space and a set of thresholds or a hyper-plane is required to separate the changed paddocks from those that are unchanged. A number of methods can be used to achieve an accurate hyper-plane with some assumptions and/or iterative optimization ([Bazi et al., 2005](#), [Gong et al., 2012](#)). Despite the satisfactory performance in specific applications, the main drawback of these methods is the complexity to be a pre-processing stage of multi-temporal soil moisture retrieval. A simple strategy inspired by the ensemble machine learning is used here. In the framework of ensemble leaning ([Zhang and Ma, 2012](#)), the combination of multiple poor to moderate results from different learners is expected to result in an accurate result. Similarly, the combination of multiple over-detected change maps for the period of interest derived from different SAR pairs are also expected to have a satisfactory result. Generating over-detected change maps is easier than an accurate one.

Given a time series of SAR images $O = \{O_1, \dots, O_k, \dots, O_t\}$, the anomaly surface changes that occurred between the acquisitions $t-1$ and t are recorded by $t-1$ SAR pairs $O_t/O_{t-1}, \dots, O_t/O_k, \dots, O_t/O_1$ ($1 < k < t-1$). Based on these SAR pairs, $t-1$ over detected change maps $C = \{C_{t,t-1}, \dots, C_{t,k}, \dots, C_{t,1}\}$ ($1 < k < t-1$) can be generated. Obviously, a change map $C_{t,k}$ includes not only the changed paddocks for the target period ($t-1$ and t) but also these for the period of $t-1$ to k . The latter can be removed by simply subtracting the change map $C_{t-1,k}$ generated from O_{t-1}/O_k from the $C_{t,k}$. Accordingly, $t-1$ change maps for the target period are generated $C = \{C_{t,t-1}, \dots, C_{t,k} - C_{t-1,k}, \dots, C_{t,1} - C_{t-1,1}\}$ ($1 < k < t-1$). These poor to moderate change maps were finally merged to get a more accurate one through:

$$C = \sum_k (C_{t,k} - C_{t-1,k}) \geq N_k - 1, (1 < k < t) \quad \text{Eq. 6-9}$$

where N_k is the number of k . A straightforward explanation of Eq. 6-9 is as follows: multiple change maps for the period t and $t-1$ can be treated as independent “voters” which are more likely to vote the real changed paddocks. The maximum number of votes that one paddock can get is N_k and the real changed paddocks are expected to receive near N_k votes, which is significantly larger than that of falsely identified paddocks. Accordingly, a threshold N_k-1 can help remove most of the false alarms. An example of how multiple change detection results are merged is provided in Figure 6-6, using the time series L-band data.

Eq. 6-9 requires multiple over-detected change maps which are generated using a simple clustering algorithm, i.e. Density-Based Spatial Clustering of Applications with Noise (DBSCAN) ([Ester et al., 1996](#)). DBSCAN is capable of dealing with a large dataset and discovering clusters with arbitrary shape and noise without predetermination of a cluster number. Since the DBSCAN is only used to identify the noise which is the changed paddocks in this study, only a brief introduction relating to the noise is included. Please refer to [Ester et al. \(1996\)](#) for detail.

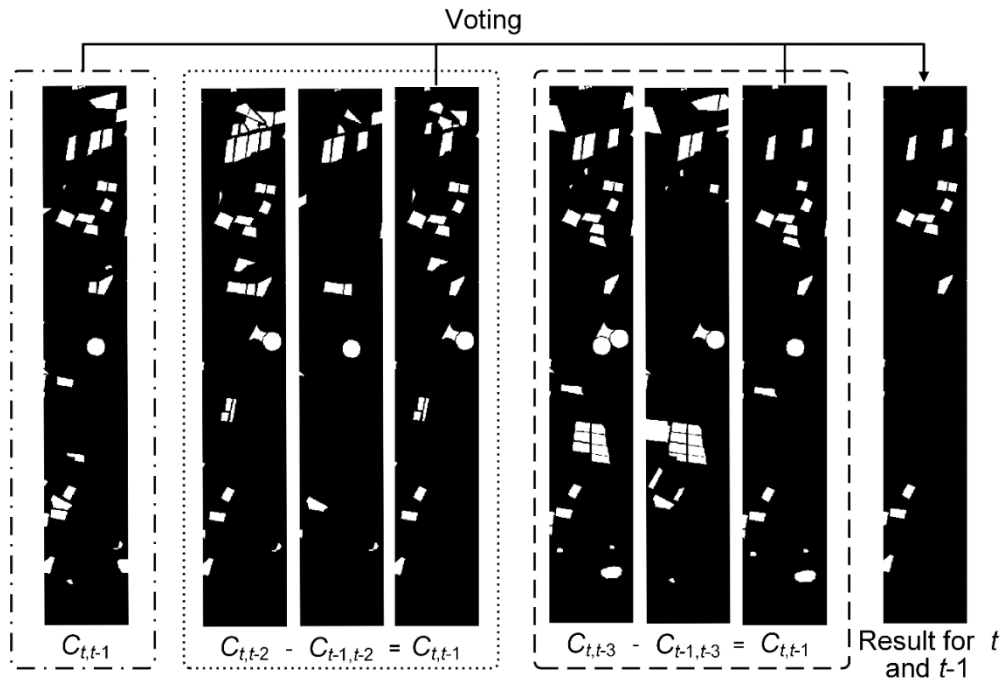


Figure 6-6: An example showing the process of generating the change map for the period of t and $t-1$ using an L-band series. White paddocks are those identified as changed. The label C refer to over-detected maps with the subscripts denoting the periods. Three over-detected maps for the periods of t and $t-1$ were generated first and then merged to remove the false alarms.

In DBSCAN ([Ester et al., 1996](#)), a point p_i of a dataset \mathbf{P} belongs to one of the following three types: core point, border point, and noise. The definitions of these types are based on the conception of local density $D(p_i) = \text{Cardinality}(N_{Eps}(p_i))$, where $N_{Eps}(p_i)$ is the number of neighbor points of p_i within a given radius (Eps) defined as $N_{Eps}(p_i) = \{p_j \mid \forall j, \text{distance}(p_i, p_j) < Eps\}$. In other words, this refers to the number of points within a radius Eps . A core point p_c refers to a point containing at least a user-defined minimum number of other points ($MinPts$) within Eps , i.e. $D(p_c) \geq MinPts$. A noise point p_n refers to one that does not contain core points in their neighbours and $D(p_n) < MinPts$.

6.5 Results

Three experiments were designed to evaluate the performance of the proposed method. The parameter N_k was set to 3, indicating that four SAR images in the time series were used to produce three over-detected change maps in the single detection step, with these merged in the ensemble detection. This is an appropriate value for real applications, considering the requirement of producing multiple change maps for the period of interest and a short time span to eliminate the effect of gradual roughness and vegetation changes (e.g., 24 days for 4 Sentinel-1 observations). The detail of each experiment is introduced below with the input data sets described in Table 6-4.

The first experiment was designed to select the optimal feature spaces for roughness and/or VWC changes based on two synthetic data sets (DS-1 and DS-2). Specifically, optimal feature spaces for L-, C-, and X-band and two polarization modes i.e., Quad (HH+HV+VH+VV) and Dual (VH+VV), were selected. These optimal spaces therefore are independent from the later change detection over real data set.

The proposed change detection method was comprehensively evaluated in the second experiment using the optimal spaces selected in Experiment A. The evaluation was first carried out on DS-1 and DS-2 to show the performance at different frequencies and incidence angles, followed by an investigation on the effect of noise and change amplitude using DS-3. The time series of PLIS, RADARSAT-2 and COSMO SkyMed images were used in the last experiment to show the performance on a real data set.

Table 6-4: Synthetic data sets used in this study. DS denotes dataset

	Frequency (GHz)	Incidence angle (°)	#Look	Types of anomaly changes
DS1	1.26 & 5.41	20,30,40,50	1	VWC & Roughness
DS2	9.3	20,30,40,50	1	Roughness
DS3	1.26	30	1:2:11	VWC & Roughness

All synthetic data were generated ten times with different random presence/absence of roughness and VWC changes and thus ten values are available for each validation metric. The mean and standard deviation of these values was reported below to show the average performance and stability of the proposed method. For simplicity, F score, AR , and FAR are used to denote the average F score, AR , and FAR of the 10 trials hereafter.

6.5.1 Optimal feature space

Table 6-5 introduces the optimal feature space for different radar configurations (frequency and polarization). In general, the J-M distance for all cases was larger than 1.28 showing a satisfactory separability between changed and unchanged paddocks in the selected feature space. The number of selected features was relatively small (3 - 4) compared to the 18 available features for fully polarized data. More specifically, the $HV_t/VV_t - HV_{t+1}/VV_{t+1}$ combination was selected by all radar configurations, followed by the $VV_t - VV_{t+1}$, $HV_t - HV_{t+1}$, and HV_t / HV_{t+1} , which were selected in 5, 3 and 2 cases, respectively. Since $VV_t - VV_{t+1}$, and VV_t / VV_{t+1} are highly correlated, the features based only on time series VV were selected by all configurations. Similarly, time series of HV polarization were selected in 5 cases, including either $HV_t - HV_{t+1}$ or HV_t / HV_{t+1} . These results can be explained by the different sensitivities of features to surface changes. For example, the cross-polarized ratio (HV/VV) is very sensitive to the change of roughness, especially for roughness changes at small values ($k\sigma < 2$ where k is the wavenumber; (Oh, 2004)). The HV polarization is sensitive to both VWC and roughness changes (Ulaby et al., 2014). The VV polarization has larger attenuation than HH over vegetation with a dominant vertical structure (e.g., wheat) and thus VWC changes can result larger changes in VV. Despite the great similarity, slight changes in feature constitution were observed among different radar configurations, which may result from the existence of multiple solutions with similar fitness.

L-band achieved the largest J-M distance in both Quad and Dual polarized data, followed by C- and X-band. However, the difference was limited with the largest difference (0.16) observed between L-band Quad and X-band Dual. Quad data achieved a slightly larger J-M distance than Dual data for L- and X-band, with the aid of an additional feature related to the co-polarized ratio (HH/VV); i.e. HH_t/VV_{t+1} for X-band and $(HH_t/VV_t)/(HH_{t+1}/VV_{t+1})$ for L-band. The effect of HH/VV here is

Table 6-5: Selected optimal feature space and the corresponding J-M distance for different radar configurations based on synthetic SAR data sets with various surface changes, where the grey grids denote the unavailable features. Q and D denote Quad and Dual (HV+VV) polarization, respectively.

Feature	X-band		C-band		L-band	
	Q	D	Q	D	Q	D
$HH_t - HH_{t+1}$						
$HH_t - HV_{t+1}$						
$HH_t - VV_{t+1}$						
$HV_t - HV_{t+1}$	×		×	×		
$HV_t - VV_{t+1}$		×				
$VV_t - VV_{t+1}$		×	×	×	×	×
HH_t / HH_{t+1}						
HH_t / HV_{t+1}						
HH_t / VV_{t+1}	×					
HV_t / HV_{t+1}					×	×
HV_t / VV_{t+1}						
VV_t / VV_{t+1}	×					
$HV_t/VV_t - HV_{t+1}/VV_{t+1}$	×	×	×	×	×	×
$(HV_t/VV_t)/(HV_{t+1}/VV_{t+1})$						
$HV_t/HH_t - HV_{t+1}/HH_{t+1}$						
$(HV_t/HH_t)/(HV_{t+1}/HH_{t+1})$						
$HH_t/VV_t - HH_{t+1}/VV_{t+1}$						
$(HH_t/VV_t)/(HH_{t+1}/VV_{t+1})$					×	
J-M distance	1.32	1.28	1.35	1.35	1.39	1.37

unclear, because i) the elevation angle of vegetation was assumed to follow a fixed distribution and thus VWC changes cannot introduce significant changes in HH/VV; and ii) HH/VV is relatively insensitive to roughness changes, changing from 0.6 dB-3.5 dB when σ changes from 0.3 to 4.8 cm at C-band ([Oh, 2004](#)). Accordingly, a uniform feature space including the HV_t/VV_t , HV_{t+1}/VV_{t+1} , HV_t/HV_{t+1} and $VV_t - VV_{t+1}$ is sufficient for all radar configurations listed in Table 6-5. The J-M distances in this space were around 1.37, 1.34 and 1.27 for L-, C- and X-band, respectively.

However, this does not mean that the dual polarized data is sufficient for all future applications. For example, HH can be required for vegetated areas with more complex structures (e.g., soybean). In addition, the effect of vegetation structure and its interaction with VWC changes were not considered, because of the simplistic vegetation scattering representation in the DBA ([Lang and Sighu, 1983](#)). To address this, some cases based on the Numerical Maxwell Model of three-dimensional simulations ([Tsang et al., 2017](#)) can be promising as this model can fully simulate the scattering of vegetation in detail. The polarimetric parameters calculated from fully polarized data ([Cloude and Pottier, 1996](#)) are expected to be more sensitive to the vegetation structure changes than simple polarization difference/ratio. Finally, the J-M distance is only part of the cost function used in the feature selection and a more complex feature space can be used for full polarized data for a better performance at the expense of a drastic increase in computational expense.

6.5.2 Evaluation using synthetic data sets

Figure 6-7 shows the performance of the proposed method on single-look synthetic data with different frequencies and incidence angles. In general, moderate performance was achieved in all cases with the F score, AR and FAR ranging from 0.81 to 0.87, 0.76 to 0.82 and 0.09 to 0.15, respectively. These are lower than the results of other methods in identifying the change of landcover types ([Marin et al., 2015](#), [Pantze et al., 2014](#)), flooded area ([Brisco et al., 2013](#)), ship ([Wei et al., 2014](#)) and oil spills ([Konik and Bradtke, 2016](#)), which commonly have an AR and FAR of better than 0.9 and 0.1 respectively. However, detecting soil roughness and VWC changes is more challenging

as the amplitudes of these changes are much smaller than that of landcover type change, presence/absence of a ship etc.

The proposed method performed best at L-band, followed by C- and X-bands but with a slight F score difference of less than 0.06. These results are coincident with the difference of J-M distance listed in Table 6-5. The standard deviation of F score, AR and FAR was all less than 0.02 showing a good stability of the proposed method. All three metrics demonstrated no clear angular pattern although the same roughness and/or VWC change resulted in quite different backscatter changes at different incidence angles. This can be partly explained by the multiple dependence of detection accuracy on the sensitivity of radar configuration, noise level and the spatial variation

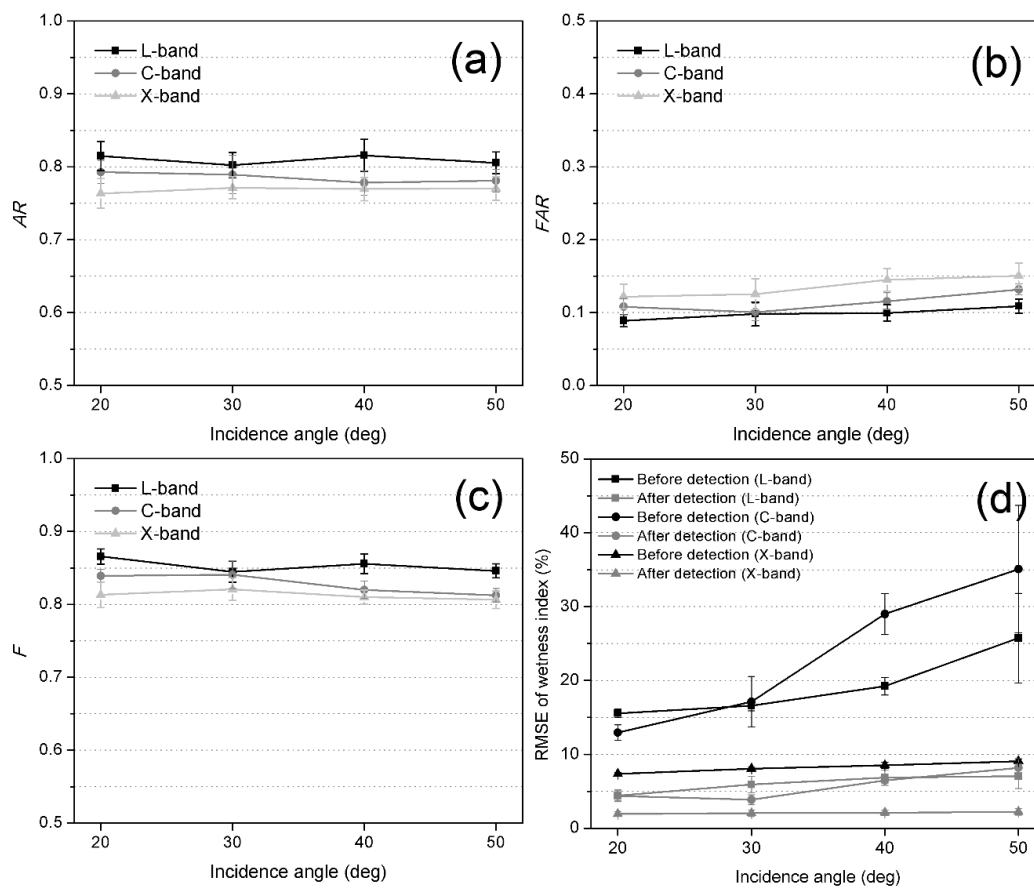


Figure 6-7: Performance of the proposed method on single-look synthetic data sets. (a) - (d) are the AR , FAR , F and RMSE of wetness index at L-, C- and X-bands with various incidence angles, respectively. The error bars denote the standard deviation of metrics.

of moisture changes. For time series with slight roughness and vegetation changes, noise could be the dominant factor and similar detection accuracy at different incidence angles was achieved regardless of the difference in sensitivity. The binary process (absence/presence) in change detection could be another reason. For these with large roughness and vegetation changes, the backscatter changes at less sensitivity radar configurations (e.g., small incidence angles) could be large enough to be identified.

Despite the moderate performance in view of accuracy metrics (Figure 6-7 a-c), the proposed method can greatly remove the error caused by roughness and VWC changes in multi-temporal soil moisture retrieval as depicted in Figure 6-7 (d). About 68.30% (L-band), 74.48% (C-band) and 74.75% (X-band) of the initial RMSE was removed after change detection. The residual RMSE was less than 8%, 7% and 3% for L-, C-, and X-band respectively. This difference is mainly caused by the different amount of changed paddocks. At X-band, 10% of bare soil paddocks have random roughness changes, while additional VWC changes in 10% of the vegetated paddocks were included at L- and C-bands. Significant angular dependence of RMSE was observed at L- and C-bands. This is mainly caused by the heavy dependence of backscattering coefficient on incidence angle and frequency over vegetated areas. The same VWC change at larger incidence angles and/or higher frequencies resulted in larger backscattering coefficient changes and consequently larger error in the multi-temporal retrieval. In contrast, the same roughness change at different angles resulted in similar backscattering coefficient changes and thus no clear angular pattern was observed in the results of X-band. For instance, a σ change from 0.3 cm to 3 cm results in a HH difference of 8.13 dB at an incidence angle of 20° according to the Oh model, which is 10.01 dB at 50° given a soil moisture value of 0.3 m³/m³.

The relationship between the performance and the number of independent looks for L-band is presented in Figure 6-8, where a larger number of looks indicates a lower noise level. As expected, AR and F gradually increased as noise decreased and reached their highest values when the number of looks was larger than 7, while the opposite

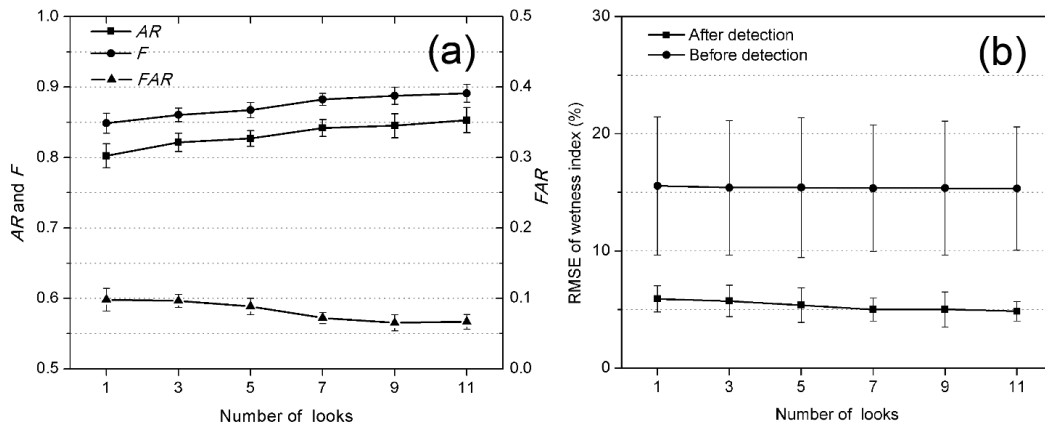


Figure 6-8: Impact of noise on performance at L-band synthetic data. (a) shows the average AR , FAR , and F versus the number of looks; (b) shows the RMSE of wetness index versus the number of looks. The error bars denote the standard deviation of metrics.

was found for FAR . This is consistent with the process of noise reduction using the multi-look operation. The main part of the noise was removed changing the number of looks from 1 to 7, with further multi-lookings contributing little to the result. After removing the major part of the noise, a satisfactory performance was achieved with an F score, AR and FAR of 0.90, 0.85, and 0.07, respectively. However, the improvement in the residual RMSE of wetness index was negligible ($\sim 1\%$), as depicted in Figure 6-8 (b). One explanation is that the improvement in AR mainly comes from additional identification instances of small roughness and VWC changes whose effect on radar observations is close to the noise level. Such small roughness and VWC changes could have limited effect on multi-temporal soil moisture retrieval with negligible improvement.

A further investigation on the relationship between detection accuracy and surface change amplitude in percentage for single-look L-band data is presented in Figure 6-9. The proposed pre-processing method had a relatively poor performance in identifying small roughness and VWC changes with an AR of 0.62 for a 10% change, but fortunately the effect of these small changes on multi-temporal soil moisture retrieval is also small. The residual RMSE in wetness index after change detection is only 2.46%. An important implication based on this is that the gradual (natural) roughness and VWC changes should not have a significant effect on soil moisture retrieval. When the

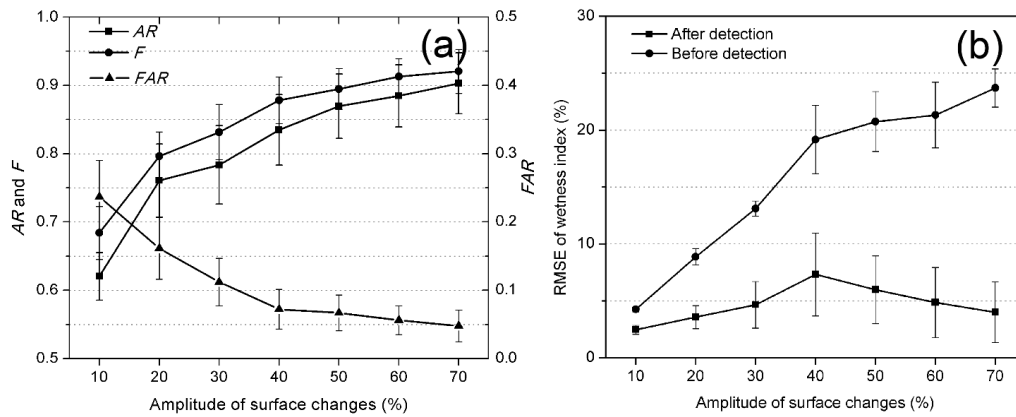


Figure 6-9: Impact of roughness and VWC change amplitude on performance at L-band synthetic data. (a) shows the average AR , FAR , and F versus change amplitude; (b) shows the RMSE of wetness index versus change amplitude. The error bars denote the standard deviation of metrics.

amplitude of roughness and VWC change increases from 10% to 70%, AR and F increased from 0.62 to 0.90 and 0.68 to 0.92 respectively, with a sharp FAR decrease of 0.19. However, the residual RMSE in soil wetness first slightly increased from 2.46% to 7.32% and then decreased to 4%. This can be explained by the different effect of surface change amplitude on AR and RMSE. An increase in change amplitude resulted in large errors caused by missed alarms, which however increased the detection accuracy and resulted in fewer missed alarms. The negative effect of increasing change amplitude on RMSE is larger than the positive effect of AR increase for change amplitudes less than 40%, which was reversed for larger surface changes.

6.5.3 Evaluation using real observational data set

The sudden surface change detection results over time series of PLIS, RADARSAT-2 and COSMO SkyMed acquisitions are presented in Figure 6-10, with the dashed lines showing the start and end time of the period of interest for each change map. The detection agreement is shown in light grey for the unchanged paddocks and in blue for the changed paddocks. The false alarms and missed alarms are depicted in

dark grey and green, respectively. In general, the proposed method achieved satisfactory results for L- and C-band data. Only one changed paddock was missed in L-band data with a total of 9 false alarms. Despite the relatively high FAR (0.3), only

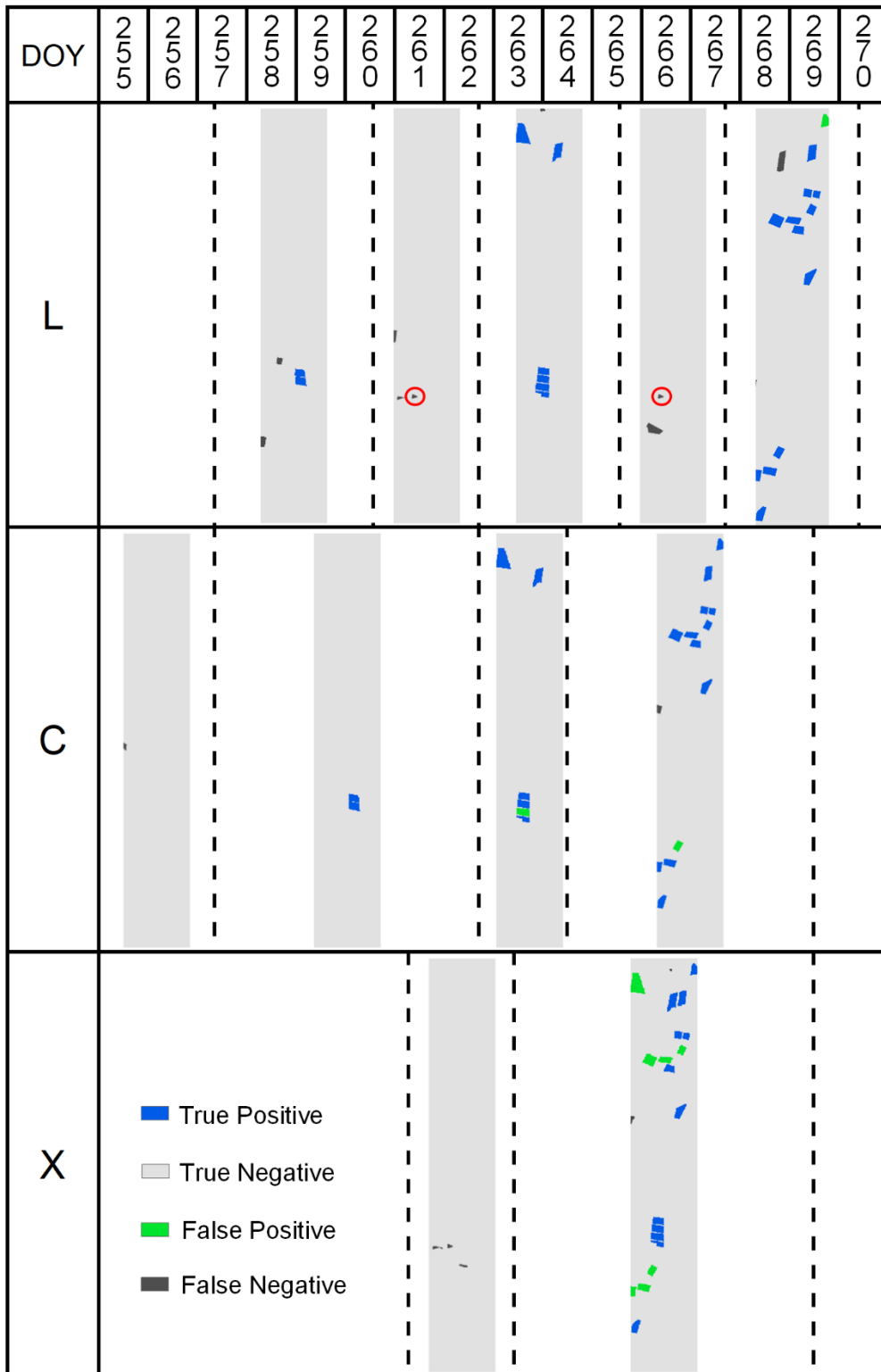


Figure 6-10: Change detection results versus ground truth at real SAR data collected during SMAPEX-5 study period. The dashed lines show the start and end time of the period of interest for each change map.

one paddock was erroneously identified as changed twice in this period (the red circle in Figure 6-10). These false alarms only have a negative influence on soil moisture retrieval methods that need a long time series of SAR data, e.g. ([Wagner et al., 1999a](#)). Taking the paddock in the red circle as an example, it was falsely detected as changed between DOY 260-262 and DOY 265-267. Consequently, the relevant time series of the L-band observations should be separated into three sub-series, i.e. DOY 255-260, DOY 262-265, and DOY 267-end. Soil moisture retrieval algorithms can still be applied on these respective sub-series.

In the detection results of C-band, acceptable results (AR 0.91; FAR 0.09) were achieved with two false and two missed alarms. This demonstrates the robustness of the proposed method in dealing with time series images acquired by different observation modes, with the assistance of a simple incidence angle normalization process. However, the detection results of X-band data were much poorer. A number of changed paddocks for DOY 263-269 were not identified. This is mainly caused by the feature space used in X-band; the COSMO SkyMed data only has HH polarization which is not sufficient to detect all changed paddocks.

6.6 Chapter Summary

The objective of this chapter was to identify abrupt roughness and vegetation changes caused by cultivation activities, to ensure that soil moisture variation is the only source of backscattering variation for the time period being processed for soil moisture. While the proposed method only achieved a moderate detection accuracy with the AR and FAR ranging from 0.75 - 0.85 and 0.08 - 0.15 for single-look data, evaluation based on synthetic data sets demonstrated that the proposed approach can effectively eliminate the major errors in multi-temporal soil moisture caused by VWC and roughness changes. To serve as a pre-processing procedure of operational soil moisture retrieval, time series data are separated into multiple subseries according to the detection results first. For multi-temporal soil moisture retrieval methods without a calibration process, e.g., [Balenzano et al. \(2011\)](#), [Kim et al. \(2012a\)](#), and [Ouellette et al. \(2017\)](#), and the retrieval method presented in Chapter 7 and 8, soil moisture retrieval can be carried

out on each sub-series independently. However, for those retrieval methods requiring either calibration or multi-temporal vegetation correction, e.g., [Wagner et al. \(1999a\)](#) and [Pierdicca et al. \(2010\)](#), the proposed method could provide an alarm for uncertainty caused by roughness and/or vegetation changes.

7 Time Series Multi-Angular Retrieval

This chapter presents a time series method for collective soil moisture retrieval from radar data collected by the same satellite/constellation. While several time series retrieval approaches have been developed in the past three decades, it is still challenging to retrieve soil moisture from data with different polarizations and incidence angles caused by the transition of imaging modes (e.g., ScanSAR, StripMap and Spotlight), radar beams, look directions (left and right) and orbits (ascending and descending). Consequently, a method that is compatible with varying polarization and incidence angle over time is proposed based on the forward model LUTS built in Chapter 5, the data introduced in Chapter 3 as calibrated in Chapter 4 and the change detection method proposed in Chapter 6. The work presented in this chapter has been published in [Zhu et al. \(2019a\)](#).

7.1 Background

The rational and advantage of using the different temporal behavior of soil moisture and other surface parameters in soil moisture retrieval, as well as several multi-temporal retrieval approaches, have been introduced in Chapter 2. The main limitation of those multi-temporal methods is the availability of radar data with a short time lag and similar radar configuration ([Balenzano et al., 2011](#), [Kornelsen and Coulibaly, 2013](#)). More specifically, current SAR missions commonly operate with multiple imaging modes in both ascending and descending orbits, resulting in the transition of both incidence angle and polarization in time. As an example, the SAOCOM constellation and ALOS-2/PALSAR-2 operate at both ascending and descending orbits with multiple imaging modes alternating in time, namely ScanSAR, StripMap and Spotlight ([Rosenqvist et al., 2014](#), [Giraldez, 2003](#)). As a result, a much longer time interval is required for acquiring multi-temporal data with a consistent radar configuration than the reported satellite revisit. The use of multi-angular time series data with different polarizations is therefore questionable in change detection techniques ([Wagner et al., 1999c](#), [Wickel et](#)

[al., 2001](#), [Balenzano et al., 2011](#), [Notarnicola, 2014](#), [Ouellette et al., 2017](#)), while scattering models that accurately describe the angular dependence of SAR data are needed for multi-temporal inversion methods ([Kim and Van Zyl, 2009](#), [Mattia et al., 2009](#), [Pierdicca et al., 2010](#), [Kim et al., 2012a](#), [Kim et al., 2014a](#), [Kweon and Oh, 2014](#)).

Consequently, a multi-angular time series method for operational soil moisture mapping from time series L-band SAR data, e.g. the joint data sets of PALSAR-2 and the SAOCOM constellation, was developed. The method applies the assumption of constant soil roughness and vegetation over the retrieval period with the main difference from the multi-temporal methods introduced above being that *a priori* information of dry-down soil moisture is integrated into a genetic algorithm (GA) based inversion of LUTs to partly remove the uncertainties in calibration, speckle noise removal, and in the forward models. The method was evaluated using the multi-angular airborne L-band data collected during the SMAPEX-5 data set (Chapter 3 and 4). The effect of data time interval and polarization combinations on retrieval accuracy are also here investigated to guide the use of the method in future applications.

7.2 Data set

Similar to the Chapter 5, three SMAPEX-5 focus farms (YA4, YA7 and YE) were selected for validation of the proposed method. The ground sampling of m , VWC H_R collected during the three-week campaign (Chapter 3) were used for evaluation of the proposed retrieval method in this chapter. Apart from the major vegetation types (wheat and grass), the open wood land in Figure 5-2 was also treated as grass land for the purpose of soil moisture retrieval here, because of the low tree coverage in the open wood land (less than 5%; $\sim 2000 - 3000$ trees /km²). The paddock boundaries in Figure 5-2 were used for analyzing the results at the paddock scale, while soil moisture retrieval at the pixel scale was made for the whole research area, with the water bodies removed.

As mentioned in Chapter 3, eight flights were conducted coincident with the SMAPEX-5 soil moisture sampling dates, providing L-band (1.26 GHz) radar data

using the airborne PLIS oriented to West and East (Figure 7-1). Consequently, radar observations of each location had two local (across track) incidence angles within $20^\circ - 50^\circ$. In this chapter, a multi-angular time series data set was built using data collected alternatively from right and left sides of the aircraft, which can be treated as being similar to a series of ascending and descending orbits. The incidence angle difference of two successive PLIS measurements ranged from 0 to 30° , with the smallest and largest difference being at the center and boundaries respectively, covering the general incidence angle difference of satellite data. PLIS backscatter data were calibrated, geo-referenced, multi-looked (12×7 looks) and resampled to 25 m.

7.3 Method

In the proposed method, soil roughness and vegetation are assumed to be time-invariant over the retrieval time window, the descriptions of which are simplified as a single parameter for H_R and VWC, respectively. Given N radar acquisitions sequentially collected within a short time span, $N+1$ unknowns need to be determined for bare soil consisting of N ϵ_s' ($\epsilon_{s1}', \epsilon_{s2}', \dots, \epsilon_{sN}'$) and one H_R , while an extra parameter of VWC needs to be derived for vegetated area. For full-polarized PLIS data (HH+HV+VH+VV), $3N$ independent measurements are available resulting in an over-determined inversion problem without considering the dependence among

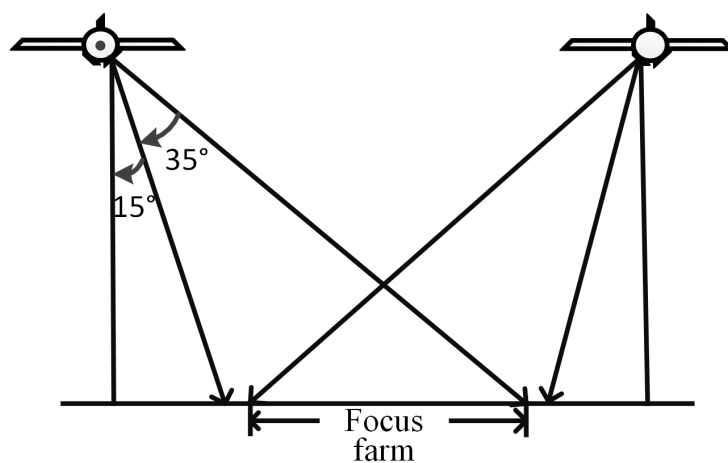


Figure 7-1: Observation geometry of airborne PLIS for each flight in SMAPEX-5.

different channels. This is also commonly true for operational polarimetric SAR missions, e.g. PALSAR-2, because either two dual-polarized or one full-polarized acquisition are acquired in time series ensuring at least $N+2$ measurements.

The general formulation therefore is to minimize the cost function:

$$f = \sqrt{\frac{1}{N} \sum_{i=1}^N w_{pq,i} (\sigma_{pq}^0(t_i, \theta_i) - \sigma_{pq,\text{LUT}}^0(H_R, \epsilon'_{si}, VWC, \theta_i))^2}, \quad \text{Eq. 7-1}$$

where σ_{pq}^0 and $\sigma_{pq,\text{LUT}}^0$ are the backscattering coefficients in dB from measurements and LUTs, respectively. The subscript i denotes the time sequence from 1 to N . The weight $w_{pq,i}$ accounts for the differing error of LUTs and/or radar observations. The main sources of this error include:

- i) **Speckle.** SAR data inherently suffer from the speckle noise, originated by the SAR system's coherent nature ([Ulaby et al., 2014](#)). The speckle noise can be partly removed by the multi-look operation at the expense of spatial resolution ([Thoma et al., 2006](#)), with the available single look SAR pixels however being different among imaging modes and also varying across the swath. Consequently, it is impossible to multi-look the data with the same number of looks for a consistent retrieval grid, resulting in different levels of residual speckle noise.
- ii) **Calibration uncertainty.** Time series data collected by different imaging modes may have inconsistent calibration and geometric accuracy, e.g. the difference between PALSAR-2 ScanSAR and StripMap mode reported by [Shimada et al. \(2009\)](#). Similar difference was also observed among different beams of the COSMO SkyMed and among different X-band missions ([Pettinato et al., 2013](#)).
- iii) **Forward model error.** A forward model could have different accuracy at different incidence angle and polarizations. Currently available surface scattering models are more prone to larger errors at high than at low incidence angles ([Mattia et al., 2006a](#), [Mancini et al., 1999](#)). The NMM3D-DBA used in

this study may also have error imbalance at different incidence angles. [Huang et al. \(2017b\)](#) has demonstrated a significant overestimated attenuation of DBA at C-band which can be worse for VV at larger incidence angles than for other radar configurations.

Different from these using time series data with the same radar configuration (e.g., [Kim et al., 2012a](#)), none of the three sources can be accurately modeled because of the time varying incidence angle, polarization and available SLC pixels. In order to keep the method as general as possible, it is not suitable to have a determined assumption of w_{pq} in Eq. 7-1 for a given multi-angular data series. Hence, the weights are taken as uniform for all items and a *prior* information of mv trend in time was involved:

$$30 \geq \varepsilon'_{s,i+1} \geq \varepsilon'_{s,i+1} \geq 3, \quad (i < N), \quad \text{Eq. 7-2}$$

denoting a drying down process during the period of radar observations. This can be guaranteed for a period after a rainfall like the SMAPE_{x-5}. In addition, rainfall can be identified considering the significant increase of backscattering coefficients in all polarizations after a rainfall. With this constraint, the effect of anomaly fluctuations in time series caused by various non-surface factors is expected to be partly removed.

A genetic algorithm (GA) was used to find the optimal solution of Eq. 7-1, because of its efficiency to search large spaces, low risk of reaching a local optimum ([Gen and Cheng, 2000](#)) and its convenience to integrate with constraints. Figure 7-2 shows the flowchart of the proposed retrieval method. The inputs include the LUTs, landcover map and the time series radar data, with the landcover map used to determine the type of LUT (bare soil, grass, wheat). The method starts from the generation of 20 random solutions (known as chromosomes in GA), with each solution consisting of N unknown values of ε'_s , one unknown value of H_R and VWC. An 8-bit binary was used to encode each unknown parameter with an example of ε'_s included in Figure 7-2. Consequently, the length of each solution was $8 \times (N+1)$ bits and $8 \times (N+2)$ bits for bare soil and vegetated areas, respectively. These solutions were then adaptively optimized using three genetic operations (selection, crossover, and mutation) according to the fitness estimated using Eq. 7-1. Please refers to [Gen and Cheng \(2000\)](#)

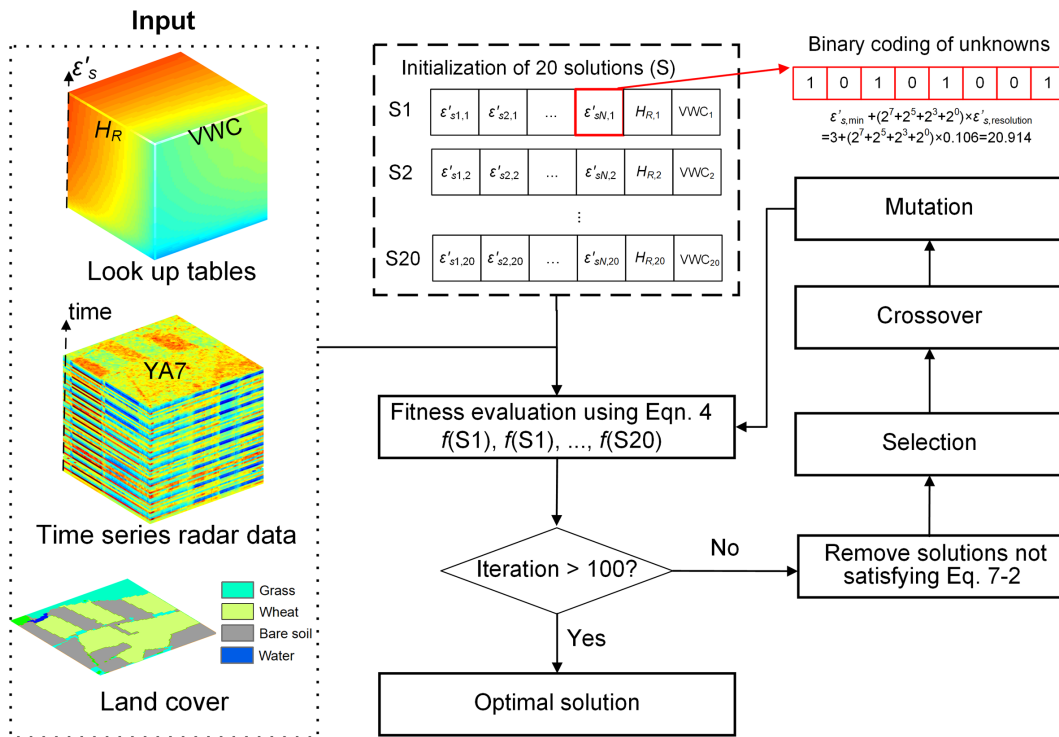


Figure 7-2: Flowchart of the soil moisture retrieval method

for more details about genetic operations. Specially, the dry down constraint was integrated as a pre-selection step, discarding solutions not satisfying Eq. 7-2. A maximum iteration number of 100 was set. The $N \epsilon_s'$ of the optimal solution was finally converted to $N mv$ using the relationship between mv and ϵ_s' (Dobson et al., 1985b), because the soil texture of Yanco area (Table 3-1) is very close to the data set used in the development of Dobson model.

7.4 Results

7.4.1 Retrieval results

Eight full polarized images with the look direction alternating between left and right were used to simulate combining descending and ascending radar observations from space-borne sensors, to evaluate the proposed method. The multi-angular time series for a paddock with cultivation activity identified in Chapter 6 was separated into two sub-series, according to the presence of the cultivation event, with mv retrieval carried out independently for each sub-series. The mv retrieval results at the pixel scale (25 m)

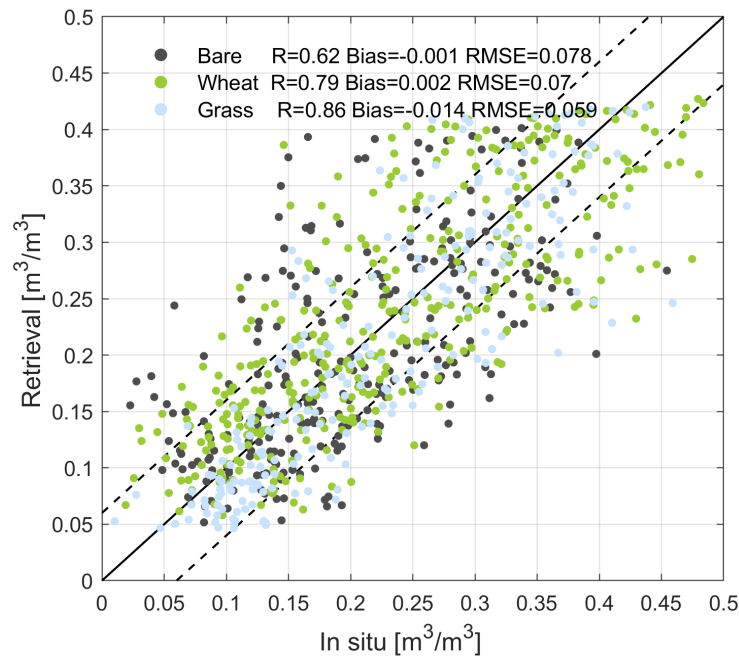


Figure 7-3: In-situ versus retrieved soil moisture at the 25m pixel scale. The dash lines denote the target accuracy of $\pm 0.06 \text{ m}^3/\text{m}^3$

and their comparisons with ground measurements are depicted in Figure 7-3. Generally, an overall correlation coefficient (R) of 0.77 and a RMSE of $0.07 \text{ m}^3/\text{m}^3$ was achieved for a wide range of mv ($0.04 - 0.42 \text{ m}^3/\text{m}^3$). Different from the forward model accuracy of co-polarizations (Figure 5-3), the proposed method achieved the best results over grassland, followed by the wheat and bare soil. This may result from the poor modeling of cross-polarization at bare soil and wheat as well as the relatively simple roughness features in grassland. Underestimation was observed for high mv conditions (larger than $0.42 \text{ m}^3/\text{m}^3$), which can be caused by i) the lower ϵ_s' upper bound of LUTs ($\sim 0.42 \text{ m}^3/\text{m}^3$) compared to the wettest condition of SMAPEX-5 period in the Yanco area and ii) the decreased sensitivity of the radar signal to mv at large values.

Despite the relatively poor results compared to the $0.05 \text{ m}^3/\text{m}^3$ requirement suggested by [Walker and Houser \(2004\)](#) and the target ($0.06 \text{ m}^3/\text{m}^3$) of SMAP radar products ([Kim et al., 2012b](#)), great spatial details of soil moisture were retained as depicted in Figure 7-4. The paddocks with cultivation activities occurring between the last two radar acquisitions were masked for the last retrieval because only one acquisition was

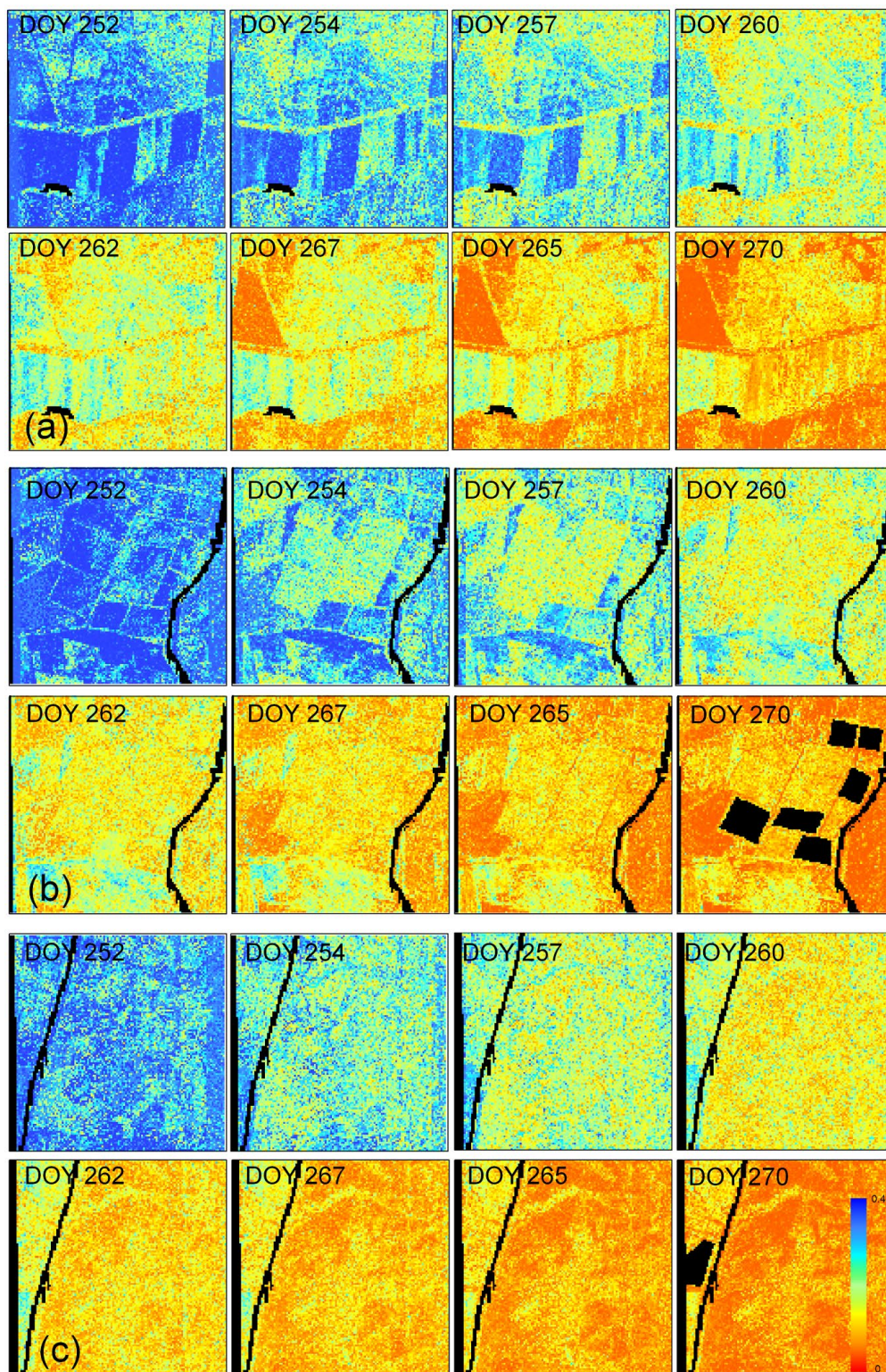


Figure 7-4: Time series soil moisture maps of focus farms YA4 (a), YA7 (b) and YE (c) during the eight observation dates of the SMAPEX-5 period.

available after cultivation activities. The dry-down process of the SMAPEX-5 period was accurately captured over all three focus farms with the RMSE of daily averaged m_v being 0.031, 0.017, and 0.020 m^3/m^3 for bare soil, grass and wheat, respectively. Different spatial patterns of m_v were also obtained with clear boundaries, showing relative wet patches for vegetated area, particularly for the wheat farms. Besides, m_v retrieval was also made for one canola and one lupine paddock in YA7 with acceptable results (RMSE: 0.072 m^3/m^3) using the wheat LUT, because they have a similar vertical dominant structure.

The proposed method was also compared with two other retrieval methods, i.e., LUT snapshot retrieval and multi-temporal retrieval without the dry down constraint. The snapshot method minimizes Eq. 7-1 using only one SAR acquisition (here, one HH, HV and VV measurement) and thus the retrieved roughness and VWC can be different in time. The results for m_v retrieval at the paddock scale using these three algorithms are shown in Figure 7-5 with the corresponding retrieved roughness and VWC shown in Figure 7-6. It is noted that the roughness ground truths for ploughed paddocks used in Figure 7-6 are those measured along the row direction, while the retrieved roughness were the equivalent ones. The roughness values retrieved by the snapshot algorithm were averaged over time for each paddock.

As expected, relatively poor results were achieved by the snapshot algorithm with a RMSE of 0.088-0.112 m^3/m^3 , 1.274 cm and 1.183 kg/m^2 for m_v , H_R and VWC retrieval, respectively, which is ascribed to the ambiguities among soil moisture, roughness and vegetation effect ([Satalino et al., 2002](#)) as well as the larger sensitivity of snapshot method to noise ([Kim et al., 2012a](#)). The impact of these uncertainties is clearly shown by the low correlation coefficients. The m_v , H_R and VWC retrieval were significantly improved using a time series retrieval even without the dry down constraint, showing a decrease of RMSE as much as 0.03 m^3/m^3 , 0.5 cm and 0.1 kg/m^2 for soil moisture, H_R , and VWC, respectively. These improvements mainly come from the insensitivity of the time series retrieval to system measurement noise ([Kim et al., 2012a](#)). Further improvement was made for the m_v retrieval to an acceptable level (RMSE < 0.06

m^3/m^3) by adding the dry down constraint, while only slight changes in H_R and VWC retrieval were found. A possible explanation is that the dry down constraint forced slight adjustments in the H_R and VWC to ensure the soil moisture trend at the expense of a somewhat larger value of the cost function to ensure the soil moisture trend at the expense of a somewhat larger value of the cost function (Eq. 7-1), and thus the effect of any anomaly fluctuations in time series σ^0 was removed.

The dry down constraint here provides *a priori* information, the use of which has been widely acknowledged to result in more reliable *mv* retrieval (Kornelsen and Coulibaly, 2013, Mattia et al., 2006b). The integration of *a priori mv* information or assumption in soil moisture retrieval is not new. For instance, the *mv* predicted by hydrological models (Mattia et al., 2006a, Mattia et al., 2009) and the assumption of time-invariant *mv* for dry or frozen conditions (Rahman et al., 2007, van der Velde et al., 2012). The merit of the dry down assumption is its generalization that can be guaranteed by a period between two rainfall events. A change detection algorithm proposed in Chapter 6 can help to separate the time series into multiple sub-series, according to the presence of rainfall events or small-scale irrigations. Notably, this constraint is difficult to apply for areas with frequent rainfall (e.g., tropics); such conditions are also a challenge for other multi-temporal algorithms because of the potential changes in roughness and vegetation after rainfall (Balenzano et al., 2011).

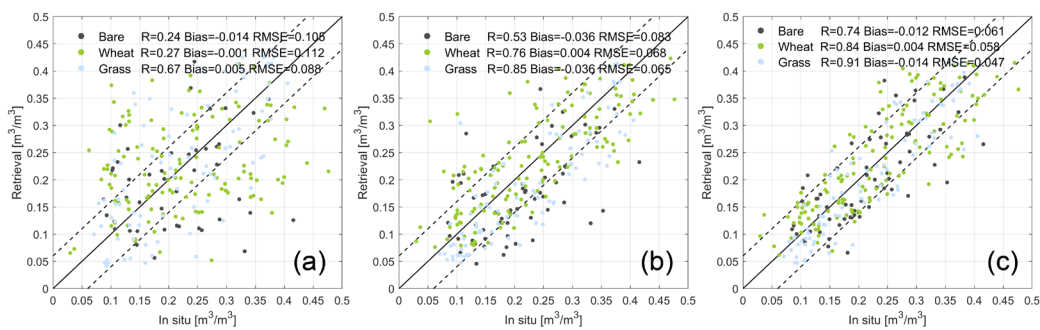


Figure 7-5: Comparison of retrieved and in situ soil moisture values for multiple algorithms at the paddock scale; (a) snapshot retrieval, (b) multi-temporal retrieval and (c) multi-temporal retrieval with the dry down constraint. The dash lines denote the target accuracy of $\pm 0.06 \text{ m}^3/\text{m}^3$.

A further investigation was conducted to show the performance of the proposed method on the paddocks with row directions nearly perpendicular to the radar look directions, consisting of two bare (#39 and #54) and three wheat paddocks (#80, #98 and #115). The RMSE and R of mv were $0.056 \text{ m}^3/\text{m}^3$ and 0.826 for the bare paddocks, which were $0.053 \text{ m}^3/\text{m}^3$ and 0.919 for wheat. No significant difference was found between the results of these paddocks and the other paddocks in terms of RMSE and R. This can be explained by the significantly large retrieved H_R and VWC (circled in Figure 7-1). Specifically, large H_R values can result in large σ^0 from the soil surface, while the attenuation by the vegetation layer with small VWC values can be negligible. As a result, the combination of large equivalent H_R values and small VWC can partly account for the strong backscattering caused by the row structure, resulting in a relatively accurate estimation of mv . Despite the satisfactory results observed in this study, there may be several other undesirable situations. For instance, relatively accurate VWC was retrieved at the expense of overestimated mv . Therefore, the mv retrieval for paddocks with their row direction perpendicular to the radar look directions still need to be further assessed using other data sets.

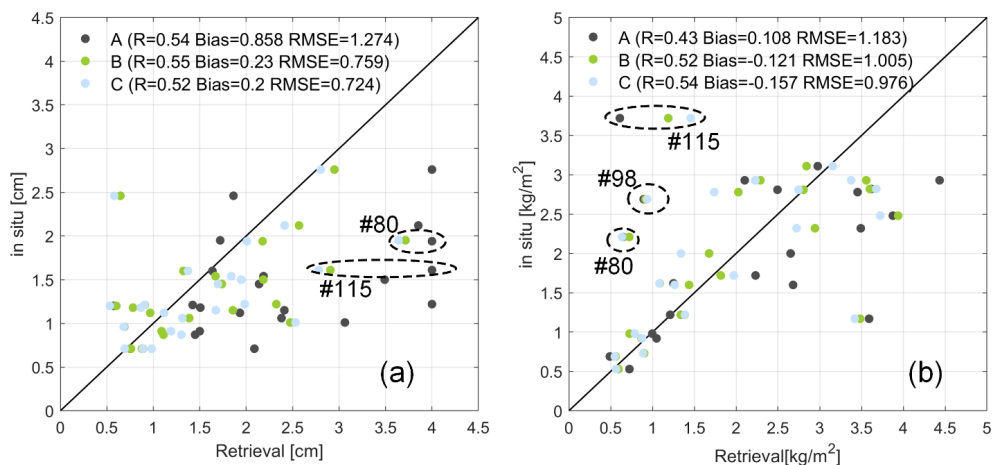


Figure 7-6: Comparison of in-situ and retrieved (a) soil surface root mean square height and (b) VWC. The cycled points belong to the paddocks ploughed nearly perpendicular to the radar look directions with their paddock ID as labeled. A, B and C denote results of snapshot retrieval, multi-temporal retrieval and multi-temporal retrieval with the dry down constraint.

7.4.2 The effect of time interval and polarization combination

The proposed method intends to retrieve soil moisture using any given L-band time series, with potentially different polarization combinations and irregularities in time interval. The performance of the proposed method with different polarization combinations was evaluated first. Soil moisture retrieval was made at the paddock scale with different polarization combinations, including HH+HV+VV, HH+VV, HH+HV, VH+VV, HH, VV, and HV. The results are presented using the Taylor diagram (Figure 7-7) which uses the standard deviation of the retrieval results, unbiased RMSE (ubRMSE) and correlation coefficient (R) between the retrievals and ground-truth data to summarize the performance of multiple algorithms in a single figure (Taylor, 2001).

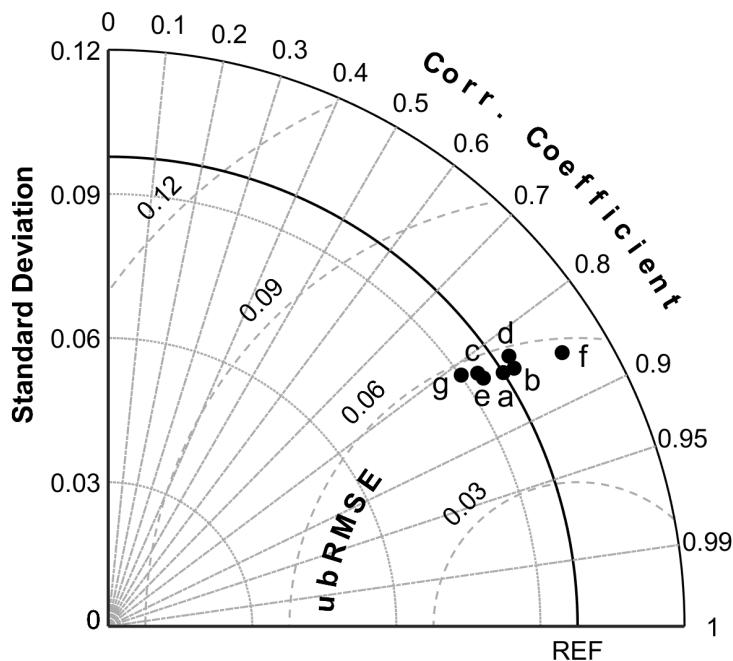


Figure 7-7: Effect of polarization combinations on soil moisture retrieval using eight multi-angular images at the paddock scale. a-f denote HH+HV+VV, HH+VV, HH+HV, VH+VV, HH, VV, and HV respectively. ubRMSE denotes the unbiased RMSE.

In general, all combinations achieved similar ubRMSE values with the largest difference ($0.003 \text{ m}^3/\text{m}^3$) observed between the HH+HV+VV (the a in Figure 7-7) and single HV (the g in Figure 7-7) series. Full polarized data performed slightly better than dual polarized series or single HH, HV and VV in term of ubRMSE and R, but the difference is hardly significant. A possible explanation is that more observations introduce more uncertainties and thus cannot improve the performance for an already well-determined inversion problem. For the single polarized series, VV achieved the best results (ubRMSE: $0.056 \text{ m}^3/\text{m}^3$; R:0.858), followed by HH (ubRMSE: $0.056 \text{ m}^3/\text{m}^3$; R:0.833) and HV (ubRMSE: $0.058 \text{ m}^3/\text{m}^3$; R:0.813). Similarly, insignificant differences between VV and HH were observed in other studies ([Lievens and Verhoest, 2012](#), [Kweon and Oh, 2014](#), [Ouellette et al., 2017](#), [Satalino et al., 2012](#)) with various multi-temporal algorithms, although the HH was suggested for the multi-temporal alpha approximation method at C-band ([Balenzano et al., 2011](#)).

The effect of time interval was also evaluated with the results presented using the Taylor diagram (Figure 7-8). The last PLIS acquisition of SMAPEX-5 acquired at DOY 270 was respectively combined with acquisitions collected in the previous seven flights to form seven SAR pairs with different time intervals ranging from 2 - 17 days. The m retrieval was then carried out at the paddock scale using these SAR pairs respectively. As expected, retrieval with short time intervals (G, E, and F in Figure 7-8) achieved relatively better results than those with long time intervals (A, B, C and D). However, the ubRMSE and R difference was less than $0.003 \text{ m}^3/\text{m}^3$ and 0.07, respectively and the performance was not strictly consistent with the time intervals. Since the abrupt changes were removed before m retrieval, this may suggest that the proposed method is insensitive to the gradual roughness and VWC changes in the SMAPEX-5 period. In particular, the proposed method can be directly used as a multi-angular algorithm for a period with a near-zero m change, e.g. the case of G (m difference is $0.007 \text{ m}^3/\text{m}^3$).

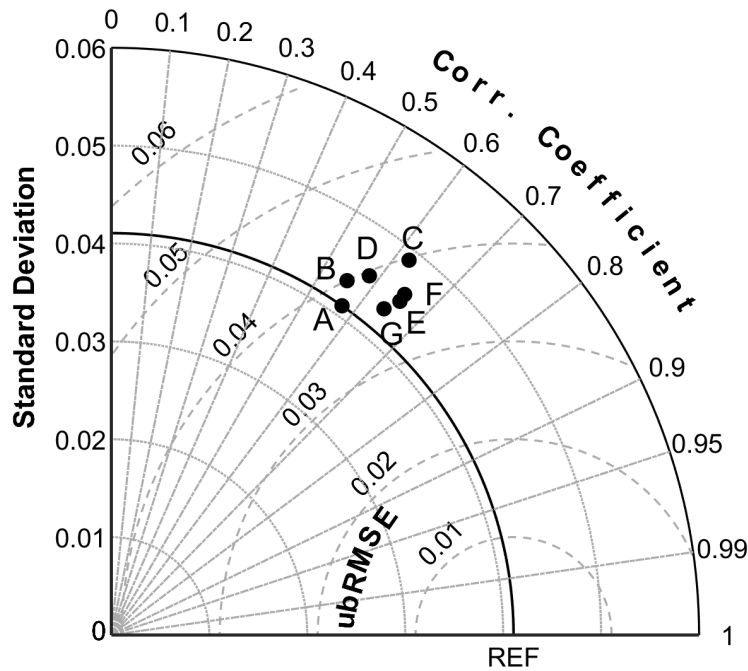


Figure 7-8: Effect of time interval on soil moisture retrieval using two multi-angular images at the paddock scale. A-G denote two images with a time interval of 17, 15, 12, 9, 7, 4 and 2 days with the corresponding average soil moisture difference being 0.218, 0.181, 0.136, 0.094, 0.052, 0.015 and 0.007 m^3/m^3 respectively.

7.5 Chapter Summary

A time series multi-angular method was proposed for mv retrieval from the joint time series of multiple L-band SAR missions with various observation modes. Similar to other multi-temporal retrieval algorithms, this method also follows the assumption of time-invariant roughness and vegetation with the main difference being: i) the capability to deal with multi-angular data acquired from both ascending and descending orbits without needing incidence angle normalization and ii) the use of a dry down constraint to further reduce noise. The performance of the proposed method has been comprehensively evaluated using the time series multi-angular L-band data collected during the SMAPEX-5, showing an mv RMSE (R) of 0.07 m^3/m^3 (0.77) at the 25-m pixel scale and 0.056 m^3/m^3 (0.83) at the paddock scale respectively. The investigation on the effect of time interval and polarization combinations has demonstrated the robustness of the proposed method using irregularly collected L-

band SAR data with inconsistent polarizations. The acceptable mv retrieval in ploughed paddocks confirmed the effectiveness of assuming effective isotropic roughness values. For paddocks with row directions perpendicular to radar look directions, the effective isotropic roughness was much larger than those measured along the row directions with the corresponding VWC typically underestimated.

8 Time series multi-frequency retrieval

This chapter presents a multi-frequency framework as an extension of the time series L-band multi-angular method for joint multi-SAR mission soil moisture retrieval developed in Chapter 7. The framework consists of the LUTs built in Chapter 5, the anomaly surface change detection method of Chapter 6 and a variant of the GA-based inversion method developed in Chapter 7, and an additional pre-processing step to remove the radar observations with insufficient soil surface backscattering contribution (calibration uncertainty equivalent signal) over densely vegetated areas and/or at higher frequency. While several main components have been introduced in previous chapters, the framework outlines how to combine time series data collected from multiple SAR missions. The framework is demonstrated using the SMAPEX-5 data presented in Chapter 3 and calibrated PLIS radar data presented in Chapter 4.

8.1 Background

As discussed in Chapter 2, the joint use of multiple SAR missions operating at different wavelengths provides a great opportunity for soil moisture mapping with a satisfactory temporal resolution. While several snapshot methods have been developed for soil moisture retrieval from multi-frequency data ([Bindlish and Barros, 2000](#), [Bindlish and Barros, 2001](#), [Pierdicca et al., 2008](#), [Zhang et al., 2018](#)), this approach is quite inconvenient for soil moisture retrieval from multiple SAR missions, because multiple snapshot algorithms are required to deal with the irregular observations acquired at different time instances.

In Chapter 7, a time series multi-angular method was proposed for joint soil moisture retrieval from multiple L-band SAR missions. This method has been extended to account for multi-frequency data in this chapter, with expansion to include C- and X-band data. To incorporate these shorter wavelengths (C- and X-band), the effectiveness of these bands in soil moisture retrieval over vegetated area needed to be

further addressed. A number of studies have reported the considerable sensitivity of C-band (~5.4 GHz; Sentinel-2, RADARSAT-2) to soil moisture over densely vegetated areas, especially for small incidence angles ([Romshoo et al., 2002](#), [Toure et al., 1994](#), [Brown et al., 2003](#), [Balenzano et al., 2011](#)). Despite the higher attenuation, X-band was also suggested to be effective for soil moisture retrieval over dense grass ([Aubert et al., 2011](#), [El Hajj et al., 2016](#)). In addition, HH commonly has a higher sensitivity than VV for vegetation layers dominated by vertical structures ([Ulaby et al., 2014](#), [Bindlish and Barros, 2001](#), [Balenzano et al., 2011](#)). These results provide important implications of selecting radar data in soil moisture retrieval but are still not straightforward for determining whether a backscattering measurement contains sufficient information of soil moisture.

Consequently, a method that could be easily implemented in an operational context was developed as a step of the proposed framework to determine the effectiveness of a given radar measurement in soil moisture retrieval. Moreover, a faster variant of the inversion method developed in Chapter 7 was proposed, with the capability to include temporal variation of other surface parameters. The proposed framework was evaluated using the time series multi-frequency data collected during the SMAPEX-5 campaign as presented in Chapter 3. The effect of frequency combinations on retrieval accuracy were also investigated to guide the use of the method.

8.2 Data set

The radar data used in Chapter 5 (Figure 8-1) was also used in this chapter, covering three frequency bands, L-, C- and X-band with varying incidence angle and polarizations over time. Radar data was available for 15 days of the three-week SMAPEX-5 campaign, confirming the desirable temporal resolution if multiple SAR missions can be combined. The available observations varied from day to day, with five and ten days having dual frequency (L+C or C+X) and single-frequency data respectively.

DOY	250	251	252	253	254	255	256	257	258	259	260	261	262	263	264	265	266	267	268	269	270
L-band			A		D			A			D		A			D		A			D
C-band			D		A	D		A				D		A							D
X-band		D		A							D		A								D

HH+VH+HV+VV
 VH+VV
 HH
 A: Ascending D: Descending

Figure 8-1: Summary of SAR data used in this chapter, showing acquisition date (day of year), frequency, polarization and orbit.

As in Chapter 7, soil moisture (m), VWC and soil roughness (H_R) were retrieved at the 25-m pixel scale and paddock scale, with the paddock boundaries as depicted in Figure 5-2. Ground measurements of three SMAPEX-5 focus farms (YA4, YA7 and YE) were used for comparison with the retrieved values.

8.3 Method

8.3.1 Overview of the framework

Figure 8-1 outlines the proposed framework. Inputs include the landcover of the research area and time series radar data from three platforms (but not limited to those platforms). The framework starts from the construction of forward LUTs, covering the commonly used configurations in radar remote sensing, and the range of soil roughness, soil moisture and vegetation water content (VWC). The time series data was first used to detect the potential roughness and VWC changes caused by cultivation activities and rainfall events. Time series with detected changes were then separated into multiple sub-series accordingly, ensuring the assumption of time-invariant roughness and vegetation. Soil moisture retrieval was then carried out independently on each sub-series. For the vegetated area, the relative backscatter contribution relating to that from the soil surface (C_s) was calculated using the forward models. Radar data with negligible (equivalent to the data calibration uncertainty) soil contribution was removed before soil moisture retrieval. Finally, soil moisture retrieval was carried out independently for each landcover type using an optimization method

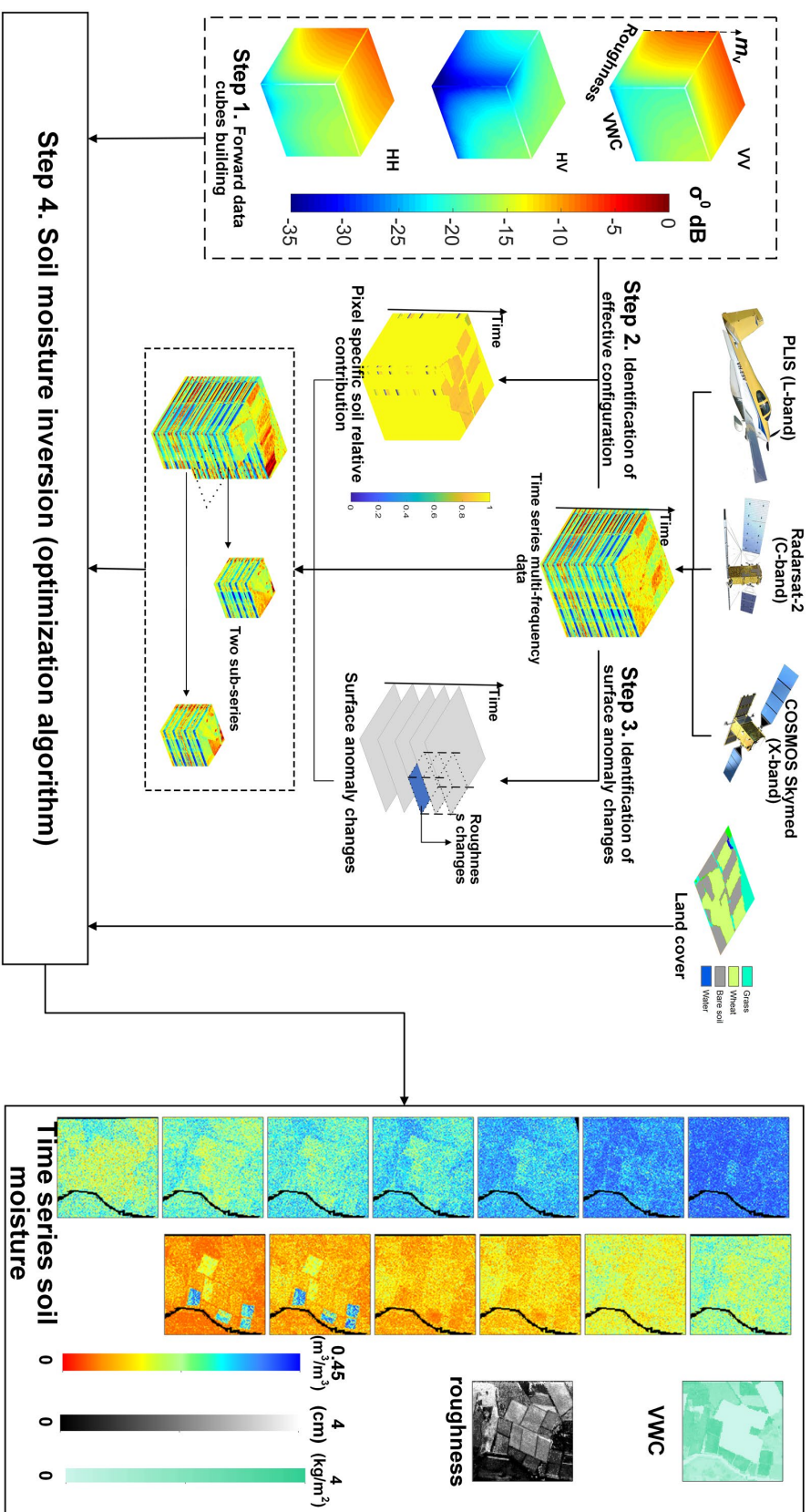


Figure 8-2: Conceptual framework of the proposed time series multi-frequency retrieval method. The inputs include time series L-, C- and X-band data acquired from both ascending and descending orbits, the landcover map, and the forward data cubes (multi-

and forward LUTs. The output includes time series soil moisture maps, one VWC map and roughness (H_R) map.

The LUTs were built in Chapter 5 (step 1 in Figure 8-2) for three land cover types (bare soil, grass and wheat) and the commonly used radar configurations in remote sensing. The step 2 and 3 in Figure 8-2 can be treated as pre-processing stages of soil moisture retrieval, which are designed to ensure the assumptions of the method and remove noisy data, respectively. The details of step 3 is provided in Chapter 6, with the step 2 and 4 being presented below.

8.3.2 Determination of effective radar configuration

As no straightforward method for determining the effective radar configuration could be found in literature, a model-based quantitative method was presented here. The basis of the method is that when the backscattered signal related to the soil surface falls below a certain level it is no longer making a detectable contribution to the total returned signal. Such a radar measurement may therefore only contribute noise in the soil moisture retrieval. In principle, the effectiveness of a radar measurement in linear units is determined by the volume (σ_v^0), double bounce (σ_{db}^0) and soil surface scattering (σ_s^0) over a vegetated area:

$$\frac{\sigma_s^0 + \sigma_{db}^0}{\sigma_v^0 + \sigma_s^0 + \sigma_{db}^0} \geq \partial \sigma_{all}^0(mv, E_{cal}), \quad \text{Eq. 8-1}$$

where the left and right sides are the relative contribution related to the soil (C_s) and the sensitivity of backscattering ($\partial \sigma_{all}^0$) to mv and calibration accuracy (E_{cal}), respectively. For a $0.02 \text{ m}^3/\text{m}^3$ change of soil moisture, the corresponding backscattering coefficient changes can be 0.15 to 1 dB depending on radar configurations and soil properties ([Altese et al., 1996](#)). The absolute radiometric calibration is commonly on the order of 1 dB ([Christensen et al., 1998](#), [Shimada et al., 2009](#), [Zhu et al., 2018](#)). Therefore, a sensitivity of 1 dB was considered as being appropriate, yielding a ratio of ~ 0.23 .

The volume, double bounce and soil surface scattering in Eq. 8-1 can be determined by Eq. 5-5 – Eq. 5-8 with the knowledge of VWC, H_R and soil moisture. This is, however, impractical for real applications as these geophysical parameters are those to be determined. Figure 8-3 shows, as an example, the C_s of wheat at C-band VV polarization generated by the forward model. As expected, VWC was the dominant parameter, while H_R and ϵ_s' were insensitive to C_s . Hence, given the radar frequency, incidence angle and polarization, an initial guess of VWC is probably to be sufficient for determining C_s . Accordingly, the VWC of each grid was estimated using the radar vegetation index (RVI; [Kim and Van Zyl, 2009](#)):

$$RVI = \frac{8\sigma_{HV}^0}{\sigma_{HH}^0 + \sigma_{VV}^0 + 2\sigma_{HV}^0}. \quad \text{Eq. 8-2}$$

RVI is a sensitive indicator of biomass and VWC, with several empirical relationships between VWC and RVI available in literature ([Huang et al., 2016](#), [Kim et al., 2012c](#), [Kim et al., 2014b](#)). To consider the vegetation condition in the whole retrieval period, all available full-polarized radar data were used to calculate the RVI and then the average VWC over time of each pixel estimated using the empirical relationships. The average relative soil contribution (C_s) of each input radar measurement (σ^0) was subsequently determined from the corresponding soil contribution LUTs. For instance, given a σ^0 (C-band VV polarization; $\theta = 30^\circ$) with an estimated VWC of 2 kg/m², the average C_s can be determined from the middle cube of Fig.2 by averaging the slice

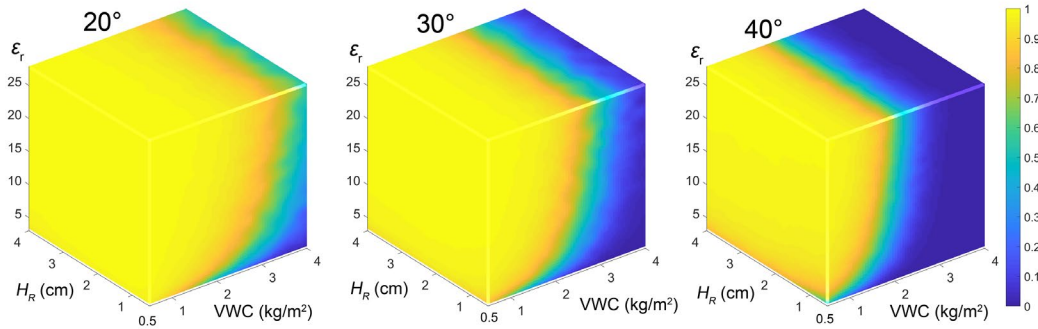


Figure 8-3: Relative contributions related to the soil surface (C_s) for wheat at C-band VV polarization with incidence angles from left to right being 20° , 30° and 40° .

corresponding to the VWC of 2 kg/m². Radar measurements with an average C_s less than 0.23 were removed before soil moisture retrieval. It is worth noting that the estimated VWC here is not used in the soil moisture retrieval. Compared with the sensitive analysis widely used in earlier studies ([Quesney et al., 2000](#), [Hégarat-Masclé et al., 2002](#), [Zribi et al., 2007](#), [Kim and Van Zyl, 2009](#)), the main advantage of the proposed method is its independence on study-specific analysis, with the main disadvantage being the uncertainty of forward model, e.g., the DBA's overestimation of attenuation as discussed above.

8.3.3 Multi-frequency retrieval method

The time series multi-angular retrieval algorithm proposed in Chapter 7 was extended for multi-frequency data. Radar data with the same acquisition date was treated as data collected simultaneously. Given a time series acquired at N dates with the i th date containing M_i multi-configured channels or σ^0 measurements, the soil moisture retrieval is a search process to minimize the cost function between simulated and observed σ^0 :

$$f = \frac{X(\varepsilon'_{s,1}, \varepsilon'_{s,2}, \dots, \varepsilon'_{s,N})}{N} \sum_{i=1}^N \sqrt{\frac{1}{M_i} \sum_{j=1}^{M_i} w_{ij} \cdot (\sigma_{ij}^0 - \sigma_{\text{LUT},ij}^0(H_R, \varepsilon'_{s,i}, \text{VWC}))^2}, \quad \text{Eq. 8-3}$$

where $\sigma_{\text{LUT},ij}^0(s, \varepsilon'_{s,i}, \text{VWC})$ and σ_{ij}^0 are backscattering coefficients from the LUT and observation in dB respectively, with the subscript i and j being the time index and the order of available channels on the i th date. The weight w_{ij} was set as a uniform value of 1 because of the difficulty to model the noise, the accuracy imbalance of the forward models and calibration accuracy at different channels. The assumption of a monotonic dry down in the time series, proposed in Chapter 7 as a constraint to partly remove the effect of random fluctuations over time, was also used here. However, this assumption is directly integrated into the cost function as:

$$X(\varepsilon'_{s,1}, \varepsilon'_{s,2}, \dots, \varepsilon'_{s,N}) = \sum_{i=1}^N |k_i - i| + 1 \quad \text{Eq. 8-4}$$

where k_i is the descending order of $\varepsilon_{s,i}'$ in the relative permittivity series. X has a minimum value of 1 for a non-increasing relative permittivity series, while the

maximum value is either $0.5(N^2+1)$ (N is odd) or $0.5N^2+1$ (N is even) for a strictly increasing series. A genetic algorithm similar to the one in Chapter 7 was used to find the optimal solution of Eq. 8-3, with N permittivity values, one time-invariant H_R and VWC value retrieved simultaneously. A dielectric model presented in [Dobson et al. \(1985a\)](#) converts the estimated dielectric constants into soil moisture.

Several assumptions were made for Eq. 8-3, including: 1) a uniform soil moisture profile for the soil layer above the penetration depth of L-band; 2) time-invariant physical roughness and vegetation; and 3) input data dependent effective roughness for the period of interest. With the first assumption, different radar configurations in remote sensing have the same perceived soil moisture although this may not be satisfied under dry conditions ([Ulaby et al., 1996](#)). The second assumption helps to eliminate the effect of natural roughness and vegetation evolution but does not account for the fact that effective roughness varies for different radar configurations. Accordingly, an effective H_R was assumed to represent the perceived roughness of the available radar configurations at each retrieval grid. Different effective roughness values were thus expected for single-, dual- and triple-frequency retrieval at the same location and are discussed below.

8.4 Results

8.4.1 Effective radar configuration

For a given σ^0 with the knowledge of frequency, incidence angle, and polarization, the relative soil contribution (C_s) of this measurement and its effectiveness in soil moisture retrieval can be determined using Eq. 8-1. The C_s for all available data is provided in Figure 8-2 (the cube named as pixel specific soil relative contribution). For the area without roughness or vegetation changes, the number of effective channels (σ^0 measurements) in soil moisture retrieval ranged from 57 – 63 out of 70 channels, with the C-band VV polarization being removed in most areas. An investigation of the C_s for wheat is provided in Figure 8-4 as an example. Not surprisingly, L-band had the largest C_s , followed by C- and X-band. Moreover, across all three frequency bands, it

was observed that 1) HH polarization had the largest C_s followed by HV and VV polarization; and 2) the C_s decreased as the incidence angle and VWC increased, with the largest decrease being observed at VV polarization. An interpretation for the different response among the three polarizations is the predominant vertical structure that exists in a wheat canopy.

More specifically, a C_s of ~ 1 was observed for L-band at HH and HV polarization with almost no dependence on VWC and incidence angle. This can be explained by the dominant surface scattering that at HH, and the dominant double-bounce in HV

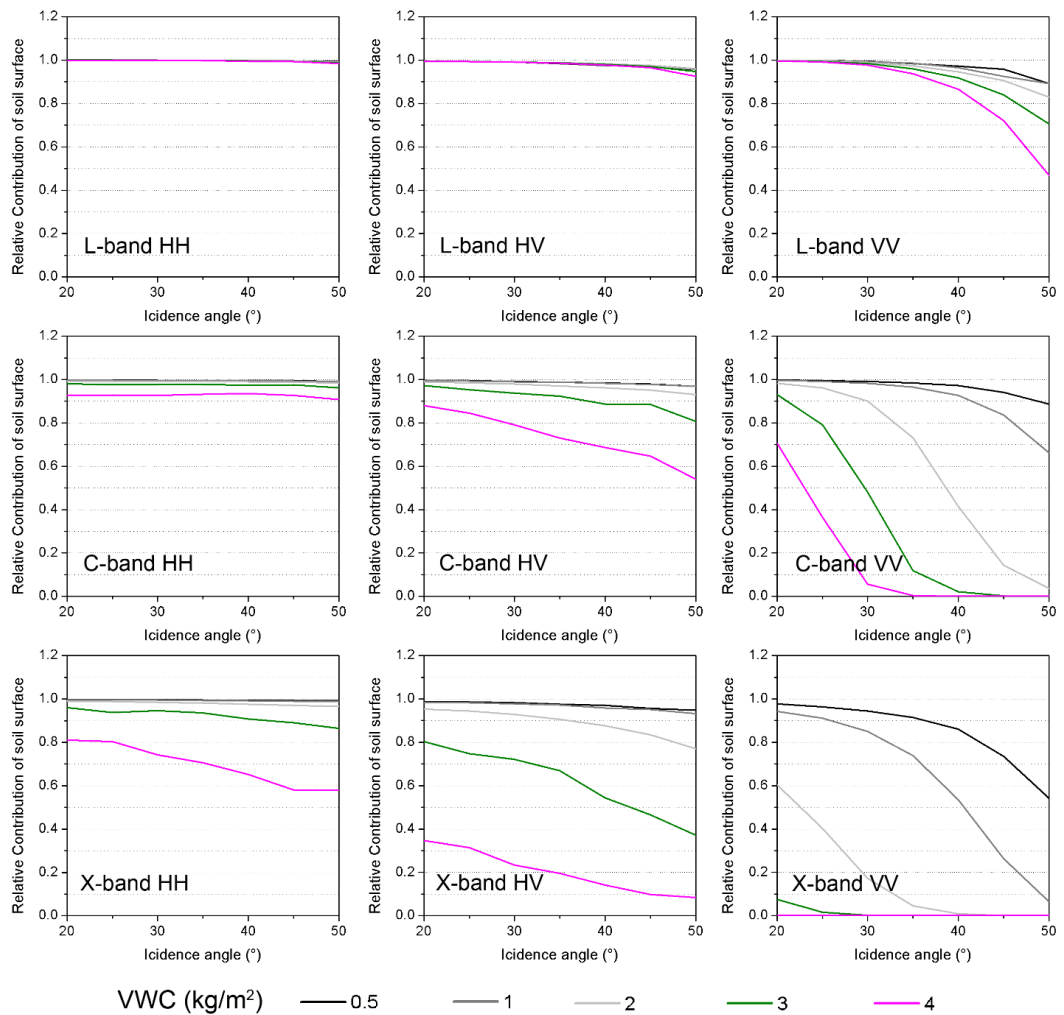


Figure 8-4: Simulated relative contribution of the soil surface from under a wheat canopy. The m_v and H_R were $0.15 \text{ m}^3/\text{m}^3$ and 2 cm.

with a negligible volume scattering in both polarizations. In contrast, the C_s for VV decreased to 0.5 - 0.9 as the VWC and incidence angle increased, because of the increased attenuation and volume scattering. The smallest C_s (~ 0.47) for VV was, however, still larger than the 1 dB sensitivity (0.23). This confirms the capability of L-band in soil moisture retrieval under dense wheat. C-band HH and HV polarization also showed great potential, given the considerable C_s in all cases (> 0.5). This was coincident with a number of other studies ([Romshoo et al., 2002](#), [Toure et al., 1994](#), [Brown et al., 2003](#), [Balenzano et al., 2011](#)). However, C-band at VV polarization should be used carefully for wheat-like crops, because the volume scattering gradually becomes dominant as the VWC and incidence angle is increased. For a layer with a VWC of 4 kg/m², the C_s of C-band at VV polarization was less than 0.23 for an incidence angle larger than 27°, being 33° and 43° for a VWC of 3 kg/m² and 2 kg/m², respectively. For X-band, HH and HV polarization could still provide sufficient information about the soil surface over wheat fields, in accordance with previous experimental studies ([Aubert et al., 2011](#), [El Hajj et al., 2016](#)). The figure also suggests a much lower validity range of VWC (< 2 kg/m²) for X-band at VV polarization.

8.4.2 Multi-frequency retrieval

Soil moisture retrieval was made at the 25-m pixel and paddock scales respectively, using all available radar data (20 acquisitions from 15 dates). The 25 m pixel soil moisture maps for the YA7 area are depicted in Figure 8-5 as an example, while the pixel and paddock scale comparison against corresponding ground measurements shown in Figure 8-6. The retrieved time series soil moisture maps agree well with the dry down process observed during SMAPEX-5, with a faster dry down observed over bare soil paddocks. The observed cultivation activities in the circled paddocks were detected between DOY 267 and 269, with the sudden soil moisture increases being successfully recorded.

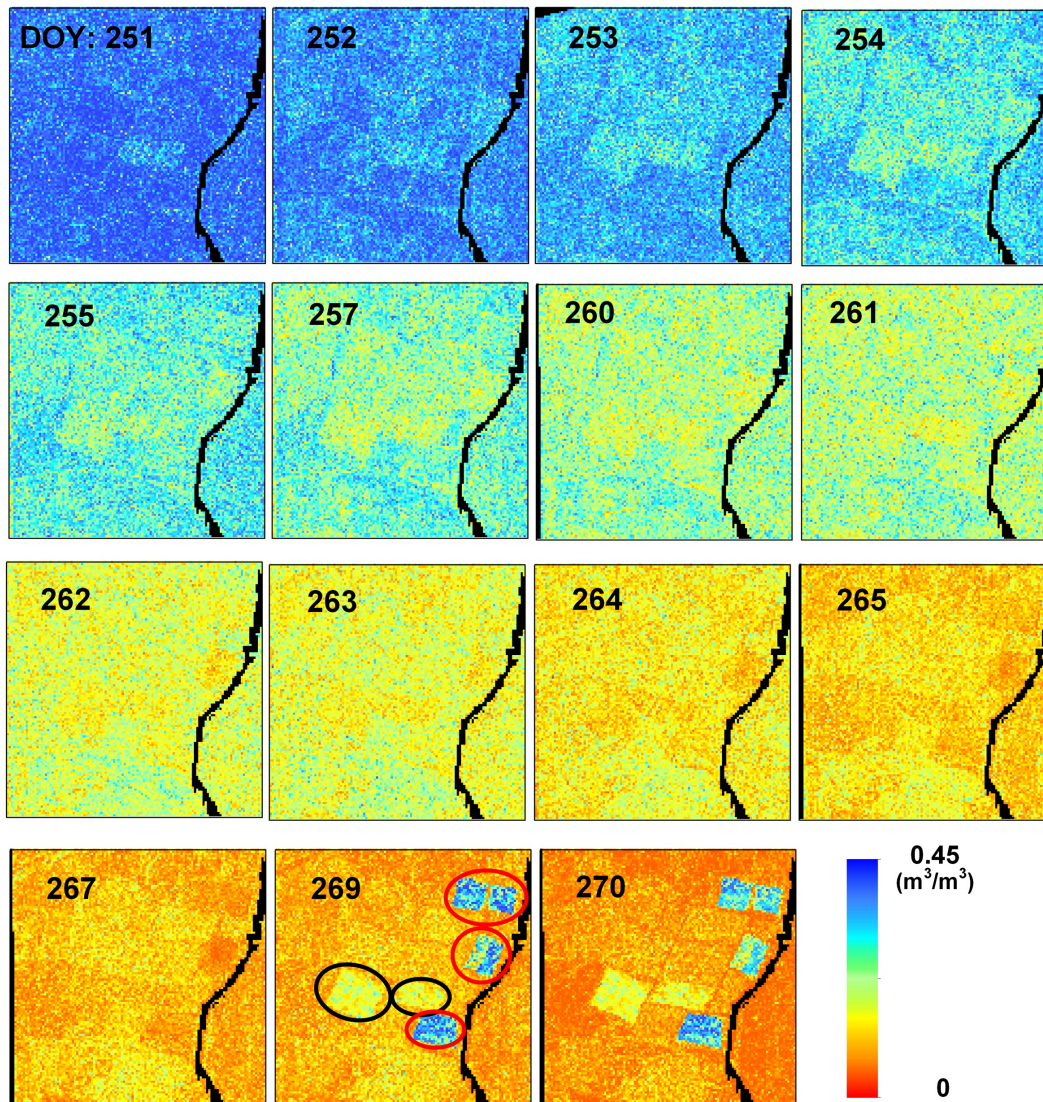


Figure 8-5: Retrieved soil moisture maps in YA7 with the day of year listed in top left. The paddocks in black circles are these with soil ploughing, while the red circles are those with irrigation.

Moderate accuracy was achieved at the pixel scale, showing an RMSE of $0.07 - 0.08 \text{ m}^3/\text{m}^3$ and a correlation coefficient (R) of $0.6 - 0.8$. No clear difference was found between the results of isotropic paddocks and of these with a periodic soil surface. The retrieved soil moisture for wet conditions (larger than $0.4 \text{ m}^3/\text{m}^3$) was slightly underestimated, which is consistent with the single L-band retrieval in Chapter 7. Such underestimations were also observed and ascribed to the decreased sensitivity of σ^0 in moist areas in other studies ([Bai et al., 2016](#), [Wang et al., 2011](#)). The other

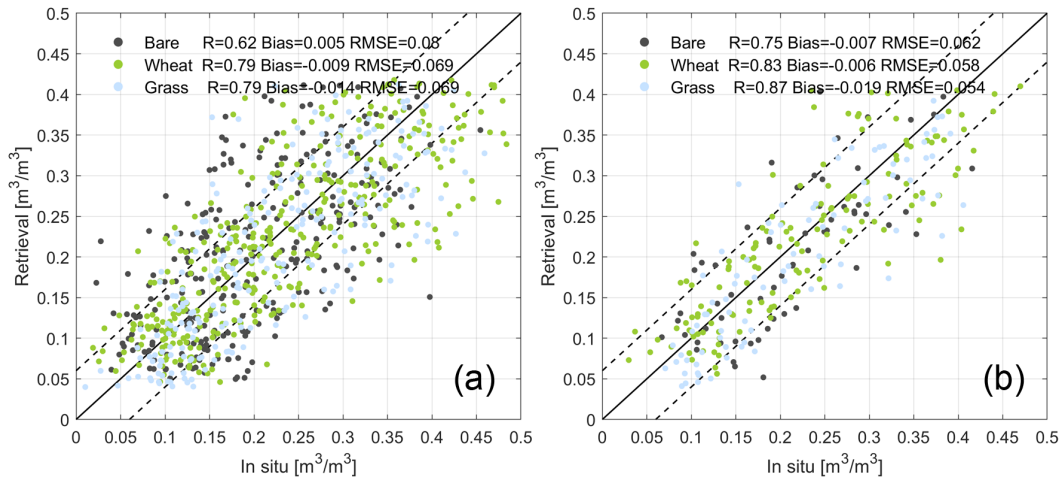


Figure 8-6: In situ versus retrieved soil moisture at the 25-m pixel (a) and paddock scale (b) using time series L-, C- and X-band data. The dash lines denote the $\pm 0.06 \text{ cm}^3/\text{cm}^3$

interpretation could be the relatively low upper bound of soil moisture in the LUTs ($\sim 0.43 \text{ m}^3/\text{m}^3$) compared to the ground measurements at first days of SMAPEX-5. As expected, the results were greatly improved at the paddock scale. The RMSE decreased to 0.062 , 0.058 and $0.054 \text{ m}^3/\text{m}^3$ in bare, wheat and grass, respectively, roughly reaching the $0.06 \text{ m}^3/\text{m}^3$ accuracy target of SMAP radar products. A good correlation ($R: 0.75 - 0.87$) was observed at the paddock scale with negligible biases ($< 0.02 \text{ m}^3/\text{m}^3$). However, the retrieved accuracy was still slightly worse than the requirement of $0.05 \text{ m}^3/\text{m}^3$ suggested by [Walker and Houser \(2004\)](#) and World Meteorological Organization (available at <http://www.wmosat.info/oscar/requirements>).

Soil moisture retrieval was also carried out at the paddock scale using all available single- and dual-frequency series, with the results summarized in Table 8-1. Not surprisingly, the use of single L-band series observations retrieved better results than single C- or X-band, confirming the merit of using long wavelengths in soil moisture retrieval. The larger number of channels (polarizations) at L-band could be another reason for its better performance. Moreover, the time offset between ground measurements and the C- and X-band acquisitions could have introduced a bias of less than $0.02 \text{ m}^3/\text{m}^3$, in the comparison according to station measurements ([Ye et al., In Review](#)). The inconsistency of the penetration depths at the three wavelengths ($0.5 -$

Table 8-1: Accuracy of soil moisture retrieval at the paddock scale. The bold styles denote the best case for each land cover.

	Bare soil			Grass			Wheat			#date/ #image
	RMSE	R	Bias	RMSE	R	Bias	RMSE	R	Bias	
L*	0.061	0.74	-0.012	0.047	0.91	-0.014	0.058	0.84	-0.004	8/8
C	0.061	0.71	0.012	0.052	0.87	0.002	0.071	0.69	-0.006	7/7
X	0.080	0.50	0.021	0.065	0.80	-0.019	0.084	0.58	-0.008	5/5
L+C	0.061	0.73	-0.004	0.050	0.89	-0.022	0.059	0.82	-0.003	11/15
L+X	0.062	0.73	-0.007	0.055	0.87	0.006	0.058	0.83	0.006	13/13
C+X	0.067	0.61	-0.009	0.056	0.87	-0.026	0.071	0.80	-0.014	11/12
L+C+X	0.062	0.75	-0.007	0.054	0.87	-0.019	0.058	0.83	0.006	15/20

*: Chapter 7

5 cm) and the single depth of ground measurements could have also resulted in evaluation uncertainty.

In contrast to expectations and earlier studies using multi-frequency data ([Oh, 2004](#), [Pierdicca et al., 2008](#), [Zhang et al., 2016](#)), the time series multi-frequency retrieval did not achieve the best results in this study. The L-band retrieved results were slightly deteriorated by combining the C-band series, and further deteriorated with the addition of the X-band series. Similarly, the joint use of C- and X-band series performed worse than using the C-band series alone, but better than using the X-band series alone. This could be partly explained by the relatively poor performance of using single C- and X-band series alone, which made a negative effect on the multi-frequency retrieval. Single L-band series retrieval in this study was a well-posed inversion problem, and so additional observations (e.g., the X-band series) may only introduce noise, while those additional observations in snapshot methods ([Pierdicca et al., 2008](#), [Zhang et al., 2016](#)) can help to turn the ill-posed L-band retrieval to a well-posed one, thus improving the retrieval accuracy. While slight deterioration in accuracy was observed to combine C- and X-band data, the revisit was greatly enhanced to be ~ 1.4 days during the SMAPEX-5, reaching the requirements of most applications ([Engman, 1992](#), [Walker and Houser, 2004](#)).

Table 8-2: Accuracy of rms height and VWC retrieval at the paddock scale. The bold styles denote the best case in RMSE. ubRMSE refers to unbiased RMSE.

	H_R (cm)				VWC (kg/m ²)			
	RMSE	R	Bias	ubRMSE	RMSE	R	Bias	ubRMSE
L*	0.397	0.577	-0.084	0.389	0.775	0.506	0.054	0.773
C	0.664	0.034	-0.509	0.426	1.008	0.603	0.449	0.802
X	1.080	0.002	-0.693	0.828	0.590	0.651	-0.063	0.587
L+C	0.469	0.361	-0.145	0.447	0.799	0.713	0.310	0.737
L+X	0.428	0.425	-0.122	0.411	0.610	0.695	-0.039	0.609
C+X	1.069	-0.041	-0.680	0.851	0.695	0.697	0.145	0.680
L+C+X	0.406	0.551	-0.121	0.356	0.646	0.708	0.191	0.617

*: Chapter 7

The soil H_R and VWC were also retrieved using the proposed method. The results for paddocks with an isotropic soil surface are listed in Table 8-2. for paddocks with in-situ measurements. Similar to the soil moisture retrieval, the L-band observations yield the best results for H_R in single frequency retrieval, followed by C-band and X-band. Negative biases were observed at all three frequencies, with the largest bias observed at X-band, indicating that smaller effective roughness values were retrieved at shorter wavelengths. An interpretation can be the dependence of effective roughness on wavelength. Similarly, larger effective H_R were observed for long wavelengths in earlier studies calibrating the IEM ([Lievens et al., 2011b](#), [Baghdadi et al., 2004](#)). Moreover, the cost function formation used in the retrieval may also slightly change the effective roughness, with larger H_R retrieved at L-band after removing the dry-down constraint (Chapter 7).

For single frequency retrieval of VWC, C- and L-band had similar accuracy in terms of ubRMSE, while X-band achieved the best results in all four metrics; this may be explained by its larger sensitivity to vegetation. The multi-frequency retrieval of both H_R and VWC seemed to follow the same law of soil moisture retrieval, i.e., an additional frequency with poor retrieval results did not have a positive effect on the multi-frequency retrieval, suggesting that the proposed multi-frequency retrieval may

not necessarily have the highest accuracy, especially when low frequency data are in abundance.

An investigation of H_R and VWC retrieval over paddocks with periodic soil surface features was also made, using the wheat paddocks with row directions nearly perpendicular or parallel to the radar look directions (Figure 8-7). For those paddocks with perpendicular row features (red lines in Figure 8-7), L-band had a significantly larger H_R and smaller VWC value than that retrieved from C- and X-band. This can be explained by the different effects of row structure on radar signals with different wavelengths. Specifically, the co-polarized σ^0 observed perpendicular to the row structure has been found to be much larger than those observed parallelly ([Blanchard and Chang, 1983](#), [Champion and Faivre, 1996](#), [Ulaby and Bare, 1979](#), [Zribi et al., 2002](#)). However, this effect has been found negligible for frequencies larger than 4 GHz ([Ulaby and Bare, 1979](#)). Consequently, for perpendicular rows, larger H_R and smaller VWC values were retrieved at longer wavelengths in order to have a larger soil surface scattering and a smaller vegetation attenuation. For paddocks with parallel row features

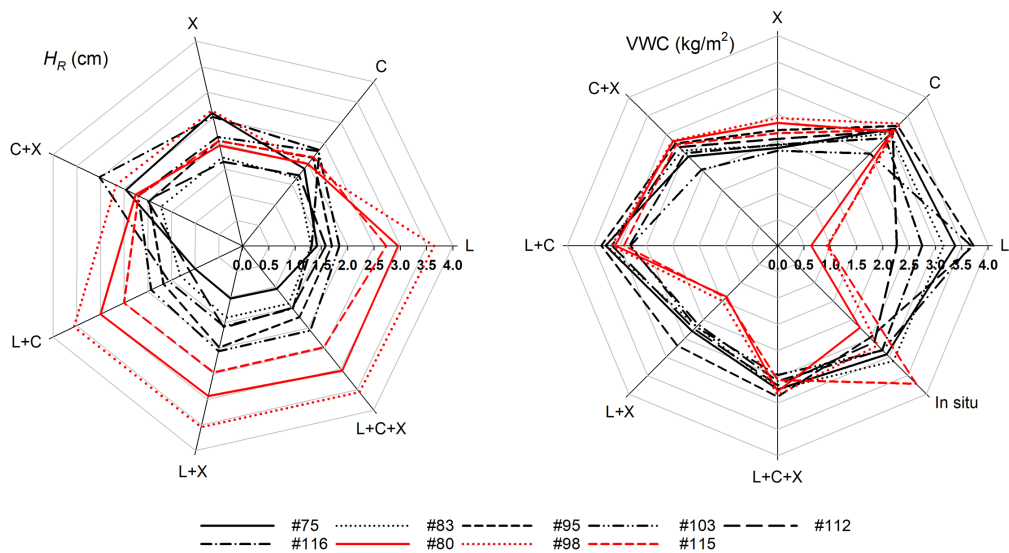


Figure 8-7: Retrieved H_R and VWC values for wheat paddocks with a periodical soil surface. The red and black lines are paddocks with a row direction perpendicular and parallel to the radar look direction, respectively.

(black lines in Figure 8-7), L-band tended to have similar H_R and VWC with C- and X-band, confirming the reduced effect of parallel row structures.

With respect to multi-frequency retrieval, the combinations of L+C, L+X, and L+C+X retrieved a similar H_R compared to that of the single L-band retrieval, especially for those with perpendicular row structures. The potential reason is that L-band is more sensitive to the row structure and thus was dominant in the cost function. Multi-frequency VWC retrieval seemed to have a value similar to the average of the values retrieved by single frequency series. For instance, the combination of L+X series had a VWC of 1.4 kg/m² in paddocks #80, #98 and #115, which was close to the average value from X-band (2.3 kg/m²) and L-band (0.84 kg/m²) retrievals on their own. This may suggest that multi-frequency retrievals may not necessarily have the best results but can be less sensitive to effect of complex surface conditions, e.g., the effect of periodic features at long wavelengths. Moreover, this also confirms the risk of retrieving VWC and H_R from one radar configuration (frequency, incidence angle and polarization) and subsequently soil moisture at another using the former derived VWC and H_R ([Lievens et al., 2011a](#)).

8.4.3 The effect of abrupt cultivation activities

The framework performance was presented in previous sections. Here, the effect of the change detection information produced by the first step on soil moisture retrieval was investigated, using a comparison with soil moisture retrieval without change detection information. The results of six selected paddocks with cultivation activities is shown in Figure 8-8. Other paddocks with cultivation activities were not included because of the similar results. For example, the proposed method had similar results over paddock #48 and #30 as depicted in the time series soil moisture maps (Figure 8-5) and thus only paddock #48 was included for discussion.

In general, the dry down process was successfully captured by both approaches (with/without change detection) with the main differences after the roughness changes or irrigation. The soil moisture retrieved with the change detection information

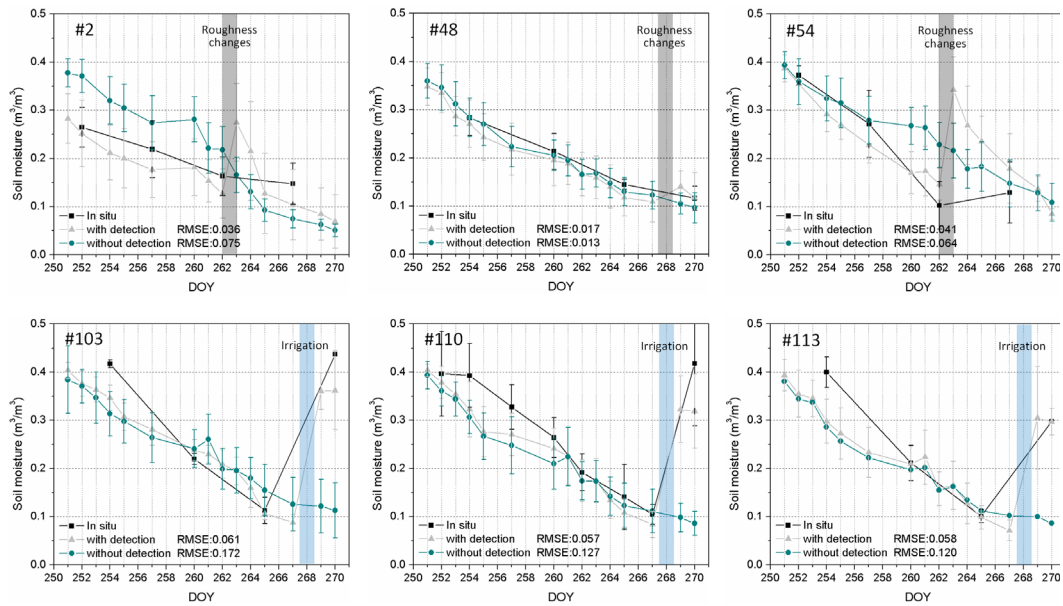


Figure 8-8: Time series average soil moisture of paddocks with/without integrating change detection results. The error bar denotes the standard deviation.

showed a sudden increase after both soil tillage and irrigation in all paddocks, which is consistent with the ground observations in paddocks #54, #103, #110 and #113. Since the shadow root zone commonly has higher soil moisture than the surface layer (< 5 cm), a slight increase of soil moisture after the soil practice was also expected for paddocks #2 and #48. This suggests that the proposed method can accurately reflect the soil moisture evolution in time despite the split of time series in the presence of cultivations activities. In view of RMSE, the integration of change detection information outperformed in five of six cases, especially for these with irrigation events. Different from other multi-temporal methods, an additional dry down constraint was used here. The preprocessing step of change detection potentially ensure both the dry down constraint and the assumption of time-invariant roughness and VWC is met

8.5 Chapter Summary

A multi-frequency soil moisture retrieval framework was presented as an integration of the forward modeling in Chapter 5, the change detection method proposed in Chapter 6, and the time-series multi-angular soil moisture retrieval method presented in Chapter 7 and an operational method to select effect radar input for vegetated area.

The development of multi-frequency retrieval starts from solving an ill-posed problem and takes all available data as equally weighted input, with the dilemma that more radar configurations means more unknown parameters being partially addressed through several assumptions (Section 8.3.3). Evaluation based on the SMAPE_{x-5} dataset consisting of L-band airborne data, C-band RADARSAT-2 data and X-band COSMO-SkyMed data confirmed the robustness of the proposed framework, showing an acceptable overall RMSE of 0.058 cm³/cm³ at the paddock scale (~0.1 – 0.5 km). The comparison with single and dual frequency retrieval suggested that multi-frequency retrieval does not necessarily provide the highest accuracy. However, it is valuable to jointly use multi-frequency data considering the limited deterioration in accuracy and the significantly enhanced temporal resolution for capturing the soil moisture variation over time.

9 Conclusions and Future Work

9.1 Conclusions

The application of radar remote sensing in soil moisture retrieval has recently entered a new era, with operational use now possible due to the increased number of existing and planned SAR missions in the next decade. While significant advances have been made in developing the algorithms for retrieving soil moisture using radar remote sensing in the past four decades, it is still challenging to derive reliable soil moisture at appropriate spatial and temporal resolutions from a single mission. Therefore, the main contribution of this research is to develop a multi-SAR-mission framework that can be applied to the joint use of current and forthcoming SAR missions to produce reliable soil moisture with high spatial (tens m) and temporal (2 – 3 days) resolution. This research consists of five parts with the conclusions described as follows:

9.1.1 Calibration and validation of PLIS

The stability, accuracy and image quality of PLIS data were comprehensively evaluated in Chapter 4 using two airborne campaigns (SMAPEX-4 and 5) as the basis of this study. The radiometric accuracy (RMSE) was found to be better than 0.65 dB over trihedrals, with satisfactory short-term stability (better than 0.2 dB) during the SMAPEX-4 and -5 experiments (a half-year period). Long-term stability was also confirmed with an average system-shift of around 1 dB since the first use of the PLIS system in 2010. The imbalance of different channels was 0.17 ± 0.15 dB and $3.87 \pm 2.86^\circ$ over PARCs. The residual HH and VV imbalance over trihedrals after calibration was 0.04 ± 0.05 dB and $0.86 \pm 1.49^\circ$. The residual crosstalk estimated from distributed targets was on the order of -30 dB.

PLIS / PALSAR-2 cross validation confirmed the calibration accuracy of the PLIS data over various land cover types and demonstrated the potential for cross-calibration of SAR systems. High correlation ($R > 0.8$) between PLIS and PALSAR-2

backscattering coefficients was observed for both ScanSAR and Stripmap images. However, the comparison of PLIS and PALSAR-2 ScanSAR showed larger RMSD and lower R than that of PLIS and PALSAR-2 Stripmap, which was ascribed to the change of surface conditions during the acquisitions of images and the uncertainty of the ScanSAR geometric accuracy. The latter was confirmed to be partly removed by selecting a large homogenous area. Moreover, the use of homogenous grass, wheat and forest grid cells were found to be insensitive to the azimuth difference between sensors, thus being optimal choices for cross-validation of multiple SAR systems.

9.1.2 Forward scattering models

A combination of scattering models was selected (NMM3D-DBA for L-band and Oh-DBA for C- and X-band) to cover the potential remote sensing radar configurations and natural surface conditions. Landcover specific multi-configuration LUTs were built for operational soil moisture retrieval. The performance of these LUTs was evaluated using ground measurements and airborne/spaceborne radar data, showing acceptable forward modeling over bare soil using the NMM3D (RMSE: ~ 2.3 dB) with a near-zero bias. Overestimations of 2 to 5.5 dB for C- and X-band were observed using the Oh model, with biases removed in the LUTs. The use of a single soil roughness parameter of H_R with a fixed L_C of $10H_R$ was confirmed to have acceptable forward accuracy at paddock scale. However, it was noted that careful attention should be paid to paddocks with perpendicular row directions to radar look directions, with the effective roughness potentially being out of the range of the LUTs.

The DBA achieved satisfactory forward predictions at most radar configurations but had great underestimation (~ 12 dB) at C-band VV polarization, as a result of the overestimation of attenuation in a vertical dominant vegetation layer. A single vegetation parameter of VWC together with vegetation type specific allometric relationships was confirmed to well represent the complex vegetation layer. After removing the biases, the LUTs showed acceptable modeling of the angular behavior and a forward ubRMSE of 1 – 3.2 dB, dependent on polarization, frequency and land cover type.

9.1.3 Surface anomaly change detection

An unsupervised change detection method was proposed to serve as a pre-processing procedure of multi-temporal retrieval, ensuring the assumption of time-invariant roughness and vegetation. Investigation based on the SMPAEx-5 ground measurements and L-band PLIS data showed that the abrupt roughness and vegetation changes caused by cultivation practices commonly occurred at the paddock scale, and thus object-based techniques were implemented to identify changed paddocks. The sensitivity of different polarizations to those changes differed as a result of the varying dominant scattering mechanisms. The temporal ratio of HV polarization, the temporal difference of HV/VV, and the temporal difference of VV polarization were selected as the optimal feature space, using a GA-based feature selection algorithm and an extensive synthetic data set. The J-M distance of the selected optimal feature space was larger than 1.27 at all three frequency bands, confirming that slight roughness and vegetation changes can be detected.

In the selected feature space, a two-step procedure was proposed to identify the changed paddocks, with the first step producing multiple over-detected change maps for the period of interest. The second step merges the multiple change maps to remove the false alarms with a principle similar to the ensemble machine learning. Evaluation on synthetic data sets demonstrated that the proposed approach can effectively eliminate the major part of error in multi-temporal soil moisture caused by roughness and VWC changes, although only a moderate AR (0.75 - 0.85) and FAR (0.08 - 0.15) was achieved for single look data. Experiments on real L- and C-band data also confirmed the effectiveness of the method showing an accurate identification of changed paddocks (> 0.9), while presenting a low false-alarm rate (< 0.1).

As a preprocessing step, the proposed method can work independently with the subsequent multi-temporal soil moisture. Time series data are separated into multiple subseries according to the detection results. For multi-temporal soil moisture retrieval methods without a calibration process, soil moisture retrieval can be carried out on each sub-series independently. However, for those requiring calibration or multi-

temporal vegetation correction, the proposed method could be used to provide an indication of areas where these methods are invalid.

9.1.4 Time series multi-angular retrieval

A time series multi-angular method was proposed for soil moisture retrieval from the joint time series of multiple L-band SAR missions with various observation modes. Apart from the assumption of time-invariant vegetation and roughness, the period of interest was assumed to have a dry down soil moisture, which was guaranteed by the change detection method proposed in Chapter 6. The performance of the proposed method has been comprehensively evaluated using the time series multi-angular L-band data collected during the SMAPEX-5, showing an *mv* RMSE (R) of 0.07 m³/m³ (0.77) at the 25-m pixel scale and 0.056 m³/m³ (0.83) at the paddock scale respectively. In comparison, the RMSE and R of the LUT snapshot retrieval at the paddock scale are 0.105 m³/m³ and 0.41 respectively, or 0.073 m³/m³ and 0.73 for multi-temporal retrieval without a dry down constraint, showing the effectiveness of including the dry down constraint. Acceptable soil moisture was also achieved over paddocks with periodic row structures, without significant difference compared with the isotropic ones in terms of RMSE and R.

An investigation on the effect of polarization combinations showed that full polarized data performed slightly better than dual polarized series or single HH, HV and VV in terms of ubRMSE and R. However, the difference can be hardly significant (< 0.003 m³/m³), showing the robustness of the proposed method even with single polarized data. Moreover, retrieval with short time intervals was demonstrated to achieve relatively better results than those with long time intervals. However, the observed ubRMSE and R difference was less than 0.003 m³/m³ and 0.07, denoting the negligible effect of gradual roughness and vegetation changes after removing the abrupt changes.

9.1.5 Time series multi-frequency retrieval

The time-series multi-angular method proposed in Chapter 7 was extended to cover L-, C- and X-band. An additional preprocessing step was integrated to determine the effectiveness of input radar data over vegetated areas. Simulation based on forward models confirmed the capability of L-band in soil moisture retrieval over dense wheat (VWC: 4 kg/m²). However, C- and X-band data should be used carefully over the same area, as the contribution of the underlying soil surface can be less than the general calibration uncertainty in several cases (e.g., C-band VV polarization for an incidence angle larger than 27°).

Evaluation based on the SMAPEX-5 dataset consisting of L-band airborne data, C-band RADARSAT-2 data and X-band COSMO-SkyMed data confirmed the robustness of the proposed framework, showing an acceptable overall RMSE of 0.058 cm³/cm³ at the paddock scale (~0.1 – 0.5 km). The effectiveness of the change detection was confirmed, showing a significant improvement (up to 0.1 m³/m³) for areas with cultivation activities. The comparison with single and dual frequency retrieval suggests that multi-frequency retrieval will not necessarily have the highest accuracy. However, it is still valuable to jointly use multi-frequency data considering the limited deterioration in accuracy and the significantly enhanced temporal resolution. Different effective roughness values were achieved for single-, dual- and triple-frequency retrieval, denoting that the share of roughness parameters among different radar configurations is questionable.

9.2 Future Work

Improvement and future work mainly include:

1. While the LUTs built in Chapter 5 showed satisfactory forward predictions, calibration was still required to remove the bias of the Oh model for C- and X-band. Moreover, the DBA needs several vegetation parameters, e.g. the radius and the distribution of elevation angle, which depend on

vegetation types and growth stages. As a result, the use of these LUTs in other areas needs to be further assessed. Limited by the ground measurements available in this thesis, in particular the allometric relationships, the LUTs developed here only cover two vegetation types, i.e. grass and wheat. Therefore, the development of LUTs for other vegetation types will be conducted in the future, with the possibility of auto-calibration investigated through machining learning techniques. The assumption of effective isotropic roughness for paddocks with periodical features and a fixed L_C/H_R of 10 should be further evaluated over a wider range of cultivation conditions. The use of multi-scale scattering models is currently being investigated as an extension of this PhD study, with the information of row orientation and row periods estimated from very high-resolution optical data.

2. To serve as a pre-processing procedure of operational soil moisture retrieval, the proposed change detection method should be further simplified. The future work could be a global paddock map extracted from available global land cover maps. The selected optimal feature space should be evaluated and enhanced for other landcover types. A parallel version of the proposed method can be integrated for large scale applications. A longer time series is required for a more comprehensive evaluation, e.g., those covering a whole crop season.
3. Future work should also focus on improving the generalization capability of the multi-angular and multi-frequency retrieval approaches. A more general assumption about the soil moisture tendency may be used for areas with frequent rainfalls, e.g., these from *in situ* stations or hydrological models. An increasing or decreasing VWC could be integrated for a retrieval period with significant VWC variations.

References

- AINSWORTH, T. L., FERRO-FAMIL, L. & LEE, J.-S. 2006. Orientation angle preserving a posteriori polarimetric SAR calibration. *IEEE Transactions on Geoscience and Remote Sensing*, 44, 994-1003.
- ALBERGEL, C., RÜDIGER, C., PELLARIN, T., CALVET, J.-C., FRITZ, N., FROISSARD, F., SUQUIA, D., PETITPA, A., PIGUET, B. & MARTIN, E. 2008. From near-surface to root-zone soil moisture using an exponential filter: an assessment of the method based on in-situ observations and model simulations. *Hydrology and Earth System Sciences*, 12, 1323-1337.
- ALTESE, E., BOLOGNANI, O., MANCINI, M. & TROCH, P. A. 1996. Retrieving soil moisture over bare soil from ERS 1 synthetic aperture radar data: Sensitivity analysis based on a theoretical surface scattering model and field data. *Water Resources Research*, 32, 653-661.
- ALVAREZ-GARRETON, C., RYU, D., WESTERN, A., CROW, W. & ROBERTSON, D. 2014. The impacts of assimilating satellite soil moisture into a rainfall-runoff model in a semi-arid catchment. *Journal of hydrology*, 519, 2763-2774.
- ÁLVAREZ-MOZOS, J., CASALÍ, J., GONZÁLEZ-AUDÍCANA, M. & VERHOEST, N. E. 2006. Assessment of the operational applicability of RADARSAT-1 data for surface soil moisture estimation. *IEEE Transactions on Geoscience and Remote Sensing*, 44, 913-924.
- ÁLVAREZ-MOZOS, J., GONZALEZ-AUDÍCANA, M. & CASALÍ, J. 2007. Evaluation of empirical and semi-empirical backscattering models for surface soil moisture estimation. *Canadian Journal of Remote Sensing*, 33, 176-188.
- ASKNE, J. I., SOJA, M. J. & ULANDER, L. M. 2017. Biomass estimation in a boreal forest from TanDEM-X data, lidar DTM, and the interferometric water cloud model. *Remote Sensing of Environment*, 196, 265-278.
- ATTEMA, E. & ULABY, F. T. 1978. Vegetation modeled as a water cloud. *Radio science*, 13, 357-364.
- AUBERT, M., BAGHDADI, N., ZRIBI, M., DOUAOUI, A., LOUMAGNE, C., BAUP, F., EL HAJJ, M. & GARRIGUES, S. 2011. Analysis of TerraSAR-X data sensitivity to bare soil moisture, roughness, composition and soil crust. *Remote Sensing of Environment*, 115, 1801-1810.
- BAATZ, M. 2000. Multiresolution segmentation: an optimization approach for high quality multi-scale image segmentation. *Angewandte geographische informationsverarbeitung*, 12-23.
- BAGHDADI, N., AUBERT, M., CERDAN, O., FRANCHISTÉGUY, L., VIEL, C., ERIC, M., ZRIBI, M. & DESPRATS, J. F. 2007. Operational mapping of soil moisture using synthetic aperture radar data: application to the Touch basin (France). *Sensors*, 7, 2458-2483.
- BAGHDADI, N., CERDAN, O., ZRIBI, M., AUZET, V., DARBOUX, F., EL HAJJ, M. & KHEIR, R. B. 2008. Operational performance of current synthetic aperture radar sensors in mapping soil surface characteristics in agricultural environments: application to hydrological and erosion modelling. *Hydrological Processes*, 22, 9-20.

- BAGHDADI, N., CHAAYA, J. A. & ZRIBI, M. 2011. Semiempirical calibration of the integral equation model for SAR data in C-band and cross polarization using radar images and field measurements. *IEEE Geoscience and Remote Sensing Letters*, 8, 14-18.
- BAGHDADI, N., DUBOIS-FERNANDEZ, P., DUPUIS, X. & ZRIBI, M. 2013. Sensitivity of main polarimetric parameters of multifrequency polarimetric SAR data to soil moisture and surface roughness over bare agricultural soils. *IEEE Geoscience and Remote Sensing Letters*, 10, 731-735.
- BAGHDADI, N., GAULTIER, S. & KING, C. 2002a. Retrieving surface roughness and soil moisture from synthetic aperture radar (SAR) data using neural networks. *Canadian Journal of Remote Sensing*, 28, 701-711.
- BAGHDADI, N., GHERBOUDJ, I., ZRIBI, M., SAHEBI, M., KING, C. & BONN, F. 2004. Semi-empirical calibration of the IEM backscattering model using radar images and moisture and roughness field measurements. *International Journal of Remote Sensing*, 25, 3593-3623.
- BAGHDADI, N., HOLAH, N. & ZRIBI, M. 2006a. Calibration of the Integral Equation Model for SAR data in C-band and HH and VV polarizations. *International Journal of Remote Sensing*, 27, 805-816.
- BAGHDADI, N., HOLAH, N. & ZRIBI, M. 2006b. Soil moisture estimation using multi-incidence and multi-polarization ASAR data. *International Journal of Remote Sensing*, 27, 1907-1920.
- BAGHDADI, N., KING, C., BOURGUIGNON, A. & REMOND, A. 2002b. Potential of ERS and RADARSAT data for surface roughness monitoring over bare agricultural fields: application to catchments in Northern France. *International journal of remote sensing*, 23, 3427-3442.
- BAGHDADI, N., KING, C., CHANZY, A. & WIGNERON, J. 2002c. An empirical calibration of the integral equation model based on SAR data, soil moisture and surface roughness measurement over bare soils. *International Journal of Remote Sensing*, 23, 4325-4340.
- BAGHDADI, N., PAILLOU, P., GRANDJEAN, G., DUBOIS, P. & DAVIDSON, M. 2000. Relationship between profile length and roughness variables for natural surfaces. *International Journal of Remote Sensing*, 21, 3375-3381.
- BAGHDADI, N. & ZRIBI, M. 2006. Evaluation of radar backscatter models IEM, OH and Dubois using experimental observations. *International Journal of Remote Sensing*, 27, 3831-3852.
- BAGHDADI, N. & ZRIBI, M. 2011. Evaluation of radar backscatter models IEM, OH and Dubois using experimental observations. *International Journal of Remote Sensing*, 27, 3831-3852.
- BAI, X., HE, B. & LI, X. 2016. Optimum surface roughness to parameterize advanced integral equation model for soil moisture retrieval in prairie area using Radarsat-2 data. *IEEE Transactions on Geoscience and Remote Sensing*, 54, 2437-2449.
- BAI, X., HE, B., XING, M. & LI, X. 2015. Method for soil moisture retrieval in arid prairie using TerraSAR-X data. *Journal of Applied Remote Sensing*, 9, 096062-096062.
- BALDWIN, D., MANFREDA, S., KELLER, K. & SMITHWICK, E. 2017. Predicting root zone soil moisture with soil properties and satellite near-surface moisture data across the conterminous United States. *Journal of Hydrology*, 546, 393-404.

References

- BALENZANO, A., MATTIA, F., SATALINO, G. & DAVIDSON, M. W. 2011. Dense temporal series of C-and L-band SAR data for soil moisture retrieval over agricultural crops. *IEEE Journal of Selected Topics in Applied Earth Observations and Remote Sensing*, 4, 439-450.
- BALENZANO, A., MATTIA, F., SATALINO, G., PAUWELS, V. & SNOEIJ, P. SMOSAR algorithm for soil moisture retrieval using Sentinel-1 data. *IEEE Geoscience and Remote Sensing Symposium (IGARSS)*, 2012, 2012. IEEE, 1200-1203.
- BALENZANO, A., SATALINO, G., LOVERGINE, F., RINALDI, M., IACOBELLIS, V., MASTRONARDI, N. & MATTIA, F. 2013. On the use of temporal series of L-and X-band SAR data for soil moisture retrieval. Capitanata plain case study. *European Journal of Remote Sensing*, 46, 721-737.
- BAYER, A., MAHBUB, I., CHAPPELL, M., RUTER, J. & VAN IERSEL, M. W. 2013. Water use and growth of Hibiscus acetosella 'Panama Red' grown with a soil moisture sensor-controlled irrigation system. *HortScience*, 48, 980-987.
- BAZI, Y., BRUZZONE, L. & MELGANI, F. 2005. An unsupervised approach based on the generalized Gaussian model to automatic change detection in multitemporal SAR images. *IEEE Transactions on Geoscience and Remote Sensing*, 43, 874-887.
- BAZZI, H., BAGHDADI, N., EL HAJJ, M. & ZRIBI, M. 2019. Potential of Sentinel-1 Surface Soil Moisture Product for Detecting Heavy Rainfall in the South of France. *Sensors*, 19, 802.
- BINDLISH, R. & BARROS, A. P. 2000. Multifrequency soil moisture inversion from SAR measurements with the use of IEM. *Remote Sensing of Environment*, 71, 67-88.
- BINDLISH, R. & BARROS, A. P. 2001. Parameterization of vegetation backscatter in radar-based, soil moisture estimation. *Remote Sensing of Environment*, 76, 130-137.
- BLAES, X. & DEFOURNY, P. 2008. Characterizing bidimensional roughness of agricultural soil surfaces for SAR modeling. *IEEE Transactions on geoscience and remote sensing*, 46, 4050-4061.
- BLANCHARD, B. & CHANG, A. 1983. Estimation of soil moisture from Seasat SAR data. *Journal of the American Water Resources Association*, 19, 803-810.
- BOISVERT, J., GWYN, Q., CHANZY, A., MAJOR, D., BRISCO, B. & BROWN, R. 1997. Effect of surface soil moisture gradients on modelling radar backscattering from bare fields. *International Journal of Remote Sensing*, 18, 153-170.
- BOLTER, R., GELAUTZ, M. & LEBERL, F. 1996. SAR speckle simulation. *International archives of photogrammetry and remote sensing*, 31, 20-25.
- BOURGEAU-CHAVEZ, L., KASISCHKE, E., RIORDAN, K., BRUNZELL, S., NOLAN, M., HYER, E., SLAWSKI, J., MEDVECZ, M., WALTERS, T. & AMES, S. 2007. Remote monitoring of spatial and temporal surface soil moisture in fire disturbed boreal forest ecosystems with ERS SAR imagery. *International Journal of Remote Sensing*, 28, 2133-2162.
- BRACAGLIA, M., FERRAZZOLI, P. & GUERRIERO, L. 1995. A fully polarimetric multiple scattering model for crops. *Remote Sensing of Environment*, 54, 170-179.
- BRISCO, B., SCHMITT, A., MURNAGHAN, K., KAYA, S. & ROTH, A. 2013. SAR polarimetric change detection for flooded vegetation. *International Journal of Digital Earth*, 6, 103-114.

- BROCCA, L., MELONE, F., MORAMARCO, T., WAGNER, W., NAEIMI, V., BARTALIS, Z. & HASENAUER, S. 2010. Improving runoff prediction through the assimilation of the ASCAT soil moisture product. *Hydrology and Earth System Sciences*, 14, 1881-1893.
- BROCCA, L., MORAMARCO, T., MELONE, F., WAGNER, W., HASENAUER, S. & HAHN, S. 2012. Assimilation of surface-and root-zone ASCAT soil moisture products into rainfall-runoff modeling. *IEEE Transactions on Geoscience and Remote Sensing*, 50, 2542-2555.
- BROWN, S. C., QUEGAN, S., MORRISON, K., BENNETT, J. C. & COOKMARTIN, G. 2003. High-resolution measurements of scattering in wheat canopies-Implications for crop parameter retrieval. *IEEE Transactions on Geoscience and Remote Sensing*, 41, 1602-1610.
- BRUZZONE, L. & PRIETO, D. F. 2002. An adaptive semiparametric and context-based approach to unsupervised change detection in multitemporal remote-sensing images. *IEEE Transactions on image processing*, 11, 452-466.
- BRUZZONE, L., ROLI, F. & SERPICO, S. B. 1995. An extension of the Jeffreys-Matusita distance to multiclass cases for feature selection. *IEEE Transactions on Geoscience and Remote Sensing*, 33, 1318-1321.
- BRYANT, R., MORAN, M., THOMA, D., COLLINS, C., SKIRVIN, S., RAHMAN, M., SLOCUM, K., STARKS, P., BOSCH, D. & DUGO, M. G. 2007. Measuring surface roughness height to parameterize radar backscatter models for retrieval of surface soil moisture. *IEEE Geoscience and Remote Sensing Letters*, 4, 137-141.
- BURGIN, M., CLEWLEY, D., LUCAS, R. M. & MOGHADDAM, M. 2011. A generalized radar backscattering model based on wave theory for multilayer multispecies vegetation. *IEEE Transactions on Geoscience and Remote Sensing*, 49, 4832-4845.
- CÁCERES, M. D., VILALTA, J. M., COLL, L., LLORENS, P., CASALS, P., POYATOS, R., PAUSAS, J. G. & BROTONS, L. 2015. Coupling a water balance model with forest inventory data to predict drought stress. *Agricultural and Forest Meteorology*, 213, 77-90.
- CALLENS, M., VERHOEST, N. E. & DAVIDSON, M. W. 2006. Parameterization of tillage-induced single-scale soil roughness from 4-m profiles. *IEEE Transactions on Geoscience and Remote Sensing*, 44, 878-888.
- CALVET, J.-C. & NOILHAN, J. 2000. From near-surface to root-zone soil moisture using year-round data. *Journal of hydrometeorology*, 1, 393-411.
- CAMPBELL, G. S. & ANDERSON, R. Y. 1998. Evaluation of simple transmission line oscillators for soil moisture measurement. *Computers and Electronics in Agriculture*, 20, 31-44.
- CHAMBERLAIN, N., ZAWADZKI, M., SADOWY, G., OAKES, E., BROWN, K. & HODGES, R. The UAVSAR phased array aperture. Proc. IEEE Aerospace Conference, March 4-11 2006. IEEE, 13 pp.
- CHAMPION, I. & FAIVRE, R. 1996. The field row direction relative to the radar azimuth considered as an apparent surface roughness for smooth bare soils. *International Journal of Remote Sensing*, 17, 3305-3311.
- CHAUHAN, N. 2002. Soil moisture inversion at L-band using a dual-polarization technique: a model-based sensitivity analysis. *International Journal of Remote Sensing*, 23, 3209-3227.
- CHEN, K.-S., WU, T.-D., TSANG, L., LI, Q., SHI, J. & FUNG, A. K. 2003. Emission of rough surfaces calculated by the integral equation method with comparison to three-

References

- dimensional moment method simulations. *IEEE Transactions on Geoscience and Remote Sensing*, 41, 90-101.
- CHEN, K.-S., WU, T.-D., TSAY, M.-K. & FUNG, A. K. 2000. Note on the multiple scattering in an IEM model. *IEEE Transactions on Geoscience and Remote Sensing*, 38, 249-256.
- CHIFFLARD, P., KRANL, J., ZUR STRASSEN, G. & ZEPP, H. 2018. The significance of soil moisture in forecasting characteristics of flood events. A statistical analysis in two nested catchments. *Journal of Hydrology and Hydromechanics*, 66, 1-11.
- CHOKER, M., BAGHDADI, N., ZRIBI, M., EL HAJJ, M., PALOSCIA, S., VERHOEST, N. E., LIEVENS, H. & MATTIA, F. 2017. Evaluation of the Oh, Dubois and IEM backscatter models using a large dataset of SAR data and experimental soil measurements. *Water*, 9, 38.
- CHRISTENSEN, E. L., SKOU, N., DALL, J., WOELDERS, K. W., JORGENSEN, J. H., GRANHOLM, J. & MADSEN, S. N. 1998. EMISAR: An absolutely calibrated polarimetric L-and C-band SAR. *IEEE Transactions on Geoscience and Remote Sensing*, 36, 1852-1865.
- CLEVERLY, J., EAMUS, D., COUPE, N. R., CHEN, C., MAES, W., LI, L., FAUX, R., SANTINI, N. S., RUMMAN, R. & YU, Q. 2016. Soil moisture controls on phenology and productivity in a semi-arid critical zone. *Science of the Total Environment*, 568, 1227-1237.
- CLOUDE, S. R. & POTTIER, E. 1996. A review of target decomposition theorems in radar polarimetry. *IEEE Transactions on Geoscience and Remote Sensing*, 34, 498-518.
- COVELLO, F., BATTAZZA, F., COLETTA, A., LOPINTO, E., FIORENTINO, C., PIETRANERA, L., VALENTINI, G. & ZOFFOLI, S. 2010. COSMO-SkyMed an existing opportunity for observing the Earth. *Journal of Geodynamics*, 49, 171-180.
- CRAEYE, C., SOBIESKI, P., ROBIN, E. & GUISSARD, A. 1997. Angular errors in trihedrals used for radar calibrations. *International Journal of Remote Sensing*, 18, 2683-2689.
- CUMMING, I. G. & WONG, F. H. 2005. *Digital Signal Processing of Synthetic Aperture Radar Data: Algorithms and Implementation*, Norwood, MA, Artech House.
- DAVIDSON, M. W., LE TOAN, T., MATTIA, F., SATALINO, G., MANNINEN, T. & BORGEAUD, M. 2000. On the characterization of agricultural soil roughness for radar remote sensing studies. *Geoscience and Remote Sensing, IEEE Transactions on*, 38, 630-640.
- DAVIDSON, M. W., MATTIA, F., SATALINO, G., VERHOEST, N. E., LE TOAN, T., BORGEAUD, M., LOUIS, J. & ATTEMA, E. 2003. Joint statistical properties of RMS height and correlation length derived from multisite 1-m roughness measurements. *IEEE Transactions on Geoscience and Remote Sensing*, 41, 1651-1658.
- DAVIS, J. & CHUDOBIK, W. 1975. In situ meter for measuring relative permittivity of soils. *Geol. Surv. Can. Pap*, 75, 75-79.
- DE ROO, R. D., DU, Y., ULABY, F. T. & DOBSON, M. C. 2001. A semi-empirical backscattering model at L-band and C-band for a soybean canopy with soil moisture inversion. *IEEE Transactions on Geoscience and Remote Sensing*, 39, 864-872.
- DE ZAN, F. & GUARNIERI, A. M. 2006. TOPSAR: Terrain observation by progressive scans. *IEEE Transactions on Geoscience and Remote Sensing*, 44, 2352-2360.
- DEMARGNE, J., WU, L., REGONDA, S. K., BROWN, J. D., LEE, H., HE, M., SEO, D.-J., HARTMAN, R., HERR, H. D. & FRESCH, M. 2014. The science of NOAA's

- operational hydrologic ensemble forecast service. *Bulletin of the American Meteorological Society*, 95, 79-98.
- DOBSON, M. C., PIERCE, L., SARABANDI, K., ULABY, F. T. & SHARIK, T. 1992. Preliminary analysis of ERS-1 SAR for forest ecosystem studies. *Geoscience and Remote Sensing, IEEE Transactions on*, 30, 203-211.
- DOBSON, M. C. & ULABY, F. T. 1986. Active microwave soil moisture research. *IEEE Transactions on Geoscience and Remote Sensing*, 23-36.
- DOBSON, M. C., ULABY, F. T., HALLIKAINEN, M. T. & EL-RAYES, M. 1985a. Microwave dielectric behavior of wet soil-Part II: Dielectric mixing models. *Geoscience and Remote Sensing, IEEE Transactions on*, 35-46.
- DOBSON, M. C., ULABY, F. T., HALLIKAINEN, M. T. & EL-RAYES, M. 1985b. Microwave dielectric behavior of wet soil-Part II: Dielectric mixing models. *IEEE Transactions on Geoscience and Remote Sensing*, 35-46.
- DUBOIS, P. C., EVANS, D. & ZYL, J. V. 1992. Approach to derivation of SIR-C science requirements for calibration. *IEEE Transactions on Geoscience and Remote Sensing*, 30, 1145-1149.
- DUBOIS, P. C., VAN ZYL, J. & ENGMAN, T. 1995. Measuring soil moisture with imaging radars. *IEEE Transactions on Geoscience and Remote Sensing*, 33, 915-926.
- EL HAJJ, M., BAGHDADI, N., ZRIBI, M., BELAUD, G., CHEVIRON, B., COURAULT, D. & CHARRON, F. 2016. Soil moisture retrieval over irrigated grassland using X-band SAR data. *Remote Sensing of Environment*, 176, 202-218.
- ELFOUHAILY, T. M. & GUÉRIN, C.-A. 2004. A critical survey of approximate scattering wave theories from random rough surfaces. *Waves in Random Media*, 14, R1-R40.
- ELHASSAN, S., WU, X. & WALKER, J. P. Standing Water Detection Using Radar. 20th International Congress on Modelling and Simulation, 1-6 December 2013 2013 Adelaide, Australia.
- ENGMAN, E. T. 1991. Applications of microwave remote sensing of soil moisture for water resources and agriculture. *Remote Sensing of Environment*, 35, 213-226.
- ENGMAN, E. T. 1992. Soil moisture needs in earth sciences. *1992 IEEE International Geoscience and Remote Sensing Symposium (IGARSS)*, 1, 477 - 479.
- ENTEKHABI, D., NJOKU, E. G., O'NEILL, P. E., KELLOGG, K. H., CROW, W. T., EDELSTEIN, W. N., ENTIN, J. K., GOODMAN, S. D., JACKSON, T. J. & JOHNSON, J. 2010. The soil moisture active passive (SMAP) mission. *Proceedings of the IEEE*, 98, 704-716.
- ENTEKHABI, D., RODRIGUEZ-ITURBE, I. & CASTELLI, F. 1996. Mutual interaction of soil moisture state and atmospheric processes. *Journal of Hydrology*, 184, 3-17.
- ENTIN, J. K., ROBOCK, A., VINNIKOV, K. Y., HOLLINGER, S. E., LIU, S. & NAMKHAI, A. 2000. Temporal and spatial scales of observed soil moisture variations in the extratropics. *Journal of Geographical Research*, 105, 11865-11877.
- ESTER, M., KRIEGEL, H.-P., SANDER, J. & XU, X. A density-based algorithm for discovering clusters in large spatial databases with noise. Proceedings of Second International Conference on Knowledge Discovery and Data Mining, 1996 Portland. 226-231.
- FASCETTI, F., PIERDICCA, N. & PULVIRENTI, L. A multitemporal algorithm for SMAP data: Overview and preliminary results using experimental data. IEEE Geoscience and Remote Sensing Symposium (IGARSS), 2015, 2015. IEEE, 1292-1295.

References

- FORE, A. G., CHAPMAN, B. D., HAWKINS, B. P., HENSLEY, S., JONES, C. E., MICHEL, T. R. & MUELLERSCHOEN, R. J. 2015. UAVSAR polarimetric calibration. *IEEE Transactions on Geoscience and Remote Sensing*, 53, 3481-3491.
- FREEMAN, A. 1992. SAR calibration: an overview. *IEEE Transactions on Geoscience and Remote Sensing*, 30, 1107-1121.
- FREEMAN, A. & DURDEN, S. L. 1998a. A three-component scattering model for polarimetric SAR data. *Geoscience and Remote Sensing, IEEE Transactions on*, 36, 963-973.
- FREEMAN, A. & DURDEN, S. L. 1998b. A three-component scattering model for polarimetric SAR data. *IEEE Transactions on Geoscience and Remote Sensing*, 36, 963-973.
- FREEMAN, A., SHEN, Y. & WERNER, C. L. 1990. Polarimetric SAR calibration experiment using active radar calibrators. *IEEE Transactions on Geoscience and Remote Sensing*, 28, 224-240.
- FUNG, A. & CHEN, K. 1992. Dependence of the surface backscattering coefficients on roughness, frequency and polarization states. *International journal of remote sensing*, 13, 1663-1680.
- FUNG, A. K. 1994. *Microwave Scattering and Emission Models and Their Applications*, Artech House.
- FUNG, A. K. & CHEN, K. 2004. An update on the IEM surface backscattering model. *IEEE Geoscience and Remote Sensing Letters*, 1, 75-77.
- FUNG, A. K., LI, Z. & CHEN, K. 1992. Backscattering from a randomly rough dielectric surface. *IEEE Transactions on Geoscience and Remote Sensing* 30, 356-369.
- GAO, Y. 2016. *Joint active passive microwave soil moisture retrieval*. Ph. D. dissertation, Dept. Civil Eng., Monash Univ., Clayton, VIC, Australia, 2016.[Online]. Available: <http://users.monash.edu.au/~jpwalker/theses/YingGao.pdf>.
- GAO, Z., XU, X., WANG, J., YANG, H., HUANG, W. & FENG, H. 2013. A method of estimating soil moisture based on the linear decomposition of mixture pixels. *Mathematical and Computer Modelling*, 58, 606-613.
- GEN, M. & CHENG, R. 2000. *Genetic algorithms and engineering optimization*, John Wiley & Sons.
- GHERBOUDJ, I., MAGAGI, R., BERG, A. A. & TOTH, B. 2011. Soil moisture retrieval over agricultural fields from multi-polarized and multi-angular RADARSAT-2 SAR data. *Remote Sensing of Environment*, 115, 33-43.
- GIRALDEZ, A. E. SAOCOM-1 Argentina L-band SAR mission overview. Coastal and Marine Applications of SAR Symposium, 2003.
- GONG, M., ZHOU, Z. & MA, J. 2012. Change detection in synthetic aperture radar images based on image fusion and fuzzy clustering. *IEEE Transactions on Image Processing*, 21, 2141-2151.
- GORRAB, A., ZRIBI, M., BAGHDADI, N., MOUGENOT, B., FANISE, P. & CHABAANE, Z. 2015. Retrieval of both soil moisture and texture using TerraSAR-X images. *Remote Sensing*, 7, 10098-10116.
- GRAHAM, A. & HARRIS, R. 2003. Extracting biophysical parameters from remotely sensed radar data: a review of the water cloud model. *Progress in physical geography*, 27, 217-229.
- GRAY, A. L., VACHON, P. W., LIVINGSTONE, C. E. & LUKOWSKI, T. I. 1990. Synthetic aperture radar calibration using reference reflectors. *IEEE Transactions on Geoscience and Remote Sensing*, 28, 374-383.

- GUPTA, M., SHARMA, A. & KARTIKEYAN, B. 2016. Evaluation of RISAT-1 SAR Radiometric Calibration Using Extended Amazon Rainforest. *Journal of the Indian Society of Remote Sensing*, 1-13.
- GUTMAN, G. & IGNATOV, A. 1998. The derivation of the green vegetation fraction from NOAA/AVHRR data for use in numerical weather prediction models. *International Journal of remote sensing*, 19, 1533-1543.
- GUYON, I. & ELISSEEFF, A. 2003. An introduction to variable and feature selection. *Journal of machine learning research*, 3, 1157-1182.
- HAJNSEK, I., JAGDHUBER, T., SCHÖN, H. & PAPATHANASSIOU, K. P. 2009. Potential of estimating soil moisture under vegetation cover by means of PolSAR. *IEEE Transactions on Geoscience and Remote Sensing*, 47, 442-454.
- HALLIKAINEN, M. T., ULABY, F. T., DOBSON, M. C., EL-RAYES, M. & WU, L.-K. 1985. Microwave dielectric behavior of wet soil-part 1: empirical models and experimental observations. *IEEE Transactions on Geoscience and Remote Sensing*, 25-34.
- HASSAN-ESFAHANI, L., TORRES-RUA, A., TICLAVILCA, A. M., JENSEN, A. & MCKEE, M. Topsoil moisture estimation for precision agriculture using unmanned aerial vehicle multispectral imagery. 2014 IEEE International Geoscience and Remote Sensing Symposium (IGARSS), 2014. IEEE, 3263-3266.
- HE, L., PANCIERA, R., TANASE, M. A., WALKER, J. P. & QIN, Q. 2016. Soil Moisture Retrieval in Agricultural Fields Using Adaptive Model-Based Polarimetric Decomposition of SAR Data. *IEEE Transactions on Geoscience and Remote Sensing*, 54, 4445-4460.
- HÉGARAT-MASCLE, L., ZRIBI, M., ALEM, F., WEISSE, A. & LOUMAGNE, C. 2002. Soil moisture estimation from ERS/SAR data: Toward an operational methodology. *IEEE Transactions on Geoscience and Remote Sensing*, 40, 2647-2658.
- HIRSCHI, M., SENEVIRATNE, S. I., ALEXANDROV, V., BOBERG, F., BORONEANT, C., CHRISTENSEN, O. B., FORMAYER, H., ORLOWSKY, B. & STEPANEK, P. 2011. Observational evidence for soil-moisture impact on hot extremes in southeastern Europe. *Nature Geoscience*, 4, 17-21.
- HOEBEN, R. & TROCH, P. A. 2000. Assimilation of active microwave observation data for soil moisture profile estimation. *Water Resources Research*, 36, 2805-2819.
- HORNÁČEK, M., WAGNER, W., SABEL, D., TRUONG, H.-L., SNOEIJ, P., HAHMANN, T., DIEDRICH, E. & DOUBKOVÁ, M. 2012. Potential for high resolution systematic global surface soil moisture retrieval via change detection using Sentinel-1. *IEEE Journal of Selected Topics in Applied Earth Observations and Remote Sensing*, 5, 1303-1311.
- HOSHINO, B., KUDO, G., KANEKO, M., TANIUCHI, H., IINO, H. & YABUKI, T. Estimated soil moisture in vegetated area using multitemporal multipolarization data. IEEE Geoscience and Remote Sensing Symposium (IGARSS), 2012, 2012. IEEE, 654-657.
- HOSSEINI, M. & MCNAIRN, H. 2017. Using multi-polarization C-and L-band synthetic aperture radar to estimate biomass and soil moisture of wheat fields. *International Journal of Applied Earth Observation and Geoinformation*, 58, 50-64.
- HSIEH, C.-Y., FUNG, A. K., NESTI, G., SIEBER, A. J. & COPPO, P. 1997. A further study of the IEM surface scattering model. *IEEE Transactions on Geoscience and Remote Sensing*, 35, 901-909.

References

- HUAN-JUN, L., ZHANG, Y.-Z., ZHANG, X.-L., ZHANG, B., KAI-SHAN, S., ZONG-MING, W. & NA, T. 2009. Quantitative analysis of moisture effect on black soil reflectance. *Pedosphere*, 19, 532-540.
- HUANG, H., LIAO, T.-H., TSANG, L., NJOKU, E. G., COLLIANDER, A., JACKSON, T. J., BURGIN, M. S. & YUEH, S. 2017a. Modelling and Validation of Combined Active and Passive Microwave Remote Sensing of Agricultural Vegetation at L-Band. *Progress In Electromagnetics Research*, 78, 91-124.
- HUANG, H., TSANG, L., NJOKU, E. G. & COLLIANDER, A. A new vegetation model based on numerical 3D solutions of maxwell equations. 2017 IEEE International Geoscience and Remote Sensing Symposium (IGARSS), 2017b. IEEE, 2903-2906.
- HUANG, H., TSANG, L., NJOKU, E. G., COLLIANDER, A., LIAO, T.-H. & DING, K.-H. 2017c. Propagation and scattering by a layer of randomly distributed dielectric cylinders using monte carlo simulations of 3D Maxwell equations with applications in microwave interactions with vegetation. *IEEE Access*, 5, 11985-12003.
- HUANG, S. & TSANG, L. 2012. Electromagnetic scattering of randomly rough soil surfaces based on numerical solutions of Maxwell equations in three-dimensional simulations using a hybrid UV/PBTG/SMCG method. *IEEE Transactions on Geoscience and Remote Sensing*, 50, 4025-4035.
- HUANG, S., TSANG, L., NJOKU, E. G. & CHAN, K. S. 2010. Backscattering coefficients, coherent reflectivities, and emissivities of randomly rough soil surfaces at L-band for SMAP applications based on numerical solutions of Maxwell equations in three-dimensional simulations. *IEEE Transactions on Geoscience and Remote Sensing*, 48, 2557-2568.
- HUANG, Y., WALKER, J. P., GAO, Y., WU, X. & MONERRIS, A. 2016. Estimation of vegetation water content from the radar vegetation index at L-band. *IEEE Transactions on Geoscience and Remote Sensing*, 54, 981-989.
- HUNSAKER, D., CLEMMENS, A. & FANGMEIER, D. 1999. Cultural and irrigation management effects on infiltration, soil roughness, and advance in furrowed level basins. *Transactions of the ASAE*, 42, 1753-1762.
- HUNT, K. M. & TURNER, A. G. 2017. The effect of soil moisture perturbations on Indian monsoon depressions in a numerical weather prediction model. *Journal of Climate*, 30, 8811-8823.
- HUSSAIN, M., CHEN, D., CHENG, A., WEI, H. & STANLEY, D. 2013. Change detection from remotely sensed images: From pixel-based to object-based approaches. *ISPRS Journal of Photogrammetry and Remote Sensing*, 80, 91-106.
- IMHOFF, M. L. 1995. Radar backscatter and biomass saturation: ramifications for global biomass inventory. *IEEE Transactions on Geoscience and Remote Sensing*, 33, 511-518.
- INES, A. V., DAS, N. N., HANSEN, J. W. & NJOKU, E. G. 2013. Assimilation of remotely sensed soil moisture and vegetation with a crop simulation model for maize yield prediction. *Remote Sensing of Environment*, 138, 149-164.
- JACKSON, T., BRAS, R. & ENGLAND, A. Soil moisture research mission (EX-4). NASA Post-2002 Land Surface Hydrology Mission Workshop, April 12-14th 1999 Irvine, CA, NASA.
- JACKSON, T. & LE VINE, D. E. 1996. Mapping surface soil moisture using an aircraft-based passive microwave instrument: Algorithm and example. *Journal of Hydrology*, 184, 85-99.

- JACKSON, T., MCNAIRN, H., WELTZ, M., BRISCO, B. & BROWN, R. 1997. First order surface roughness correction of active microwave observations for estimating soil moisture. *IEEE Transactions on Geoscience and Remote Sensing*, 35, 1065-1069.
- JAGDHUBER, T., HAJNSEK, I., BRONSTERT, A. & PAPATHANASSIOU, K. P. 2013. Soil moisture estimation under low vegetation cover using a multi-angular polarimetric decomposition. *IEEE Transactions on Geoscience and Remote Sensing*, 51, 2201-2215.
- JAGDHUBER, T., HAJNSEK, I. & PAPATHANASSIOU, K. P. 2015. An iterative generalized hybrid decomposition for soil moisture retrieval under vegetation cover using fully polarimetric SAR. *IEEE Journal of Selected Topics in Applied Earth Observations and Remote Sensing*, 8, 3911-3922.
- JAKOWATZ, C. V., WAHL, D. E., EICHEL, P. H., GHIGLIA, D. C. & THOMPSON, P. A. 2012. *Spotlight-Mode Synthetic Aperture Radar: A Signal Processing Approach: A Signal Processing Approach*, Springer Science & Business Media.
- JARUWATANADILOK, S., STILES, B. W. & FORE, A. G. 2014. Cross-Calibration Between QuikSCAT and Oceansat-2. *IEEE Transactions on Geoscience and Remote Sensing*, 52, 6197-6204.
- JOSEPH, A., VAN DER VELDE, R., O'NEILL, P., LANG, R. & GISH, T. 2010. Effects of corn on C-and L-band radar backscatter: A correction method for soil moisture retrieval. *Remote Sensing of Environment*, 114, 2417-2430.
- JOSEPH, A. T., VAN DER VELDE, R., O'NEILL, P. E., LANG, R. H. & GISH, T. 2008. Soil moisture retrieval during a corn growth cycle using L-band (1.6 GHz) radar observations. *IEEE Transactions on Geoscience and Remote Sensing*, 46, 2365-2374.
- KAHNY, D. & VAN ZYI, J. How Does Corner Reflector Construction Affect Polarimetric Sar-calibration? *IEEE Geoscience and Remote Sensing Symposium*, 1990. IGARSS'90.'Remote Sensing Science for the Nineties', 10th Annual International, 1990. 1093-1097.
- KANKAKU, Y., SAGISAKA, M. & SUZUKI, S. PALSAR-2 launch and early orbit status. 2014 *IEEE International Geoscience and Remote Sensing Symposium (IGARSS)*, 2014. IEEE, 3410-3412.
- KARAM, M., FUNG, A. K., LANG, R. H. & CHAUHAN, N. S. 1992. A microwave scattering model for layered vegetation. *IEEE Transactions on Geoscience and Remote Sensing*, 30, 767-784.
- KARTHIKEYAN, L., PAN, M., WANDERS, N., KUMAR, D. N. & WOOD, E. F. 2017a. Four decades of microwave satellite soil moisture observations: Part 1. A review of retrieval algorithms. *Advances in Water Resources*, 109, 106-120.
- KARTHIKEYAN, L., PAN, M., WANDERS, N., KUMAR, D. N. & WOOD, E. F. 2017b. Four decades of microwave satellite soil moisture observations: Part 2. Product validation and inter-satellite comparisons. *Advances in Water Resources*, 109, 236-252.
- KARVONEN, J., SIMILÄ, M. & MÄKYNEN, M. An iterative incidence angle normalization algorithm for sea ice sar images. *IEEE International Geoscience and Remote Sensing Symposium*, 2002. IGARSS'02. 2002 2002. IEEE, 1524-1527.
- KERR, Y. H. 2007. Soil moisture from space: Where are we? *Hydrogeology journal*, 15, 117-120.
- KERR, Y. H., WALDTEUFEL, P., WIGNERON, J.-P., MARTINUZZI, J., FONT, J. & BERGER, M. 2001. Soil moisture retrieval from space: The Soil Moisture and Ocean

References

- Salinity (SMOS) mission. *IEEE transactions on Geoscience and remote sensing*, 39, 1729-1735.
- KIM, S.-B., MOGHADDAM, M., TSANG, L., BURGIN, M., XU, X. & NJOKU, E. G. 2014a. Models of L-band radar backscattering coefficients over global terrain for soil moisture retrieval. *IEEE Transactions on Geoscience and Remote Sensing*, 52, 1381-1396.
- KIM, S.-B., TSANG, L., JOHNSON, J. T., HUANG, S., VAN ZYL, J. J. & NJOKU, E. G. 2012a. Soil moisture retrieval using time-series radar observations over bare surfaces. *IEEE Transactions on Geoscience and Remote Sensing*, 50, 1853-1863.
- KIM, S., ZYL, J., DUNBAR, S., NJOKU, E., JOHNSON, J. & MOGHADDAM, M. 2012b. Algorithm Theoretical Basis Document SMAP L2 & L3 Radar Soil Moisture (Active) Data Products. Pasadena, California: Jet Propulsion Laboratory.
- KIM, Y., JACKSON, T., BINDLISH, R., HONG, S., JUNG, G. & LEE, K. 2014b. Retrieval of wheat growth parameters with radar vegetation indices. *parameters*, 20, 23.
- KIM, Y., JACKSON, T., BINDLISH, R., LEE, H. & HONG, S. 2012c. Radar vegetation index for estimating the vegetation water content of rice and soybean. *IEEE Geoscience and Remote Sensing Letters*, 9, 564-568.
- KIM, Y. & VAN ZYL, J. J. 2009. A time-series approach to estimate soil moisture using polarimetric radar data. *IEEE Transactions on Geoscience and Remote Sensing*, 47, 2519-2527.
- KIZITO, F., CAMPBELL, C., CAMPBELL, G., COBOS, D., TEARE, B., CARTER, B. & HOPMANS, J. 2008. Frequency, electrical conductivity and temperature analysis of a low-cost capacitance soil moisture sensor. *Journal of Hydrology*, 352, 367-378.
- KONIK, M. & BRADTKE, K. 2016. Object-oriented approach to oil spill detection using ENVISAT ASAR images. *ISPRS Journal of Photogrammetry and Remote Sensing*, 118, 37-52.
- KORNELSEN, K. C. & COULIBALY, P. 2013. Advances in soil moisture retrieval from synthetic aperture radar and hydrological applications. *Journal of Hydrology*, 476, 460-489.
- KOSTER, R. D., DIRMEYER, P. A., GUO, Z., BONAN, G., CHAN, E., COX, P., GORDON, C., KANAE, S., KOWALCZYK, E. & LAWRENCE, D. 2004. Regions of strong coupling between soil moisture and precipitation. *Science*, 305, 1138-1140.
- KRAMER, P. J. 2017. Water and plant productivity or yield. *Handbook of agricultural productivity*. CRC Press.
- KRISHNAN, P., BLACK, T. A., GRANT, N. J., BARR, A. G., HOGG, E. T. H., JASSAL, R. S. & MORGENSTERN, K. 2006. Impact of changing soil moisture distribution on net ecosystem productivity of a boreal aspen forest during and following drought. *Agricultural and Forest Meteorology*, 139, 208-223.
- KUROSAKI, Y., SHINODA, M., MIKAMI, M. & NANDINTSETSEG, B. 2011. Effects of soil and land surface conditions in summer on dust outbreaks in the following spring in a Mongolian grassland. *SOLA*, 7, 69-72.
- KURUCU, Y., SANLI, F. B., ESETLILI, M., BOLCA, M. & GOKSEL, C. 2009. Contribution of SAR images to determination of surface moisture on the Menemen Plain, Turkey. *International Journal of Remote Sensing*, 30, 1805-1817.
- KURUM, M., LANG, R. H., O'NEILL, P. E., JOSEPH, A. T., JACKSON, T. J. & COSH, M. H. 2009. L-band radar estimation of forest attenuation for active/passive soil moisture inversion. *IEEE Transactions on Geoscience and Remote Sensing*, 47, 3026-3040.

- KWEON, S.-K. & OH, Y. 2014. Estimation of soil moisture and surface roughness from single-polarized radar data for bare soil surface and comparison with dual-and quad-polarization cases. *IEEE Transactions on Geoscience and Remote Sensing*, 52, 4056-4064.
- LANG, R. H. & SIGHU, J. S. 1983. Electromagnetic backscattering from a layer of vegetation: A discrete approach. *IEEE Transactions on Geoscience and Remote Sensing*, 62-71.
- LE TOAN, T., QUEGAN, S., DAVIDSON, M., BALZTER, H., PAILLOU, P., PAPATHANASSIOU, K., PLUMMER, S., ROCCA, F., SAATCHI, S. & SHUGART, H. 2011. The BIOMASS mission: Mapping global forest biomass to better understand the terrestrial carbon cycle. *Remote sensing of environment*, 115, 2850-2860.
- LENG, P., SONG, X., DUAN, S.-B. & LI, Z.-L. 2016. A practical algorithm for estimating surface soil moisture using combined optical and thermal infrared data. *International Journal of Applied Earth Observation and Geoinformation*, 52, 338-348.
- LI, J. & WANG, S. 2018. Using SAR-Derived Vegetation Descriptors in a Water Cloud Model to Improve Soil Moisture Retrieval. *Remote Sensing*, 10, 1370.
- LIAO, T.-H., KIM, S.-B., TAN, S., TSANG, L., SU, C. & JACKSON, T. J. 2016a. Multiple scattering effects with cyclical correction in active remote sensing of vegetated surface using vector radiative transfer theory. *IEEE Journal of Selected Topics in Applied Earth Observations and Remote Sensing*, 9, 1414-1429.
- LIAO, T.-H., TSANG, L., HUANG, S., NIAMSUWAN, N., JARUWATANADILOK, S., KIM, S.-B., REN, H. & CHEN, K.-L. 2016b. Copolarized and cross-polarized backscattering from random rough soil surfaces from L-Band to Ku-Band using numerical solutions of Maxwell's equations with near-field precondition. *IEEE Transactions on Geoscience and Remote Sensing*, 54, 651-662.
- LIEVENS, H., VERHOEST, N., DE KEYSER, E., VERNIEUWE, H., MATGEN, P., ÁLVAREZ-MOZOS, J. & DE BAETS, B. 2011a. Effective roughness modelling as a tool for soil moisture retrieval from C-and L-band SAR. *Hydrology and Earth System Sciences Discussions*, 7, 4995-5031.
- LIEVENS, H. & VERHOEST, N. E. 2011. On the retrieval of soil moisture in wheat fields from L-band SAR based on Water Cloud modeling, the IEM, and effective roughness parameters. *IEEE Geoscience and Remote Sensing Letters*, 8, 740-744.
- LIEVENS, H. & VERHOEST, N. E. 2012. Spatial and temporal soil moisture estimation from RADARSAT-2 imagery over Flevoland, The Netherlands. *Journal of Hydrology*, 456, 44-56.
- LIEVENS, H., VERHOEST, N. E., KEYSER, E. D., VERNIEUWE, H., MATGEN, P., ÁLVAREZ-MOZOS, J. & BAETS, B. D. 2011b. Effective roughness modelling as a tool for soil moisture retrieval from C-and L-band SAR. *Hydrology and Earth System Sciences*, 15, 151-162.
- LIN, H., CHEN, J., PEI, Z., ZHANG, S. & HU, X. 2009. Monitoring sugarcane growth using ENVISAT ASAR data. *IEEE Transactions on Geoscience and Remote Sensing*, 47, 2572-2580.
- MACELLONI, G., NESTI, G., PAMPALONI, P., SIGISMONDI, S., TARCHI, D. & LOLLI, S. 2000. Experimental validation of surface scattering and emission models. *IEEE Transactions on Geoscience and Remote Sensing*, 38, 459-469.

References

- MALTESE, A., BATES, P., CAPODICI, F., CANNAROZZO, M., CIRAIOLO, G. & LA LOGGIA, G. 2013a. Critical analysis of thermal inertia approaches for surface soil water content retrieval. *Hydrological sciences journal*, 58, 1144-1161.
- MALTESE, A., CAPODICI, F., CIRAIOLO, G. & LA LOGGIA, G. 2013b. Mapping soil water content under sparse vegetation and changeable sky conditions: Comparison of two thermal inertia approaches. *Journal of Applied Remote Sensing*, 7, 073548.
- MANCINI, M., HOEBEN, R. & TROCH, P. A. 1999. Multifrequency radar observations of bare surface soil moisture content: A laboratory experiment. *Water Resources Research*, 35, 1827-1838.
- MARIN, C., BOVOLO, F. & BRUZZONE, L. 2015. Building change detection in multitemporal very high resolution SAR images. *IEEE transactions on geoscience and remote sensing*, 53, 2664-2682.
- MASSARI, C., BROCCA, L., BARBETTA, S., PAPATHANASIOU, C., MIMIKOU, M. & MORAMARCO, T. 2014a. Using globally available soil moisture indicators for flood modelling in Mediterranean catchments. *Hydrology and Earth System Sciences*, 18, 839-853.
- MASSARI, C., BROCCA, L., MORAMARCO, T., TRAMBLAY, Y. & LESCOT, J.-F. D. 2014b. Potential of soil moisture observations in flood modelling: estimating initial conditions and correcting rainfall. *Advances in Water Resources*, 74, 44-53.
- MATSUSHIMA, D., ASANUMA, J. & KAIHOTSU, I. 2018. Thermal Inertia Approach Using a Heat Budget Model to Estimate the Spatial Distribution of Surface Soil Moisture over a Semiarid Grassland in Central Mongolia. *Journal of Hydrometeorology*, 19, 245-265.
- MATTIA, F., BALENZANO, A., SATALINO, G., LOVERGINE, F., LOEW, A., PENG, J., WEGMULLER, U., SANTORO, M., CARTUS, O. & DABROWSKA-ZIELINSKA, K. Sentinel-1 high resolution soil moisture. 2017 IEEE International Geoscience and Remote Sensing Symposium (IGARSS), 2017. IEEE, 5533-5536.
- MATTIA, F., BALENZANO, A., SATALINO, G. & PAUWELS, V. A SAR soil moisture retrieval algorithm inverting the temporal changes of radar backscatter. 10th European Conference on Synthetic Aperture Radar (EUSAR 2014), 2014. VDE, 1-4.
- MATTIA, F., DAVIDSON, M. W., LE TOAN, T., D'HAESE, C. M., VERHOEST, N. E., GATTI, A. M. & BORGEAUD, M. 2003. A comparison between soil roughness statistics used in surface scattering models derived from mechanical and laser profilers. *Geoscience and Remote Sensing, IEEE Transactions on*, 41, 1659-1671.
- MATTIA, F. & LE TOAN, T. 1999. Backscattering properties of multi-scale rough surfaces. *Journal of Electromagnetic Waves and Applications*, 13, 493-527.
- MATTIA, F., SATALINO, G., DENTE, L. & PASQUARIELLO, G. 2006a. Using a priori information to improve soil moisture retrieval from ENVISAT ASAR AP data in semiarid regions. *IEEE Transactions on Geoscience and Remote Sensing*, 44, 900-912.
- MATTIA, F., SATALINO, G., DENTE, L. & PASQUARIELLO, G. 2006b. Using a priori information to improve soil moisture retrieval from ENVISAT ASAR AP data in semiarid regions. *Geoscience and Remote Sensing, IEEE Transactions on*, 44, 900-912.
- MATTIA, F., SATALINO, G., PAUWELS, V. & LOEW, A. 2009. Soil moisture retrieval through a merging of multi-temporal L-band SAR data and hydrologic modelling. *Hydrology and Earth System Sciences*, 13, 343-356.

- MCDONALD, K. C., ZIMMERMANN, R. & KIMBALL, J. S. 2002. Diurnal and spatial variation of xylem dielectric constant in Norway spruce (*Picea abies* [L.] Karst.) as related to microclimate, xylem sap flow, and xylem chemistry. *IEEE transactions on geoscience and remote sensing*, 40, 2063-2082.
- MCNAIRN, H. & BRISCO, B. 2004. The application of C-band polarimetric SAR for agriculture: a review. *Canadian Journal of Remote Sensing*, 30, 525-542.
- MENGES, C., BARTOLO, R., BELL, D. & HILL, G. E. 2004. The effect of savanna fires on SAR backscatter in northern Australia. *International Journal of Remote Sensing*, 25, 4857-4871.
- MERLIN, O., WALKER, J., PANCIERA, R., YOUNG, R., KALMA, J. & KIM, E. 2007. Calibration of a Soil Moisture Sensor in Heterogeneous Terrain. In: OXLEY, L. & KULASIRI, D. (eds.) *2007 International Congress on Modelling and Simulation (MODSIM)*. Modelling and Simulation Society of Australia and New Zealand.
- MERZOUKI, A. & MCNAIRN, H. 2015. A Hybrid (Multi-Angle and Multi-Polarization) Approach to Soil Moisture Retrieval Using the Integral Equation Model: Preparing for the RADARSAT Constellation Mission. *Canadian Journal of Remote Sensing*, 00-00.
- MERZOUKI, A., MCNAIRN, H. & PACHECO, A. 2010. Evaluation of the Dubois, Oh, and IEM radar backscatter models over agricultural fields using C-band RADARSAT-2 SAR image data. *Canadian Journal of Remote Sensing*, 36, S274-S286.
- MERZOUKI, A., MCNAIRN, H. & PACHECO, A. 2011. Mapping soil moisture using RADARSAT-2 data and local autocorrelation statistics. *IEEE Journal of Selected Topics in Applied Earth Observations and Remote Sensing*, 4, 128-137.
- MINACAPILLI, M., AGNESE, C., BLANDA, F., CAMMALLERI, C., CIRAOLO, G., D'URSO, G., IOVINO, M., PUMO, D., PROVENZANO, G. & RALLO, G. 2009. Estimation of actual evapotranspiration of Mediterranean perennial crops by means of remote-sensing based surface energy balance models. *Hydrology and Earth System Sciences*, 13, 1061-1074.
- MIRONOV, V. L., KOSOLAPOVA, L. G. & FOMIN, S. V. 2009. Physically and mineralogically based spectroscopic dielectric model for moist soils. *IEEE Transactions on Geoscience and Remote Sensing*, 47, 2059-2070.
- MOEREMANS, B. & DAUTREBANDE, S. 2000. Soil moisture evaluation by means of multi-temporal ERS SAR PRI images and interferometric coherence. *Journal of Hydrology*, 234, 162-169.
- MOGHADDAM, M. & SAATCHI, S. 1995. Analysis of scattering mechanisms in SAR imagery over boreal forest: Results from BOREAS'93. *IEEE Transactions on Geoscience and Remote Sensing*, 33, 1290-1296.
- MONTZKA, C., BOGENA, H., ZREDA, M., MONERRIS, A., MORRISON, R., MUDDU, S. & VEREECKEN, H. 2017. Validation of spaceborne and modelled surface soil moisture products with cosmic-ray neutron probes. *Remote sensing*, 9, 103.
- MORAN, M. S., HYMER, D. C., QI, J. & SANO, E. E. 2000. Soil moisture evaluation using multi-temporal synthetic aperture radar (SAR) in semiarid rangeland. *Agricultural and Forest meteorology*, 105, 69-80.
- MORENA, L., JAMES, K. & BECK, J. 2004. An introduction to the RADARSAT-2 mission. *Canadian Journal of Remote Sensing*, 30, 221-234.
- NADLER, A. & LAPID, Y. 1996. An improved capacitance sensor for in situ monitoring of soil moisture. *Soil Research*, 34, 361-368.

References

- NAEIMI, V., SCIPAL, K., BARTALIS, Z., HASENAUER, S. & WAGNER, W. 2009. An improved soil moisture retrieval algorithm for ERS and METOP scatterometer observations. *IEEE Transactions on Geoscience and Remote Sensing*, 47, 1999-2013.
- NIED, M., HUNDECHA, Y. & MERZ, B. 2013. Flood-initiating catchment conditions: a spatio-temporal analysis of large-scale soil moisture patterns in the Elbe River basin. *Hydrology and Earth System Sciences*, 17, 1401-1414.
- NIETO, H., KUSTAS, W. P., TORRES-RÚA, A., ALFIERI, J. G., GAO, F., ANDERSON, M. C., WHITE, W. A., SONG, L., DEL MAR ALSINA, M. & PRUEGER, J. H. 2018. Evaluation of TSEB turbulent fluxes using different methods for the retrieval of soil and canopy component temperatures from UAV thermal and multispectral imagery. *Irrigation Science*, 1-18.
- NOTARNICOLA, C. 2014. A Bayesian Change Detection Approach for Retrieval of Soil Moisture Variations Under Different Roughness Conditions. *IEEE Geoscience and Remote Sensing Letters*, 11, 414-418.
- NOTARNICOLA, C., ANGIULLI, M. & POSA, F. 2008. Soil moisture retrieval from remotely sensed data: Neural network approach versus Bayesian method. *IEEE Transactions on Geoscience and Remote Sensing*, 46, 547-557.
- O'NEILL, P., CHAUHAN, N. & JACKSON, T. 1996. Use of active and passive microwave remote sensing for soil moisture estimation through corn. *International Journal of Remote Sensing*, 17, 1851-1865.
- OH, Y. 2004. Quantitative retrieval of soil moisture content and surface roughness from multipolarized radar observations of bare soil surfaces. *IEEE Transactions on Geoscience and Remote Sensing*, 42, 596-601.
- OH, Y., SARABANDI, K. & ULABY, F. T. 1992. An empirical model and an inversion technique for radar scattering from bare soil surfaces. *IEEE Transactions on Geoscience and Remote Sensing*, 30, 370-381.
- OH, Y., SARABANDI, K. & ULABY, F. T. An inversion algorithm for retrieving soil moisture and surface roughness from polarimetric radar observation. *IEEE Geoscience and Remote Sensing Symposium, 1994. IGARSS'94. Surface and Atmospheric Remote Sensing: Technologies, Data Analysis and Interpretation., International, 1994. IEEE, 1582-1584.*
- OH, Y., SARABANDI, K. & ULABY, F. T. 2002. Semi-empirical model of the ensemble-averaged differential Mueller matrix for microwave backscattering from bare soil surfaces. *IEEE Transactions on Geoscience and Remote Sensing*, 40, 1348-1355.
- OLSON, D. L. & DELEN, D. 2008. *Advanced data mining techniques*, Springer Science & Business Media.
- OUCHI, K. 2013. Recent trend and advance of synthetic aperture radar with selected topics. *Remote Sensing*, 5, 716-807.
- OUELLETTE, J. D., JOHNSON, J. T., BALENZANO, A., MATTIA, F., SATALINO, G., KIM, S.-B., DUNBAR, R. S., COLLIANDER, A., COSH, M. H. & CALDWELL, T. G. 2017. A time-series approach to estimating soil moisture from vegetated surfaces using L-band radar backscatter. *IEEE Transactions on Geoscience and Remote Sensing*, 55, 3186 - 3193.
- PALOSCIA, S., PAMPALONI, P., PETTINATO, S. & SANTI, E. 2008. A comparison of algorithms for retrieving soil moisture from ENVISAT/ASAR images. *IEEE Transactions on Geoscience and Remote Sensing*, 46, 3274-3284.

- PAN, M. & WOOD, E. F. 2010. Impact of accuracy, spatial availability, and revisit time of satellite-derived surface soil moisture in a multiscale ensemble data assimilation system. *IEEE Journal of Selected Topics in Applied Earth Observations and Remote Sensing*, 3, 49-56.
- PANCIERA, R., TANASE, M. A., LOWELL, K. & WALKER, J. P. 2014a. Evaluation of IEM, Dubois, and Oh radar backscatter models using airborne L-band SAR. *IEEE Transactions on Geoscience and Remote Sensing*, 52, 4966-4979.
- PANCIERA, R., WALKER, J. P., JACKSON, T. J., GRAY, D. A., TANASE, M. A., RYU, D., MONERRIS, A., YARDLEY, H., RUDIGER, C. & WU, X. 2014b. The soil moisture active passive experiments (SMAPEX): Toward soil moisture retrieval from the SMAP mission. *IEEE Transactions on Geoscience and Remote Sensing*, 52, 490-507.
- PANTZE, A., SANTORO, M. & FRANSSON, J. E. 2014. Change detection of boreal forest using bi-temporal ALOS PALSAR backscatter data. *Remote sensing of environment*, 155, 120-128.
- PARINUSSA, R. M., LAKSHMI, V., JOHNSON, F. M. & SHARMA, A. 2016. A new framework for monitoring flood inundation using readily available satellite data. *Geophysical Research Letters*.
- PATEL, N., ANAPASHSHA, R., KUMAR, S., SAHA, S. & DADHWAL, V. 2009. Assessing potential of MODIS derived temperature/vegetation condition index (TVDI) to infer soil moisture status. *International Journal of Remote Sensing*, 30, 23-39.
- PAUWELS, V. R., HOEBEN, R., VERHOEST, N. E. & DE TROCH, F. P. 2001. The importance of the spatial patterns of remotely sensed soil moisture in the improvement of discharge predictions for small-scale basins through data assimilation. *Journal of Hydrology*, 251, 88-102.
- PEPLINSKI, N. R., ULABY, F. T. & DOBSON, M. C. 1995. Dielectric properties of soils in the 0.3-1.3-GHz range. *IEEE Transactions on Geoscience and Remote Sensing*, 33, 803-807.
- PETROPOULOS, G. P., IRELAND, G. & BARRETT, B. 2015. Surface soil moisture retrievals from remote sensing: Current status, products & future trends. *Physics and Chemistry of the Earth, Parts A/B/C*.
- PETTINATO, S., SANTI, E., PALOSCIA, S., PAMPALONI, P. & FONTANELLI, G. 2013. The intercomparison of X-band SAR images from COSMO-SkyMed and TerraSAR-X satellites: Case studies. *Remote Sensing*, 5, 2928-2942.
- PIERDICCA, N., CASTRACANE, P. & PULVIRENTI, L. 2008. Inversion of electromagnetic models for bare soil parameter estimation from multifrequency polarimetric SAR data. *Sensors*, 8, 8181-8200.
- PIERDICCA, N., PULVIRENTI, L. & BIGNAMI, C. 2010. Soil moisture estimation over vegetated terrains using multitemporal remote sensing data. *Remote Sensing of Environment*, 114, 440-448.
- PIERDICCA, N., PULVIRENTI, L. & PACE, G. 2014. A Prototype Software Package to Retrieve Soil Moisture From Sentinel-1 Data by Using a Bayesian Multitemporal Algorithm. *IEEE Journal of Selected Topics in Applied Earth Observations and Remote Sensing*, 7, 153-166.
- PILES, M., ENTEKHABI, D. & CAMPS, A. 2009. A change detection algorithm for retrieving high-resolution soil moisture from SMAP radar and radiometer observations. *IEEE Transactions on Geoscience and Remote Sensing*, 47, 4125-4131.

References

- PRAKASH, R., SINGH, D. & PATHAK, N. P. 2012. A fusion approach to retrieve soil moisture with SAR and optical data. *Selected Topics in Applied Earth Observations and Remote Sensing, IEEE Journal of*, 5, 196-206.
- PRATT, D. & ELLYETT, C. 1979. The thermal inertia approach to mapping of soil moisture and geology. *Remote sensing of environment*, 8, 151-168.
- QUESNEY, A., LE HÉGARAT-MASCLE, S., TACONET, O., VIDAL-MADJAR, D., WIGNERON, J., LOUMAGNE, C. & NORMAND, M. 2000. Estimation of watershed soil moisture index from ERS/SAR data. *Remote sensing of environment*, 72, 290-303.
- RAHIMZADEH-BAJGIRAN, P., OMASA, K. & SHIMIZU, Y. 2012. Comparative evaluation of the Vegetation Dryness Index (VDI), the Temperature Vegetation Dryness Index (TVDI) and the improved TVDI (iTVDI) for water stress detection in semi-arid regions of Iran. *ISPRS Journal of Photogrammetry and Remote Sensing*, 68, 1-12.
- RAHMAN, M., MORAN, M., THOMA, D., BRYANT, R., COLLINS, C. H., JACKSON, T., ORR, B. & TISCHLER, M. 2008. Mapping surface roughness and soil moisture using multi-angle radar imagery without ancillary data. *Remote Sensing of Environment*, 112, 391-402.
- RAHMAN, M., MORAN, M., THOMA, D., BRYANT, R., SANO, E., HOLIFIELD COLLINS, C., SKIRVIN, S., KERSHNER, C. & ORR, B. 2007. A derivation of roughness correlation length for parameterizing radar backscatter models. *International Journal of Remote Sensing*, 28, 3995-4012.
- RINCON, R. F., VEGA, M. A., BUENFIL, M., GEIST, A., HILLIARD, L. & RACETTE, P. 2011. NASA's L-band digital beamforming synthetic aperture radar. *IEEE Transactions on Geoscience and Remote Sensing*, 49, 3622-3628.
- ROBINSON, D. A. 2009. Field Estimation of Soil Water Content: A Practical Guide to Methods, Instrumentation and Sensor Technology. *Soil Science Society of America Journal*, 73, 1437.
- ROMSHOO, S. A., KOIKE, M., ONAKA, S., OKI, T. & MUSIAKE, K. 2002. Influence of surface and vegetation characteristics on C-band radar measurements for soil moisture content. *Journal of the Indian Society of Remote Sensing*, 30, 229.
- ROSEN, P., HENSLEY, S., SHAFFER, S., EDELSTEIN, W., KIM, Y., KUMAR, R., MISRA, T., BHAN, R. & SAGI, R. The NASA-ISRO SAR (NISAR) mission dual-band radar instrument preliminary design. 2017 IEEE International Geoscience and Remote Sensing Symposium (IGARSS), 2017. IEEE, 3832-3835.
- ROSEN, P. A., HENSLEY, S., WHEELER, K., SADOWY, G., MILLER, T., SHAFFER, S., MUELLERSCHOEN, R., JONES, C., ZEBKER, H. & MADSEN, S. UAVSAR: A new NASA airborne SAR system for science and technology research. 2006 IEEE Conference on Radar, 2006. IEEE, 8 pp.
- ROSENQVIST, A., SHIMADA, M., SUZUKI, S., OHGUSHI, F., TADONO, T., WATANABE, M., TSUZUKU, K., WATANABE, T., KAMIJO, S. & AOKI, E. 2014. Operational performance of the ALOS global systematic acquisition strategy and observation plans for ALOS-2 PALSAR-2. *Remote Sensing of Environment*, 155, 3-12.
- ROY, D. P., WULDER, M., LOVELAND, T. R., WOODCOCK, C., ALLEN, R., ANDERSON, M., HELDER, D., IRONS, J., JOHNSON, D. & KENNEDY, R.

2014. Landsat-8: Science and product vision for terrestrial global change research. *Remote sensing of Environment*, 145, 154-172.
- RÜDIGER, C., WESTERN, A. W., WALKER, J. P., SMITH, A. B., KALMA, J. D. & WILLGOOSE, G. R. 2010. Towards a general equation for frequency domain reflectometers. *Journal of hydrology*, 383, 319-329.
- SAATCHI, S. S. & MCDONALD, K. C. 1997. Coherent effects in microwave backscattering models for forest canopies. *IEEE Transactions on Geoscience and Remote Sensing*, 35, 1032-1044.
- SABAGHY, S., WALKER, J. P., RENZULLO, L. J. & JACKSON, T. J. 2018. Spatially enhanced passive microwave derived soil moisture: Capabilities and opportunities. *Remote Sensing of Environment*, 209, 551-580.
- SAHEBI, M. & ANGLES, J. 2010. An inversion method based on multi-angular approaches for estimating bare soil surface parameters from RADARSAT-1. *Hydrology and Earth System Sciences*, 14, 2355-2366.
- SANO, E. E., HUETE, A. R., TROUFLEAU, D., MORAN, M. S. & VIDAL, A. 1998. Relation between ERS-1 synthetic aperture radar data and measurements of surface roughness and moisture content of rocky soils in a semiarid rangeland. *Water Resources Research*, 34, 1491-1498.
- SARABANDI, K. & LIN, Y.-C. 2000. Simulation of interferometric SAR response for characterizing the scattering phase center statistics of forest canopies. *IEEE Transactions on Geoscience and Remote Sensing*, 38, 115-125.
- SARABANDI, K., PIERCE, L. E., DOBSON, M. C., ULABY, F. T., STILES, J. M., CHIU, T., DE ROO, R., HARTIKKA, R., ZAMBETTI, A. & FREEMAN, A. 1995. Polarimetric calibration of SIR-C using point and distributed targets. *IEEE transactions on geoscience and remote sensing*, 33, 858-866.
- SARABANDI, K., PIERCE, L. E., OH, Y., DOBSON, M. C., ULABY, F. T., FREEMAN, A. & DUBOIS, P. 1994. Cross-calibration experiment of JPL AIRSAR and truck-mounted polarimetric scatterometer. *IEEE transactions on geoscience and remote sensing*, 32, 975-985.
- SATALINO, G., BALENZANO, A., MATTIA, F. & DAVIDSON, M. W. 2014. C-band SAR data for mapping crops dominated by surface or volume scattering. *IEEE Geoscience and Remote Sensing Letters*, 11, 384-388.
- SATALINO, G., MATTIA, F., DAVIDSON, M. W., LE TOAN, T., PASQUARIELLO, G. & BORGEAUD, M. 2002. On current limits of soil moisture retrieval from ERS-SAR data. *IEEE Transactions on Geoscience and Remote Sensing*, 40, 2438-2447.
- SATALINO, G., PANCIERA, R., BALENZANO, A., MATTIA, F. & WALKER, J. COSMO-SkyMed multi-temporal data for land cover classification and soil moisture retrieval over an agricultural site in Southern Australia. *Geoscience and Remote Sensing Symposium (IGARSS), 2012 IEEE International, 2012. IEEE*, 5701-5704.
- SCHIRMBECK, L. W., FONTANA, D. C., SCHIRMBECK, J. & MENGUE, V. P. 2017. Understanding TVDI as an index that expresses soil moisture. *Journal of Hyperspectral Remote Sensing*, 7, 82-90.
- SCHMUGGE, T., JACKSON, T. & MCKIM, H. 1980. Survey of methods for soil moisture determination. *Water Resources Research*, 16, 961-979.

References

- SCHULTE, R., FEALY, R., CREAMER, R., TOWERS, W., HARTY, T. & JONES, R. 2012. A review of the role of excess soil moisture conditions in constraining farm practices under Atlantic conditions. *Soil Use and Management*, 28, 580-589.
- SCIPAL, K., DRUSCH, M. & WAGNER, W. 2008. Assimilation of a ERS scatterometer derived soil moisture index in the ECMWF numerical weather prediction system. *Advances in water resources*, 31, 1101-1112.
- SENEVIRATNE, S. I., CORTI, T., DAVIN, E. L., HIRSCHI, M., JAEGER, E. B., LEHNER, I., ORLOWSKY, B. & TEULING, A. J. 2010. Investigating soil moisture–climate interactions in a changing climate: A review. *Earth-Science Reviews*, 99, 125-161.
- SENEVIRATNE, S. I., LÜTHI, D., LITSCHI, M. & SCHÄR, C. 2006. Land–atmosphere coupling and climate change in Europe. *Nature*, 443, 205-209.
- SHI, J., WANG, J., HSU, A. Y., O'NEILL, P. E. & ENGMAN, E. T. 1997. Estimation of bare surface soil moisture and surface roughness parameter using L-band SAR image data. *IEEE Transactions on Geoscience and Remote Sensing* 35, 1254-1266.
- SHIMADA, M. 2011. Model-based polarimetric SAR calibration method using forest and surface-scattering targets. *IEEE Transactions on Geoscience and Remote Sensing*, 49, 1712-1733.
- SHIMADA, M., ISOGUCHI, O., TADONO, T. & ISONO, K. 2009. PALSAR radiometric and geometric calibration. *IEEE Transactions on Geoscience and Remote Sensing*, 47, 3915-3932.
- SHIMADA, M., KAWANO, N., WATANABE, M., MOTOOKA, T. & OHKI, M. Calibration and validation of the Pi-SAR-L2. Asia-Pacific Conference on Synthetic Aperture Radar (APSAR), 2013 2013a Tsukuba, Japan. IEEE, 194-197.
- SHIMADA, M., WATANABE, M., MOTOOKA, T. & KANKAKU, Y. PALSAR-2 polarimetric performance and the simulation study using the PI-SAR-L2. 2013 IEEE International Geoscience and Remote Sensing Symposium-IGARSS, 2013b.
- SONG, X., MA, J., LI, X., LENG, P., ZHOU, F. & LI, S. 2014. First Results of Estimating Surface Soil Moisture in the Vegetated Areas Using ASAR and Hyperion Data: The Chinese Heihe River Basin Case Study. *Remote Sensing*, 6, 12055-12069.
- SRIVASTAVA, H. S., PATEL, P., MANCHANDA, M. & ADIGA, S. 2003. Use of multiincidence angle RADARSAT-1 SAR data to incorporate the effect of surface roughness in soil moisture estimation. *IEEE Transactions on Geoscience and Remote Sensing*, 41, 1638-1640.
- SRIVASTAVA, H. S., PATEL, P., SHARMA, Y. & NAVALGUND, R. R. 2009. Large-area soil moisture estimation using multi-incidence-angle RADARSAT-1 SAR data. *IEEE Transactions on Geoscience and Remote Sensing*, 47, 2528-2535.
- STEVENS, M. T., MCKINLEY, G. B. & VAHEDIFARD, F. 2016. A comparison of ground vehicle mobility analysis based on soil moisture time series datasets from WindSat, LIS, and in situ sensors. *Journal of Terramechanics*, 65, 49-59.
- STILES, J. M. & SARABANDI, K. 2000. Electromagnetic scattering from grassland. I. A fully phase-coherent scattering model. *Geoscience and Remote Sensing, IEEE Transactions on*, 38, 339-348.
- SU, Z., TROCH, P. & DE TROCH, F. Remote sensing of soil moisture using EMAC/ESAR data. 1997 IEEE International Geoscience and Remote Sensing Symposium (IGARSS), 1997. IEEE, 1303-1305.

- TANASE, M., PANCIERA, R., LOWELL, K. & APONTE, C. 2015. Monitoring live fuel moisture in semiarid environments using L-band radar data. *International Journal of Wildland Fire*, 24, 560-572.
- TANASE, M. A., PANCIERA, R., LOWELL, K., APONTE, C., HACKER, J. M. & WALKER, J. P. 2014a. Forest biomass estimation at high spatial resolution: Radar versus lidar sensors. *IEEE Geoscience and Remote Sensing Letters*, 11, 711-715.
- TANASE, M. A., PANCIERA, R., LOWELL, K., HACKER, J. & WALKER, J. P. Estimation of forest biomass from L-band polarimetric decomposition components. 2013 IEEE International Geoscience and Remote Sensing Symposium-IGARSS, 2013. IEEE, 949-952.
- TANASE, M. A., PANCIERA, R., LOWELL, K., TIAN, S., HACKER, J. M. & WALKER, J. P. 2014b. Airborne multi-temporal L-band polarimetric SAR data for biomass estimation in semi-arid forests. *Remote Sensing of Environment*, 145, 93-104.
- TAYLOR, K. E. 2001. Summarizing multiple aspects of model performance in a single diagram. *Journal of Geophysical Research: Atmospheres*, 106, 7183-7192.
- THOMA, D., MORAN, M., BRYANT, R., RAHMAN, M., HOLIFIELD-COLLINS, C., SKIRVIN, S., SANO, E. & SLOCUM, K. 2006. Comparison of four models to determine surface soil moisture from C-band radar imagery in a sparsely vegetated semiarid landscape. *Water resources research*, 42.
- TOMER, S. K., AL BITAR, A., SEKHAR, M., ZRIBI, M., BANDYOPADHYAY, S., SREELASH, K., SHARMA, A., CORGNE, S. & KERR, Y. 2015. Retrieval and Multi-scale Validation of Soil Moisture from Multi-temporal SAR Data in a Semi-Arid Tropical Region. *Remote Sensing*, 7, 8128-8153.
- TORRES, R., SNOEIJ, P., GEUDTNER, D., BIBBY, D., DAVIDSON, M., ATTEMA, E., POTIN, P., ROMMEN, B., FLOURY, N. & BROWN, M. 2012. GMES Sentinel-1 mission. *Remote Sensing of Environment*, 120, 9-24.
- TOURE, A., THOMSON, K. P., EDWARDS, G., BROWN, R. J. & BRISCO, B. G. 1994. Adaptation of the MIMICS backscattering model to the agricultural context-wheat and canola at L and C bands. *IEEE Transactions on Geoscience and Remote Sensing*, 32, 47-61.
- TSANG, L., KONG, J. A. & SHIN, R. T. 1985. *Theory of microwave remote sensing*, New York, Wiley.
- TSANG, L., LIAO, T.-H., TAN, S., HUANG, H. & QIAO, T. Microwave remote sensing of soil, ocean, snow and vegetation based on 3D Numerical Solutions of Maxwell Equations (NMM3D). 2017 IEEE International Geoscience and Remote Sensing Symposium (IGARSS), 2017. IEEE, 1413-1414.
- ULABY, F. T. & BARE, J. 1979. Look direction modulation function of the radar backscattering coefficient of agricultural fields. *Photogrammetric Engineering and Remote Sensing*.
- ULABY, F. T., DUBOIS, P. C. & VAN ZYL, J. 1996. Radar mapping of surface soil moisture. *Journal of hydrology*, 184, 57-84.
- ULABY, F. T., KOUYATE, F., FUNG, A. K. & SIEBER, A. J. 1982a. A backscatter model for a randomly perturbed periodic surface. *IEEE Transactions on Geoscience and Remote Sensing*, 518-528.

References

- ULABY, F. T., LONG, D. G., BLACKWELL, W. J., ELACHI, C., FUNG, A. K., RUF, C., SARABANDI, K., ZEBKER, H. A. & VAN ZYL, J. 2014. *Microwave radar and radiometric remote sensing*, Ann Arbor, The University of Michigan Press.
- ULABY, F. T., MOORE, R. K. & FUNG, A. K. 1982b. *Microwave Remote Sensing Active and Passive-Volume II: Radar Remote Sensing and Surface Scattering and Emission Theory*, Norwood, Artech House.
- ULABY, F. T., MOORE, R. K. & FUNG, A. K. 1986. *Microwave remote sensing active and passive-volume III: from theory to applications*, Norwood, Artech House.
- ULABY, F. T., SARABANDI, K., MCDONALD, K., WHITT, M. & DOBSON, M. C. 1990. Michigan microwave canopy scattering model. *International Journal of Remote Sensing*, 11, 1223-1253.
- VAN DER VELDE, R., SU, Z., VAN OEVELEN, P., WEN, J., MA, Y. & SALAMA, M. S. 2012. Soil moisture mapping over the central part of the Tibetan Plateau using a series of ASAR WS images. *Remote Sensing of Environment*, 120, 175-187.
- VAN OEVELEN, P. J. & HOEKMAN, D. H. 1999. Radar backscatter inversion techniques for estimation of surface soil moisture: EFEDA-Spain and HAPEX-Sahel case studies. *IEEE Transactions on Geoscience and Remote Sensing*, 37, 113-123.
- VERHOEST, N. E., LIEVENS, H., WAGNER, W., ÁLVAREZ-MOZOS, J., MORAN, M. S. & MATTIA, F. 2008. On the soil roughness parameterization problem in soil moisture retrieval of bare surfaces from synthetic aperture radar. *Sensors*, 8, 4213-4248.
- VIJAYA KUMAR, P., RAMAKRISHNA, Y., BHASKARA RAO, D., SRIDHAR, G., SRINIVASA RAO, G. & RAO, G. 2005. Use of remote sensing for drought stress monitoring, yield prediction and varietal evaluation in castor beans (*Ricinus communis* L.). *International Journal of Remote Sensing*, 26, 5525-5534.
- VOLO, T. J., VIVONI, E. R., MARTIN, C. A., EARL, S. & RUDDLELL, B. L. 2014. Modelling soil moisture, water partitioning, and plant water stress under irrigated conditions in desert urban areas. *Ecobydrology*, 7, 1297-1313.
- WAGNER, W., LEMOINE, G., BORGEAUD, M. & ROTT, H. 1999a. A study of vegetation cover effects on ERS scatterometer data. *IEEE Transactions on Geoscience and Remote Sensing*, 37, 938-948.
- WAGNER, W., LEMOINE, G. & ROTT, H. 1999b. A method for estimating soil moisture from ERS scatterometer and soil data. *Remote sensing of environment*, 70, 191-207.
- WAGNER, W., NOLL, J., BORGEAUD, M. & ROTT, H. 1999c. Monitoring soil moisture over the Canadian Prairies with the ERS scatterometer. *IEEE Transactions on Geoscience and Remote Sensing*, 37, 206-216.
- WAGNER, W., REIMER, C., BAUER-MARSCHALLINGER, B., ENENKEL, M., HAHN, S., MELZER, T., NAEIMI, V., PAULIK, C. & DORIGO, W. 2015. Long-term Soil Moisture Time Series Analyses based on Active Microwave Backscatter Measurements. *International Archives of the Photogrammetry, Remote Sensing & Spatial Information Sciences*.
- WAITE, W. P., SADEGHI, A. M. & SCOTT, H. D. 1984. Microwave bistatic reflectivity dependence on the moisture content and matric potential of bare soil. *IEEE Transactions on Geoscience and Remote Sensing*, 394-405.
- WALKER, J. P. & HOUSER, P. R. 2004. Requirements of a global near-surface soil moisture satellite mission: accuracy, repeat time, and spatial resolution. *Advances in water resources*, 27, 785-801.

- WALKER, J. P., WILLGOOSE, G. R. & KALMA, J. D. 2001. One-dimensional soil moisture profile retrieval by assimilation of near-surface measurements: A simplified soil moisture model and field application. *Journal of Hydrometeorology*, 2, 356-373.
- WANDERS, N., KARSSENBERG, D., ROO, A. D., DE JONG, S. & BIERKENS, M. 2014. The suitability of remotely sensed soil moisture for improving operational flood forecasting. *Hydrology and Earth System Sciences*, 18, 2343-2357.
- WANG, H., MAGAGI, R. & GOITA, K. 2017. Comparison of different polarimetric decompositions for soil moisture retrieval over vegetation covered agricultural area. *Remote Sensing of Environment*, 199, 120-136.
- WANG, L., HE, B., BAI, X. & XING, M. 2019. Assessment of Different Vegetation Parameters for Parameterizing the Coupled Water Cloud Model and Advanced Integral Equation Model for Soil Moisture Retrieval Using Time Series Sentinel-1A Data. *Photogrammetric Engineering & Remote Sensing*, 85, 43-54.
- WANG, S., LI, X., HAN, X. & JIN, R. 2011. Estimation of surface soil moisture and roughness from multi-angular ASAR imagery in the Watershed Allied Telemetry Experimental Research (WATER). *Hydrology and Earth System Sciences*, 15, 1415-1426.
- WEI, J., LI, P., YANG, J., ZHANG, J. & LANG, F. 2014. A New Automatic Ship Detection Method Using L-Band Polarimetric SAR Imagery. *IEEE Journal of Selected Topics in Applied Earth Observations and Remote Sensing*, 7, 1383-1393.
- WEIDONG, L., BARET, F., XINGFA, G., QINGXI, T., LANFEN, Z. & BING, Z. 2002. Relating soil surface moisture to reflectance. *Remote sensing of environment*, 81, 238-246.
- WICKEL, A., JACKSON, T. & WOOD, E. 2001. Multitemporal monitoring of soil moisture with RADARSAT SAR during the 1997 Southern Great Plains hydrology experiment. *International Journal of Remote Sensing*, 22, 1571-1583.
- WIGNERON, J.-P., PARDE, M., WALDTEUFEL, P., CHANZY, A., KERR, Y., SCHMIDL, S. & SKOU, N. 2004. Characterizing the dependence of vegetation model parameters on crop structure, incidence angle, and polarization at L-band. *IEEE Transactions on Geoscience and Remote Sensing*, 42, 416-425.
- WU, T.-D., CHEN, K.-S., SHI, J. & FUNG, A. K. 2001. A transition model for the reflection coefficient in surface scattering. *IEEE Transactions on Geoscience and Remote Sensing*, 39, 2040-2050.
- WU, X., WALKER, J. P., DAS, N. N., PANCIERA, R. & RÜDIGER, C. 2014. Evaluation of the SMAP brightness temperature downscaling algorithm using active-passive microwave observations. *Remote Sensing of Environment*, 155, 210-221.
- WU, X., WALKER, J. P., RÜDIGER, C. & PANCIERA, R. 2015a. Effect of land-cover type on the SMAP active/passive soil moisture downscaling algorithm performance. *IEEE Geoscience and Remote Sensing Letters*, 12, 846-850.
- WU, X., WALKER, J. P., RÜDIGER, C., PANCIERA, R. & GAO, Y. 2016. Intercomparison of Alternate Soil Moisture Downscaling Algorithms Using Active-Passive Microwave Observations. *IEEE Geoscience and Remote Sensing Letters*.
- WU, X., WALKER, J. P., RÜDIGER, C., PANCIERA, R. & GRAY, D. A. 2015b. Simulation of the SMAP data stream from SMAPEX field campaigns in Australia. *IEEE Transactions on Geoscience and Remote Sensing*, 53, 1921-1934.
- YAMAGUCHI, Y., MORIYAMA, T., ISHIDO, M. & YAMADA, H. 2005. Four-component scattering model for polarimetric SAR image decomposition. *IEEE Transactions on Geoscience and Remote Sensing*, 43, 1699-1706.

References

- YE, N., WALKER, J. P. & RÜDIGER, C. 2015. A cumulative distribution function method for normalizing variable-angle microwave observations. *IEEE Transactions on Geoscience and Remote Sensing*, 53, 3906-3916.
- YE, N., WALKER, J. P., X. WU, JEU, R. D., GAO, Y., JACKSON, T. J., JONARD, F., KIM, E., MERLIN, O., PAUWELS, V., RENZULLO, L. J., RÜDIGER, C., SABAGHY, S., C., HEBEL, V., YUEH, S. H. & ZHU, L. In Review. The Soil Moisture Active Passive Experiments: Towards calibration and validation of the SMAP mission. *Remote Sensing of Environment*.
- ZHANG, C. & MA, Y. 2012. *Ensemble machine learning: methods and applications*, Springer.
- ZHANG, X., CHEN, B., FAN, H., HUANG, J. & ZHAO, H. 2016. The Potential Use of Multi-Band SAR Data for Soil Moisture Retrieval over Bare Agricultural Areas: Hebei, China. *Remote Sensing*, 8, 7.
- ZHANG, X., CHEN, B., ZHAO, H., LI, T. & CHEN, Q. 2018. Physical-based soil moisture retrieval method over bare agricultural areas by means of multi-sensor SAR data. *International Journal of Remote Sensing*, 39, 3870-3890.
- ZHANG, X., FENG, X., XIAO, P., HE, G. & ZHU, L. 2015. Segmentation quality evaluation using region-based precision and recall measures for remote sensing images. *ISPRS Journal of Photogrammetry and Remote Sensing*, 102, 73-84.
- ZHANG, Y., GONG, J., SUN, K., YIN, J. & CHEN, X. 2017. Estimation of Soil Moisture Index Using Multi-Temporal Sentinel-1 Images over Poyang Lake Ungauged Zone. *Remote Sensing*, 10, 12.
- ZHAO, W. & LI, Z.-L. 2013. Sensitivity study of soil moisture on the temporal evolution of surface temperature over bare surfaces. *International Journal of Remote Sensing*, 34, 3314-3331.
- ZHU, L., WALKER, J. P., TSANG, L., HUANG, H., YE, N. & RÜDIGER, C. 2019a. Soil moisture retrieval from time series multi-angular radar data using a dry down constraint. *Remote Sensing of Environment*, 231, 111237.
- ZHU, L., WALKER, J. P., YE, N. & RUDIGER, C. The effect of radar configuration on effective correlation length. *Electromagnetics in Advanced Applications (ICEAA)*, 2016 International Conference on, 2016. IEEE, 820-823.
- ZHU, L., WALKER, J. P., YE, N. & RÜDIGER, C. 2019b. Roughness and vegetation change detection: a pre-processing for soil moisture retrieval from multi-temporal SAR imagery. *Remote Sensing of Environment*, 225, 93-106.
- ZHU, L., WALKER, J. P., YE, N., RÜDIGER, C., HACKER, J., PANCIERA, R., TANASE, M. A., WU, X., GRAY, D., STACY, N., GOH, A., YARDLEY, H. & MEAD, J. 2018. The Polarimetric L-band Imaging Synthetic aperture radar (PLIS): description, calibration and cross-validation. *IEEE Journal of Selected Topics in Applied Earth Observations and Remote Sensing*, 11, 4513 - 4525.
- ZINK, M., OLIVIER, P. & FREEMAN, A. 1993. Cross-calibration between airborne SAR sensors. *IEEE Transactions on geoscience and remote sensing*, 31, 237-245.
- ZOBECK, T. M. & ONSTAD, C. 1987. Tillage and rainfall effects on random roughness: a review. *Soil and Tillage Research*, 9, 1-20.
- ZRIBI, M., BAGHDADI, N., HOLAH, N. & FAFIN, O. 2005a. New methodology for soil surface moisture estimation and its application to ENVISAT-ASAR multi-incidence data inversion. *Remote Sensing of Environment*, 96, 485-496.

- ZRIBI, M., BAGHDADI, N., HOLAH, N., FAFIN, O. & GUÉRIN, C. 2005b. Evaluation of a rough soil surface description with ASAR-ENVISAT radar data. *Remote Sensing of Environment*, 95, 67-76.
- ZRIBI, M., CHAHBI, A., SHABOU, M., LILI-CHABAANE, Z., DUCHEMIN, B., BAGHDADI, N., AMRI, R. & CHEHBOUNI, A. 2011. Soil surface moisture estimation over a semi-arid region using ENVISAT ASAR radar data for soil evaporation evaluation. *Hydrology and Earth System Sciences Discussions*, 15, 345-358.
- ZRIBI, M. & DECHAMBRE, M. 2003. A new empirical model to retrieve soil moisture and roughness from C-band radar data. *Remote Sensing of Environment*, 84, 42-52.
- ZRIBI, M., GORRAB, A. & BAGHDADI, N. 2014. A new soil roughness parameter for the modelling of radar backscattering over bare soil. *Remote Sensing of Environment*, 152, 62-73.
- ZRIBI, M., SAUX-PICART, S., ANDRÉ, C., DESCROIX, L., OTTLÉ, C. & KALLEL, A. 2007. Soil moisture mapping based on ASAR/ENVISAT radar data over a Sahelian region. *International journal of remote sensing*, 28, 3547-3565.
- ZRIBI, M., TACONET, O., CIARLETTI, V. & VIDAL-MADJAR, D. 2002. Effect of row structures on radar microwave measurements over soil surface. *International Journal of Remote Sensing*, 23, 5211-5224.
- ZRIBI, M., TACONET, O., LE HÉGARAT-MASCLE, S., VIDAL-MADJAR, D., EMBLANCH, C., LOUMAGNE, C. & NORMAND, M. 1997. Backscattering behavior and simulation comparison over bare soils using SIR-C/X-SAR and ERASME 1994 data over Orgeval. *Remote Sensing of Environment*, 59, 256-266.